Spectroscopic Probes of Reactive Potential Energy Surfaces

Jeremy Miles Merritt

A dissertation submitted to the faculty of the University of North Carolina at Chapel Hill in partial fulfillment of the requirements for the degree of Doctor of Philosophy in the Department of Chemistry.

Chapel Hill

2006

Approved by

Adviser: Tom Baer

Reader: Lee Pederson

Reader: John Paponikolas

ABSTRACT

JEREMY MILES MERRITT: Spectroscopic Probes of Reactive Potential Energy Surfaces

(Under the direction of Roger E. Miller)

Free radicals play an important role in many important atmospheric and combustion reactions. Their study however, is often hampered due to their high reactivity, and thus short lifetimes, limiting the number densities which can be generated in the laboratory. While a great deal of progess has been made by studying radicals isolated in the gas-phase, much less is known about the interactions between radicals, or the interaction between a radical and another closed shell species. Clearly of interest is what happens at the transition state of a chemical reaction, the point at which bonds are broken and reformed. The areas of the potential energy surface that lead up to the transition state are the entrance and exit channel valleys, which represent weakly bound clusters between two (or more) reagent or product molecules in a chemical reaction. Due to the fact that at long-range the interaction potential is almost always attractive, minima develop near the base of the transition state which may support bound or quasi-bound states. Given that the barriers to a chemical reaction are typically several orders of magnitude larger than the dispersion forces holding these entrance channel complexes together, their importance to reaction dynamics has largely been neglected. However, there is now compelling evidence that these weak forces may actually control the dynamics in some instances due to the corresponding orientational effects. The work detailed in this thesis is focused on applying superfluid helium droplets to the study of these entrance and exit channel complexes. The extremely cold and gentle nature of the helium matrix allows us to stabilize highly reactive complexes and using high-resolution infrared spectroscopy we are able to probe the structure and dynamics of these systems.

ACKNOWLEDGEMENTS

I am so very grateful to have had the opportunity to work with Roger Miller. His enthusiasm and dedication to science has left a longstanding impression on me. Without his guidance and encouragement much of this work would not have been possible. I want to thank many of Rogers colleagues, especially Tom Baer and Mike Duncan for their support. I would also like to thank all of the members of the Miller group with whom I had the pleasure of working with. Special thanks go to Jochen Kupper, Gary Douberly, and Svemir Rudic whose contributions to some of the work detailed in this thesis does not go unnoticed. Bob Field and Ad van der Avoird are also gratefully acknowledged for their help and collaboration. I wish to thank my parents, for their love and for always believing in me. Amy DeBaillie, Myong-yong Choi, Travis Falconer, Paul Stiles, and Will Lewis I thank you for your friendship. Last but not least I want to thank the Air Force Office of Scientific Research and the National Science Foundation for funding through grants, and the Chemistry department at the University of North Carolina at Chapel Hill for funding through the James T. Dobbins fellowship for graduate research.

Dedicated in memory of Roger Miller and Kimberly Ferrell

TABLE OF CONTENTS

LIST OF TABLES

LIST OF FIGURES

Chapter 1

The Importance of the Entrance and Exit Channels

The effects of the moderately strong long-range electrostatic interactions in ion-molecule reactions are well known to have a significant influence on the associated reaction rates. In contrast, the importance of the weaker van der Waals forces in the entrance channels of neutral reactions have been only recently fully appreciated [1–4].

Experimental and theoretical work on the Cl + HD $\rightarrow$ HCl (DCl) + D (H) reaction [5–8] shows that the torque experienced by the HD in the entrance valley of the potential has a significant effect on the overall reaction rates and branching ratios. Thus two potentials (with and without the van der Waals interaction) that are rather similar in the transition state region display quite different reaction dynamics, owing to the fact that the one is repulsive at long-range (particularly in the perpendicular geometry), while the other is attractive (0.5 kcal mol^{-1}), with a T-shaped equilibrium geometry. As an extension to this work, the rotational excitation of HCl products formed from other Cl + organic molecule reactions can be accurately described by taking into account the features of the exit channel, where the dipole-dipole interaction of the departing fragments was found to be important in determining the product final state distributions [9].

Recently a completely new dissociation mechanism for formaldehyde has been discovered, which owes its existence to dispersion forces. The dissociation of formaldehyde is known to occur via two mechanisms, namely atomic (H + HCO) and molecular hydrogen (H_2 + CO) loss. The barrier to the H_2 channel is approximately 29500 cm^{-1} where as energies above 30300 cm^{-1} are needed to access the atomic channel. Towsend *et al.* observed that when the decomposition reaction is driven at the threshold for H atom loss, the H_2 and CO products exhibit very different energy partitioning (into the H_2 and CO rovibrational states) than when the reaction is promoted just below threshold [10,11]. A "roaming hydrogen atom" mechanism describes the departing H atom as wandering around the HCO because it does not have enough translational recoil to overcome the attractive dispersion forces of the potential. After some period of time, the H atom abstracts the H atom from HCO, to form the same products as the lower energy dissociation channel, but now the H_2 is much more vibrationally excited. Reactions of this type represent a significant problem for transition state theories since it has bypassed the conventional transition state altogether.

A phenomenon that has also been linked to long-range forces is the breakdown of Arrhenius behavior (Equation 1.1) for the temperature dependence of reaction rates.

$$k = Ae^{-E_a/RT} \tag{1.1}$$

Indeed, many important atmospheric reactions involving the hydroxyl radical (OH), exhibit strongly curved Arrhenius plots (ln(k) vs 1/T) [12], or negative activation energies [13, 14]. There is now theoretical evidence that this behavior is also an indication that intermediate complexes are playing a role in the dynamics [15, 16].

Each of these observations illustrate that the orientational effects of the long range potential can significantly influence reaction dynamics, reinforcing the need to have experimental and theoretical probes of these areas of the potential energy surface. Over the past twenty years it has been amply demonstrated that intermolecular potential energy surfaces can be probed by high-resolution spectroscopy of the corresponding weakly bound complexes [17]. Theory has again played a crucial role in these developments, providing the means for solving the multidimensional problem standing between the experimental results and the potential energy surface [18]. More recently, these methods have found application to reactive systems [19], where the experimental methods have the added challenge of stabilizing the entrance channel complexes, namely preventing the reactants from proceeding to form products. The cooling provided by a free jet expansion is sometimes sufficient to stabilize these complexes, which can then be subjected to spectroscopic study. The most widely studied systems are those involving OH [20–23] and NH [24] radicals, for which UV spectroscopy provides high sensitivity. These systems are analogous to the well studied HF systems [25, 26], with the exception that in some cases the barriers to reaction for the former systems can be quite low. In particular, the OH + CO system has been extensively studied in an effort to access the entrance channel of the corresponding reaction, which is of fundamental importance in both atmospheric and combustion chemistries [21–23,27–30]. The main limitation of using seeded beams to stabilize

reactive species is the relatively warm conditions early in the expansion, which in many cases prohibits stabilizing the complex before reaction occurs.

Cryogenic rare-gas matrices have also been utilized to stabilize reactive species [31–33]. The solid matrix has several advantages including controlled doping and accumulation times. Large number densities of the species of interest can be obtained due to isolation of the reactants in the inert cage of the matrix which limits their reactivity. Annealing the matrix provides some mobility, so that experiments can be carried out before and after the reaction takes place. The primary difficulty here is that the associated spectroscopy has rather poor resolution due to the matrix effects thus limiting the information that can be extracted. For instance, the anisotropic interaction of a species with the solid cage is found to quench free rotation for most molecules.

In recent years helium nanodroplets have been shown to provide many of the advantages of conventional matrices with the added benefit of high spectral resolution [34]. Indeed, rotationally resolved vibrational spectra can be obtained for complexes solvated in helium [35]. These complexes are easily grown in the helium nanodroplets by simple pick-up of two or more molecules or atoms. The high mobility of the molecules within the droplets and the low temperature (0.4 K) ensures that they quickly condense to form a complex. As a result of the rapid cooling provided by the helium, the systems of interest are often trapped in local minima on the potential energy surface [36, 37]. In the case of reactive systems one expects that this rapid cooling will also allow trapping of pre-reactive species, with very shallow wells in the entrance channel to the associated chemical reaction. Infrared laser spectroscopy is particularly well suited to these experiments, given that the perturbations to the spectrum from the helium solvent are rather weak [38]. The generality of the approach comes from the fact that detection is based upon laser induced evaporation of helium atoms from the droplets following the absorption of a single infrared photon [38]. Since the dopant molecules and radicals can be added sequentially to the droplets, there is considerable control over how the complexes are formed. For example, it is possible to bring together thermally fragile molecules (picked-up

in a low temperature cell) and a radical (produced by high temperature pyrolysis in a separate region) under the cold conditions characteristic of the droplets. As a result, the entrance channel complex can be stabilized even in systems with very small barriers to reaction [39]. The ultimate goal is to use spectroscopy to detect these exit channel complexes following photo-induced reaction starting from the corresponding entrance channel complex [40], in order to study the associated orientational effects of the potential and the effects of the solvent on the reaction dynamics.

1.1 In the remainder of this thesis ...

In Chapters 2 and 3 we lay the ground work to understand the spectroscopy of molecules and clusters doped in superfluid helium droplets and illustrate why this is such an ideal technique for the study reactive species. A method to continuously dope the droplets with radicals is developed in Chapter 3, and in Chapter 4 we study the propargyl radical monomer (C_3H_3), for which quantitative comparisons can be made with previous gas-phase studies. This study serves as confirmation that radicals can be made under the appropriate conditions for helium nanodroplet pick-up. In the remaining chapters we focus mainly on the stabilization of radical-molecule clusters, for which there are no gas-phase analogues. Chapters 5, 6, 11, and 12 concern themselves with weakly bound complexes of Cl, Br, I, Ga, Al, and In atoms with HCN and HF. Due to the open-shell nature of the atoms, multiple potential energy surfaces (giving rise to multiple isomers) are important to the dynamics and these experiments have already provided benchmarks for recent theoretical calculations. Chapters 7 and 8 focus on HCN and HF complexes with a methyl radical (CH_3) in order to probe the exit channel valley of the prototypical X + CH_4 $\rightarrow$ HX + CH_3 (X = CN, F) reactions. Here we gain physical insight into the forces which control the final state distributions of the products of the corresponding reactions. In order to study the reaction dynamics of these complexes, an infrared - infrared (IR-IR) double resonance (DR) technique is developed. Since the role of the solvent is likely

to be important to these studies, Chapter 9 applies this DR technique to HCCCN monomer, for which no reaction can occur. This experiment shows that a significant source of inhomogeneous broadening in our spectra results from the distribution of droplet sizes in the beam. By burning a hole in this distribution, a more in depth look into the vibrational relaxation dynamics of solvated molecules is possible. In Chapter 10 we apply IR-IR DR to the study of conformal isomerization of a binary complex made up of HCN and HF, and in Chapter 11 we extend these studies to photo-induced reaction of novel reactive metal atom complexes.

Chapter 2

Liquid Helium Droplet Spectroscopy

Liquid helium continues to fascinate experimentalists and theoreticians even today due to the uniqueness of its superfluid state, despite being liquefied almost 100 years ago. At one atmosphere of pressure, helium liquefies at 4.22 K but even at temperatures approaching absolute zero, never becomes a solid. When cooled below a certain critical temperature, liquid helium is found to exhibit several unusual properties, including the ability to "creep" or flow through small capillaries without friction. Objects immersed in this new liquid "state" are also found to experience no drag below a certain critical velocity, which is dependent on the temperature of the liquid. This critical temperature is identified on the phase diagram as the λ point, because a plot of the heat capacity versus temperature shows a discontinuity which resembles the Greek symbol. This transition temperature is somewhat dependent on pressure, and so the line separating the two liquid phases is called the λ-line. At saturated vapor pressure the lambda point is found at 2.17 K. The uniqueness of this "superfluid phase", as it became known, can be traced to the extremely weak interactions between helium atoms and their large zero-point energy. As a result, helium is the only known substance that can theoretically remain a liquid down to 0 K. In many respects these properties would make helium the ultimate spectroscopic matrix [41].

2.1 Historical overview

In the 1940's a theoretical understanding of the phenomenon of superfluidity was taken up by Landau [42] and independently by Tisza [43]. Landau proposed that liquid helium when cooled below its λ point, consisted of two fluids, a normal fluid fraction and a superfluid fraction. The normal fluid fraction was thought to carry all of the viscosity where as the superfluid fraction was responsible for frictionless motion. The superfluid fraction of the liquid was predicted to be zero at the λ point, but steadily increase to 100% at absolute zero. In 1946 Andronikashvili provided experimental confirmation of the two-fluid model by suspending a stack of disks into the bulk liquid and measuring their moment of inertia [44]. He observed that the added moment of inertia due to the liquid slowly decreased as the temperature was lowered from the λ point, which is exactly the opposite behavior expected for a classical liquid. Since only the normal fluid fraction of the liquid can contribute to the moment of inertia, the added moment of inertia to the disks was a direct measure of its density.

In order to explain this result, Landau proposed a form for the excitation spectrum of superfluid ^{4}He which consisted of two distinct types of collective excitations, namely "phonons" and "rotons". Phonons are long-wavelength density fluctuations where as rotons are more localized, and may be characterized by voritcal motion. Neutron scattering later confirmed Landau's hypothesis about the shape of the dispersion curve[1] and the density of states derived from such a relation is shown in Figure 2.1. The lack of low energy phonons is a characteristic feature of superfluidity.

While direct study of bulk liquid helium has been hampered by its transparency to photons below 20 eV, it was quickly realized that its properties could be interrogated by doping impurities into the liquid, and to study their interactions with the solvent, taking advantage of the optical transparency. Initial attempts to dope the liquid with impurities failed due to the very property which made it such a fascinating solvent, namely the weak interactions. As a

[1] A dispersion curve shows the energy vs momentum relationship of the collective excitations.

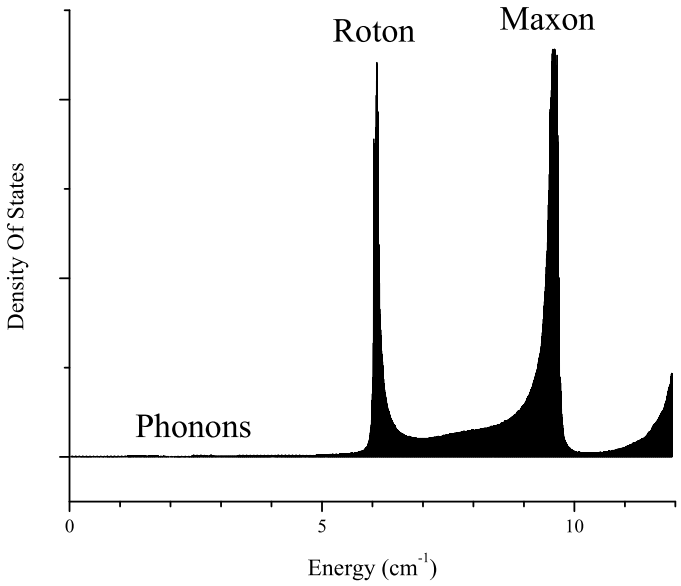

Figure 2.1: Density of states for superfluid ^{4}He. The lack of low energy phonons (density wave excitations) is a characteristic feature of superfluidity. At higher energies, rotons and maxons excitations represent vorticle motions.

result, the doped impurities were found to coagulate on the walls of the dewar, precipitating out of the bulk liquid. Several experimental techniques have been developed in order to continuously dope the liquid, including laser ablation of a metal rod immersed in the liquid, and using electric fields to hold charged species in the liquid, however only atomic impurities have been studied in this way.

An experiment which is particularly interesting to the material presented in this thesis was performed by Gordon and coworkers in which a beam of nitrogen atoms (formed by microwave discharge) was directed into bulk liquid helium [45–50]. The authors found that a temperature rise of the liquid past the λ point resulted in thermal detonation. This observation was attributed to the stabilization of nanoscale radical solids, with atomic concentrations of up to 10%. Upon heating, the atoms become more mobile in the liquid and may react with one another to give back N_2. This was probably the first example of the power of liquid helium to stabilize highly reactive species.

A more general technique to force the dopant to interact with the liquid is to solvate it in a droplet of helium. In this way the walls of the container have been removed, and since the interaction with helium is certainly better than vacuum, the dopants only choice is to interact with the liquid. Droplets of liquid helium have also gained considerable study in their own right due to the finite size effects on a quantum system. Indeed the large surface to volume ratio of a small droplet will make the effects of the surface very important. Although droplets of helium were first observed in the form of a fog soon after helium was first liquefied, it was not until 1961 when Becker and coworkers [51] formed nanoscale droplets by free jet expansion. Initial studies were still focused on studying the properties of the isolated droplets, and it wasn't until 1990 that Toennies *et al.* first showed that the droplets may be efficiently doped by passing them through a low pressure scattering chamber [52].

The first spectroscopic study of a molecule doped helium droplet was performed in 1992 when Scoles *et al.* recorded the vibrational spectrum of SF_6 [53] with a line tunable CO_2 laser. Despite the poor resolution, there were many remarkable observations. First, very sharp transitions were observed in contrast to classical liquids or even cryogenic matrices indicating that the vibrational relaxation was quite slow. Secondly, the spectrum was only shifted from the gas-phase origin by -1.7 cm^{-1}, illustrating that the interaction with the solvent was very weak. Spectral bands were also assigned to the SF_6 dimer, showing that cluster formation is facile. An apparent splitting of the normally triply degenerate ν_3 vibrational mode, led the authors to speculate that SF_6 might reside on the surface in analogy to that found for argon droplets [54][2], despite theoretical calculations which predicted that it should be solvated [55]. Soon after, Frochtenicht *et al.* rescanned the spectrum using continuously tunable diode lasers and found that the spectrum was rotationally resolved, and could be simulated by using the gas-phase Hamiltonian with only slightly modified constants. The rotational fine structure indicated that the symmetry of the complex is preserved, consistent with being solvated somewhere near the center of the droplet. It was later discovered that the apparent splitting originally

[2]Note that the argon "droplets" are solid at these experimental conditions.

observed was due to a complex between SF_6 and background nitrogen. The long coherence times needed for nearly free rotation were taken as an indication of superfluidity, however it wasn't fully clear that this behavior might simply be a consequence of the extremely weak solute-solvent interaction. The relative intensities of the rovibrational transitions provided the first experimental measurement of the droplet temperature, namely 0.38 K, which is in excellent agreement with theoretical predictions [56]. Although this is strictly a rotational temperature, the other degrees of freedom are believed to be at least approximately in equilibrium[3].

The rotational constant for SF_6 was determined to be a factor of approximately three smaller than the gas-phase value, suggesting that the helium adds to the effective moment of inertia. The magnitude of this effect could be explained by placing 8 helium atoms in the octahedral sites of the van der Waals potential, and having them rotate rigidly with the molecule. Given the rather large zero-point effects for helium, the notion that the helium was rigidly bound to the SF_6 was certainly a crude model, but the idea that some of the helium density is able to adiabatically follow the motion is one that has gained considerable theoretical support [35, 57–63].

The first direct evidence for the superfluidity of the droplets came from the electronic spectrum of glyoxal ($C_2H_2O_2$) [64, 65]. In contrast to rotational and vibrational spectroscopy in helium droplets, where the effects of the droplet are quite small, electronic excitation causes a much stronger coupling with the compressional (phonon) modes of the droplet, and can lead to phonon wings[4] in the spectra. Interestingly a distinct 5 cm^{-1} gap was observed between the onset of the phonon wing and the zero-phonon line. The nature of this gap is clear from Figure 2.1, namely the density of phonons with this energy is small. In addition, the overall shape and fine structure observed in the phonon wing closely matches the bulk density of states for the rotons [65].

[3] An exception would be nuclear spin isomers, which do not relax on the timescale of the experiment.

[4] A phonon wing results from the simultaneous excitation of the electronic transition and the collective modes of the helium.

Grebenev *et al.* performed diode laser studies on OCS, which again revealed sharp rotational structure. Interestingly when the experiment was repeated in pure ^{3}He droplets, the rotational motion was found to be highly quenched [58]. Since bulk liquid ^{3}He is not superfluid at the equilibrium temperature of the droplets, the loss of the long rotational lifetimes definitively showed that superfluidity played an important role. This is consistent with the fact that bulk superfluid ^{4}He has a "phonon gap" that extends up to approximately 5 cm^{-1}, which places the low-lying rotational states (those populated at 0.37 K) in a region where the density of bulk phonons is low. This correspondingly weak coupling between molecular rotation and the bulk phonons gives rise to the long rotational lifetimes. In ^{3}He there is no phonon gap, and the rotational states are able to couple to a larger density of phonon states, thus decreasing their lifetimes. In what became known as the "microscopic Andronikashvili" experiment, Grebenev *et al*. showed that OCS doped in mixed ^{3}He / ^{4}He droplets regained its rotational structure upon the addition of about 60 ^{4}He atoms [58]. Due to the larger zero-point energy of ^{3}He, the helium is believed to phase-separate, and the ^{4}He clusters around the OCS forming a small superfluid droplet embedded in the ^{3}He. These experiments proved that it was not simply the weak interactions which gave rise to the rotational resolution, since ^{3}He exhibits an even weaker interaction than ^{4}He.

The definition of superfluidity is based upon bulk thermodynamic quantities, and the notion of "superfluidity" in a finite size system is still debated [42]. What is clear is that ^{4}He is a boson, and the Pauli principle requires the total wavefunction to be symmetric with respect to the exchange of two particles ($\Psi(x_1, x_2) = \Psi(x_2, x_1)$). In contrast ^{3}He is a fermion, and thus the total wavefunction must be antisymmetric ($\Psi(x_1, x_2) = -\Psi(x_2, x_1)$). Two acceptable wavefunctions for a two particle system are given below:

$$\begin{aligned} \Psi_{boson}(x_1, x_2) &= \phi_i(x_1)\phi_j(x_2) + \phi_i(x_2)\phi_j(x_1) \\ \Psi_{fermion}(x_1, x_2) &= \phi_i(x_1)\phi_j(x_2) - \phi_i(x_2)\phi_j(x_1) \end{aligned}$$

where ϕ_i and ϕ_j are different spatial wavefunctions. For bosons, another equally acceptable wavefunction is:

$$\Psi_{boson}(x_1, x_2) = \phi_i(x_1)\phi_i(x_2)$$

where both particles share the same spatial wavefunction. In this case it is easy to see how each particle looses its identity, becoming delocalized. Despite the fact that even at 0 K, the Bose-Einstein Condensate (BEC) fraction is predicted to only account for ~ 10% of the total density [66], there is considerable support for a description of the dynamics in terms of these individual quantum mechanical exchanges [67–72].

2.2 Dynamics of cluster growth

The growth of molecular clusters in helium droplets has been observed to been quite different than in gas-phase expansions, where typically only the global minimum is observed. Cluster formation is facilitated by the high mobility of the dopants in the liquid and the small volume of the droplets, such that the attractive interactions between the dopants ensures that they will quickly find each other and condense to form a complex. Pick-up of multiple dopants is sequential, meaning that each dopant is cooled to 0.37 K on a timescale faster than cluster formation. By using two independent pick-up cells, Nauta *et al.* have shown that different HF-Ar$_n$ clusters are formed depending on whether the HF or the argon is picked up first [73]. When HF is picked up first, the infrared spectra were consistent with the argon solvating the HF. In contrast, when HF is picked up second, an argon cluster is formed (and cooled back down to 0.37 K) which then binds HF to the surface. Since the global minimum structures all correspond to the HF being solvated, the helium droplet is found to prevent rearrangement of the argon cluster when the HF is picked up second. This is due to the fact that the helium is continuously maintaining equilibrium by evaporation, and thus the condensation energy from forming the complex must removed on a timescale faster than it can anneal the cluster. Cluster formation in helium may be thought of as an experimental realization of geometry optimiza-

tion by minimization of the energy by steepest decent, given that the helium tries to force the cluster to stay at the zero-point level. Using multiple pick-up cells the design of taylor made clusters is possible.

Long-range forces will also be important in determining the approach geometries of the dopants. As an illustrative example, consider the fact that the lowest energy configuration of two point dipoles at long range, is a head to tail arrangement. At 0.37 K, the dipole-dipole interaction of two 3 debye dipoles is greater than the thermal energy at a distance of ~6 nm, which acts to pre-orient the dipole moments as the two come together. Such behavior was first observed by Nauta *et al.* for HCN, in which linear chains of up to 10 monomer units have been assigned [36][5]. No evidence for cyclic or stacked structures were observed, despite the fact that the global minimum arrangement becomes cyclic for $(HCN)_{n\geq 4}$. Cyclic structures are found to be exclusively formed in gas-phase expansions. Here again, the helium is found to dissipate the ~1000 cm^{-1} hydrogen bond energy upon each successive addition to the chain, which would otherwise give the cluster enough energy to isomerize to the global minimum.

In lighter systems such as $(H_2O)_n$ [37] and $(HF)_n$ [39], the situation is more complicated due to tunneling, and in the case of $(H_2O)_{n=3-6}$ only cyclic structures are observed. The observation of a cyclic hexamer, illustrates that the sixth water molecule is able to insert into the precooled cyclic pentamer.

The goals of the experiments presented in this thesis are to take advantage of this non-equilibrium cluster growth, and apply it to the stabilization of more highly reactive species.

2.3 Helium vs the gas-phase

The list of molecules studied in helium droplets has grown significantly over the past decade, and now a large enough database has been compiled to make quantitative compar-

[5]The vibrational frequency shift becomes progressively smaller upon the addition of each HCN, and so the spectra converge to a limiting value, preventing definitive assignment of larger chains.

isons with the gas-phase. The importance of observed "trends" in the properties of solvated molecules cannot be over-emphasized, because helium nanodroplets provide us with a medium to stabilize species which may not be possible using any other method. Indeed, only one of the molecules presented in this thesis has been observed previously in the gas-phase, and so we need to be able to make reliable comparisons with *ab initio* calculations.

2.3.1 Vibrational band origins

One of the greatest advantages to helium droplet spectroscopy when compared to other rare-gas matrices is that the vibrational frequencies are typically shifted less than 0.1% from the gas-phase. Thus when gas-phase data is unavailable, a direct comparison with *ab initio* theory can be made. Such a small frequency shift is predicted to result from two competing effects, namely a blue-shift from short-range repulsive interactions due to a crowding by the helium atoms in the first solvation shell, and a red-shift due to the longer-range dispersion interaction with the helium more remote from molecule [74]. Since only the latter interaction changes significantly with droplet size, the vibrational frequency typically shifts slightly to the red with increasing droplet size. This shift converges to a "bulk" value because now adding more helium to the droplet places it too far away from the molecule to add significantly to the interaction. Due to the distribution of droplet sizes in the beam, this effect can give rise to inhomogeneous broadening. A discussion of this effect is presented in Chapter 9.

Vibrational modes which are involved in linear hydrogen bonds are found to have systematically larger droplet induced red-shifts as the strength of the hydrogen bond increases. Figure 2.2 shows the gas-phase origin minus the helium droplet origin plotted against the complexation shift (helium origin for the complex minus the helium origin for the monomer) for many complexes. The presence of the solvent might decrease the magnitude of the intermolecular bending motion, thus changing the strength of the hydrogen bond. Indeed, a more linear hydrogen bond (vibrationally averaged) would give rise to a larger red-shift, in agreement with the experimental results. Such an effect might also be due to a transition dipole induced dipole po-

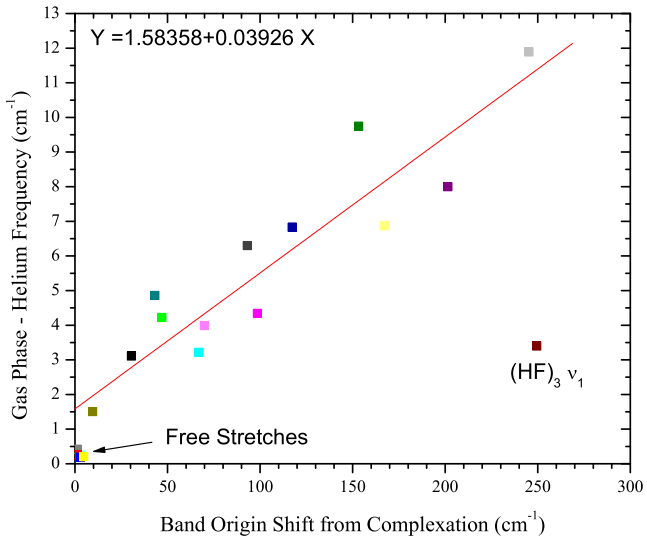

Figure 2.2: A graph of the gas-phase - helium droplet band origin versus the shift observed in helium from complexation for several binary molecular complexes measured in our group. The plot clearly shows that for free stretches the effect of the helium is typically a very small redshift (> 1 cm^{-1}) where as for hydrogen bonded modes there is a strong correlation between helium induced shift from gas-phase and hydrogen bond strength. The data points for the free stretches have not been included in the fit.

larization effect of the surrounding helium, which lowers the energy of the excited state by an amount proportional to the transition intensity. Using the best fit equation shown in the figure, we have estimated the gas-phase transitions for several of the complexes studied in this thesis, in order to make a more quantitative comparison with high-level theoretical calculations. Repeating this analysis for complexes studied in argon matrices, we find that the perturbation is an order of magnitude stronger in argon, which is consistent with the larger polarizability of argon compared with helium. The scatter of the data points is also much greater, limiting the use of such an estimator.

2.3.2 Rotational dynamics

2.3.2.1 Rotational relaxation rates

As pointed out above, the long rotational coherence times observed in helium droplets are directly connected to superfluidity, in that there is a low density of phonon states (below 5 cm^{-1} [65]) to which the populated rotational states may couple. When the rotational relaxation energy meets, and eventually exceeds the phonon gap however, the lifetimes are shortened significantly. See for example Figure 11 of Reference [75]. In addition to very light rotors such as HF [76], the population of rotational states at 0.37 K with high enough energy to couple to the phonons may result from nuclear spin statistics [77, 78]. For "heavy" molecules (B < 1 cm^{-1}) it is interesting that despite the weak coupling between the elementary excitations and the rotational states that the molecules do somehow manage to cool down to the droplet temperature of 0.37 K. Since the flight time of the droplets through the experiment is on the order of milliseconds, even a very weak coupling may be enough to achieve relaxation. Double resonance experiments have been carried out which indicate that the low energy surface "ripplon" states may be responsible for such relaxation [79]. Since in general the molecule is confined to the interior of the droplet, this coupling is weak consistent with the fact that the ripplons have limited penetration depths.

2.3.2.2 Rotational constants

Much has been written about the fact that the rotational constants of solvated molecules are smaller than those of the corresponding gas-phase complex. Figure 2.3 shows a plot of the helium rotational constant versus the gas-phase constants for essentially all of the molecules studied to date. In general, the effect of the helium decreases with increasing rotational constant. This can be understood given that for light rotors (B > 1 cm^{-1}) the rotational motion is simply too fast for the helium to follow, and the solvated rotational constants are thus only slightly decreased compared to the gas-phase. Another way of stating this is that the interaction

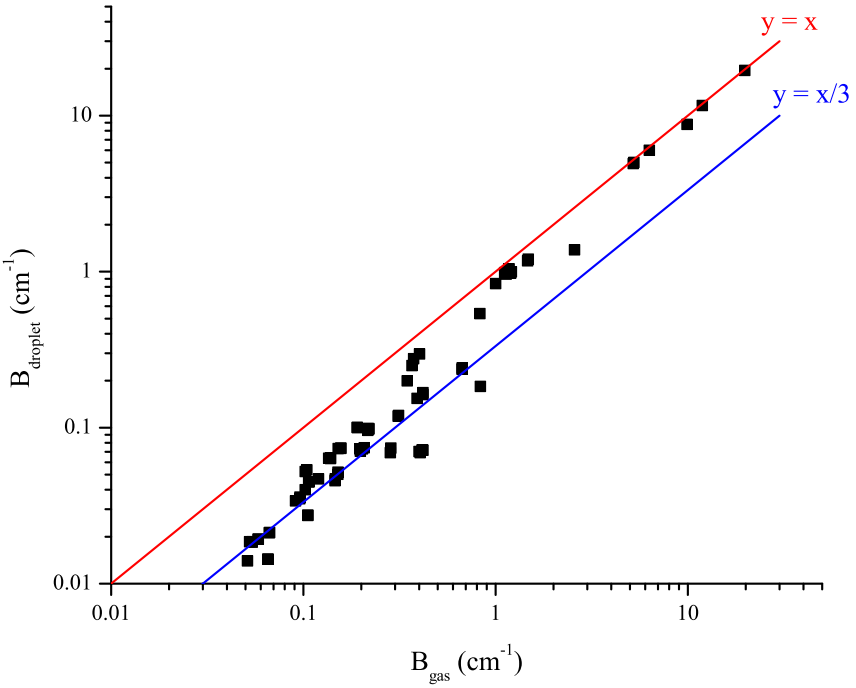

Figure 2.3: A plot of the rotational constants (gas-phase vs helium droplet) for a large body of molecules and complexes studied. The lines are meant to illustrate the two different dynamical regimes of the effect of the helium droplet on the moments of inertia of the solvated molecule. For light rotors, (B $\geq$ 1 cm^{-1}) the helium is unable to adiabatically follow the motion and thus the helium droplet rotational constant is only slightly reduced from the gas-phase. For heavier rotors however, the helium clearly adds to the moment of inertia and a reduction factor of approximately 2.5 - 3.0 is commonly observed.

potential is too isotropic, and there is no handle for the molecule to "stir up" the helium. For heavier rotors, rotational constants are typically reduced by a factor of 2.5 $\pm$ 0.5, illustrating that the helium does add to the molecules moment of inertia. Because these rotational constants are determined to spectroscopic accuracy, the scatter in the graph is important, and is reflective of the individual molecule-helium interaction potential. Indeed, N_2O and CO_2 have very similar gas-phase rotational constants however the reduction factor for N_2O is much larger [69]. Fully quantum mechanical calculations have reproduced this effect, which is based on the differences of the interaction potentials with helium [72, 80, 81]. This theoretical understanding is important if structural information, including bond lengths, are to be extracted from helium

spectra. Nevertheless, the rotational fine structure can be used to determine the symmetry of many species, even though the bond lengths may be poorly determined.

2.3.2.3 Centrifugal distortion

In order to fit helium droplet spectra with the corresponding gas-phase Hamiltonian, centrifugal distortion constants that are 10^2 - 10^4 times larger than the gas-phase values are typically needed. These constants are representative of the rotational-state dependence of the helium-molecule interaction, rather than a break-down of the rigid-rotor approximation for the dopant. Based on the trends observed in the rotational constants, it was initially a surprise that the centrifugal distortion constants were positive, based on the assumption that as the molecule rotates faster, the helium would have a greater difficulty following. This would be consistent with the fact that lighter rotors have smaller rotational constant reductions. Thus higher J states were expected to decouple from the helium, giving rise to a negative distortion constant. Lehmann has treated this problem theoretically using a 'toy model' for a planar rotor coupled to a ring of helium atoms [82]. He finds that the stronger interaction with the helium as J increases is due to the increase in the angular anisotropy of the rotational wavefunction, giving rise to the positive D values. An empirical relation between the rotation and centrifugal constants has been experimentally observed (See Figure 15 of reference [75]) :

$$D = 0.031(4) * B^{1.82(4)}$$

Such a correlation is not observed in the gas-phase, which shows that the interaction arises from a completely different mechanism. Theoretical calculations have also been able to quantitatively reproduce this correlation for a few small molecules [81, 83].

2.3.3 Vibrational dynamics

Based on the experimental detection technique, it is obvious that for SF_6 and OCS vibrational relaxation occurs on the time scale of the experiment. The molecule couples this vibrational energy to the fundamental excitations of the droplet, which then leads to evaporation, depleting the beam intensity. In contrast, HF monomer is observed not to relax on the timescale of the experiment, simply carrying its vibrational energy to the bolometer [76]. Such a long relaxation time is consistent with the large mismatch in energy that must be accommodated by the helium. An excitation of several hundred phonons and rotons would be necessary to relax this much energy, thus one might expect this to be a slow process. The difference between these cases is the presence of intermediate vibrational levels in polyatomic molecules which may facilitate relaxation by a cascading process. Smaller amounts of energy are removed in each step of the relaxation thus enhancing the rates. Interestingly for the Ar-HF complex, vibrational relaxation was observed in large droplets, due to the addition of the low frequency modes, however for small droplets the lifetime again became longer than the experiment. In the gas-phase, Ar-HF is found to have an excited lifetime greater than the timescale for the helium droplet experiment, so relaxation must be facilitated by the helium. This is reasonable given that vibrational relaxation for these small clusters is typically in the sparse density of states regime, so that the helium is able to fill in the energetic gaps needed to facilitate relaxation. The droplet size dependence of the relaxation time is consistent with the fact that the density of phonon states increases rapidly with droplet size. In a related experiment, clusters of HF with up to five neon atoms did not relax. Thus it appears that the HF stretching vibration is too weakly coupled to the low frequency modes, to allow for relaxation. It is important to point out that all of the spectra presented in this thesis were observed by depletion of the helium beam, illustrating that they do vibrationally relax on the timescale of the experiment.

For polyatomic molecules it is clear that vibrational relaxation occurs on the timescale of the experiment, yet is relatively slow owing to the sharp lines observed in their spectra. Indeed the lifetimes are usually long enough, that the linewidth is dominated by inhomogeneous

broadening due to the finite size of the droplet and the distribution of droplet sizes (See Chapter 9). Relaxation rates have been observed to be much faster is systems with anharmonic resonances however [77, 84]. This suggests that the the low frequency modes (involved in the resonance) are more easily relaxed to the helium, and thus act as a "doorway" to relax population out of the initially populated "bright" state. A similar effect is reported on in Chapter 11, where fast vibrational relaxation is observed when exciting a combination band which involves a low frequency vibrational mode.

It is known from gas-phase studies that after infrared excitation of weakly bound complexes, the end result is typically vibrational predissociation. Roger Miller was one of the first to exploit this behavior to actually measure the infrared spectra of these complexes in a free jet expansion, monitoring the change in beam intensity using either a "flop out" [85] or "flop in" [86] detection scheme. These results raise the interesting question regarding the ultimate fate of a vibrationally excited complex in a helium droplet. It is clear that the effect of the solvent may take on two different dynamical regimes. If the cooling of the helium is competitive the intramolecular vibrational energy redistribution (IVR) rates, then the complex might be cooled before the needed energy is channeled into the dissociation coordinate, and thus never comes apart. In contrast, if the complex does manage to come apart, one expects that on a longer timescale the helium will act as a cage, facilitating recombination. This important question is addressed in Chapter 10. Assuming that we can photo-initiate an isomerization or chemical reaction, the helium will cool the complex back down to 0.37 K on some longer timescale. Much like classical matrices, we can then use double resonance techniques to probe for the cold reaction products.

Chapter 3

Experimental Methods

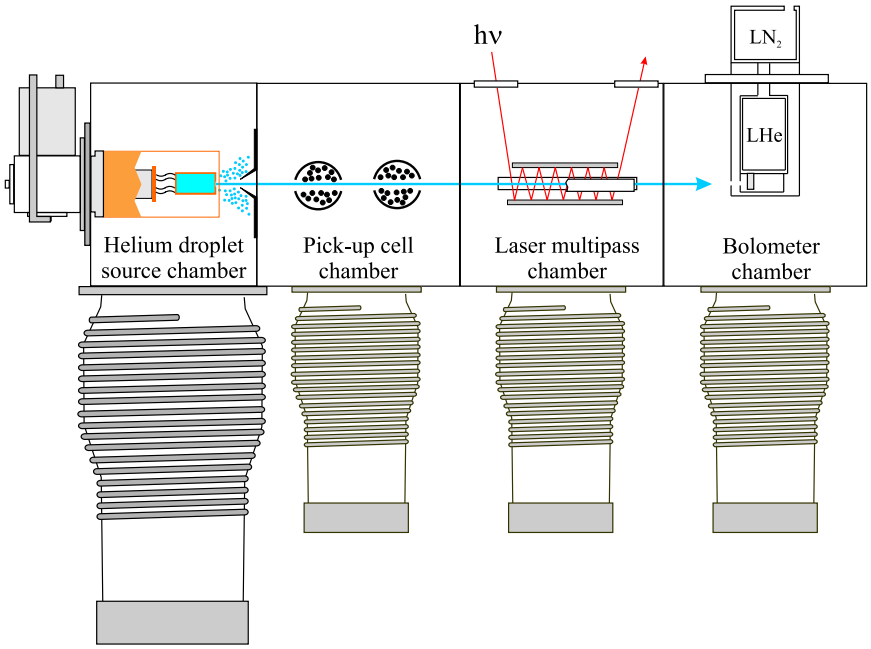

Figure 3.1: A schematic diagram of the helium droplet apparatus used in this work. The laser induced attenuation of the droplet beam intensity is monitored with a liquid helium cooled bolometer using phase sensitive detection.

The studies presented in this thesis have been carried out with the helium droplet machine shown schematically in Figure 3.1. The reader is referred to the doctoral dissertations of Klaus Nauta (UNC-2000) and Gary Douberly (UNC-2006) for the fine details of the experimental setup, so only the most important details will be given here.

3.1 Droplet production

Helium droplets are formed in the first of 4 differentially pumped chambers by expanding high-pressure, ultra-high purity helium gas into vacuum through a cooled nozzle. Typical source conditions for our machine are 40 - 50 Bar backing pressure and nozzle temperatures of 12-25 K. The helium gas expands through a 5 μm pinhole and by condensation, the helium clusters to form droplets. Such cold nozzle temperatures are necessary to form droplets due to the extremely weak interactions between helium atoms. The size of the nozzle aperture is largely determined by the pumping speed of the source chamber pump. Our setup uses a 8000 l/s diffusion pump which can adequately handle the continuous flux. The droplets are formed in the early, high pressure portion of the expansion. As the pressure falls below the equilibrium vapor pressure of the droplets, they cool by evaporation. The evaporation rate becomes negligible (on the order of microseconds) when the droplet reaches a temperature of 0.37 K for ^{4}He droplets [56, 87]. Droplet formation is a statistical process which results in a distribution of sizes. In the early 1990's the size and velocity distributions of these droplet beams, as well as their dependence on the nozzle conditions, were determined. Figure 3.2 shows a set of calibration curves for the mean droplet size ($\bar{N}$) based on the nozzle temperature and backing pressure for a 5 μm nozzle. For $\bar{N} < 10^4$ atoms, the droplet sizes were measured by crossed molecular beam scattering, and Knuth *et al.* have determined an empirical scaling law with the nozzle temperature, backing pressure, and orifice diameter as free parameters [88]. For droplet sizes larger than 10^4 their size has been analysed by first embedding an electron and then measuring its deflection in an electric field [89]. The discontinuity in droplet size occurs when helium liquefies in the nozzle, and for nozzle temperatures less than about 14.0 K these droplets are formed from fragmentation of the liquid. Depending on the nozzle temperature, the droplet velocities [90, 91] typically fall in the range of 200 - 400 m/s, meaning that in a typical apparatus with a beam path of 1 meter, the flight time of the droplets is approximately 2 - 5 ms. The ability to change the droplet size is an important variable because the droplet size limits the total amount of coolant available. For example, a 10000 atom droplet has a

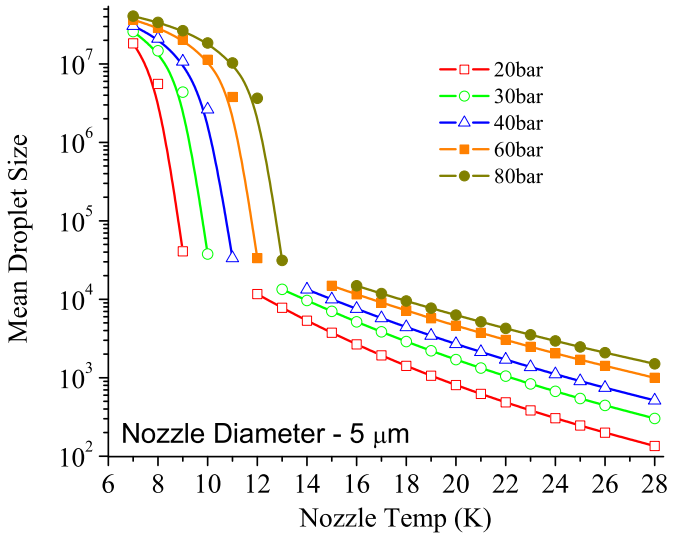

Figure 3.2: A series of curves representing the mean droplet sizes produced for various source conditions based upon the published empirical results [88]. The sudden change of slope occurs when the helium liquefies in the nozzle, giving rise to a qualitatively different expansion regime.

heat capacity of ~6 eV, assuming each atom carries away 5 cm^{-1} of energy [56]. It is usually advantageous to work with the smallest droplets possible however, because more droplets are formed when their mean size is small.

It is now generally accepted that for source conditions which produce mean droplet sizes of a few thousand atoms or less, the size distribution is Log-Normal:

$$P_N(N) = \frac{1}{N\sigma\sqrt{2\pi}}\, e^{-\frac{(lnN-\bar{N})^2}{2\sigma^2}}$$

where σ is a empirically fit standard deviation which depends on the mean droplet size [91]. For our typical experimental conditions, a few of these distributions are plotted in Figure 3.3, and it is clear that there are a wide range of droplet sizes present in the beam. A rule of thumb for the full width at half maximum of the distribution is ~ $0.7\bar{N}$.

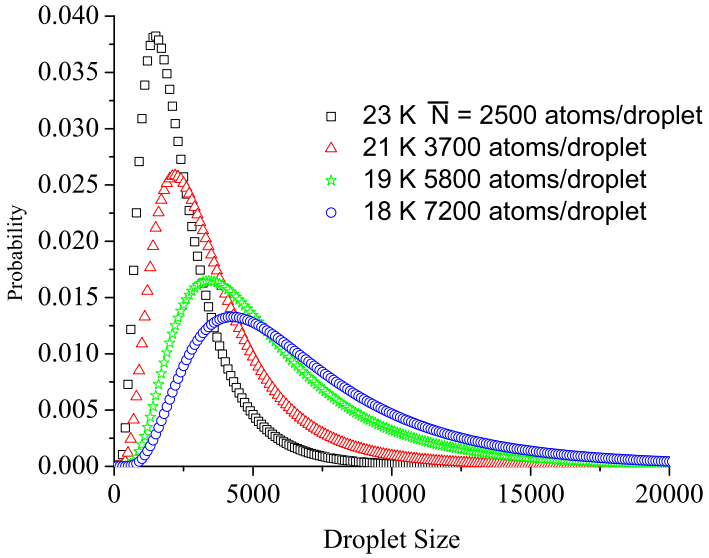

Figure 3.3: A series of curves representing the log-normal distribution of droplet sizes produced for given a nozzle temperature at 50 Bar backing pressure. As the mean droplet size increases, so does the width.

The droplet radius may be calculated if the density is known. Assuming the density is the same as the bulk, ρ = 0.0218 Å^{-3}, the droplet radius is given by $V = \frac{4}{3}\pi R^2 = N/\rho$, or:

$$R = 2.22\sqrt[3]{N}\ (\text{Å})$$

Thus a 3000 atom droplet has a radius of 32 Å. In reality the average density of a droplet is somewhat less than the bulk value and only approaches the bulk for large droplets [92]. Scattering experiments and calculations have shown that the helium density drops off rapidly near the surface and falls from 90% to 10% over approximately 6 Å for ^{4}He droplets [93]. This fall-off in density creates a trapping potential, effectively confining a dopant away from the surface [94].

The pinhole nozzle in our experiment is cooled by a closed cycle helium refrigerator which provides 1 watt of cooling power at 4.2 K (Sumitomo). The refrigerator also has a more powerful, higher temperature stage (50 watts @ 50 K), which is used to cool a copper shield around

the nozzle in order to reduce the blackbody load, and to precool the helium gas. A silicon diode is attached near the tip of the nozzle in order to measure its temperature. Flexible strip heaters are placed between the cold head and nozzle, to raise it to a desired temperature, and a PID feedback loop maintains the temperature to ± 0.05 K (Lakeshore Model 321 controller). The nozzle is connected to the cold head via 3 tightly woven copper braids, which make the thermal connection, as well as providing flexibility to align the nozzle while under vacuum. About 1 cm downstream from the nozzle the expansion is skimmed by a 0.4 mm conical skimmer to form a beam. This small aperture also allows the necessary differential pumping to prevent contamination of the droplets by background gas in the subsequent chambers.

3.2 Doping the droplets

After passing through the skimmer the droplets enter a second differentially pumped chamber where intensional doping of impurities may take place. The "pick-up" technique was pioneered in 1985 by Scoles, by crossing a molecular beam of argon droplets with an effusive SF_6 source [54]. From its infrared spectrum, SF_6 was found be efficiently picked up, residing on the surface of the solid Ar droplets. In 1990 Toennies first showed that helium droplets may also pick-up foreign species [52], and in 1992 Scoles recorded the vibrational spectrum of SF_6 in helium droplets [53]. Doping was found to be easily achieved by crossing the helium droplet beam with either an effusive beam or a molecular beam from a jet expansion. In addition, efficient doping was also observed by simply passing the droplet beam through a static gas cell, where the dopant pressure was maintained at approximately 1×10^{-6} Torr. The collision velocities are above the Landau critical velocity, so there is no worry about the dopant passing directly through the droplet. Pick-up cross-sections have been determined to be 50 - 90% of the geometrical cross-section [95].

In our experimental setup we have a 3 cm long differentially pumped tube in which the helium beam passes through holes drilled in both sides. Using a needle valve, gases and liquids

with high vapor pressure can be introduced into this cell for pick-up. The geometrical cross section of a droplet is $\sigma = \pi R^2 = 15.5N^{2/3}$ (Å^2). As a 3000 atom droplet travels through the pick-up cell it sweeps out a volume (V) of approximately 10^{12} Å^3. Assuming a sticking coefficient of 1 (pick-up cross-section = geometric cross-section), the gas pressure (P), needed to dope the droplet with just one impurity is:

$$P = \frac{\rho RT}{N_A}$$

where ρ is the gas density (1/V), R is the ideal gas constant, T is the gas temperature, and N_A is Avogadro's constant. For a 3000 atom droplet and a pick-up cell length of 3 cm, a pressure of approximately 1×10^{-5} Torr is all that is needed to dope the droplets with just one impurity. For low vapor pressure materials an oven may be used to heat the sample to get the needed vapor pressure. Note that helium droplet experiments need some 4 orders of magnitude less vapor pressure than that typically needed for seeded beams. Thus materials which thermally decompose before sufficient vapor pressure is generated for seeded beams are ideally suited for helium droplet study. Also materials which may require impractical temperatures for sufficient vapor pressure may also be more easily studied. The need for such a low pick-up cell pressure illustrates that the background pressure in the experiment must be as low as possible to prevent picking up background gases. For large droplets which have extremely large collision cross sections, we find that pressures of $< 10^{-8}$ Torr are needed to prevent contamination. For the droplet sizes typically used for spectroscopy, much more modest pressures are needed. Each of the chambers in our experiment (neglecting the source chamber) has a typical background pressure of 1×10^{-7} Torr.

Initially there was some controversy over whether SF_6 resided on the surface of the droplet or was solvated. The experimental results first favored a surface site in analogy to argon droplets, however theoretical calculations said it should be solvated. Higher resolution experiments confirmed that SF_6 was solvated, but later, alkali atoms were shown conclusively to

reside on the surface [96–100]. Using the dopant molecule-helium atom pair potential, Ancilotto *et al.* have devised a simple formula to predict whether an impurity will be solvated or instead reside on the surface of the helium droplet [101]. Formally,

$$\lambda = 2^{-\frac{1}{6}}\,\sigma^{-1}\rho\,\epsilon\,R_e$$

where σ is the surface tension of the liquid (0.179 cm $^{-1}$ Å^{-2}), ρ is the bulk superfluid helium density (0.022 Å^{-3}), and ϵ and R_e are the well depth and equilibrium bond distance of the pair potential respectively. λ represents the gain in energy due to the interaction between the dopant and the helium atoms against the cost of creating a cavity within the droplet. If the dopant helium interaction is favorable (λ > 1.9), the dopant will be solvated. For alkali and heavy alkaline earth atoms, this parameter correctly predicts that they reside on the surface. Almost all other atoms and molecules are solvated because of their much more favorable interaction with the helium.

As noted above, the pick-up collision velocities are above the Landau critical velocity and are easily coupled the excitations of the droplet. These excitations then lead to quantum evaporation of helium atoms from the surface of the droplet, efficiently quenching the translational, solvation, and internal energy of the dopant. According to the liquid drop model, each evaporating helium atom removes approximately 5 cm^{-1} of energy, which corresponds to the energies of phonons [56]. The lower excitation energy of the ripplons brings the droplet and dopant back down to the equilibrium temperature of 0.37 K.

If the pressure is high enough in the pick-up cell then a given droplet may pick-up more than one impurity. Since this process is statistical, a distribution of cluster sizes will be formed. The chance of picking up a particular number of molecules (k) at a given gas density (ρ) at a given droplet size is given by a Poisson Distribution [102]:

$$P_k(\mu) \;=\; \frac{\mu^k}{k!}\,e^{-\mu}$$

$$\mu = \rho \sigma L$$

where σ is the collisional cross section of the droplet and L the pick-up cell length. The maximum in the distribution is found when $\mu = k$ and thus the optimum pick-up cell pressure of two dopants is twice that of the monomer. Figure 3.4 shows a plot of the spectroscopic

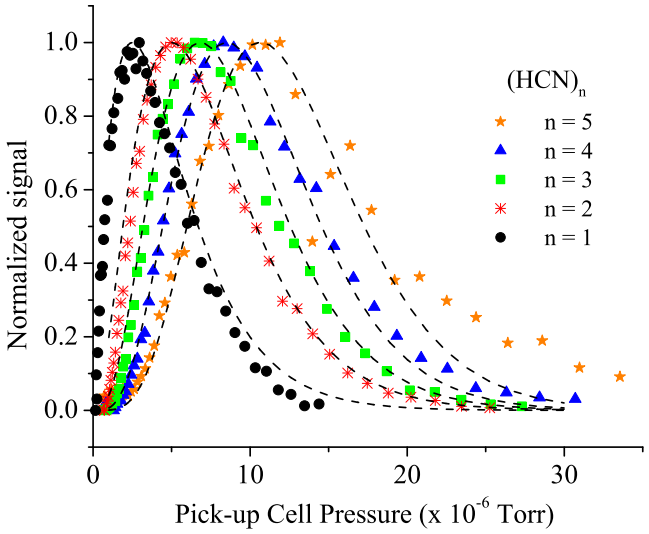

Figure 3.4: Normalized signals for $(HCN)_n$ clusters plotted as a function of the pick-up cell pressure. The signals correspond to the pendular spectra for each species, which are well separated in the infrared spectrum. The dotted lines are the Poisson distribution probabilities for each cluster size weighted by the appropriate log-normal distribution of droplet sizes. Measurement of these curves allows one to quickly determine the stoichiometry of a cluster.

signals for the HCN chains [36] as function of the pick-up cell pressure illustrating this point. The dotted lines are the optimum pressure predicted by the Poisson distribution, which have been weighted over the appropriate log-normal distribution of droplet sizes. Measurement of the pick-up cell pressure dependencies is clearly a powerful tool to identify the number of dopants in a cluster.

The Poisson distribution assumes that pick-up events are rare and independent of one another. This is not exactly true for helium droplets because the formation of the X_{n-1} cluster reduces the droplet size (due to evaporatively cooling the complex back down to 0.37 K) be-

fore the next dopant is picked up. The error in assuming a Poisson distribution will depend on how much energy is released in between each pick-up event and thus agreement is expected to become gradually worse for larger cluster sizes. A Monte Carlo simulation could be used to incorporate these effects, however for the weakly bound van der Waals complexes studied here, these errors are quite small as can be inferred from the agreement in Figure 3.4.

3.2.1 Doping droplets with radicals

Although free radicals play a central role in many gas-phase chemical processes, their spectroscopic study is often hampered by their reactivity, which limits the gas-phase number densities that can be achieved in practical experiments. In recent years, however, a number of methods have been developed for producing such radicals in sufficiently high concentrations to permit high-resolution spectroscopic studies in the gas-phase [103–125]. In the infrared region of the spectrum, direct absorption methods have been used to obtain rotationally resolved spectra of a number of such systems, in both gas cells [104, 105] and free jet expansions [106–117]. The radicals of interest are typically produced by pyrolysis [106, 107], microwave discharge [108–113], electric discharge [114–117] or photolysis [118–125]. For example, flash pyrolysis has been used to generate radicals in cold supersonic jets, as first demonstrated by Kohn *et al*. [106]. In these and subsequent studies, small organic radicals were produced from the pyrolysis of halogenated precursors seeded in helium or argon. It was often possible to obtain essentially complete depletion of the precursor molecules [126].

3.2.1.1 Pyrolysis source

It should be noted that while all of the above methods of producing radicals are widely used, none of them is ideally suited for helium nanodroplet pick-up. This is due to the rather low concentration of radicals when compared to the other species present, whether it be undissociated precursor, unwanted reaction complexes, or buffer gas. Indeed, the concentration of radicals is often so low that high sensitivity techniques have been developed solely for their de-

tection. The issue of purity does not necessarily represent a problem for gas-phase experiments so long as the background pressure is kept low enough to prevent collisions, and that the concentration is high enough for the experimental sensitivity. The slit-jet apparatus of Nesbitt for example can produce approximately 10^{13} OH radicals / cm^3 however this still only represents 1 - 2% fragmentation of the available 0.1% H_2O mixture [127]. The need for a much higher purity radical source for helium nanodroplet doping stems from the fact that helium droplets easily pick up any species it collides with. Therefore the probability that a droplet picks up only the desired radical becomes very small with decreasing cleanliness.

To overcome the issue of cleanliness an effusive pyrolysis source was designed which operates with no buffer gas. A schematic diagram of our first generation source is shown in Figure 3.5. The source is built on a standardized design using a vacuum load-lock system, so that it can be easily introduced and removed from the experimental apparatus. The heart of the source is a quartz or alumina tube with a 6mm (1mm) outside (inside) diameter in which the end section is heated resistively. Heating is accomplished by wrapping the end 2.5 cm of the tube with a 0.25 mm diameter tantalum wire and encasing it in a high temperature ceramic paste (Aremco Ceramacast 576 / Aremco Ceramabond 552) to increase contact between the filament and tube. A K-type thermocouple is also embedded in the ceramic for temperature measurement. A water cooled copper block is used to cool the tube a few inches from the tip and to prevent outgassing from the rest of the source. The source can be routinely operated at 1500 K for periods in excess of 100 hours and higher temperatures of up to 1800 K for shorter periods of time. Typically 30 Volts (5 Amps) is sufficient to reach these temperatures. The flow of precursor is regulated from a static reservoir at room temperature by a stainless-steel needle valve. At typical operating pressures of a few militorr within the source, the flow from the tube is in the effusive regime, and the molecules only make a few collisions with the walls at the tip of the source. A weak bond in an appropriately selected precursor molecule may be broken when the source is heated, but the low pressure helps prevent radical-radical and radical-wall collisions which minimizes recombination of the newly formed radicals. The

source is positioned such that the droplet beam passes approximately 1 mm from of the exit from the pyrolysis source. The need for the source to operate as a supersonic jet is eliminated because the radicals are cooled by the droplets.

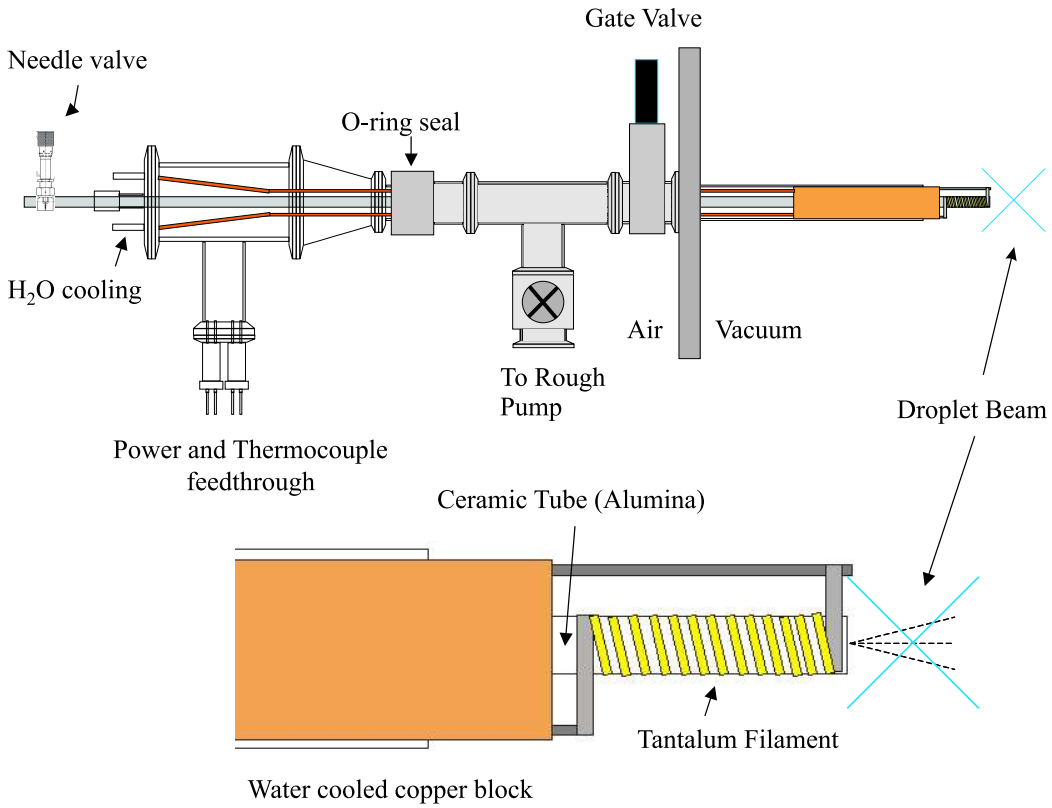

Figure 3.5: A schematic diagram of the pyrolysis source used in the current studies to dope the helium droplets with free radical species. The source is based on a resistive heating element which provides the excess energy needed to break the weak bonds of a radical precursor. Temperatures of 1500 K can be routinely achieved.

In order to address the issue of source lifetime a second generation source was designed which uses a 1 mm tantalum filament. This design requires significantly more current to heat the filament due to its small resistance. A 20 times step-down transformer was used in combination with a variac to supply the necessary power. Substantially better water cooling of the electrodes supplying the current to the filament was also implemented.

We have also developed a pyrolysis source design based upon direct resistive heating of a silicon-carbide tube in which the gas is flowed. Our design is based upon that of Ellison's [128], using a silicon carbide tube of approximately 2mm OD (1mm ID) in size (Saint Gobain Ceramics). The smaller size when compared with our earlier design uses less power to achieve the same temperature and also does not suffer from outgassing of the ceramic paste. In contrast to a metal filament, silicon carbide's resistance decreases with increasing temperature and so great care was taken upon initial heating because a constant voltage source was used. The ultimate upper temperature limit of the source is similar to the filament design however a thermocouple is not easily attached for accurate temperature measurement.

Each of the three pyrolysis source designs were used interchangeably and only small differences were observed in the signal levels associated with the radicals.

3.2.1.2 Optimizing radical production

Where applicable, the pyrolysis source was optimized for radical production by first looking for an infrared absorption of the precursor molecule or a complex of the precursor with another chromophore. Typically the experiment was optimized on a known HCN or HF absorption and the source was put into position. The pyrolysis source has a water cooled shield covering the heated portion of the tip, which has two holes drilled in it for the helium beam to enter and exit. These two holes are used to roughly align the source with the helium beam, and to shield the rest of the machine from blackbody radiation. The precursor molecule was then regulated into the apparatus with a room temperature pyrolysis source. As a rule of thumb, the HCN (or HF) signal was decreased to a value of approximately 2/3 which accounts for some complexation. Pendular survey scans were then performed to find an absorption due to either the precursor itself or a complex with HCN or HF. If such an absorption is found, optimizing the signal allows us to determine the appropriate pressures for pick-up using the effusive source. Once optimized, the source temperature is raised until nearly 100% of the precursor signal is depleted. Pyrolysis occurs over a narrow temperature range and it is usually

disadvantageous to continue raising the temperature beyond this point due to the possibility of further decomposition. Survey scans are repeated and compared with the cold source scans, specifically looking for peaks which are only present with the pyrolysis source hot.

If a precursor absorption could not be found, the source temperature and pressures can also be optimized via mass spectrometry. An example is given for the production of methyl radicals in Chapter 7.

3.2.1.3 High temperature oven

Experiments have also been performed to elucidate the structure and reaction dynamics of weakly bound clusters of aluminum and gallium atoms with organic molecules. While these metals are not typically thought of as being radicals, their atoms are highly reactive and contain unpaired electrons. These properties make aluminum and gallium prototypical catalytic reaction centers. The generation of a suitable vapor pressure of the respective metals is achieved using a oven capable of heating solid samples to temperatures in excess of 1500 K. The source is built on the same basic design as the pyrolysis source, i.e. one that is load-lockable. The sample is held by an alumina coated crucible formed from a 1 mm diameter tungsten filament (Ladd Research). The source is positioned such that the droplet beam passes directly over the mouth of the crucible. Again, the probability of picking up one or more metal atoms is simply a function of its vapor pressure, which is easily controlled by the temperature.

3.3 Vibrational spectroscopy and detection

It is clear that spectroscopy of doped helium droplets provides a unique probe of both the solute and solvent. The effects of the solvent however are in general so small that they are only observed because of the high-resolution nature of the experiment. Due to the weak binding energy of a helium atom to the droplet, depletion techniques have been exploited for spectro-

scopic detection. It is now known that for most molecules[1] vibrational excitation couples to the fundamental excitations of the droplet resulting in the evaporation of several hundred helium atoms. For a 3000 cm^{-1} vibrational transition, approximately 600 helium atoms will be evaporated from the droplet (assuming the removal of 5 cm^{-1} per atom [56]). This reduction of on-axis beam flux is used to detect the excitation.

Bolometers and mass spectrometers are the two most commonly used methods to measure the droplet beam flux. All of the spectroscopic studies in this thesis have been carried out using bolometric detection with the exception of one experiment (see Chapter 5) where a mass spectrometer was used. A bolometer is a semiconducting device whose resistance is extremely sensitive to its temperature. By aligning the droplet beam to impinge upon the bolometer, the (mainly kinetic) energy of the beam is transfered to the bolometer, thus heating it up. The bolometer element is wired in series with a load resistor to form a voltage divider circuit, converting the change in resistance into a voltage drop. In order to achieve the needed sensitivity, the bolometer is cooled to 1.6 K[2] in order to decrease its heat capacity and to reduce Johnson noise. To further increase signal levels the surface area of the bolometer is enhanced with a diamond collector (2 mm $\times$ 5 mm). A JFET preamplifier is also placed close to the bolometer (with in a few centimeters) reducing microphonic noise induced by vibrations.

The laser interacts with the helium droplet beam using multipass optics in order increase the effective path length of the interaction. Both linear and spherical (not shown in Figure 3.1) multipass cells have been used and yield a factor of approximately 50 greater signal to noise ratio when compared to a single pass. A mechanical chopper is used to modulate the laser intensity, so that the droplet beam intensity may be measured with the laser beam on and off. The wavelength dependent attenuation of the helium droplet beam is demodulated using a lock-in amplifier, giving rise to the depletion spectrum. In the case of HF, where

[1] An exception would be diatomic molecules which do not vibrationally relax on the timescale of the experiment.

[2] Cooling to 1.6 K is achieved by pumping away the vapor from a liquid helium reservoir.

vibrational relaxation is not observed, the excess energy from the excitation is simply carried to the bolometer resulting in a net increase in the signal reaching the bolometer. All of the spectra presented in this thesis are of the depletion type, which shows that vibrational relaxation does occur on the time scale of the experiment. Two spherical multipass cells are used in the double resonance studies of Chapters 9 and 10 which gives well defined, spatially separated, interaction volumes for the pump and probe lasers. The multipass cells are also equipped with electrodes which allow Stark and Pendular spectroscopy to be performed.

For the HCN monomer R(0) transition (the only transition observed due to the cold temperature and HCN's relatively large rotational constant), with an F-center laser power of ~5 mW, a 1 - 1.5% depletion of the helium droplet beam intensity is observed which corresponds to a signal to noise ratio of approximately 700. Heavier molecules will have more states populated at the droplet temperature and so the intensity will be spread out making our sensitivity less. For these molecules that are polar, Pendular spectroscopy is an important analytical tool which can be used to collapse the rotational fine structure, integrating the signal into one peak.

3.3.1 Stark and pendular spectroscopy

3.3.1.1 Pendular spectroscopy

An important tool used in this thesis is Pendular spectroscopy [25, 129, 130]. It relies on brute force orientation of the permanent dipole moment of a molecule (or complex) in the lab fixed frame, which is defined by application of large DC electric fields. For the linear molecule case, the torque associated with the orienting field on the rotational motion of the molecule causes a mixing of the field-free $|J, M\rangle$ states (M is conserved) which transforms the normally isotropic rotational motion into a libration (or pendulum) motion which is constrained about the field axis, hence the term "pendular" states. The extent of mixing is given by the orientability, $\omega = \frac{\mu E}{B}$ where μ is the dipole moment, E is the electric field strength and B is the rotational constant. In the limit of $\omega \rightarrow \infty$, the energies of the pendular states are given by E(J,M;ω) = -ω+ $(\nu_p + 1)(2\omega)^{1/2}$, or that of a two-dimensional angular oscillator [129]. The pendular

quantum number ν_p = 2J - |M| , takes on values of $\nu_p = 0, 1, 2, \cdots$. The electric dipole selection rules allow the usual $\Delta M = 0$ (laser polarization parallel to the electric field) and $\Delta M = 1$ (polarization perpendicular to the electric field) transitions which give rise to the selection rules $\Delta\nu_p = 0$ and $\Delta\nu_p = \pm 1$ for parallel and perpendicular polarization respectively. As $\omega \rightarrow \infty$ the $\Delta J = \pm 1$ selection rule breaks down due to the mixing of J states. For vibrational excitation, the allowed transition frequencies are given as ν_0+ (E'(J,M;ω) - E"(J,M;ω)):

$$\nu_0 + \left\{ -\frac{\mu' E}{B'} + (\nu_p' + 1)\left(\frac{2\mu' E}{B'}\right)^{1/2} - \left[-\frac{\mu'' E}{B''} + (\nu_p'' + 1)\left(\frac{2\mu'' E}{B''}\right)^{1/2} \right] \right\}$$

Assuming that the dipole moment and rotational constant do not change upon vibrational excitation, $\Delta\mu = \Delta B = 0$, the transition frequencies simplify to $\nu_0 + (2\omega)^{1/2}(\nu_p' - \nu_p'')$. For a parallel transition ($\nu_p' - \nu_p'' = 0$) all of the transitions stack up at the zero-field band origin, which we will denote as a pendular "Q" branch. This has the effect of a considerable enhancement of the signal to noise ratio which is useful when searching for new species and separating out overlapping bands. In addition, since the transition dipole moment (for linear molecules) is also on average more oriented with the laser polarization, the signal can be enhanced further by a factor of three. Figure 3.6 shows a series of spectra taken for cyanoacetylene as the magnitude of the electric field strength is increased, illustrating the pendular effect for a parallel transition of a linear molecule. For a perpendicular transition ($\nu_p' - \nu_p'' = \pm 1$) the transition frequencies are found to be $\nu_0 \pm (2\omega)^{1/2}$ also leading to a considerable simplification of the band structure. At very high fields however, the signal levels decrease because the transition moment is oriented perpendicular to the laser polarization. When the assumption that $\Delta\mu = \Delta B = 0$ is not valid, the pendular transitions no longer lie exactly on top of one another, and a progression of peaks is observed. An example of this is observed for Br-HF in Figure 5.15.

With the low rotational temperatures observed in helium droplet experiments and the ability to apply electric field strengths of up to 120 kV cm^{-1}, the pendular limit can be reached in systems with large permanent dipole moments (> 1 D) and small rotational constants (> 1 cm^{-1}).

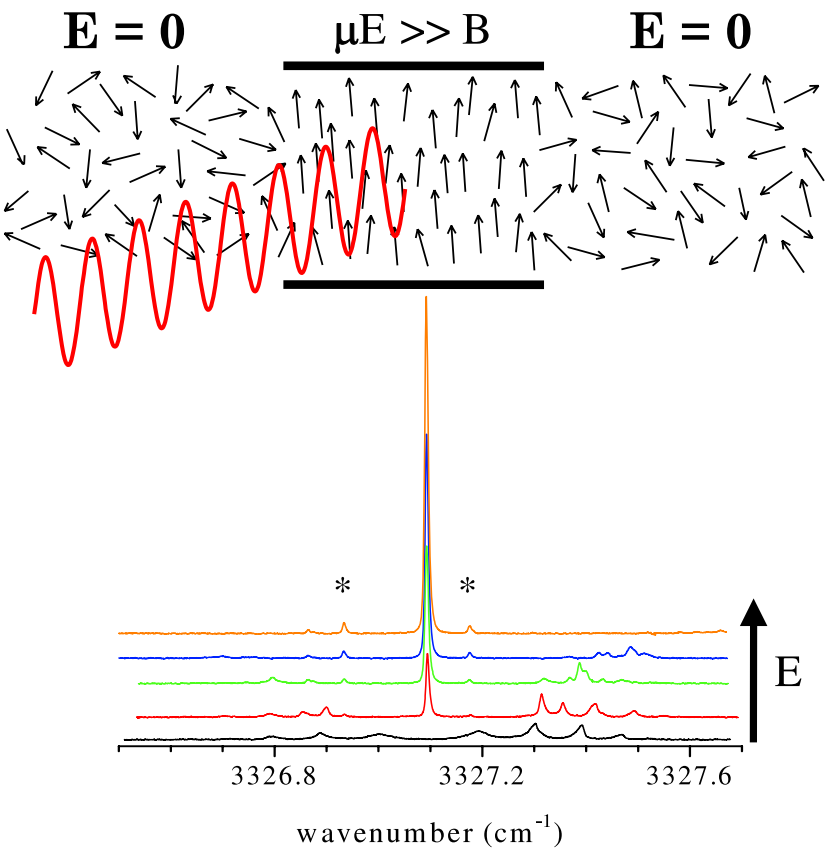

Figure 3.6: A series of spectra of the HCCCN molecule with varying electric field strengths. The lowest trace was recorded under field-free conditions. At the highest fields, the free rotation of the molecule is quenched, resulting in a single pendular peak. The two peaks marked with an asterisk are related to HCCCN-N_2 complexes.

For an asymmetric top, the vibrational transition dipole moment no longer necessarily points in the same direction as the permanent dipole moment. Therefore by orienting the permanent moment by the field, the angle between the transition moment and laser polarization is important in determining the band strength. By measuring the relative magnitude of enhancement or diminishment of the band intensity under parallel and perpendicular polarizations (laser polarization oriented with respect to the electric field direction), the angle between the vibrational transition moment and the permanent dipole moment can be measured [131]. This method provides a unique structural assignment tool, given that these angles can be accurately calculated using even modest levels of *ab initio* theory.

3.3.1.2 Stark spectroscopy

At the high field strengths used for pendular spectroscopy, the spectrum is rather insensitive to the dipole moment. To determine a molecule's dipole moment, the spectrum is recorded at somewhat lower field strengths where the change in the spectrum is maximized by the field strength. Due to the inherent broadening associated with solvation in helium, we are often not able to assign transitions resulting from individual M_J states, so the field strength is increased until significant mixing of J states has occurred. A modeling of the resulting spectra under these conditions is not amenable to perturbation theory, and therefore a fully variational calculation is undertaken. The full Hamiltonian matrix is setup including the interaction with the field, and numerically diagonalized to get eigenvalues and eigenvectors. From fitting the experimental Stark spectra (of which the field-free constants are already determined) one can then determine μ' and μ''. The electric field strength for these measurements is calibrated by measuring the Stark splitting of the R(1) transition of gas-phase HCN into is $M_J = 0 \leftarrow 0$ and $\pm 1 \leftarrow \pm 1$ transitions. Since the applied voltage is known and the dipole moments for HCN are known in both the ground and excited vibrational states [132, 133], the distance between the stark plates can be accurately determined.

3.3.1.3 Dipole moments measured in helium droplets

Now that we can measure dipole moments, the next logical question is: are the dipole moments of solvated molecules different than in the gas-phase? This question has been addressed previously by our group using the HCN and HCCCN molecules as examples [134], since both the helium and gas-phase dipole moments are accurately known. It that work, it was shown that the helium dipole moments are consistently lower than the gas-phase values, by 2.3% and 4% respectively. Although this deviation is already quite small, and thus in general allowing one to make direct comparisons with gas-phase, its value may be approximated by considering the effect of the dipole moment's polarization on the surrounding helium. Since the embedded molecule acts to carve out a cavity in the helium, the induced dipole moment of the solvent

will be critically dependent on the shape of this cavity. For a non-spherical molecule, HCN for example, the induced polarization on the ends of the molecule will be in the same direction as the permanent dipole moment. Along the sides of HCN however, the helium will be polarized oppositely than that of the permanent moment. Since for a prolate ellipsoidal cavity, appropriate for HCN, there will be more helium atoms contributing along the belt of the molecule than on the ends, the measured dipole moment will be somewhat smaller than the gas-phase value, in agreement with that observed. Interestingly for an oblate top, the measured dipole is predicted to be larger than the gas-phase, however an experimental example is lacking.

It is important to point out that we have not attempted to correct the measured dipole moments in this thesis for such a helium droplet interaction. It is clear that this effect is quite small and typically amounts to just a few percent. The reader is referred to reference [134] for a full discussion of the calculation of the helium correction factor.

3.3.2 Laser systems

3.3.2.1 Burleigh F-center laser

The main laser system used to generate infrared radiation was a continuous wave Burleigh F-center laser (FCL-20), which is shown schematically in Figure 3.7. Lasing action is achieved by pumping a color center crystal with the red light from a Kr-ion laser (Coherent Sabre). Two different crystals are used; (#2) KCl:Li and (#3) RbCl:Li providing infrared light between 3000 cm^{-1} and 4100 cm^{-1} , at a peak output power of approximately 15 mW. The first order reflection from a grating (~95% reflectivity) is coupled back into the cavity and the zeroth order reflection is used as the laser output. An additional intracavity etalon is used to make the laser run on a single cavity mode. The end-mirror of the cavity is mounted on a piezoelectric crystal which allows us to continuously tune the cavity length and thus the laser frequency. In order to prevent unwanted hops in frequency all three tuning elements must be tuned synchronously, which is done by computer control. The intracavity etalon is maintained at the optimum position during a scan by applying a small amplitude sine wave dither of approximately 500 Hz to

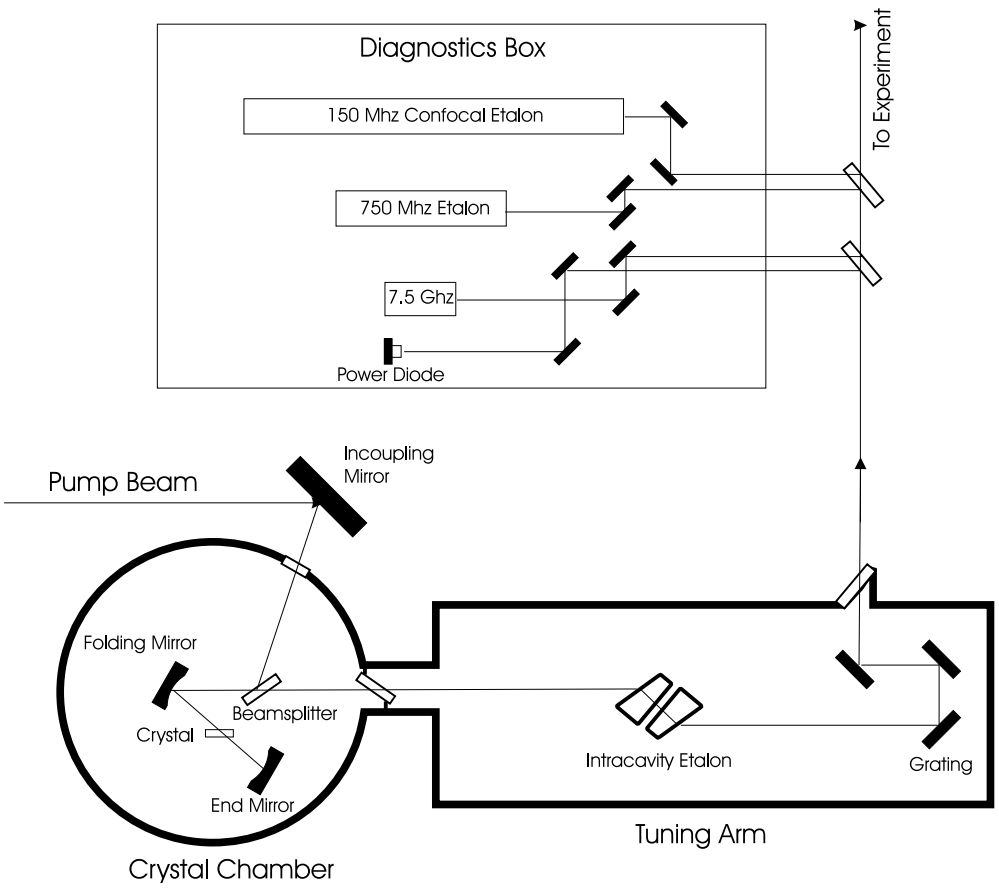

Figure 3.7: A schematic diagram of the Burleigh F-center laser (FCL-20) which generates high-resolution tunable infrared light from 4100 - 3000 cm^{-1}.

the air-gap, which is just large enough to cause a small power oscillation of the laser, due to its phase overlap with a specific cavity mode. Using phase sensitive detection the output power may be used as an error signal to lock the etalon to a cavity mode. The grating is controlled passively with a stepper motor and a series of calibration tables. The typical bandwidth of this laser is a few MHz.

Sometimes it is advantageous to give up such high resolution, in order to obtain faster tuning. This is achieved by "mode-hop" scanning, in which the cavity mirror remains fixed at a specific position, and only the etalon and grating are tuned. This has the effect of causing the

laser to hop from one cavity mode to the next, effectively scanning in 300 MHz (0.01 cm^{-1}) steps. This step size is convenient given that the linewidths observed in helium are often on this order.

Absolute frequency calibration is provided by a wavemeter (Burleigh WA-20 and WA-1000) with an accuracy of $\pm$ 0.01 cm^{-1}, while relative frequency calibration is performed with a set of high finesse confocal etalons with free spectral ranges of 7.5 GHz, 750 MHz, and 150 MHz. A few percent of the laser output is sent into the etalons using two CaF_2 windows which act as beam splitters. A fourth beam is sent into a photodiode to provide a relative power reference. Two of the etalons (7.5 GHz and 750 MHz) are scanned by applying a high voltage ramp (20 ms, 0 - 1000 V), and the voltage at which the laser transmission is observed is converted into a reference voltage. As the laser frequency is scanned, so will the reference voltage, and hops in frequency are easily detected. An even more precise frequency calibration is obtained using the 150 MHz etalon, which is temperature stabilized and the exact free spectral range determined from reference gas absorptions. A transmission "fringe" is observed every 150 MHz, and is used to linearize the scans to an estimated accuracy of 0.0001 cm^{-1}.

3.3.2.2 Optical parametric oscillators

A few of our studies were carried out using Optical Parametric Oscillators to generate mid IR photons. One such OPO is a commercially available system from Linos Photonics (OS-4000), which is based on periodically poled Lithium Niobate (PPLN) and provided 30-80 mW of power in the 3000 - 3800 cm^{-1} range. The details of this system will be presented in Appendix A, along with a home built PPLN-OPO system which produced output powers in the multi-Watt range.

Chapter 4

Propargyl Radical ($HCCCH_2$)

The propargyl radical (C_3H_3) has special significance to this thesis as it was the first molecular radical to be studied in helium droplets, and it served as the first example that our effusive pyrolysis source could be used to efficiently dope the droplets with radicals. Rotationally resolved spectra are reported for the ν_1 vibrational mode (acetylynic CH stretching) in helium droplets at 3322.15 cm^{-1}. Stark spectra are also recorded that allow for the first experimental determination of the permanent electric dipole moment of propargyl, namely -0.150 D and -0.148 D for the ground and first excited state respectively, in good agreement with previously reported *ab initio* results of -0.14 D [135]. The infrared spectrum of the ν_1 mode of propargylbromide is also reported.

4.1 Introduction

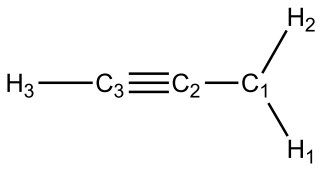

I

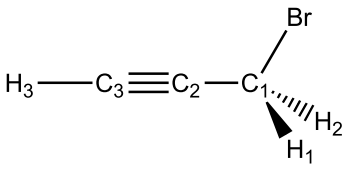

II

In light of its role in sooting flames, propargyl (2-propynyl) radical (Structure I) has been the focus of particular attention [136–139]. Propargyl is one of the simplest conjugated systems with an odd number of electrons, also making it the focus of considerable theoretical study [135, 140–142]. There is now compelling evidence that propargyl is the most important radical precursor in the formation of benzene, polycyclic aromatic hydrocarbons (PAH), and soot in certain combustion processes [136–139, 143–148]. For example, the simple dimerization of two propargyl radicals is thought to be important in the formation of benzene, as suggested by Wu and Kern [143].

Early observations of the propargyl radicals where carried out by ESR spectroscopy in liquid allene [149] and in argon matrix studies [150]. Ramsey and Thistlethwaite [151] first observed the electronic gas-phase absorption spectrum. Infrared spectra and electronic absorption spectra were obtained in neon and argon matrices [152–154], including the study by Jacox and Milligan [152], which identified four vibrational bands (at 3308, 686, 548 and 484 cm^{-1}) that they assigned to propargyl. Later studies by Maier *et al*. [155], confirmed by Huang and Graham [154], showed that the 548 cm^{-1} band is actually associated with triplet propargylene. Recently the infrared and electronic absorption spectrum of propargyl in neon matrices has been examined [153]. Additional information on the propargyl radical has been obtained from the photoelectron spectrum of the allenyl anion [156], in which a long vibrational progression with a mean spacing of approximately 515 cm^{-1} was assigned to an out-of-plane bending motion.

Propargyl radical has also been produced in supersonic jets by means of flash pyrolysis, for use in photoelectron studies [157–159]. Rotationally resolved spectra of propargyl were first obtained for the ν_1 acetylenic C-H stretching vibration at 3322.3 cm^{-1} by the group of Curl [104]. This work was extended to the ν_6 vibrational band by Tanaka *et al*. [160] and to higher rotational levels of the ν_1 band [105]. In addition, Fourier Transform microwave spectroscopy has been reported for this radical [161]. All of these rotationally resolved studies confirmed the C_{2v} symmetry of the electronic ground state of propargyl [104, 105, 160, 161], in agreement with *ab initio* quantum mechanical calculations [135, 140–142, 162], most recently at the coupled cluster level by Botschwina *et al*. [140].

In light of the importance of propargyl radicals in combustion, we have started a program of study aimed at investigating the associated interactions in the pre-reactive dimer and between propargyl and other molecules and atoms. The approach taken is to solvate the radicals in helium droplets, which act as a nearly ideal matrix for spectroscopic study [36, 37, 41, 52, 163–166]. In the present study we focus on the spectroscopy of the radical monomer and apply the pyrolysis of propargyl bromide (Structure II) to produce the radical.

4.2 Propargyl bromide (C_3H_3Br)

As noted above, the propargyl radicals were generated in this study by pyrolysis of propargyl bromide. To aid in the optimization of the radical source we first monitored the helium solvated propargyl bromide by exciting the corresponding ν_1 (C-H stretching) vibration. Propargyl bromide has been considered a replacement for methyl bromide in soil fumigation [167] and its basic physical and environmental properties [167, 168], including its infrared spectrum [169, 170] have been studied previously. The helium droplet spectrum is shown in Figure 4.1. To aid in the analysis of this spectrum we performed *ab initio* calculations at the Hartree-Fock, MP2, and CCSD(T) levels. All calculations were performed with the cc-pVTZ basis [171] using MOLPRO [172]. The C_s symmetry of propargyl bromide was applied and the

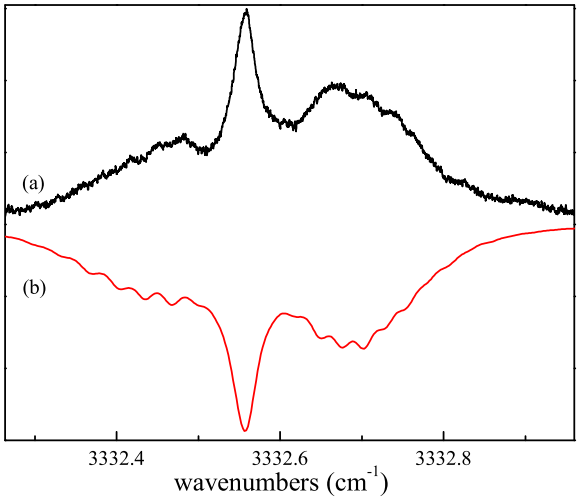

Figure 4.1: (A) An experimental spectrum of the ν_1 band of propargyl bromide (C_3H_3Br), embedded in helium droplets. (B) A calculated spectrum corresponding to A' = A" = 0.025 cm^{-1}, B' = C' = 0.0148 cm^{-1} , and B" = C" = 0.0152 cm^{-1}. See text for details.

	HF/cc-pVTZ	MP2/cc-pVTZ	CCSD(T)/cc-pVTZ
r(C3,H3) (pm)	105.36	106.11	106.32
r(C1,H1) (pm)	107.57	108.56	108.68
r(C2,C3) (pm)	118.05	121.44	121.08
r(C1,C2) (pm)	145.38	144.64	145.48
r(C1,Br) (pm)	195.38	195.25	196.50
α(H3,C3,C2) (deg)	180.0	179.9	179.7
α(C1,C2,C3) (deg)	180.0	180.6	180.8
α(C2,C1,H1) (deg)	111.4	111.6	111.5
α(C2,C1,Br) (deg)	111.7	111.7	111.8
ϕ(H1,C1,C2,Br) (deg)	118.5	118.6	118.4
A (cm^{-1})	0.7082	0.7029	0.7019
B (cm^{-1})	0.0724	0.0719	0.0711
C (cm^{-1})	0.0665	0.0660	0.0653
ν_1 (cm^{-1})	3621	3498	3457[a]
θ (deg)	41	40	40[a]

[a] Performed with the cc-pVDZ basis set.

Table 4.1: Calculated equilibrium structures, rotational constants, ν_1 (harmonic frequency), and transition moment orientation for the electronic ground state of propargyl bromide. See text for details.

ten remaining geometric parameters were optimized. The resulting geometries and rotational constants are given in Table 4.1. From the normal coordinate analysis, the transition moment orientation for the ν_1 vibration is determined to be in the *ab* plane, at an angle of $\theta = 40^\circ$ with respect to the *a* axis. Given that the propargyl bromide spectrum is only partially resolved, the fit was carried out using a symmetric top Hamiltonian. The calculation shown in Figure 4.1 corresponds to A' = A" = 0.026 cm^{-1}, B' = C' = 0.0148 cm^{-1}, B" = C" = 0.0152 cm^{-1}, ν_0 = 3332.56 $^{-1}$, and a linewidth of 0.033 cm^{-1}. Based on the *ab initio* calculations the B and C rotational constants in helium are approximately 4.5 times smaller than those of the molecule in vacuum. This is consistent with results obtained previously for closed shell molecules [94]. The more surprising result is that the A constants are approximately 20 times smaller than the *ab initio* value. Although this anomalously large reduction in the A rotational constant might be due to an unusually strong interaction between the molecule and the helium matrix, resulting from the highly polarizable bromine atom, at this point we do not have a good explanation for this effect. It is worth noting, however, that the value of A is rather sensitive to the relative contributions from the *a*- and *b*-type components of the hybrid band, which in the present calculation was simply fixed at the *ab initio* value. The experimental vibrational origin (3332.56 cm^{-1}) is consistent with the low-resolution gas-phase results (3335 $\pm$ 6 cm^{-1}) [169, 170].

4.3 Propargyl (C_3H_3) radical

The results presented above provide unambiguous identification of propargyl bromide in the droplets. The spectrum was observed to diminish in intensity and finally disappear as the temperature of the pyrolysis source was increased. Once these conditions were established, a search was carried out for the propargyl radical, using the gas-phase results as a guide. Figure 4.2 shows the resulting spectrum, which can be assigned to the ν_1 vibrational band of the propargyl radical embedded in superfluid liquid helium droplets. Table 4.2 gives a list of the transition frequencies and rotational assignments for the observed transitions. This spectrum

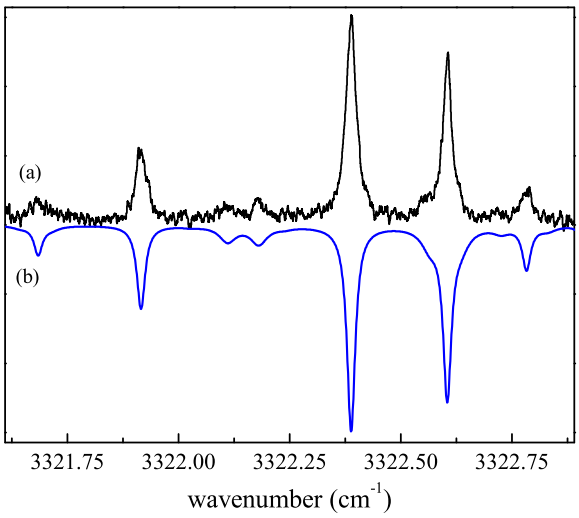

Figure 4.2: (A) An experimental infrared spectrum of the ν_1 band of the propargyl radical, embedded in helium droplets. (B) A simulated spectrum using the molecular constants given in Table 4.3, a rotational temperature of 0.37 K, and Lorentzian linewidths of 0.0225 cm^{-1} for K_a = 0 lines and 0.045 cm^{-1} for K_a = 1 lines.

corresponds to an *a*-type band of a prolate asymmetric top. Transitions are observed that originate from K_a = 1 levels even though we would not expect these states to be populated based on the temperature of the droplets (0.37 K). These results confirm that this radical has C_{2v} symmetry even when embedded in liquid helium droplets, such that the K_a = 1 levels cannot cool to K_a = 0. Since this spectrum is *a*-type, and the relative populations of the K_a = 1 and K_a = 0 states are not controlled thermodynamically, the A" rotational constant cannot be determined from the data. Within the experimental uncertainty, ΔA was also the same as in the gas-phase. Therefore, for the purpose of fitting the spectra, A" and A' were fixed at their gas-phase values, namely 9.61 cm^{-1} and 9.60 cm^{-1} respectively [105, 160, 161]. This is a reasonable approximation given that previous studies [94] have shown that the helium cannot follow such fast rotational motion, so that the rotational constants are approximately the same as in the gas-phase [76]. The five K_a = 0 lines given in Table 4.2 were fit to a linear-rotor Hamiltonian, yielding $\frac{(B"+C")}{2}$, $\frac{(B'+C')}{2}$, D_J", and D_J'. The values of B - C were determined

Transition	Experimental frequency (cm^{-1})
$3_{03} \leftarrow 2_{02}$	3322.782
$2_{02} \leftarrow 1_{01}$	3322.605
$1_{01} \leftarrow 0_{00}$	3322.388
$0_{00} \leftarrow 1_{01}$	3321.916
$1_{01} \leftarrow 2_{02}$	3321.687
$2_{12} \leftarrow 1_{11}$	3322.554
$1_{10} \leftarrow 1_{11}$	3322.182
$1_{11} \leftarrow 1_{10}$	3322.105

Table 4.2: Observed rovibrational transitions of the ν_1 band of the propargyl radical in helium droplets. The frequencies were obtained by simultaneously fitting Lorentzian profiles to the individual peaks in the field-free spectrum. More transitions are evident in the field-free spectrum but are too weak or strongly overlapped for the frequencies to be accurately determined. The estimated uncertainties of the absolute frequencies are 0.01 cm^{-1} , and relative uncertainties are 0.0002 cm^{-1} for K_a = 0 and 0.001 cm^{-1} for K_a = 1 lines.

for both vibrational states by simultaneously fitting the field-free and Stark spectrum (Figure 4.3). The resulting molecular parameters are reported in Table 4.3. The (B+C)/2 constants

Constant	Helium droplet	gas-phase[a]
A" (cm^{-1})	9.60847[b]	9.60847(18)
(B" + C")/2 (cm^{-1})	0.1198(5)	0.312386(12)
B" - C" (cm^{-1})	0.035(2)[c]	0.0105762(35)
$\Delta_N^{''}$ (cm^{-1})	0.00042(1)	$7.35(122) \times 10^{-8}$
A' (cm^{-1})	9.60258[b]	9.60258(11)
(B' + C')/2 (cm^{-1})	0.1185(5)	0.311641(7)
B' - C' (cm^{-1})	0.035(2)[c]	0.010496(13)
$\Delta_N^{'}$ (cm^{-1})	0.00062(1)	$5.37(76) \times 10^{-8}$
ν_0 (cm^{-1})	3322.15(1)	3322.292(10)
$\mu^{''}$ (D)	-0.150(5)	–
$\Delta\mu$ (D)	0.02(1)	–

[a]Reported values are from Refs. [105, 160].
[b]A" and A' have been fixed at their respective gas-phase values.
[c]Corrected value from Ref. [173].

Table 4.3: Summary of the fitted molecular constants for the propargyl radical in superfluid helium droplets, compared with those obtained in gas-phase studies [105, 160]. Numbers in parenthesis are one estimated standard deviation.

in both vibrational states are reduced by a factor of 2.6 compared to the gas-phase values [105, 160, 161], in good agreement with previous studies of closed shell molecules in helium

droplets [94, 174]. The centrifugal distortion constants are much larger than for the isolated gas-phase molecule [105, 160, 161]. These constants are presumably more indicative of the strength of the propargyl-helium interactions than of the inherent rotation-vibration coupling in propargyl [35].

High-resolution gas-phase infrared spectra have revealed line splittings due to spin-rotation coupling (Hund's case (b)) [160, 161]. The spin-rotation coupling constants determined by Tanaka *et al*. from the ν_6 band [160] and the microwave spectrum [161] are small. In fact, Yuan *et al*. [105] were unable to determine spin-rotation coupling parameters even from the gas-phase spectrum of the ν_1 band. At the resolution of the present helium droplet spectrum, where only the lowest J and K_a states of the molecule are observed, we would not expect to resolve splittings due to spin-rotation coupling. This accounts for why we are able to explore the entire spectrum using a conventional asymmetric top Hamiltonian. Although the source of the line broadening in the helium droplet spectrum is not fully understood, there is considerable evidence from previous studies that inhomogeneous effects are significant and that these are dependent upon the rotational state of the system. The best fits of the spectra were obtained with two different linewidths for the K_a = 0 and K_a = 1 states, namely 0.0225 cm^{-1} (0.0175 cm^{-1}) and 0.045 cm^{-1} (0.035 cm^{-1}) for the field-free (Stark) spectrum, respectively. Since some of the K_a = 1 transitions correspond to upper states that are the lowest rotational levels of their respective spin-symmetry, the excessive broadening here cannot be attributed to reduced rotational lifetimes. One possibility is that the spin-rotation coupling is larger for the K_a = 1 levels, in agreement with the fact that spin-rotation-coupling is (at least) approximately linear with the overall angular momentum apart from spin.

4.3.1 Nuclear spin statistics

The manner in which the intensities in the calculated spectrum were determined deserves some attention. Given the C_{2v} symmetry of propargyl care must be taken to properly account for the nuclear spin statistics. The ground electronic state of propargyl has $^2B_1$ symmetry,

giving rise to spin statistical weights of 3:1 for K_a even and odd levels, respectively. At the temperature the propargyl radicals are formed in the radical source (approx. 1000 K) the total population in all of the K_a even states will be three times the sum of population in the K_a odd states. The corresponding ground state populations in the helium droplets can then be obtained by cooling all the K_a even states into K_a = 0 and the K_a odd states into K_a = 1, assuming no nuclear spin conversion. This preserves the ratio of 3:1 for the K_a even and odd states. For a given K_a the relative populations of corresponding rotational states are computed using a Boltzmann formula, the zero in energy corresponding to the lowest energy state within each K_a manifold. The fact that the calculated intensities are in excellent agreement with the experimental results suggests that on the timescale of the present experiment (~1 ms) there is essentially no spin-relaxation. This seams reasonable given that the conversion rate would have to increase by many orders of magnitude, relative to typical gas-phase rates [175], for these effects to be important.

4.3.2 Dipole moment measurements

The dipole moment of the propargyl radical was determined from the Stark-spectrum of the ν_1 band, shown in Figure 4.3, corresponding to a static electric field of 51.2 kV cm^{-1}. The laser polarization was aligned parallel to the static field, yielding ΔM = 0 selection rules. In addition to the growth of the Q-branch feature at the band origin, the R(1) transition is observed to split with the field (Figure 4.4), into its M = 0$\leftarrow$0 and M = $\pm$1 $\leftarrow\pm$1 components. The simulation of the Stark spectrum is performed with an asymmetric rotor Stark program developed in our group [25]. The full M-matrices are set up in an asymmetric rotor basis and diagonalized to calculate Stark and pendular state spectra [25]. Again the non-thermal ground-state populations due to nuclear spin-statistics are carefully taken into account. Using the inertial parameters given in Table 4.3 and a rotational temperature of 0.37 K, we fit the spectrum and determined the ground state dipole moment μ_0 = -0.150(5) D and the change in the dipole moment upon vibrational excitation $\Delta\mu$ = 0.02(1) D. Although in this experiment we

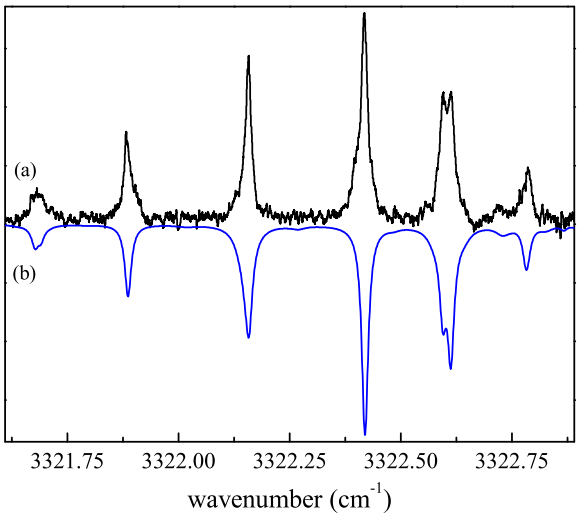

Figure 4.3: (A) An experimental Stark spectrum of the ν_1 band of propargyl radical in helium droplets, at an electric field of 51.2 kV cm^{-1}. (B) A simulation using the molecular constants given in Table 4.3, a rotational temperature of 0.37 K, and Lorentzian linewidths of 0.0175 cm $^{-1}$ K$_a$ = 0 lines and 0.035 cm^{-1} for K$_a$ = 1 lines.

only obtain the absolute value of the ground state dipole moment, the sign of μ_0 is determined by comparison with *ab initio* calculations [135]. The resulting calculated spectrum is shown in Figure 4.3.

To our knowledge this is the first experimental measurement of the permanent electric dipole moment of the propargyl radical, although from the power dependence of the signal intensity in the FT microwave spectrum Tanaka *et al.* concluded that the dipole moment value was < 0.3 D [161]. Botschwina *et al.* [135] have carried out high level *ab initio* calculations from which they recommend an equilibrium dipole moment of μ_e = -0.14(3) D in good agreement with the experimental value. However, this is not really a valid comparison, since the experimental value is vibrationally averaged, while the *ab initio* calculations give the equilibrium value. To address this issue we calculated the v = 0 and v = 1 vibrational wavefunctions which correspond to ν_1 , using the Numerov-Cooley method [176] based upon a one-dimensional slice through the corresponding potential energy surface [135]. The resulting expectation values for

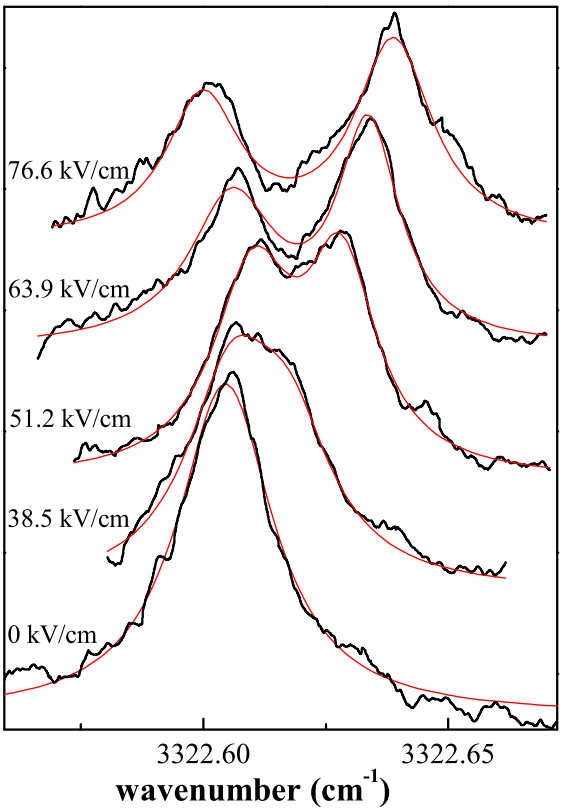

Figure 4.4: The field dependent splitting of the R(1) transition of Propargyl corresponding to the ΔM = 0 transitions. The smooth lines are a guide for the eye.

the CH bond length are $\langle r_0 \rangle = r_e + 0.014$ Å and $\langle r_1 \rangle = r_e + 0.044$ Å where $r_e = 1.0626$ Å [135] for the ground and first vibrationally excited state, respectively. The corresponding averages of the electric dipole moment function of Botschwina et al. [135], obtained by correcting the suggested equilibrium value μ_e = -0.14 D using the MR-ACPF/EV results [177], yield dipole moments of $\langle \mu \rangle_0$ = -0.134 D and $\langle \mu \rangle_1$ = -0.123 D, namely a change upon excitation of $\Delta\mu$= 0.011 D. From a five-dimensional analysis of all totally symmetric vibrations Botschwina [178] obtained a zero-point correction to the dipole moment of 0.016 D, corresponding to $\langle \mu \rangle_0$ = -0.124 D. Although this calculation still neglects the non-totally symmetric vibrations and might underestimate the vibrational effects on the ground state dipole moment, it should give a good

description of the change in the dipole moment upon excitation of ν_1. Indeed these calculations give a change upon vibrational excitation of $\Delta\mu$ = 0.029 D [178]. Although the effects of vibrational averaging make the agreement between the experimental and theoretical ground state dipole moment somewhat worse, the difference is still well within the given theoretical error of $\pm$0.03 D [135]. The change in dipole moment of $\Delta\mu$ = 0.029 D obtained from the *ab initio* calculations is within our experimental error. Overall the agreement between the *ab initio* calculations and experiment is quite satisfactory.

4.4 Summary

We reported on the application of a novel effusive pyrolysis source for generating radicals suitable for pick-up in superfluid helium droplets. The source is used to generate the propargyl radical and a rotationally resolved spectrum is reported. Analysis of a Stark spectrum provides the first experimental measurement of its permanent electric dipole moment, namely μ_0= -0.150(5) D, and the change upon vibrational excitation, $\Delta\mu$ = 0.02(1) D.

This study demonstrates the potential of the helium droplet method to study a wide range of radicals and, in the future, radical complexes. Considering the importance of propargyl and similar radicals in combustion and soot formation and the unique properties of liquid helium droplets, we are currently extending this work to the study of pre-reactive propargyl radical dimers and propargyl—Br complexes. Given the ability of helium droplets to form metastable species [36,37], there is considerable potential to stabilize highly reactive complexes, including those containing more than one radical.

Chapter 5

Halogen Atom (X) - HF Complexes (X = I, Br, Cl)

In this chapter we explore the possibility of using helium nanodroplets to study radical complexes, with specific application to the X-HF (X = Cl, Br and I) complexes formed by independent pick-up of the corresponding atoms and molecules by the nanodroplets. Rotationally resolved infrared spectra are reported for each of these complexes, and analysis of the resulting spectra confirms that the observed species have $^2\Pi_{3/2}$ ground electronic states consistent with the linear hydrogen bound structures predicted from theory. Stark spectra are also reported, from which the permanent electric dipole moments are determined. An effusive pyrolysis source is used to dope helium droplets with Cl, Br and I atoms, formed by thermal dissociation of Cl_2, Br_2 and I_2. A single hydrogen fluoride molecule is then added to the droplets, resulting in the formation of the X-HF complexes of interest.

5.1 Introduction

Heavy-light-heavy systems (X-HY, X & Y = F, Cl, Br and I) figure prominently in reaction dynamics studies, being prototypical systems for the observation of transition state resonances. Theoretical studies on these X-HY systems [179–186] have revealed many important issues related to the role of multiple electronic surfaces and spin-orbit interactions. These systems have also been the subject of considerable experimental study, including the spectroscopy of the transition states, accessed by photodetaching an electron from the [XHY]- anion complexes [187], and bond-specific photodissociation of HX dimers [188, 189]. In addition, evidence for the existence of weakly bound X-HY complexes has come from infrared spectroscopy in noble gas matrices [32, 190–192]. Unfortunately, these studies do not provide detailed information on the associated entrance channel wells.

As illustrated by the Cl + HD system discussed in Chapter 1, the structures of entrance channel complexes (which probe the associated potential energy surfaces at energies that are relevant to the reactive dynamics) are of considerable importance in understanding the nature of the reactions, particularly at low translational energies. The need for new experimental methods for probing such species is clear, given the lack of data on these X-HY systems, despite the intense interest in the associated reactions. On the one hand, the interaction between the large dipole moment of the HY molecule and the quadrupole moment of the halogen atom (X) would suggest two linear structures, namely a hydrogen bonded geometry and one with the two heavy atoms adjacent to one another. On the other hand, the HY molecules have substantial quadrupole moments as well, so that T-shaped structures are also predicted to be minima. It is actually quite surprising that the structures of these systems have not yet been conclusively determined, illustrating the primitive state of our understanding. High-level *ab initio* and semi-empirical calculations have been performed for several of these systems [179–186]. The weak interactions between a halogen atom and a HY molecule suggest that, to a first approximation, the orbital angular momentum of the atom (l) will be conserved. In this case there are three diabatic surfaces that correlate with the unpaired electron being in the p_x,

p_y, or p_z orbital. Taking the z direction as the molecular axis, two of these configurations are degenerate for linear configurations, but diverge as the molecule bends (a Renner-Teller effect). Recent calculations by Zeimen *et al*. [186] predict that the global minimum for the Cl - HCl system is T-shaped, in contrast with a linear prediction made in earlier studies [179, 193], once again illustrating the need for experimental measurements of the associated structures.

High-resolution spectroscopy is often looked upon as the definitive tool to determine accurate molecular geometries. While this statement is well supported by studies of a wide range of cluster systems, the situation is less clear for the X-HY complexes. Bound state calculations on Cl-HCl show distinct progressions of both linear and T-shaped states, even though both are believed to display the spectral signatures of a linear open-shell molecule [186]. This peculiarity is quite unique, suggesting that in some cases the high-resolution spectroscopic experiments which provide rotational constants, dipole moments, parity splitting, etc ... may not give conclusive structural information. Elucidating the structures and energetics of these complexes will clearly require extensive interactions between experiment and theory.

5.2 Electronic structure calculations

Although studies near the transition state region of the potential surface often require multi-reference calculations, to include the effects of the low lying excited electronic states, the present study of the entrance channel region of the potential, where the ground state dominates, single reference calculations are expected to be sufficient for harmonic vibrational frequencies and structural parameters (dipole moments, rotational constants, etc). *Ab initio* calculations were performed here using Gaussian 03 [194] at the UMP2 and UCCSD(T) level incorporating the aug-cc-pVTZ basis of Dunning [171]. The results of geometry optimizations and harmonic frequency calculations are summarized in Tables 5.1-5.3 for F-HF, Cl-HF and Br-HF. Binding energies were further corrected for basis-set superposition error using the method of Boys and Bernardi [195]. In agreement with previous studies, we find three stable minima corresponding

	Method	HF	F-HF	Cl-HF	Br-HF	Br-HF (ECP)	I-HF (ECP)
D_e (cm^{-1})	UMP2	-	364	672	721	645	700
	UCCSD(T)	-	360	676	720	-	-
$\nu_{harmonic}$ (cm^{-1})	UMP2	4123	4096	4030	3998	3985	3973
	UCCSD(T)	4124	4103	4045	4017	-	-
ν_{scaled} (cm^{-1})	UMP2	3959.19	3933	3870	3839	-	-
	UCCSD(T)	-	3939	3883	3856	-	-
ν_{Ar} (cm^{-1})		3962	3908	3858	3831		
R_{X-H} (Å)	UMP2	-	2.087	2.371	2.439	2.392	2.611
	UCCSD(T)	-	2.068	2.378	2.449	-	-
R_{HF} (Å)	UMP2	0.9218	0.9232	0.9258	0.9272	0.9278	0.9283
	UCCSD(T)	0.9210	0.9222	0.9246	0.9258	-	-
B (cm^{-1})	UMP2	20.70	0.195	0.125	0.0953	0.098	0.080
	UCCSD(T)	20.73	0.198	0.124	0.0948	-	-
μ (D)		1.81	2.05	2.34	2.48	2.52	2.63

Table 5.1: A summary of optimized stationary points for the hydrogen bonded (global minimum) configuration of X-HF. Structural parameters, along with other molecular constants, were calculated at the UMP2 and UCCSD(T) level of theory with the aug-cc-pVTZ basis set in Gaussian 03 [194]. Binding energies have been corrected for basis set superposition error using the method of Boys and Bernardi [195]. Dipole moments have been calculated using the UMP2 electron density. Calculations labeled by (ECP) were performed at the UMP2 level using a pseudopotential basis set for bromine and iodine, see text for details. Scaled frequencies were obtained by comparing a free HF calculation with the vibrational frequency observed in helium droplets. The argon matrix data comes from the work of Andrews [32].

UMP2/aug-cc-pVTZ	HF-F	HF-Cl	HF-Br
D_e (cm^{-1})	6	20	70
$\nu_{harmonic}$ (cm^{-1})	4123	4121	4120
R_{X-F} (Å)	3.416	3.682	3.718
R_{HF} (Å)	0.9218	0.9219	0.9220
B (cm^{-1})	0.143	0.095	0.074
μ (D)	1.83	1.90	1.94

Table 5.2: Optimized structures of the linear HF-X complexes. The dissociation energies listed have not been corrected for basis set superposition error.

to the two linear and T-shaped complexes. The calculated global minima for these systems all

UMP2/aug-cc-pVTZ	F-HF	Cl-HF	Br-HF
D_e (cm^{-1})	220	375	404
$\nu_{harmonic}$ (cm^{-1})	4116	4109	4107
R_{X-F} (Å)	2.662	2.970	3.036
R_{HF} (Å)	0.9223	0.9228	0.9229
A, B, C (cm^{-1})	23.7, 0.241, 0.238	24.5, 0.148, 0.147	26.0, 0.113, 0.112
μ (D)	1.83	1.87	1.92
Θ (deg)	109.8	112.4	116.2

Table 5.3: A summary of optimized structures for the T-shaped X-HF complexes calculated at the UMP2/aug-cc-pVTZ level. The angle theta is defined by using the F atom (in HF) as the vertex. Binding energies have been corrected for basis set superposition error.

correspond to linear hydrogen bonded structures. Calculations for I-HF were also carried out using a correlation consistent basis set, in conjunction with a small core relativistic pseudopotential (aug-cc-pVTZ-PP) [196]. In this calculation, 28 core electrons of iodine were replaced by an effective core potential, while the remaining bonding electrons and the HF molecule were treated within the aug-cc-pVTZ basis [171]. Similar calculations were carried out for bromine (10 frozen core electrons) for comparison with the all electron calculations.

Calculations were also performed for the Br_2-HF system, to aid in identifying the precursor complexes, which in turn helped in optimizing the pyrolysis source. Figure 5.1 shows a two-dimensional cut through the associated coupled rotor potential, calculated at the MP2/aug-cc-pVDZ level of theory. For each point, the two rotor angles, theta and phi were stepped incrementally by 10 degrees, while all other geometric parameters were relaxed. The energies

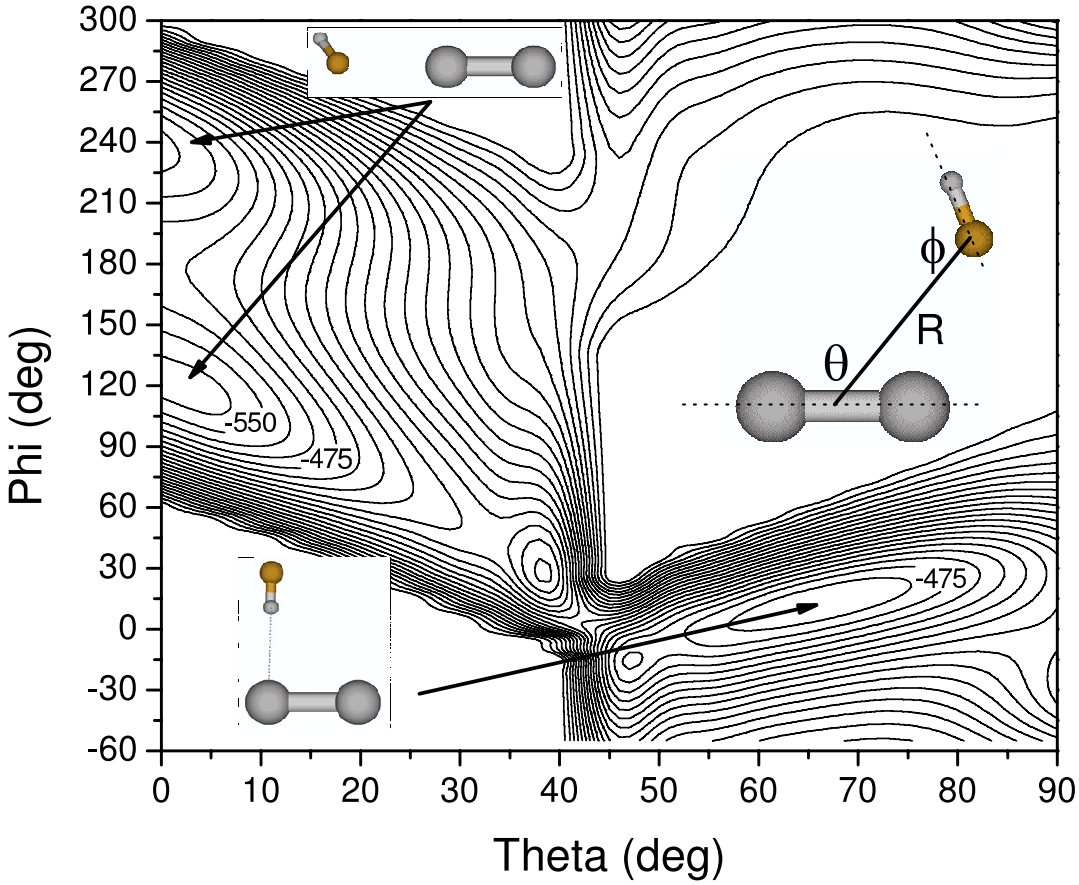

Figure 5.1: A two-dimensional cut through the MP2/aug-cc-pVDZ PES for the Br_2-HF system. At each point, the geometry was fully relaxed (except the two rotor angles) and the binding energy corrected for basis set superposition error by counterpoise correction. The surface has two minima that correspond to the "bent" and "L" shaped isomers drawn as insets. The corresponding isomers are observed in the helium droplet experiments reported here. Neighboring contours are spaced by 25 cm^{-1}

were corrected for basis set superposition error (BSSE) using counterpoise correction [195] and a bi-cubic spline interpolation was used to generate the surface. In agreement with the experimental results discussed below, we find two minima on the potential energy surface, one corresponding to a L-shaped, hydrogen bonded complex and the second to a bent isomer bonding at the fluorine end of the HF molecule. The results from fully relaxed optimizations, as well as harmonic frequency calculations, for these two isomers are summarized in Table 5.4. Comparisons with the experimental results are given below.

5.3 Br_2-HF complexes

The process of optimizing the experimental conditions began with the search for the Br_2-HF complexes discussed above, yielding the two spectra shown in Figure 5.2. Both of these

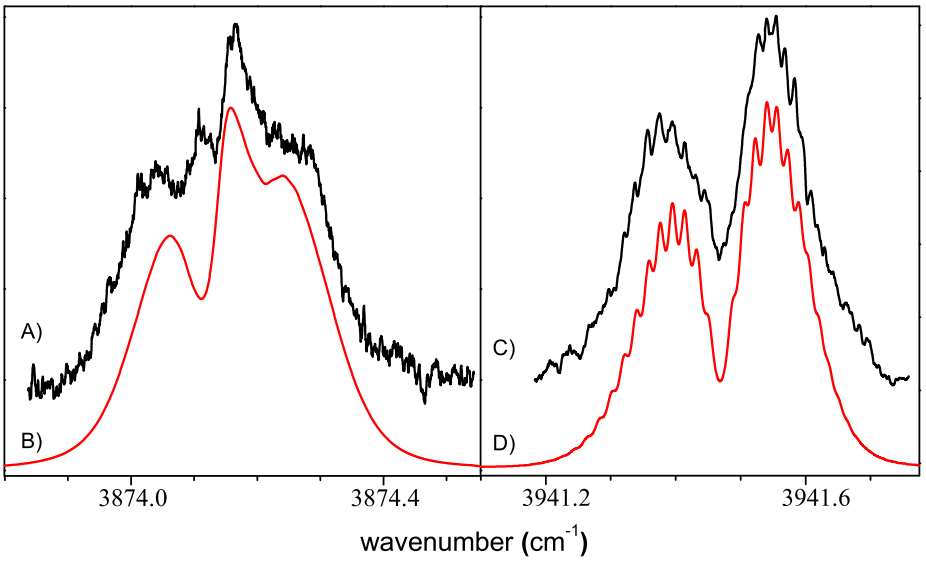

Figure 5.2: Zero-field spectra, (A) and (C), of the L-shaped and bent isomers of Br_2-HF, respectively. Inertial parameters derived from the simulation of the spectra, (B) and (D), are shown in Table 5.4 and are in good agreement with *ab initio* calculations. A rotational temperature of 0.37 K was used in the simulations.

spectra optimized under the conditions needed for the pick-up of a single molecule of each type (namely HF and Br_2), confirming that they are associated with the 1:1 complex. The significant frequency shift (-85 cm^{-1}) for the band in Figure 5.2A (relative to the HF monomer at 3959.19 cm^{-1} [76]) suggests that this is the hydrogen bonded complex. Indeed, the calculated asymmetric top spectrum, shown in Figure 5.2B, is consistent with the L-shaped isomer discussed above, with the rotational constants reduced to account for the effects of the helium [34]. Due to the small asymmetry associated with this complex the fit to the spectrum provides only (B+C)/2, as given in Table 5.4. The experimental frequency shift for this isomer is also in reasonable agreement with the *ab initio* calculations (-100 cm^{-1}), where the latter were first

Constant (cm^{-1})	Helium droplet	MP2/aug-cc-pVDZ
	Br_2-FH	
ν_0	3941.47	3940.98
(B+C)/2	0.009	0.032
D_J	1.0×10^{-6}	-
	Br_2-HF	
ν_0	3874.14	3859.16
A', (B'+C')/2	0.018, 0.01	-
A", (B"+C")/2	0.020, 0.01	0.108, 0.048
D_J	1.0×10^{-6}	-

Table 5.4: Tabulated results for the two isomers of Br_2-HF. Two distinct isomers are observed in helium droplets in agreement with *ab initio* (MP2/Aug-cc-pVDZ) calculations (See Figures 5.1 and 5.2). Br_2-HF represents the "L" shaped isomer, while Br_2-FH is the "bent" one. Calculated frequencies have been scaled to the HF monomer. The experimental constants are those obtained from fitting the corresponding spectra and are compared with the *ab initio* values.

scaled to give the correct vibrational origin for HF monomer in helium. The spectrum in Figure 5.2C has a much smaller frequency shift (-17.72 cm^{-1}, relative to the HF monomer) in excellent agreement with the calculated frequency shift (scaled to HF monomer) for the bent isomer, namely -20.43 cm^{-1}. This spectrum is well represented by a linear rotor calculation (Figure 5.2D), consistent with the fact that the bent isomer has a very large A rotational constant. As a result, only the K_a = 0 levels are populated at the temperature of the droplets (0.37 K). The resulting K_a = 0←0 band is indistinguishable from that of a linear molecule spectrum and again we report only (B+C)/2. The rotational constants used to fit this spectrum are approximately a factor of five smaller than the *ab initio* calculations, due to the effects of the helium solvent. Experimental parameters derived from the simulations, along with *ab initio* data are presented in Table 5.4 for both isomers.

5.4 Br - HF complex

Having identified the spectra associated with the Br_2-HF 1:1 complexes, we can use these as an aid in optimizing the conditions for the production of the Br-HF complex. Figure 5.3B shows a pendular spectrum of the bonded H-F stretching region, recorded with the pyrolysis

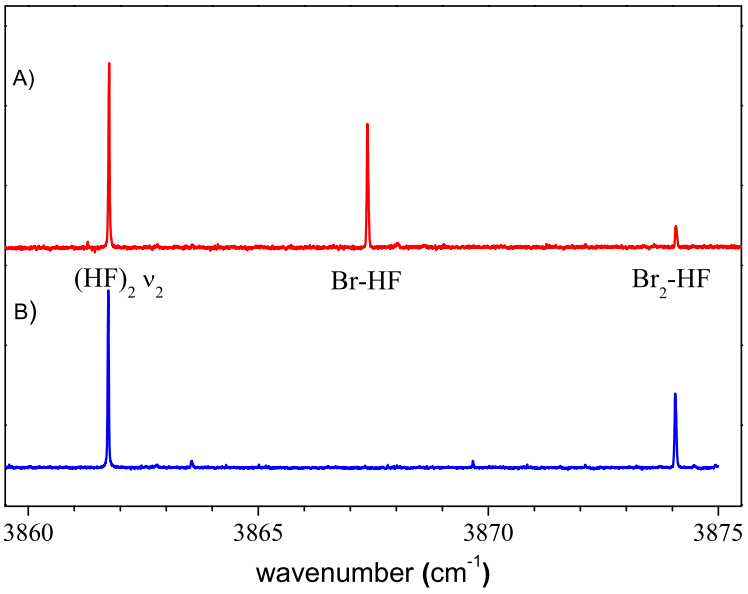

Figure 5.3: Pendular spectra recorded in the ν_2 HF dimer region, showing the appearance of bromine related complexes. In the bottom trace the pyrolysis source is at room temperature and the peak at 3874 cm^{-1} corresponds to the L-shaped isomer of Br_2-HF. The peak at 3862 cm^{-1} is due to the HF dimer. The top trace was recorded with the pyrolysis source at 1200 K, where a new peak appears that is assigned to Br-HF. Note that the intensity of the Br_2-HF peak is diminished, showing the extent of pyrolysis.

source at room temperature. The peak near 3862 cm^{-1} is well known from our previous study [166] to be due to the hydrogen bonded H-F stretch of the HF dimer, while the peak at the high frequency end of the scan is due to the L-shaped Br_2-HF complex discussed above. In both cases, the electric field has collapsed the rotational structure into a single peak. Figure 5.3A shows a scan of the same region of the spectrum, recorded with the pyrolysis source heated to 1200 K. Note that the pendular transition associated with the Br_2-HF complex is diminished in intensity, relative to that obtained with a room temperature source, and that a new peak has appeared in the spectrum. The growth of this band is complementary to the disappearance of the spectra assigned to both of the Br_2-HF isomers. This new band optimizes under conditions that correspond to, on average, the capture of a single bromine atom.

Having located a vibrational band that is tentatively assigned to the Br-HF complex, the

rotational structure in the band can be examined by turning off the electric field. Figure 5.4A

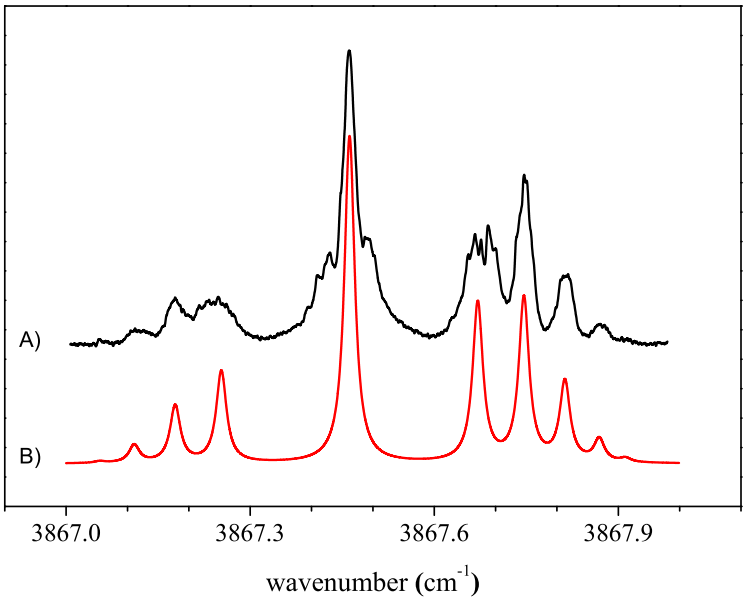

Figure 5.4: A rotationally resolved spectrum (A) of Br-HF solvated in helium droplets. The spectral shape is consistent with that of a $^2\Pi_{3/2}$ electronic state. Also shown is a simulation (B), based upon the following constants: B" = B' = 0.043 cm^{-1} , D" = D'= 0.95 $\times$ 10^{-4} cm^{-1}, and T = 0.35 K.

shows the corresponding zero-field spectrum, which has clearly resolved P, Q, and R branches. There is a substantial "gap" between the Q branch and the corresponding P and R branches, consistent with this being a linear complex with a $^2\Pi_{3/2}$ ground electronic state. Indeed, the $^2\Pi_{3/2}$ state is expected to give rise to a Q branch separated from the nearest P and R branch transitions by ~5B. This is in turn consistent with the fact that the ground electronic state of the Br atom is $^2P_{3/2}$.

Adopting a $^2\Pi_{3/2}$ model, we can simulate the spectra using the corresponding Hamiltonian. In particular, the rotational energy levels are given by:

$$E(J) = B[J(J+1) - \Omega^2] - D[J(J+1) - \Omega^2]^2$$

where B and D are the rotational and centrifugal distortion constants respectively, and Ω is the quantum number associated with projection of the total electronic angular momentum, which for the ground state is 3/2. The total angular momentum quantum number (J) must be greater than or equal to Ω (3/2). As a result, the J = 1/2 rotational level is not allowed, accounting for the missing R(1/2) and P(3/2) transitions, which would otherwise appear in the gap between the Q branch and the R and P branches, respectively. The spectroscopic constants (ν, B, and D) resulting from the fit to the spectrum (see Figure 5.4B), are summarized in Table 5.5. The rotational temperature was determined by fitting the relative transition intensities, yielding 0.35 K, in good agreement with previous results on closed shell systems [56]. The experimental (helium) rotational constant is a factor of 2.2 smaller than the *ab initio* value [197]. This ratio is in excellent agreement with that found in other systems of this size [198]. The experimental monomer-to-complex frequency shift is determined to be -91.73 cm^{-1}, which is in good agreement with the (scaled) all electron *ab initio* (CCSD(T)) calculation for the linear hydrogen bound Br-HF isomer, namely -103.2 cm^{-1}. The present work also supports the assignment made previously in argon matrices (-128 cm^{-1} [32]), noting the significantly larger matrix shift in this case.

Although the simple model presented above provides a reasonable qualitative description of the experimental spectrum, there is clearly fine structure in the experimental spectrum that is not reproduced by the simulation. It is important to point out that unusual line shapes and even splitting of transitions can result from the interactions between the molecules of interest and the helium solvent [94, 199]. However, these effects are usually highly dependent upon the helium nanodroplet size, which is not the case for the Br-HF spectrum considered here. For this reason, we explored other possible sources for the observed fine structure, which is most evident in the transitions associated with low J states. We also considered the fact that bromine has two isotopes of significant natural abundance, namely ^{79}Br (50.69%) and ^{81}Br (49.31%). Nevertheless, the corresponding moments of inertia are not different enough to explain all of the structure observed in the experimental spectrum. In contrast, the isotope effects for the

lighter Cl-HF complex (discussed below) are quite significant.

5.4.1 Nuclear magnetic hyperfine structure

For closed shell molecules, where the magnetic fields at the nuclei are zero, the leading terms in the nuclear hyperfine structure are often those associated with nuclear electric quadrupole effects. Some effort was made to fit the Br-HF spectrum with the corresponding Hamiltonian, with only limited success. For this open shell system it is more likely that the dominant hyperfine structure results from the interaction of the magnetic field associated with the unpaired electron with the nuclear magnetic dipole moment. Indeed, the two isotopes of bromine have large and comparable nuclear magnetic dipole moments [200].

The angular momentum coupling cases for complexes containing open-shell atoms have been described previously by Dubernet and Hutson [201]. In their notation, the X-HF complexes belong to case one, which assumes that upon complexation, the large spin-orbit interaction of the halogen atom is not significantly changed. The differences between Dubernet and Hutson's case one, and Hund's case (a) for linear molecules, however, would be indistinguishable in our experiment, so we resort to a treatment of the nuclear hyperfine interaction for the latter. Following the treatment of Frosch and Foley [202], the Hamiltonian describing the interactions pertinent to Hund's case (a), can be written as: $H' = a\Lambda(I\bullet k)+b(I\bullet S)+c(I\bullet k)(S\bullet k)$, where k is a unit vector along the molecular axis. Assuming Λ and Σ are good quantum numbers associated with the projections of the orbital and spin angular momenta, respectively (the definition of Hund's case (a)), this expression can be reduced to $H' = [a\Lambda+(b+c)\Sigma]I\bullet k$ [200]. Using the relation:

$$I \bullet k = \frac{(I \bullet J)(J \bullet k)}{J^2}$$

the interaction energy is then:

$$W = [a\Lambda + (b + c)\Sigma]\frac{\Omega}{J(J + 1)}I \bullet J$$

where:

$$I \bullet J = \frac{F(F+1) - J(J+1) - I(I+1)}{2}$$

The relevant selection rules for this case are ΔF = 0, $\pm$1 and ΔJ = 0, $\pm$1, with $F' = 0 \leftarrow \backslash \rightarrow F'' = 0$. The quantum number associated with the nuclear spin angular momenta (I) is 3/2. (Note that I = 3/2 for chlorine as well, while for iodine, I = 5/2). J is the quantum number associated with the total angular momentum exclusive of nuclear spin, and F is the coupling of J and I.

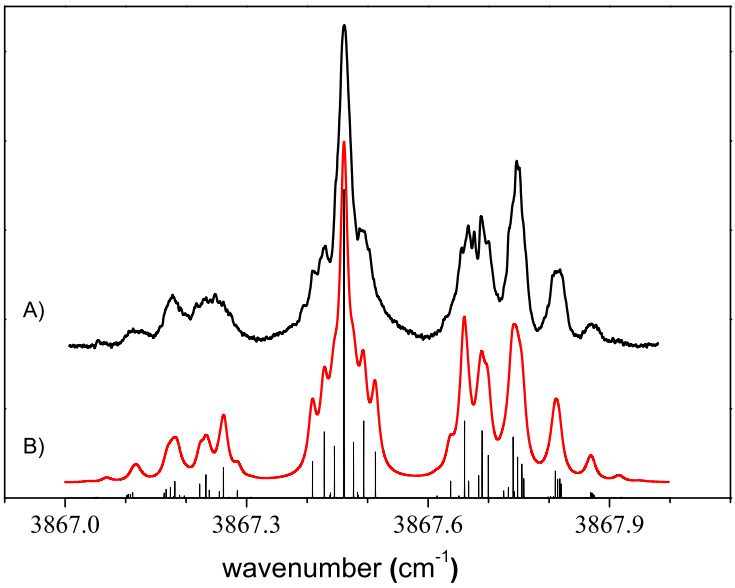

Figure 5.5: The infrared spectrum of Br-HF (A) shown with a simulation (B) that includes nuclear magnetic hyperfine interactions, I = 3/2, (see text). The stick spectrum shows all of the transitions that lie under the observed features.

The simulated spectrum for Br-HF, including nuclear magnetic hyperfine coupling, is shown in Figure 5.5B, compared to the experimental spectrum in Figure 5.5A. A stick spectrum is also shown below the simulated spectrum to illustrate the makeup of the various features in the spectrum. The addition of these hyperfine terms in the Hamiltonian clearly give results that reproduce all of the important features in the experimental spectrum. The effective hyperfine constant used in the simulation is given in Table 5.5, namely 0.045 cm^{-1}.

Constant	^{35}Cl-HF	Br-HF	I-HF
ν_0 (cm^{-1})	3887.54	3867.46	3847.82
B (cm^{-1})	0.055	0.043	0.037
D (cm^{-1})	1.2	0.95	0.3
[$a\Lambda$+(b+c)Σ] (cm^{-1})	0.005	0.045	0.035
μ (D)	1.9×10^{-4}	2.1×10^{-4}	2.2×10^{-4}
$\Delta\mu$ (D)	0	+0.25	+0.2

Table 5.5: A summary of the experimental parameters for the linear X-HF complexes, as obtained from fitting the infrared spectra. Isotope splittings of 0.038 cm^{-1} and 0.010 cm^{-1} were observed for the Cl-HF and Br-HF complexes, respectively. In each case the heavier isotope is shifted to the red due to vibrational averaging (see text).

The nuclear magnetic hyperfine splitting can be used to study the unpaired electron density at the bromine nucleus. A comparison of these effects for a van der Waals complex and the isolated atom is difficult, however, and very few examples of this exist in the literature. Important exceptions are the Ar-OH [203] and Ar-OD [204] complexes. In these cases the ground electronic state (X $^2\Pi$) hyperfine parameters are found to be virtually unchanged from the free molecules. In contrast, in the A $^2\Sigma^+$ electronically excited state of OH, a small change in the nuclear hyperfine interaction was used to argue that there was a slight change in the chemical bonding. Unfortunately, the lack of experimental data for bromine atom containing van der Waals complexes precludes any quantitative comparisons for the Br-HF system. Clearly this is an area that deserves more in depth theoretical study.

5.5 I-HF complex

A similar study was carried out for the I-HF complex, for which ^{127}I is the only naturally occurring isotope. Figure 5.6 shows a comparison between the experimental and simulated spectra, including the hyperfine effects discussed above. The molecular constants obtained from this fit are given in Table 5.5. Here again, the experimental rotational constants are consistent with those from the *ab initio* calculations, corresponding to a ratio of 2.2. For this case the experimental monomer-to-complex frequency shift is determined to be -113.6 cm^{-1}, which

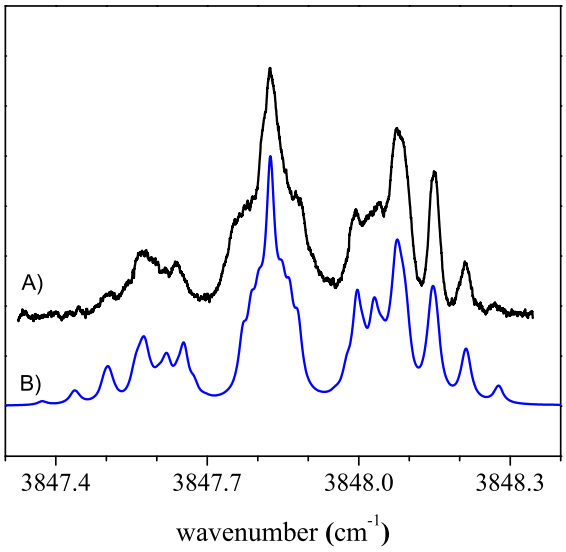

Figure 5.6: The infrared spectrum of I-HF in helium nanodroplets (A). The simulation (B) includes the effects of nuclear magnetic hyperfine structure, I = 5/2 (see text).

is in reasonable agreement with the calculations using the effective core potentials (-150 cm^{-1}). Qualitatively, the features in this spectrum are comparable with those for the Br-HF complex, again indicating that the vibrationally averaged structure is linear. The nuclear magnetic hyperfine constants derived for the isolated atoms of iodine and bromine are very similar, ^{127}I = 827.3 MHz, [205] ^{81}Br = 953.77 MHz, and ^{79}Br = 884.81 MHz [206]. It is therefore reasonable that the simulation of the Br-HF and I-HF spectra require coupling constants of approximately the same ratio (See Table 5.5).

5.6 Dipole moments

A series of Stark spectra were also recorded for the Br-HF and I-HF complexes. The data shown in Figure 5.7 for the Br-HF complex was obtained with the laser polarization aligned parallel to the applied DC electric field, yielding $\Delta M_F = 0$ (weak field limit) selection rules. Of particular interest are the two peaks that lie to either side of the main Q branch, which split

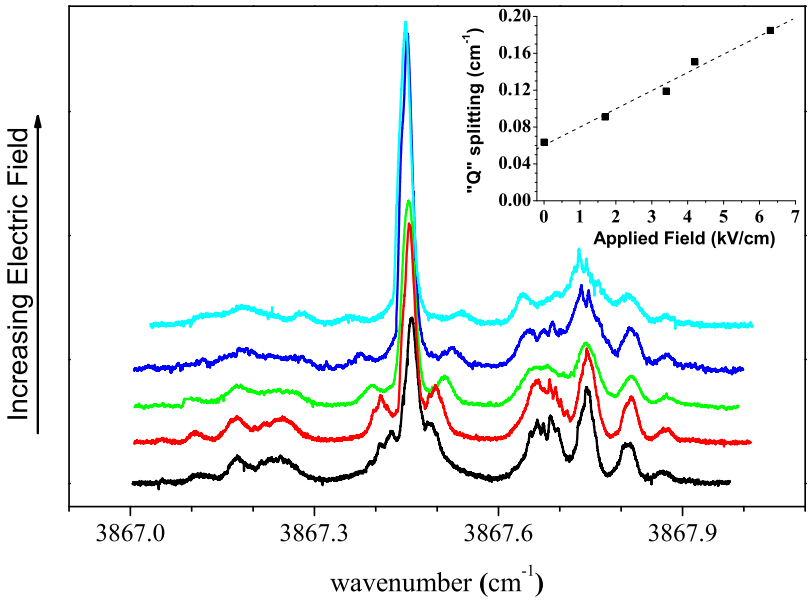

Figure 5.7: A series of spectra of Br-HF showing the dependence on the magnitude of the applied electric field, in this case aligned parallel to the laser polarization direction. Note that the transitions representing the shoulder on the Q branch split approximately linearly with the field strength, as shown in the inset.

apart as the field is increased. As shown by the inset in the figure, the splitting between these two peaks increases linearly with field, suggestive of a first order Stark effect that would be expected for a Π electronic ground state [200].

The electric fields used to obtain the spectra in Figure 5.7 are moderately large, which precludes the use of a perturbation treatment for the Stark effect. Instead, the full Hamiltonian matrix was numerically diagonalized to obtain the corresponding eigenstates and eigenvalues. In the limit of weak electric field coupling, the nuclear spin angular momentum remains coupled to the rotational angular momentum and a coupled basis set,$|J, \Omega, F\rangle$, is appropriate. In this limit, the application of the electric field does not disrupt the coupling of the angular momenta and M_F (the projection of F in the field direction) remains a good quantum number. At higher electric fields, however, the nuclear spin and electron spin become decoupled from the rotation of the molecule. In this limit the molecular eigenstates are best represented in

the decoupled representation, $|J, \Omega, M_I\rangle$, where the nuclear and electron spins form a constant projection along the electric field direction, namely M_I and M_J, respectively.

Although the use of moderately large electric fields in the present study would suggest the use of the decoupled representation, both basis sets are complete and the eigenvalues obtained with either are the same to within the numerical precision. In fact, the choice of basis set only affects the labeling of states. Since the present spectra are not fully resolved (into individual transitions) the quantum number labels are not that important, so for simplicity we used the coupled representation. The effective Hamiltonian can be written as: H_{eff} = H_R + H_{CD} + H_{HFS} + H_E, corresponding to the contributions from rotation, centrifugal distortion, nuclear hyperfine, and the Stark effect, respectively. The corresponding matrix elements are given in the literature [207]. In spherical tensor notation the Stark term can be written as:

$$H_E = -T^1(\mu_e) \times T^1(E)$$

which for the present case has the corresponding matrix elements:

$$\left\langle J, \Omega, I, F, M_F \left| -T^1_{p=0}(\mu_e) T^1_{p=0}(E) \right| J', \Omega, I, F', M_F \right\rangle =$$

$$-\mu_0 E_0 (-1)^{F-M_F} \begin{pmatrix} F & 1 & F' \\ M_F & 0 & M_F \end{pmatrix} \times (-1)^{F'+J+I+1} \{(2F'+1)(2F+1)\}^{1/2}$$
$$\times \begin{Bmatrix} J' & F' & I \\ F & J & 1 \end{Bmatrix} (-1)^{J-\Omega} \begin{pmatrix} J & 1 & J' \\ -\Omega & 0 & \Omega \end{pmatrix} \times \{(2J'+1)(2J+1)\}^{1/2} \quad (5.1)$$

Calculations were carried out with a coupled basis $|J, \Omega, F\rangle$ of sufficient size to ensure that the eigenvalues had converged to better than 10^{-4} cm^{-1}. All of the field-free constants were held fixed during the fit to the Stark spectra, so that the only adjustable parameters were the dipole moments in the ground and excited vibrational states. Figure 5.8 shows a Stark spectrum of

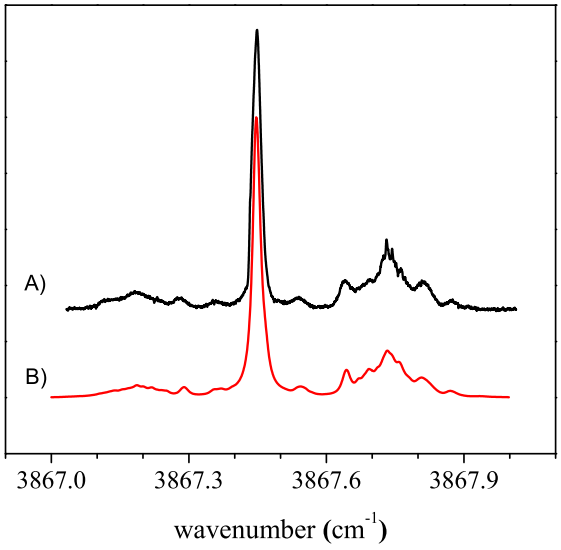

Figure 5.8: A Stark spectrum (A) of Br-HF, recorded with a 5.17 kV cm^{-1} electric field applied parallel to the laser polarization direction. The simulation (B) is based upon a fitted dipole moment of 2.10 D, with an increase in the dipole moment upon vibrational excitation of 0.25 D.

the Br-HF complex at an applied electric field of 5.17 kV cm^{-1}. The fitted spectrum is in excellent agreement with experiment, yielding a ground state dipole moment of 2.1 $\pm$ 0.1 Debye and a change upon vibrational excitation of +0.25 $\pm$ 0.05 D. In analogy with the Ar-HF complex [208], this large change in the dipole upon vibrational excitation is most likely due to a increase in the anisotropy of the intermolecular potential, resulting in a decrease in the corresponding bending amplitude. This in turn results in an increase in the vibrationally averaged dipole moment in the excited state.

The fact that the experimental dipole moment is considerably smaller than the *ab initio* value calculated here (2.48 D, corresponding to a rigidly linear complex) lends supporting evidence to large amplitude motions, which act to average the equilibrium linear geometry. A first approximation to this effect on the dipole moments and band origin shifts can be estimated by calculating their expectation values. As shown in Figure 5.5, at each point along a one-dimensional bending coordinate (represented by rotating the HF about its center of mass, mak-

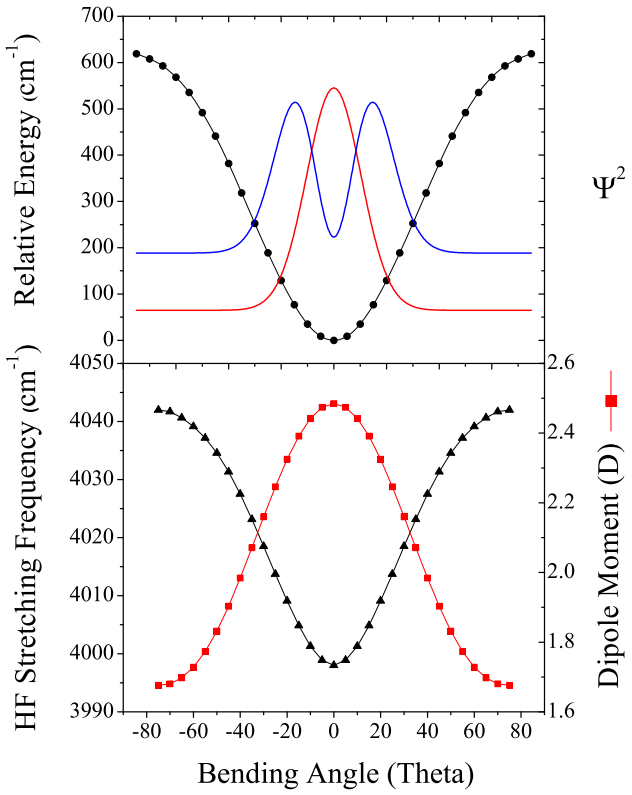

Figure 5.9: Upper panel: A one-dimensional slice through the *ab initio* (UMP2/aug-cc-pVTZ) potential ($^2A'$) for the Br-HF complex, along the H-F bending coordinate. The ground and first excited state wavefunctions were calculated (see text), and Ψ^2 is shown for reference. Lower panel: *Ab initio* calculations of the HF stretching frequency (Triangles) and the permanent dipole moment (Squares) as a function of the bending angle. The effects of vibrational averaging are found to lower the dipole moment and shift the HF stretching frequency to the blue, in agreement with experimental results.

ing an angle theta between the *a* axis of HF and the halogen atom) the resulting energy, dipole moment, and harmonic vibrational frequency were calculated at the UMP2/aug-cc-pVTZ level. As the complex bends the degeneracy in the spatial orientation of the unpaired orbital is lifted, resulting in two states, ^{2}A' and ^{2}A" respectively. Based upon simple intuition of electrostatic forces, and confirmed by *ab initio* calculations, the ^{2}A' state (in which the orbital that contains the unpaired electron is in the plane of the bending coordinate) is lower in energy than the ^{2}A" state (except where they are degenerate). The difference potential (^{2}A" - ^{2}A') becomes signif-

icant only for large bending angles (176 cm^{-1} at 40 degrees), and thus for simplicity we have only included the ^{2}A' state in our discussion. The bending wavefunctions were calculated numerically using the Numerov-Cooley method [176], and used to find expectation values given by:

$$\langle X \rangle = \frac{\int_0^\pi \Psi X \Psi \sin(\theta) \partial\theta}{\int_0^\pi \Psi \Psi \sin(\theta) \partial\theta}$$

This treatment yields values of $\langle\mu\rangle$ = 2.40 D and $\langle\nu\rangle$ = 4004 cm^{-1}. These values can be compared directly with those obtained from the equilibrium calculation, namely μ_{eq} = 2.48 D and ν_{eq} = 3998 cm^{-1}. As one can see, the vibrational averaging lowers the dipole moment and shifts the harmonic vibrational frequency by 6 cm^{-1} to the blue, in both cases improving the agreement with experiment. Quantitative agreement is not expected, however, given that the single reference *ab initio* calculations do not correctly treat the excited electronic states, which will be important in determining the potential surface away from the minimum.

It is also important to consider that the influence of the helium solvent on the measurement of the dipole moment has been addressed previously in our group [134]. We found that for a rigid molecule the solvent effect results in a few percent deviation from the gas-phase dipole moment. However, for a more floppy system of the type considered here, the effect of the solvent could be more important. In particular, the presence of the solvent could make the potential surface more anisotropic, giving rise to a larger vibrationally averaged dipole moment. It is interesting to note, however, that experiments from our group on the Ar-HF binary complex in helium droplets [209] show very small helium solvent effects, which we take as evidence that the present results for the X-HF systems are essentially the same as those for the gas-phase complexes. This said, the more subtle effects on these observables still need to be examined in detail, to further our understanding of the solute-solvent interactions in this exotic medium.

Similar Stark spectra were recorded for the I-HF system, as shown in Figure 5.10. The fitted spectrum was calculated with a dipole moment of 2.2 $\pm$ 0.1 Debye and a change of +0.2 $\pm$ 0.05 D upon vibrational excitation. These values are consistent with the trends seen in the

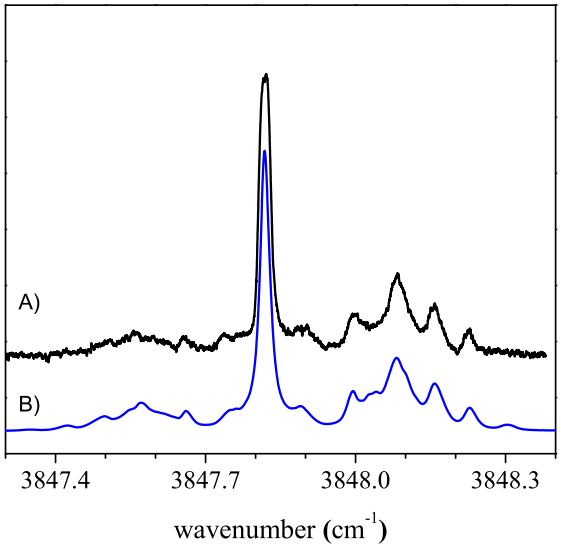

Figure 5.10: An experimental Stark spectrum of I-HF (A) recorded at an electric field strength of 3.86 kV cm^{-1}. The spectrum (B) was fit to the experimental data, yielding a dipole moment of 2.2 D. The increase in dipole moment upon vibrational excitation is 0.2 D.

a*b initio* calculations.

5.7 Cl-HF complex

Chlorine atoms are more difficult to produce by pyrolysis, requiring that the source be operated at higher temperatures (~1600 K). The spectrum of Cl-HF, obtained under these conditions, is shown in Figure 5.11. All of the tests discussed above, including the careful examination of the pick-up cell conditions required to optimize the signals, were used to confirm that this is indeed the spectrum of the binary complex. The qualitative features in this spectrum are similar to those observed for the above systems, in particular, the presence of a Q branch and the "gaps" between it and the P and R branches. Although this is consistent with a $^2\Pi_{3/2}$ ground state, the fine structure observed in the spectrum is quite different from that in the other systems. As illustrated in Figure 5.11, the entire spectrum appears to be doubled, with each strong transition having a weaker companion on the low frequency side. Indeed, the simulated

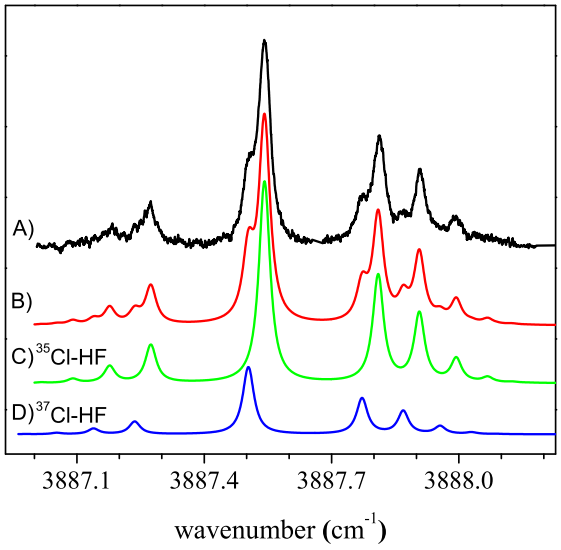

Figure 5.11: The experimental infrared spectrum (A) of Cl-HF in helium nanodroplets. The observed splitting is attributed to the two naturally occurring isotopes of chlorine. A good fit (B) is obtained using spectra (C) and (D), separated by 0.0380 cm^{-1}. The relative intensities of the two bands are scaled to the natural abundances of the two isotopes of chlorine. In addition, a nonzero nuclear magnetic hyperfine constant was necessary to reproduce the measured rotational line intensities. The simulation parameters are given in Table 5.5.

spectrum in Figure 5.11, consisting of a sum of two shifted (by 0.0380 cm^{-1}) $^2\Pi_{3/2}$ bands (also shown in Figure 5.11), accurately reproduces the experimental spectrum. The relative intensities of the two bands are in excellent agreement with the ratio of the natural abundances for ^{35}Cl and ^{37}Cl, namely 3.129 [210]. Indeed, we fit the central Q branch feature to two Lorentzian functions (see Figure 14), which gave an experimental ratio of the integrated areas of 3.174. Apparently the isotope shift is large enough in this system to observe the corresponding splitting of the transitions. It is interesting to note that although no hyperfine splittings are observed in the spectrum, a nonzero coupling coefficient was necessary to accurately reproduce the rotational line intensities, yielding a nuclear hyperfine coefficient of = 0.005 cm^{-1}. Once again, the relative magnitude of this coefficient is in quite good agreement with the relative hyperfine constants for the isolated atoms (^{35}Cl = 205.29 MHz, ^{37}Cl = 170.69 MHz) [211].

A series of Stark spectra were also recorded for the Cl-HF complex (Figure 5.12) with

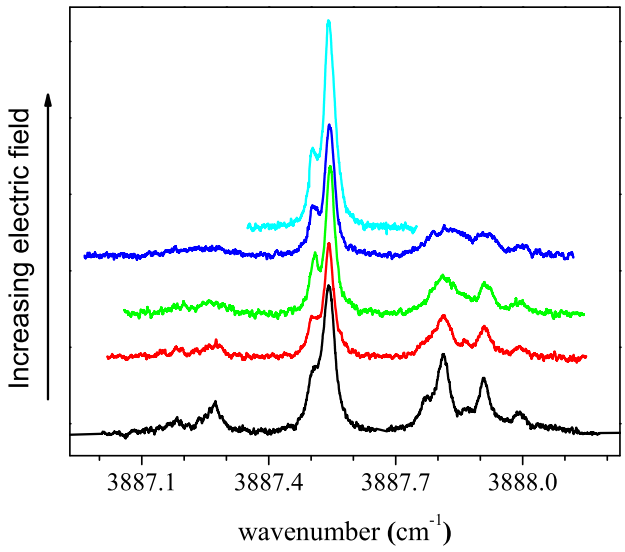

Figure 5.12: A series of spectra showing the evolution of the Cl-HF spectra as a function of applied electric field strength.

similar field strengths as used for Br-HF. The top spectrum of this series was recorded at an electric field strength of ~ 60 kV cm^{-1}, corresponding to the pendular regime, so that the P and R branches are no longer visible. In contrast to Br-HF, no discernible field dependent splitting is observed near the Q branch, which supports the assignment of the zero-field splitting to an isotope effect, rather than nuclear hyperfine interactions. Figure 5.13 shows a comparison between an experimental Stark spectrum recorded at 3.5 kV cm^{-1} and a simulated spectrum obtained by holding all of the field-free parameters fixed, yielding a dipole moment of 1.9 D. The calculated spectrum is a simple addition of the two bands arising from ^{35}Cl and ^{37}Cl isotopomers, the intensities having been scaled in accordance with the chlorine isotope natural abundance ratio. At the spectroscopic resolution available here, the isotopic dependence of the rotational constants and dipole moments could not be determined. In contrast to the bromine and iodine results, the change in dipole moment upon vibrational excitation was found to be less than our experimental accuracy. This result may be indicative of the smaller change in anisotropy of the potential upon vibrational excitation, compared to Br-HF, which is consistent

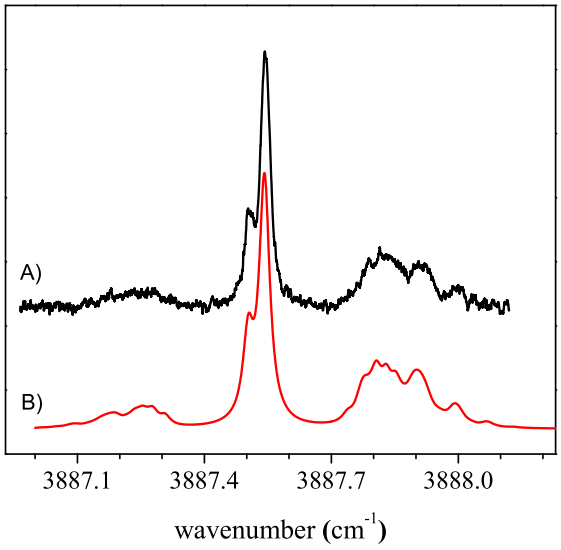

Figure 5.13: A Stark spectrum (A) of Cl-HF recorded at an electric field strength of 3.51 kV cm^{-1} applied parallel to the laser polarization direction. The fitted spectrum (B) yielded an experimental dipole moment of 1.9 D. The simulation includes contributions from both isotopes of Chlorine.

with the relatively small polarizability of a chlorine atom.

5.7.1 Optically selective mass spectrometry (OSMS)

To aid in the assignment of the zero-field spectrum to the two isotopes of chlorine, we performed a laser mass-spectrometer experiment designed to determine the origin of the observed spectroscopic signals. This experiment was performed in a second helium nanodroplet spectrometer available in our laboratory, which uses a mass spectrometer in place of the bolometer for monitoring the droplet beam depletion. In this case, vibrational excitation of the complexes upstream of the ionization region of the mass spectrometer again results in a decrease in the corresponding droplet size. This, in turn, reduces the average ionization cross section, providing us with a depletion signal similar to that obtained above using the bolometer. By amplitude modulating the laser and using phase sensitive detection of the mass spectrometer signals, we

can obtain mass spectra that are optically labeled, which is to say that the corresponding mass spectra come entirely from droplets containing the species that is being excited by the laser.

This Optically Selected Mass Spectrometry (OSMS) is used in the present study to confirm that the doubling observed in the Cl-HF spectrum is the result of isotopic splitting. Indeed, by

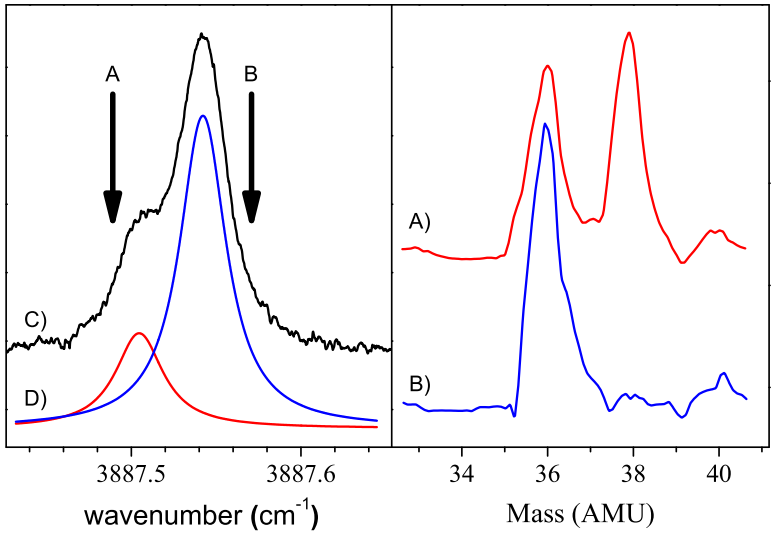

Figure 5.14: Left panel: An expanded view of the Q branch region of the Cl-HF spectrum shown in Figure 5.11. The vertical arrows show the laser frequencies used to record the two mass spectra shown in the right panel. The two Lorentzian line shapes shown in (D) indicate the relative contributions from the ^{35}Cl and ^{37}Cl isotopomers at these laser frequencies. Right panel: Optically selected mass spectra (OSMS) of Cl-HF in helium droplets. This technique is used to confirm that the observed splitting in the Cl-HF infrared spectrum is due to the two isotopes of chlorine (see text).

positioning the laser to the high frequency side of the Q branch (3887.57 cm^{-1}), indicated by arrow B in Figure 5.14, we only observe a strong peak in the mass spectrum (Figure 5.14b) corresponding to the ^{35}Cl-HF complex, namely at 36 amu (reaction occurs during the ionization of ^{35}Cl-HF to form H^{35}Cl^{+}, discussed below). In contrast, when the laser is tuned to the low frequency side of the spectrum (3887.50 cm^{-1}), indicated by arrow A in Figure 5.14, we observe peaks at both 36 and 38 amu (Figure 5.14a). We see both masses in this case simply because the signal levels (in the optical spectrum) associated with the minor isotope (^{37}Cl-HF)

are rather low and there is still significant contribution to the spectrum from the wing of the ^{35}Cl-HF Q branch. These OSMS measurements provide conclusive evidence that the proper assignment of the splitting in the observed spectrum of Cl-HF is to the two isotopes.

A detailed overview of electron impact mass spectrometry in helium droplets has been given in the literature [212–215]. Given the observed ionization reaction however, we briefly discuss its origin. Electron bombardment of the droplet results in the formation of a helium cation that "hops" towards the center of the droplet by resonant charge transfer [216]. Along its way, it may form a $(He_n)^+$ cluster (small peaks at mass 32, 36, and 40 in Figure 5.14) or transfer its charge to Cl-HF. Charge localization on the HF or Cl fragment promotes two reactions (HF^+ + Cl $\rightarrow$ HCl^+ + F and Cl^+ + HF $\rightarrow$ HCl^+ + F), explaining the appearance of HCl^+. Despite the large endothermicity of the second reaction (-1450 cm^{-1} vs. 9700 cm^{-1}) [217] the excess energy dictated by the difference in ionization potentials: IP_{He} - IP_{HF} or IP_{He} - IP_{Cl} = ~80000 cm^{-1} released in the charge transfer (from He^+ to (Cl-HF)$^+$) may drive either reaction.

5.7.2 Vibrational averaging

Having established that the H-F vibrational origins for the two isotopomers of Cl-HF ($\Delta\nu$ = 0.0380 cm^{-1}) are slightly different, it is worth discussing the possible sources of this difference. It is interesting to note that *ab initio* calculations predict the H-F vibrational frequencies for ^{35,37}Cl-HF, at the equilibrium linear geometry, to have an isotope splitting of less than 1×10^{-4} cm^{-1}. Although these calculations cannot be trusted to this absolute accuracy, they do indicate that the direct mass effect is much too small to account for the observations. Instead, we turn our attention to the fact that the complexes are not rigidly linear, but undergo significant intermolecular bending. This we already know from the dipole moment measurements presented above. Indeed, the bending potential for these systems are presumed to be rather broad, consistent with that calculated for Cl-HCl [181], meaning that the complex undergoes significant intermolecular bending. If the effective mass for this bending motion is different for the two isotopomers, the corresponding difference in the bending amplitude will change

the associated intra-molecular vibrational averaging, resulting in slightly different vibrational origins for the two isotopomers.

Flygare and co-workers [218] have discussed this issue previously for closed shell complexes, including the ^{82,83,84,86}Kr-HF isotopomers. From the microwave spectrum they estimate the vibrationally averaged bending angle (VAA) from the projection of the nuclear spin-spin interaction constant in HF onto the A inertial axis of the complex. For ^{82}Kr-HF and ^{86}Kr-HF the VAA's were estimated to be 38.67° and 37.86° respectively. Infrared measurements [219] on the HF stretch of this complex show an isotope splitting on the order of 0.005 cm^{-1}, which is attributed to this effect.

Given the magnitude of the isotope splitting in the chlorine spectra ($\Delta\nu$ = 0.0380 cm^{-1}), we do not expect a significant isotope splitting for Br-HF, due to the much smaller percent mass change in this case. Indeed, the ratios of the reduced masses in the two systems differ by a factor of four. This fact alone (assuming the bending potentials are the same) would make the isotope effect on the vibrational frequency a factor of $\sqrt{4}$ smaller for Br-HF (0.019 cm^{-1}). Within experimental resolution, a splitting of this magnitude is not evident in the field-free spectrum. However, a careful examination of several pendular scans of Br-HF does lend supporting evidence to an isotope splitting of approximately this value. Figure 5.15A shows a pendular spectrum of Br-HF recorded with an applied electric field strength of 43.4 kV cm^{-1}. The simulated spectra corresponding to only one isotope (labeled C) has quite poor agreement of the intensities for the unresolved bands. A sum of two such bands separated by 0.010 cm^{-1} is shown (B) and the agreement is found to be excellent, lending support for an isotope splitting of this magnitude. In the field-free spectrum, this splitting only contributes to a slightly larger observed linewidth.

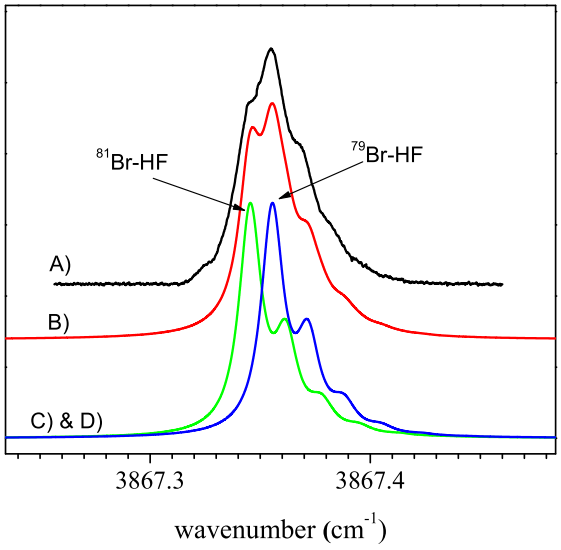

Figure 5.15: A pendular spectrum of Br-HF recorded at an applied electric field strength of 43.4 kV cm^{-1}. The fine structure in this band is well described (B) by an isotope splitting of 0.01 cm^{-1}. The smaller isotope splitting, in comparison with Cl-HF, is consistent with the correspondingly smaller ratio of the reduced masses for Br-HF. The two simulated spectra, (C) and (D), were generated using the constants derived from fitting the field-free and Stark spectra.

5.8 Summary

We reported here the direct observation of heavy-light-heavy complexes consisting of halogen atoms (Cl, Br, and I) with a single HF molecule, formed in helium nanodroplets. Infrared spectroscopy is used to determine the structures of these complexes to be (vibrationally averaged) linear, in agreement with theoretical calculations. Fine structure is observed in the spectra corresponding to isotope splittings for Cl-HF and Br-HF (Iodine has only one naturally occurring isotope) and nuclear magnetic hyperfine interactions. The isotope splittings are in general agreement with the closed shell analogues Kr-HF and Xe-HF, and as such are sensitive to the percent change in mass for each case. The splitting between these two bands provides a stringent test for theoretical surfaces and we will make this comparison in the next section using high-quality fully-dimensional theoretical potential energy surfaces. The observed nuclear

magnetic hyperfine interactions are also in general agreement with that found in the isolated atoms. Dipole moments of these complexes have been measured using Stark spectroscopy and are found to be smaller than our calculations due to vibrational averaging.

Concurrent with these studies was the pursuit of F-HF. No evidence for its formation has been observed to date, possibly calling into question the assignment of the argon matrix work [191]. It may be that the growth process in helium favors different geometrical structures, none of which were observed in this study. Given the importance of understanding the complex potentials of these systems, and the now proven ability of helium droplets to stabilize species of this type, such systems will be an active area of future work.

It has been proposed [186] that complexes of this type may posses a T-shaped structure, but display several of the properties of a linear open-shell molecule. Given the very large frequency shift from the HF monomer however, this is unlikely the case for the I-HF, Br-HF and Cl-HF complexes observed here. The dynamics of these systems can certainly be regarded as floppy, as our results have shown for the disagreement in the dipole moments and vibrational averaging, however we feel the linear equilibrium view is still a good one. The excellent agreement with both the nuclear hyperfine structure and the Stark effect also support our assignment. These theories have only included the effects believed to be present in a linear molecule case, giving very good results. In addition, the Stark effect is extremely sensitive to the relative orientation of the permanent dipole moment and the vibrational transition moment. If the two moments were not parallel (as in the linear molecule case) the resulting Stark spectrum would be expected to have quite different character. Nevertheless, the fact that this point is still the subject of considerable debate illustrates how poorly we still understand these species, calling out for more experiments and theory on these entrance channel complexes.

5.9 High-level theoretical treatment of Cl-HF and Br-HF

Since our first observation of the halogen atom - HF complexes, high-level theoretical calculations have been performed for the Br-HF and Cl-HF complexes to elucidate the structure and dynamics of these systems and to compare with our helium droplet results.

Meuwly and Hutson have reported two-dimensional semiempirical potential energy surfaces and the corresponding bound states for Br-HF [220], where the interaction potential was described as:

$$V_{Br-HF} = V_{Kr-HF} + V_{Br-Ne} - V_{Kr-Ne} + V_Q$$

The V_Q term is electrostatic in nature, and arises from the interaction of the atomic quadrupole on Br with the multipoles on HF, where as the Kr-HF and Kr-Ne pair potentials were taken from the literature. The Br-Ne potential was calculated at the RCCSD(T)/aug-cc-pVQZ level. Despite the apparent simplicity of this model, it has been applied to similar open shell molecular complexes and agrees quite well with first principles *ab initio* calculation. The spin-orbit corrected diabatic surfaces predicted the global minimum for this system to be linear (hydrogen bound) with a binding energy of 670 cm^{-1}. The ground electronic state of this system is predicted to be $^2\Pi_{3/2}$ in agreement with our experimental observation. A T-shaped minimum (395 cm^{-1} higher in energy) is also predicted, although the barrier connecting this well to the linear one is quite small (< 50 cm^{-1}). Recent calculations on Cl-HCl [186] in contrast have predicted a T-shaped global minimum. The differences between Br-HF and Cl-HCl is attributed to the large dipole of HF (compared to that of HCl) and the large polarizability of the bromine atom (compared to that of Chlorine). As a result, the linear minimum is considerably more stable in the Br-HF case. Comparing our single reference *ab initio* calculations (Tables 5.1, 5.2, and 5.3) with the spin-free adiabatic surfaces reveals that the our *ab initio* potential has a somewhat shallower T-shaped minimum (-404 cm^{-1} vs. -500 cm^{-1}), while the linear minimum (hydrogen bonded) are more similar (-720 cm^{-1} vs. -670 cm^{-1}). Their derived rotational constant for the ground $^2\Pi_{3/2}$ state is B_0 = 0.0887 cm^{-1} which is slightly smaller than our equilibrium

calculations, 0.0948 cm^{-1} at the UCCSD(T)/aug-cc-pVTZ level, due to our slightly shorter intermolecular bond length, and zero-point effects. Nevertheless, our experimentally determined B value (0.043 cm^{-1}) is reduced by a factor of approximately two from the calculations, which accounts for the effects of the helium, and is in good agreement with other systems of this size.

It is also interesting to note that Meuwly and Hutson calculated a dipole moment of 1.21 D for Br-HF, which included the effects of vibrational averaging, however, neglected the induced dipole on the bromine. Given that the dipole moment of the HF monomer has been measured to be 1.819 D [221], this difference (0.609 D) reflects the effect of vibrational averaging on their potential. If we subtract this value from the equilibrium *ab initio* calculation presented here (which does include the induced dipole on the bromine atom) one predicts a dipole moment smaller than observed (1.87 D vs. 2.1 D), indicating that the anisotropy of their potential surface is too small. In contrast, the one-dimensional vibrational averaging based upon the present *ab initio* surface gives a dipole reduction that is too small (0.08 D), suggesting that the corresponding anisotropy is too large. Future studies should be directed at more accurately determining this contribution so that more quantitative comparisons can be made using a full dimensional potential surface.

For Cl-HF, a detailed theoretical study has been undertaken by the group of van der Avoird [222, 223]. In particular, the full three-dimensional (R, θ, r_{HF}) potential energy surfaces have been computed at the RCCSD(T)/aug-cc-pVTZ+{332} level and include the transformation to diabatic states including spin-orbit coupling. In general, the results for the stationary points of the spin-free adiabatic potentials are in very good agreement with ours (Tables 5.1, 5.2, and 5.3) due to the fact that they were calculated at nearly the same level of theory (our calculations did not include the extra mid-bond functions). The bound states of the spin-orbit corrected diabatic surfaces were computed by a full 3D diagonalization of the Hamiltonian:

$$\begin{aligned} \hat{H} &= \hat{H}_{HF} + \frac{-\hbar^2}{2\mu_{ab}R}\frac{\partial^2}{\partial R^2}R + \frac{|\hat{j}_a + \hat{j}_b|^2 - 2(\hat{j}_a + \hat{j}_b) \bullet \hat{J} + \hat{J}^2}{2\mu_{ab}R^2} + A\hat{\lambda} \bullet \hat{S} + V \\ \hat{H}_{HF} &= \frac{-\hbar^2}{2\mu_b r}\frac{\partial^2}{\partial r^2}r + \frac{\hat{j}_b^2}{2\mu_b r^2} + V_{HF}(r) \end{aligned}$$

In agreement with the previous Br-HF calculations and our experimental results, the ground electronic state is predicted to be linear hydrogen bound ($^2\Pi_{3/2}$) with a zero-point corrected binding energy of 432.25 cm^{-1}, (at the 3D level with $\nu_{HF} = 0$). The calculated ground state rotational constant is 0.1188 cm^{-1} and when compared with the experimental value of 0.055 cm^{-1} we see that the reduction factor due to the helium is nearly the same as for Br-HF (~2.2).

To further explore the dynamics of Cl-HF, Fishchuk *et al.* calculated the bound levels using two-dimensional potential energy surfaces in which rHF was either frozen at $\langle rHF \rangle_0$ or $\langle rHF \rangle_1$ corresponding to the different HF vibrational states (2D$_r$ model), or averaged the full 3D potentials over the HF vibrational wavefunctions (2D$_v$ model). The calculated frequency shift from HF monomer, and the chlorine isotope shift for each of the different models and our experiment are shown in Table 5.6.

ΔE (ν_{HF} = $1 \leftarrow 0$)	red-shift (cm^{-1})	^{37}Cl - ^{35}Cl isotope shift (cm^{-1})
harmonic calculations MP2 / CCSD(T)	93 / 79	$< 1 \times 10^{-4}$
2D$_r$ model	39.86	0.019
2D$_v$ model	63.55	0.032
3D calculations	64.96	0.033
Experiment	73.69 (68.77)[a]	0.038 (0.035)[a]

[a]Values in parenthesis are corrected for the He matrix shift.

Table 5.6: Spectroscopic parameters for Cl-HF from calculations of van der Avoird [222, 223].

As one can see, the agreement of the full 3D calculations with experiment is excellent, after correcting the vibrational frequency for the effects of the helium matrix. The 2D$_v$ results are closer to the full 3D calculation than the 2D$_r$ model, an effect which has also been observed for Ar-HF [224], but the deviations between the different 2D models is much more pronounced for Cl-HF. Comparing the 2D$_v$ results to those from the full 3D solution show that the origin of red-shift of vibrational band origin is attributed to a increase of D$_0$ with HF vibrational excitation, rather than a dynamical coupling between the HF stretch mode and the intermolecular modes. The origin of the chlorine isotope effect on the HF vibrational frequency is mostly a zero-point energy effect, which is not taken into account in the harmonic frequency calculations.

The intermolecular bending and stretching levels of Br-HF and Cl-HF were also calculated, leading us to search for the corresponding combination bands with the H-F stretch. These states, which correspond to excitation of intermolecular bending and stretching modes are particularly interesting given that they are sensitive to all 3 diabatic surfaces (1^2A', 2^2A', and 1^2A") [220]. The combination bands are predicted to be 145 (169) and 172 (207) cm^{-1} above the H-F fundamental (3867.4 cm^{-1} for Br-HF, 3887.5 cm^{-1} for Cl-HF), for the |P| = 1/2 and 5/2 states of Br-HF (Cl-HF), respectively. Unfortunately, extensive searches in this region between 4000 - 4100 cm^{-1} did not reveal these bands. This may be due to the fact that the F-center laser has relatively little power in this region. Further work in this direction is planned using a higher power PPLN-OPO laser system [225].

Chapter 6

Halogen Atom (X) - HCN Complexes

Given the prototypical nature of such heavy-light-heavy complexes (X-HX) reported upon in Chapter 5, we have performed an experimental and theoretical investigation of the corresponding X-HCN complexes. As we shall see, the X-HCN interaction is substantially different from the corresponding X-HX complexes and in this case two different linear isomers are predicted theoretically and both are observed. The high resolution spectra obtained for these systems also provide a comparison with theoretical predictions about the nature of the spin-orbit interaction of the multiple electronic surfaces for these complexes.

6.1 Introduction

The reactions of halogen atoms with HCN have been the focus of extensive experimental [226–228] and theoretical study [229–231], aimed at elucidating the role of the potential energy surface in determining the associated reaction dynamics. The CN group may be regarded as a pseudo-halogen, and thus there is interest in comparing the reaction dynamics of this tetra-atomic system with the analogous X-HY (X&Y=halogen atoms) triatomic systems. HCN is an ideal test case because the CN group is usually found to act as a single unit, but there is still considerable debate about whether or not the CN bond is a spectator to the dynamics of many different reactions. The additional degrees of freedom that the HCN molecule presents, opens up many new channels of the potential that can be explored, and the X + HCN systems have provided benchmarks for the theoretical treatment of such multi-dimensional dynamics.

The Cl,H,C,N potential energy surface has been studied experimentally from three different starting positions. De Juan *et al.* [231] have investigated the H + ClCN → HCl + CN reaction, by colliding translationally hot H atoms formed from the 248 nm photolysis of H_2S, with ClCN. This experimental arrangement prepares the reactants with 21.6 kcal mol^{-1} of collision energy, which is ~43 kcal mol^{-1} above the energy of Cl + HCN (see Figure 6.2). By analyzing the nascent CN rovibrational populations, as well as the doppler profiles of the vibrational transitions, it was proposed that the CN is a spectator under these conditions, and that most of the available energy goes into HCl vibration and to translation of the two fragments. Sims and Smith [232] and Frost *et al.* [233] have studied the HCl(ν_{HCl}) + CN(ν_{CN}) → HCN + Cl reaction, and came to the conclusion that CN is also a spectator in this reaction, due to the fact that there is a negligible enhancement of the reaction rate upon exciting the CN stretching vibration. A third set of experiments were carried out by Metz *et al.* [228, 234] and Kreher *et al.* [226, 235] focusing on the reaction of translationally hot chlorine atoms with highly vibrationally excited HCN:

$$Cl + HCN(\nu_1, \nu_2, \nu_3) \rightarrow HCl + CN$$

Metz and coworkers showed that HCN, when prepared with either 4 quanta of CH stretch (004) or 3 quanta of CN stretch plus two quanta of CH stretch (302)[1] react with comparable rates, and conclude that the CN "is clearly not a spectator". Another interesting observation from this work is that only 14% of the available energy was found as HCl vibration, which is surprisingly small since this is the bond that is formed in the reaction. To justify this observation an addition-elimination mechanism was proposed which involved an intermediate HClCN product, as opposed to direct collinear abstraction. Indeed, experiments in argon matrices have now proven the existence of HFCN [236, 237]. This intermediate must survive long enough in the gas-phase to permit energy redistribution, which accounts for the transfer of energy from HCl(v) to CN(v). According to this mechanism the CN cannot be a simple spectator. Kreher *et al.* confirms these observations, however points out that HCN(302) does give rise to higher CN(v) than does HCN(004) so some memory of the initial state is retained.

The global potential energy surface for Cl + HCN was first studied theoretically by de Juan *et al.* at the MP4/3-21G* level [231], to aid in the interpretation of their experimental results. Their calculations did show the existence of a covalently bound HClCN intermediate product, but the relative energies of the reactants and products showed significant discrepancies with the experimentally determined values. Harding later revisited the Cl-HCN surface at the RHF+1+2+QC/cc-pVDZ level [230], and found the energies to be in much better agreement with experiment. Although the overall topology of the two surfaces are similar, the existence of a direct HClCN →HCl + CN pathway originally proposed by de Juan *et al.* was not found by Harding. Instead, Harding points out that they most likely found the transition state for collinear abstraction. Although an exhaustive search of the six-dimensional potential energy surface is impossible, Harding states that this HCl elimination pathway is unlikely based on the overall topology of the potential. He finds that the transition state of the Cl + HCN→ HCl + CN reaction is a collinear abstraction mechanism, and that the reaction path does not

[1]The P(4) transition of the (004)←(000) band (12623 cm^{-1}) and the P(8) transition of the (302)←(000) band (12631 cm^{-1}) were used for the excitation.

directly involve the HClCN complex, in contrast to that proposed by Metz and coworkers. Indeed the HClCN complex can be formed at energies well below the abstraction reaction, however further reaction to form HCl + CN would require surmounting barriers in excess of that for direct abstraction. In order to explain the experimental results, which clearly show vibrational excitation of the CN, Harding proposes two possible mechanisms. First, the CN stretching frequency is found in the calculations to be largely unaffected along the reaction coordinate. In contrast, the reagent CH stretch and product HCl stretches, which are initially above the CN frequency, go through a minimum at the transition state and are below the CN frequency. Because these normal modes cross the CN stretching frequency, energy could flow between these two modes along the course of the reaction. Secondly, Harding's calculations predict the existence of long-range entrance channel complexes on both sides of the abstraction transition state (X–HCN, HCN–X, and CN–HCl) which could also influence the final product state distributions.

Most recently Troya *et al.* have performed a quasiclassical trajectory study of the Cl + HCN $\rightarrow$ HCl + CN reaction [229]. Their findings are in agreement with Harding, in that the intermediate HClCN product only constitutes a minor channel (< 5%) at the translational energies relevant to the experiments. The focus of the current study is to explore the long-range entrance channel complexes of X + HCN, which have been implicated in contributing to the vibrational excitation of the CN.

6.2 *Ab initio* calculations

In order to optimize conditions for the pickup of a single halogen atom, the temperature of the pyrolysis source is adjusted, monitoring the percent dissociation of the precursor by probing both the X-HCN and X_2-HCN binary complexes. In order to characterize the precursor complexes we have calculated a two-dimensional angular potential (at the RMP2/aug-cc-pVDZ level) for HCN-Cl_2 to find all possible structures. The two rotor angles, θ and ϕ, were stepped in

increments of 10^0, and the intermolecular distance R was relaxed to find its minimum in energy. The remaining geometric parameters were held fixed at the values found for separate HCN and Cl_2 optimizations. The resulting energy was corrected for basis set superposition error [195], and a spline interpolation was used to generate the final surface shown in Figure 6.1. The

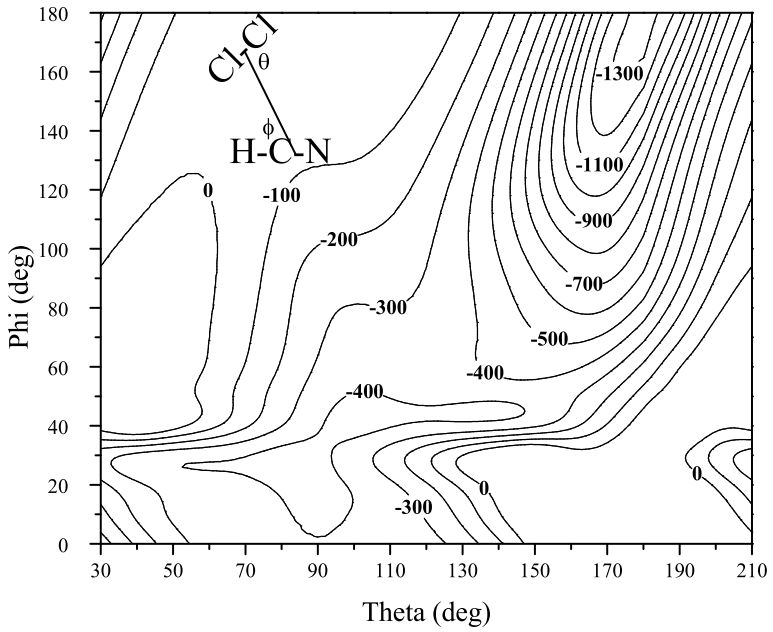

Figure 6.1: A two-dimensional angular potential for HCN-Cl_2 showing two possible local minimum structures. At each point only the intermolecular distance was optimized to find its minimum in energy. Counterpoise correction was applied and the final surface generated using a bi-cubic spline interpolation algorithm. In helium droplets both isomers are observed for I_2, Br_2, and Cl_2 complexes with HCN, whereas in the gas-phase only the global minimum (linear nitrogen bound) isomer has been identified. Interestingly only the global minimum HCN-F_2 isomer was observed in helium.

surface predicts a deep minimum for a linear nitrogen bound geometry (Theta, Phi) = (180, 180), and a very flat minimum around (90, 20) corresponding to a near T-shaped hydrogen bound complex. Previous gas-phase studies [238–240] have confirmed the linear geometry of the HCN-Cl_2, HCN-BrCl, and HCN-FCl complexes however there has been no previous evidence (nor prediction) of a hydrogen bound isomer. Fully relaxed geometry optimizations

and harmonic vibrational frequency calculations confirm that the local minimum structure is slightly bent away from an exactly T-shaped geometry.

As pointed out by Harding [230], the reactivity toward HCN by halogen atoms is such that two reaction products have been postulated, with the halogen covalently binding to either the carbon or nitrogen atom of HCN. Due to limitations of the basis set used and computational expense, Harding admits that the calculations performed to date are more qualitative in nature. In this section we extend these calculations to higher-levels of theory and calculate each of the F, Cl, and Br reactions so that they may be directly compared, but we only focus on the lowest energy channels including HXCN formation. To explore the relative energetics of these complexes, we have employed the G2 method [241], and the resulting stationary points (including zero-point energy) on the potential energy surface are shown graphically in Figure 6.2. For comparison, a few stationary points have also been calculated at the UMP2/aug-cc-pVTZ and UCCSD(T)/6-311++G(d,p) levels, which are summarized in Table 6.1, in addition to the G2 results. The calculated enthalpies of reaction are found to be in qualitative agreement with experiment at the G2 and UCCSD(T)/6-311++G(d,p) levels of theory, however the agreement is much worse at the UMP2 level.

From Figure 6.2 it is clear that the X + HCN $\rightarrow$ HCNX reactions are all quite endothermic, and therefore we expect that this reaction channel would play at most only a minor role in the dynamics at 0.37 K. More relevant to the experimental conditions is the reactivity of the halogen atoms with the carbon atom of HCN. For the F + HCN reaction, a very stable HFCN intermediate product is found in the calculations. At the G2 level no barrier is predicted for this reaction, however at the UCCSD(T)/6-311++G(d,p) level the reaction barrier is 3.05 kcal mol^{-1}. Four of the six vibrational modes of this product were first observed by Andrews *et al.* [236] in an argon matrix by codepositing F_2 and HCN, and then subjecting the matrix to broadband UV photolysis. Although rotational resolution was not achieved, the observation of the CN stretching vibration at 1672 cm^{-1} indicates that the CN bond has double-bond and not triple-bond character. Of interest to the current study, the C-H stretching vibration was

	G2	UCCSD(T) 6-311++G(d,p)	UMP2 aug-cc-pVTZ	Experimental (ΔH)	Harding [230] RHF+1+2+QC/cc-pVDZ
Cl (F) + HCN	0.0	0.0	0.0	0.0	0.0
T.S.	3.30 (-1.70)	6.97 (3.05)	-[a]	-	8.2
HClCN (HFCN)	-7.07 (-35.83)	-3.41 (-28.44)	4.91 (-27.18)	-	-2.2
HCNCl (HCNF)	-[a] (15.32)	-[a] (22.60)	-[a] (26.86)	-	27.9
HCl (HF) + CN	24.21 (-9.45)	25.37 (-6.54)	42.90 (6.18)	21.41 (-11.58)	25.9
ClCN (FCN) + H	23.11 (2.71)	26.80 (9.17)	19.03 (-3.03)	23.45 (9.26)	28.8

[a]Could not be stabilized in the geometry optimization.

Table 6.1: A summary of the calculated energetics of the halogen atom Cl (F) + HCN reactions including zero-point energy. (T.S.) corresponds to the transition state of the reaction with the carbon atom of HCN to form HXCN. The experimentally determined heats of reaction (ΔH) are also shown for reference [242]. One can see that while the G2 and UCCSD(T) methods predict the enthalpies quite well, the UMP2 method shows much larger deviations. A graphical representation of these energies is shown in Figure 6.2 for the G2 calculations. Previous calculations by Harding for Cl + HCN are also shown for reference.

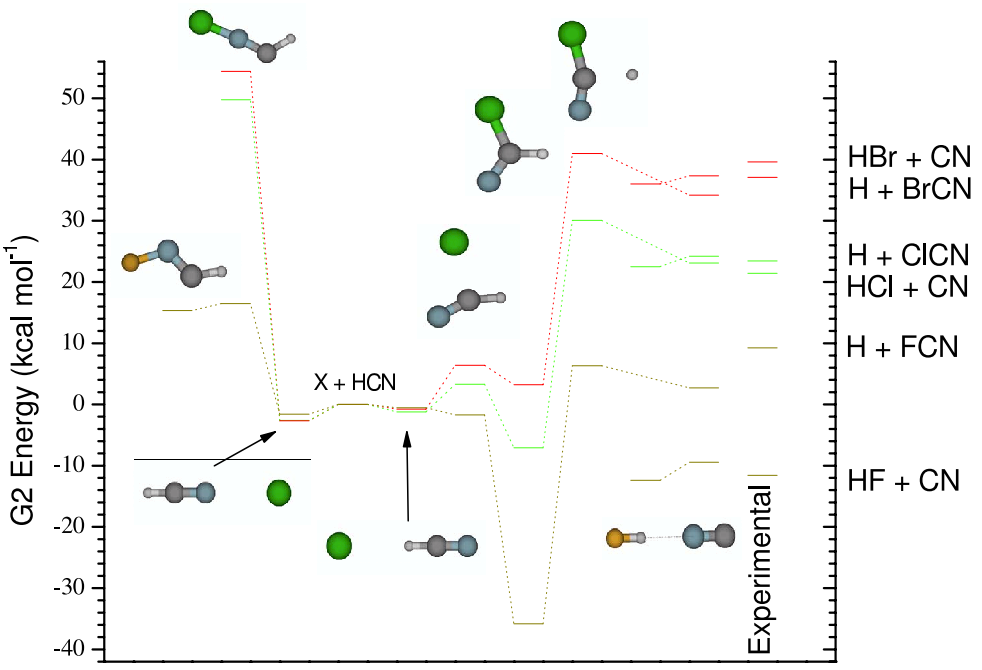

Figure 6.2: Relevant stationary points of the X + HCN reactions calculated using the composite G2 method. Two reacted complexes in addition to two weakly bound entrance channel species are predicted. The HCNX products of chlorine and bromine atoms binding on the nitrogen end of HCN could not be stabilized in our calculations, however HCNCl was found in Reference [230]. The experimental heats of formation for the X + HCN $\rightarrow$ HX + CN and X + HCN $\rightarrow$ H + XCN are taken from reference [242]. The photon energy used to study the pre-reactive X-HCN complexes is greater than the barriers to form HXCN, suggesting that it may be possible to photo-initiate reaction.

observed at 3016 cm^{-1}. Later Misochko *et al.* confirmed Andrews observations, and assigned the two remaining vibrational modes which were not observed previously [237]. Experimental evidence for a pre-reactive X+HCN complex or HClCN however is still lacking.

Harding's calculations on Cl+HCN are given in Table 6.1, and in general, agree well with our current calculations. G2 (UCCSD(T)) calculations predict that the reaction of a chlorine atoms with the carbon of HCN is exothermic by -7.07 (-3.41) kcal mol^{-1} , and that the barrier height is 3.30 (6.97) kcal mol^{-1} . For bromine atoms, the reaction to form HBrCN is predicted to be endothermic at the G2 level of theory. Since the C-H stretching vibration of the entrance channel complexes has a higher frequency than the barrier to form HXCN, it may be possible

to photo-initiate the reaction starting from the entrance channel.

While the above calculations give us an overview of the reaction energetics for the halogen atom - HCN reactions, we are particularly interested in the topology of the surface around the entrance channel. For instance, it appears that HCN+X might be most reactive in a T-shaped arrangement, so the long-range orientational effects of the potential may be very important in determining the reaction dynamics. To begin to answer these questions we have calculated three-dimensional non-relativistic adiabatic[2] potential energy surfaces for Br + HCN and Cl + HCN at the RCCSD(T)/aug-cc-pVDZ+{332} level of theory. The transformation of these surfaces to include spin-orbit coupling, and the calculation of the resulting bound states is being performed in collaboration with the group of van der Avoird. At the time of writing, these results were unavailable. In order to gain insight into our experimental results, we will focus our attention on the qualitative features of a 2D cut from our 3D non-relativistic adiabatic potentials, which are shown in Figure 6.3 for Br + HCN. The third dimension of our calculated PES corresponds to the CH bond length of HCN, and in the figure it has been held fixed at rCH = 1.0655 Å. The incorporation of this dimension into the PES's is to gain insight into the change of the potentials upon vibrational excitation of the CH stretching vibration. Calculations were performed in C_s symmetry, giving rise to the 1A', 2A', and 1A" surfaces which correspond to the three relative orientations of the unpaired orbital of the halogen atom with respect to HCN. A set of uncontracted mid-bond functions with exponents sp: 0.9, 0.3, 0.1, and d: 0.6, 0.2 (denoted as {332}) have been added to the aug-cc-pVDZ basis set and were placed at the midpoint between the halogen atom and the HCN nuclear center of mass [185, 243]. The calculations employ Jacobi coordinates, corresponding to the two intermolecular degrees of freedom (R and θ). For the plots shown in Figure 6.3, R and θ have been incremented by 0.1 Å and 10^0 respectively[3]. The rC-H and rC-N bond lengths of HCN were fixed at 1.0655

[2]The term "non-relativistic adiabatic" is used to convey that the potential surfaces neglect spin-orbit and rotational coupling.

[3]In the 3D surfaces, the C-H bond length of HCN was also varied, and a slightly different set of grid points was used to facilitate fitting the surfaces to spherical harmonics.

and 1.1532 Å respectively. Basis set superposition error has been accounted for by performing counterpoise correction [195], and a spline interpolation used to smooth the surface. As noted by Fishchuk *et al.* for Cl-HF [222], there is some choice in how counterpoise correction is applied due to the two A' states of the free halogen atom. Our procedure is the same as that reported for Cl-HF, in that the lowest RCCSD(T) energy of the free halogen atom was subtracted from both A' dimer energies, which preserves the double degeneracy of the Π state for both linear geometries. The nitrogen bound (HCN-X) geometry corresponds to $\theta = 0^0$. The

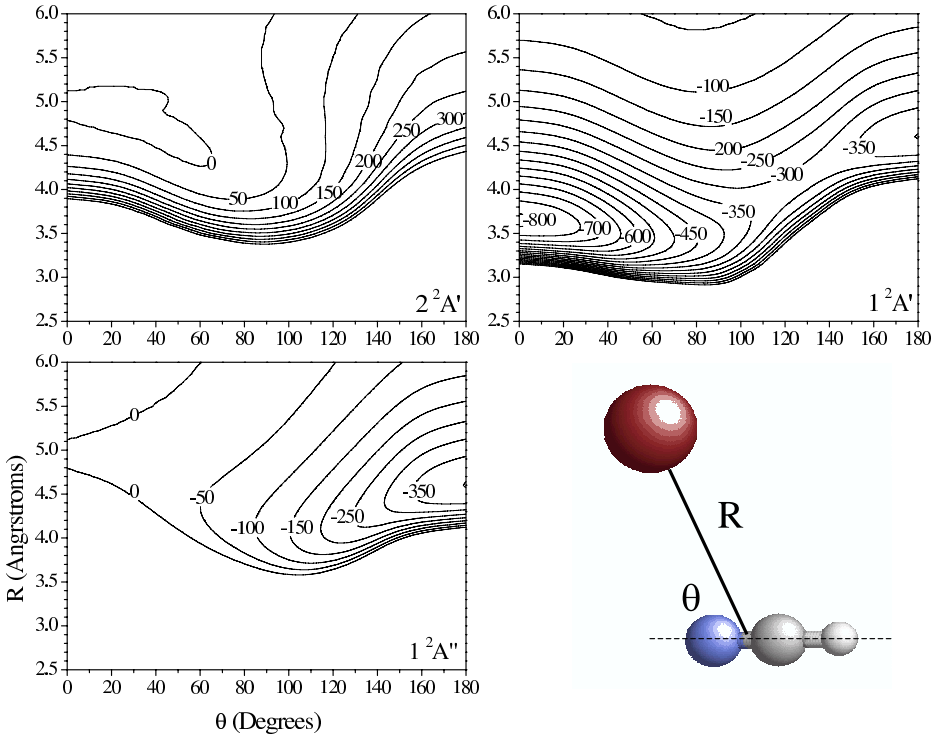

Figure 6.3: The three non-relativistic adiabatic potential energy surfaces for HCN + Br calculated at the RCCSD(T)/aug-cc-pVDZ+{332} level. The surfaces predict both linear structures to be minima.

surfaces clearly show that both linear geometries have stable minima, with well depths of -810 and -401 cm^{-1} for the HCN-Br and Br-HCN isomers respectively. The isomerization barrier connecting Br-HCN to HCN-Br is found to be only 90 cm^{-1} (neglecting zero-point effects). At $\theta = 0$, the 1A' and 2A' surfaces correlate with the doubly degenerate $^2\Pi$ state, where as for $\theta = 180$, it is the 1A' and 1A" surfaces. Thus the electronic symmetry of the HCN-Br isomer

is $^2\Sigma$ and for Br-HCN it is $^2\Pi$ in agreement with that found by Harding. These symmetries illustrate that the unpaired orbital of the halogen atom is along the axis of the molecule for $^2\Sigma$, while it is perpendicular to the molecular axis for $^2\Pi$. In order to rationalize why these different electronic symmetries arise, it is helpful to point out that the unpaired orbital in an otherwise closed shell, acts as a positive charge. Therefore when the halogen atom approaches the nitrogen end of HCN, pauli repulsion is minimized by having the unpaired orbital interact with the lone pair of HCN. Conversely, when the halogen atom approaches the hydrogen end of HCN, the hydrogen bonding interaction is maximized by interaction with a filled p orbital. Fully relaxed geometry optimizations (at the RMP2 level) were also undertaken for each of these structures to generate dipole moments and scaled harmonic frequencies to compare with our experiment, which are summarized in Table 6.2. Note that vibrational frequencies could not be calculated for the basis sets which include mid-bond functions, so we have instead used the aug-cc-pVTZ basis set. Calculations for iodine containing complexes employed the aug-cc-pVTZ-PP [196] pseudo-potential for the iodine atom, which is the same as that used earlier in the I-HF calculations (See Table 5.1). One can see that while the binding energy for Br-HCN is in very good agreement with the 2D surfaces (399.5 cm^{-1} at the RMP2/aug-cc-pVTZ level compared with the 2D RCCSD(T)/aug-cc-pVDZ+{332} result of 401 cm^{-1}), the differences found for HCN-Br are somewhat greater (910 vs. 810 cm^{-1}).

6.2.1 Relativistic - adiabatic potential energy surfaces

The effects of spin-orbit coupling on reshaping the potential energy surface is now well documented [184, 185] and to make detailed comparisons with our experiment we must incorporate it. Because the bound states on our new 3D potential surfaces are unavailable, we have chosen to incorporate spin-orbit coupling for the linear geometries (1D slices) of our 2D potentials as a starting point. To include spin-orbit coupling into the *ab initio* potentials we

RMP2 Aug-cc-pVTZ	HCN-F (F-HCN)	HCN-Cl (Cl-HCN)	HCN-Br (Br-HCN)	HCN-I (ECP) (I-HCN (ECP))
D_e (cm^{-1})	405.2	834.3	909.8	935.1
	(189.0)	(359.9)	(399.5)	(429.4)
$\nu_{harmonic}$ (cm^{-1})	-[a]	3464.21	3463.11	-[a]
	-[a]	(3443.85)	(3433.52)	(3430.88)
ν_{scaled} (cm^{-1})	-	3309.11	3308.06	-
	-	(3291.66)	(3281.78)	(3279.26)
R (Å)	3.240	3.416	3.542	3.726
	(4.015)	(4.342)	(4.475)	(4.670)
B (cm^{-1})	0.1310	0.0885	0.0636	0.0525
	(0.0881)	(0.0561)	(0.0405)	(0.0339)
μ (D)	3.24	3.66	3.77	3.91
	(3.18)	(3.40)	(3.47)	(3.58)

[a]Tight geometry convergence was achieved but imaginary frequencies were calculated

Table 6.2: Computed properties of the HCN-X (X-HCN) isomers at the RMP2/aug-cc-pVTZ level. The calculations for iodine incorporate a small core relativistic pseudo-potential (aug-cc-pVTZ-PP) in which 28 core electrons were replaced with the ECP [196]. Binding energies have been corrected for BSSE [195]. Scaled frequencies come from comparing a HCN calculation at this level to the observed helium band origin. R, is the X-HCN center of mass distance.

take note of the operator form of the spin-orbit Hamiltonian:

$$\begin{aligned} H^{so} &= AL \bullet S \\ &= A(L_z S_z + \frac{L^+ S^- + L^- S^+}{2}) \end{aligned}$$

The spin-orbit coupling constant, A, is -269.3, -587.3, -2457, and -5068 cm^{-1} for F, Cl, Br, and I respectively [244]. Note that the negative sign for A illustrates that the $^2P_{3/2}$ state lies below the $^2P_{1/2}$ state in the free atom. We make the approximation that the spin-orbit coupling is independent of the geometry of the complex, and remains that of the isolated atom. That this approximation is valid for the long-range part of our potentials is typically justified by noting that the electron-nuclear interaction scales as $\left\langle \frac{1}{r^3} \right\rangle$ [244], thus only the inner parts of the orbitals are important in determining this interaction, which one might expect to be only slightly perturbed due to the relatively weak van der Waals interaction. Recent calculations on O(^3P) + HCl by Rode *et al.* [245] have examined the validity of this approximation by explicit

calculation of the spin-orbit matrix elements using the Breit-Pauli operator [246]. Their results indicate that for internuclear distances near the van der Waals well the spin-orbit coupling is not substantially affected.

The diagonal term of the spin-orbit Hamiltonian ($L_z S_z$) gives the $^2\Pi_{1/2}$ and $^2\Pi_{3/2}$ potentials as $^2\Pi \mp \frac{A}{2}$, while the $^2\Sigma$ potential is simply $^2\Sigma_{1/2}$. That this is true is illustrated by plugging in the eigenvalues of the L_z and S_z operators, namely $\Lambda = 1$ and $\Sigma = +1/2$ for the $^2\Pi_{3/2}$ state and $\Lambda = 0$ and $\Sigma = |1/2|$ for the $^2\Sigma_{1/2}$ state. The off-diagonal spin-orbit term ($L^{\pm}S^{\mp}$) couples the $^2\Pi_{1/2}$ state with the $^2\Sigma_{1/2}$ state and has the following form [244]:

$$\left\langle {}^2\Pi_{1/2}|\frac{A}{2}L^+S^-|{}^2\Sigma_{1/2}\right\rangle = 2^{1/2}(A/2) \tag{6.1}$$

To derive the relativistic adiabatic potentials we set up a R dependent 2×2 matrix for the $\Omega = 1/2$ states, setting the diagonal elements to the energies from the *ab initio* calculation, and the off-diagonal elements to $2^{1/2}(\frac{A}{2})$, and diagonalize the matrix numerically to get its eigenvalues and eigenvectors. For this simple two level system, the potentials are given by:

$$\begin{aligned} {}^2\Sigma_{1/2} &= a({}^2\Pi - \frac{A}{2}) + (1-a^2)^{\frac{1}{2}}({}^2\Sigma) \\ {}^2\Pi_{1/2} &= a({}^2\Sigma) + (1-a^2)^{\frac{1}{2}}({}^2\Pi - \frac{A}{2}) \end{aligned} \tag{6.2}$$

where a is an R dependent mixing coefficient. The remaining $^2\Pi_{3/2}$ state is simply $^2\Pi + \frac{A}{2}$. The diagonalized relativistic and non-relativistic adiabatic potentials are shown in Figure 6.4. At long range, where the Σ and Π states are nearly degenerate, the $^2\Sigma_{1/2}$ state is pushed lower in energy (compared to $^2\Sigma$) while the $^2\Pi_{1/2}$ is pushed to higher energies (compared to $^2\Pi - A/2$) due to the coupling. In the limit of R $\rightarrow \infty$, the $^2\Pi_{3/2}$ and $^2\Sigma_{1/2}$ states converge and the separation between $^2\Pi_{1/2}$ and $^2\Pi_{3/2}$ becomes (3/2)A, or that observed in the free atom. The bound states of these potentials were calculated numerically using the program Level [247] and the binding energies, rotational constants, and the van der Waals stretching frequencies are summarized in Table 11.5. To estimate the effects of CH stretching of HCN on the potentials,

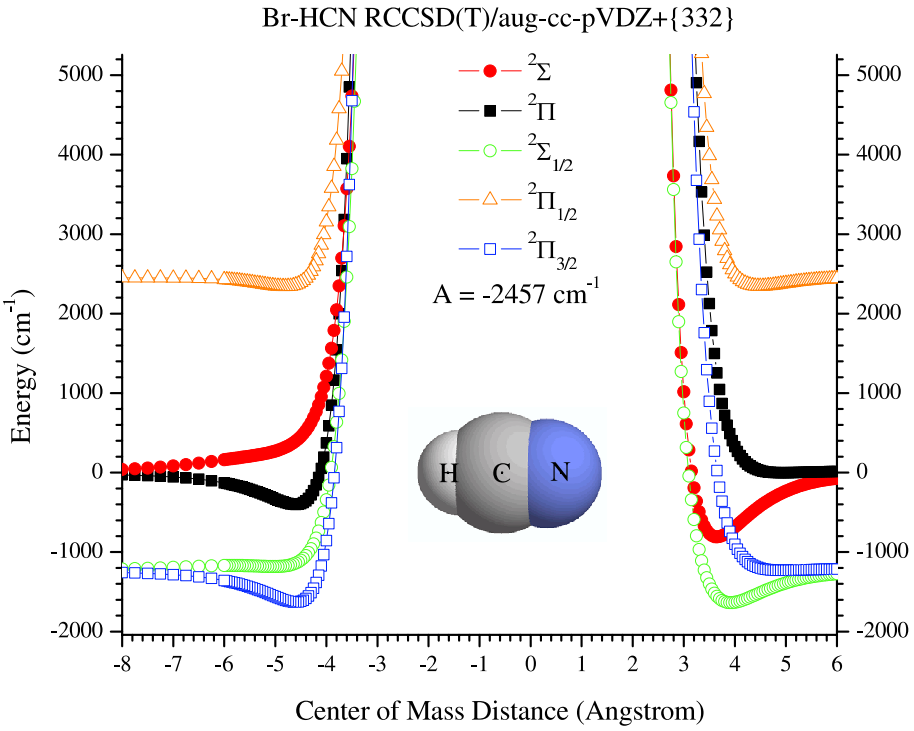

Figure 6.4: Relativistic adiabatic potential energy curves for the HCN-Br complex derived from the *ab initio* results. (See text)

computations were also performed in which the HCN geometry was constrained to have a CH bond length of rCH = 1.09 Å, which is close to the equilibrium bond length for the v=1 state. In general, the excitation of HCN results in a slight increase in the binding energy of the complex which we attribute to an increased dipole - induced dipole interaction. As noted above, spin-orbit coupling can strongly influence the potentials, and indeed the dissociation energy of the HCN-Br ($^2\Sigma_{1/2}$) complex is much smaller than in the non-relativistic calculation (383 vs 773 cm^{-1}). The spin-orbit interaction is even strong enough to create a bound state in the upper $^2\Pi_{1/2}$ well, despite the fact that the $^2\Pi$ state is purely repulsive. But since this state correlates with the excited spin-orbit component of the atom, we would not expect this isomer to be produced in helium. For the hydrogen bound isomer, the ground state is predicted to be $^2\Pi_{3/2}$. Since this potential is not distorted from the non-relativistic $^2\Pi$, we expect that the nonrelativistic *ab initio* calculations for this isomer should be sufficient to compare with experiment. This may not be the case for the HCN-X complexes, and thus the nonrelativistic *ab*

Constant (cm^{-1})		Br-HCN	
HCN $\nu_1 = 0$ ($\nu_1 = 1$)	$^2\Pi$	$^2\Pi_{1/2}$	$^2\Sigma_{1/2}$
D_0	376.43 (390.04)	[a]	[a]
B_0	0.03893 (0.03893)	[a]	[a]
ν_{vdws}	47.37 (48.36)	[a]	[a]
		HCN-Br	
	$^2\Sigma$	$^2\Sigma_{1/2}$	$^2\Pi_{1/2}$
D_0	773.23 (775.89)	383.33 (384.94)	111.24
B_0	0.06233 (0.06235)	0.05379 (0.05382)	0.04051
ν_{vdws}	69.71 (69.84)	47.88 (47.97)	26.91

[a]No bound states found

Table 6.3: A summary of the computed properties for the HCN-Br and Br-HCN isomers from bound state calculations on one-dimensional relativistic adiabatic potentials. Note that the computed bound states for the $^2\Pi_{3/2}$ state are the same as those for the non-relativistic $^2\Pi$ state.

initio results should be interpreted with caution. After inclusion of the spin-orbit coupling, we find that both isomers for bromine are now nearly isoenergetic. The smaller spin-orbit coupling constant for chlorine atoms allows the HCN-Cl complex to remain the global minimum. We look forward to the results of including spin-orbit coupling into our 2D and 3D surfaces as it will be particularly interesting to investigate how the isomerization barrier is effected. Table 6.4 collects the molecular parameters derived from the bound states for the HCN-Cl, HCN-Br and HCN-I complexes.

6.3 The HCN-X_2 complexes

Given that previous experimental [239, 240] studies have shown that halogen molecules bind to the nitrogen end of HCN, the search for the HCN-X_2 complexes was straightforward given the weak perturbation on the C-H stretching frequency. Pendular survey scans for Br_2, Cl_2, and F_2 + HCN are shown in Figure 6.5, and the new peaks are labeled according to their gas dependence. The smooth variation in frequency shifts is telling of the magnitude of the interactions. Figure 6.5 also shows the resulting zero-field spectra for the HCN-Br_2, HCN-Cl_2,

Constant (cm^{-1})	HCN-^{35}Cl		HCN-^{79}Br		HCN-I[a]	
v=0 (v=1)	$^2\Sigma$	$^2\Sigma_{1/2}$	$^2\Sigma$	$^2\Sigma_{1/2}$	$^2\Sigma$	$^2\Sigma_{1/2}$
D_0	687.65 (689.98)	476.78 (478.86)	773.23 (775.89)	383.33 (384.94)	781.08	375.61 (377.24)
B_0	0.08784 (0.08786)	0.08478 (0.08482)	0.06233 (0.06235)	0.05379 (0.05382)	0.05038	0.04245 (0.04247)
ν_{vdws}	75.85 (75.98)	64.23 (63.53)	69.71 (69.84)	47.88 (47.97)	62.37	43.44 (43.52)
A	-	-587.3	-	-2457	-	-5068

[a]This calculation was done with the aug-cc-pVDZPP+{332} basis set [196].

Table 6.4: A summary of the molecular parameters derived from the bound states of one-dimensional potential energy surfaces (see text). A, is the atomic spin-orbit coupling constant used in the calculations and ν_{vdws} is the van der Waals stretching frequency. For the "v=1" calculations, the CH bond length was fixed at 1.09 Å in order to estimate the effects of vibrational excitation of the HCN. Note that the corresponding calculations for the X-HCN isomers are not presented since the ground electronic state of these complexes is $^2\Pi_{3/2}$, which does not experience a first order coupling with the $^2\Sigma$ state, and so the molecular parameters are the same as those found in a standard *ab initio* calculation. See Table 6.2.

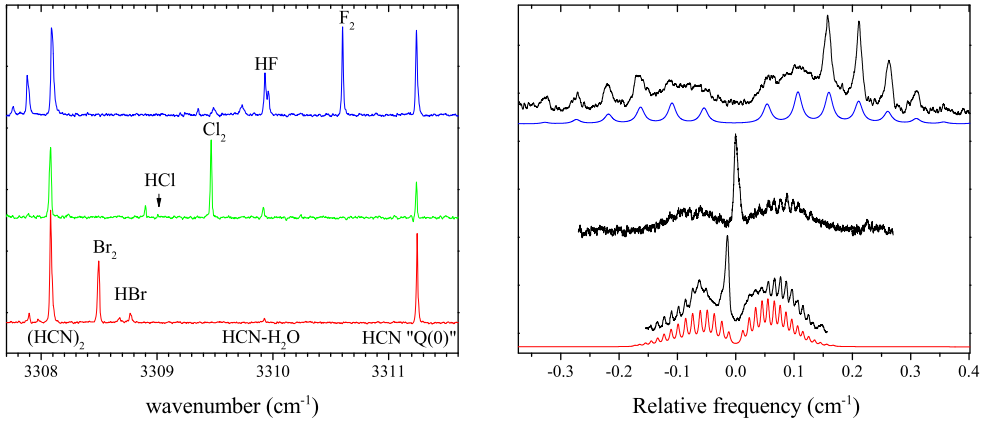

Figure 6.5: Pendular survey scans showing the formation of HCN-X_2 molecular complexes (Left) and their corresponding field-free spectra (Right). Significant perturbations are observed in the HCN-Br_2 and HCN-Cl_2 spectra (leading to the otherwise forbidden Q branch) which we ascribe to a helium droplet interaction.

and HCN-F_2 binary complexes. Molecular iodine complexes with HCN were also observed but are not shown in the figure. Due to the fact that our calculations predict that each complex is linear (in accord with the previous microwave results) the Q branches in the bromine and chlorine spectra are clearly unexpected. At this time we leave their explanation to a future study. We only postulate here that an impurity complex could be overlapping the band, or that the helium interaction with these species is quite strong (due to the increased polarizability compared to F_2), and thus more strongly influences the spectra [61, 199]. A similar effect in HCN trimer (another linear complex with a Q branch) has been treated theoretically, and the Q branch was found to result from the thermal excitation of a non-superfluid fraction of the droplet in the first few solvation shells, which rotates more rigidly about the *a*-axis [61]. Possibly these molecular halogen complexes exhibit similar behavior.

Longer pendular scans were also carried out to search the hydrogen bonded frequency region, given the prediction of a nearly T-shaped minimum. Indeed, as shown in Figure 6.6 for the case of bromine, a strong peak is observed at 3286.14 cm^{-1} which we assign to such a

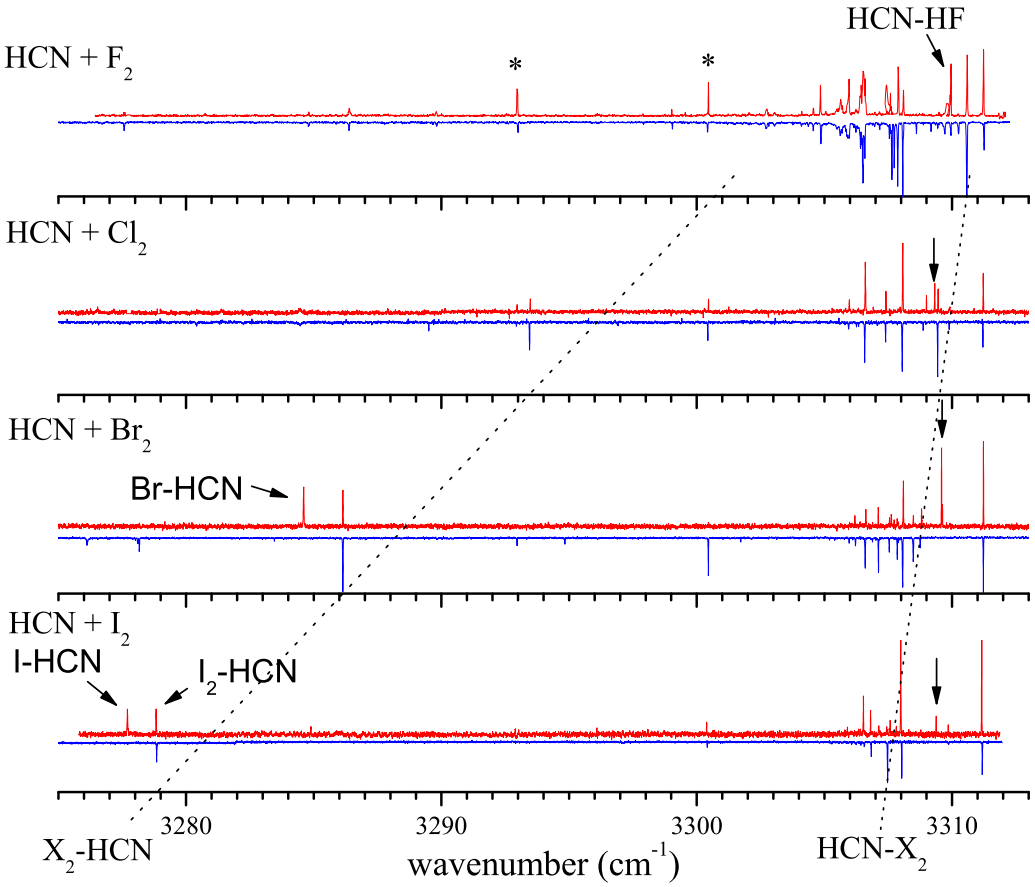

Figure 6.6: Pendular survey scans revealing the pyrolysis source temperature dependence (upward peaks are with a hot source, downward peaks are with a cold source) on the corresponding HCN + Halogen experiment. The scans show peaks which we identify as molecular and atomic halogens complexed with HCN. The dotted lines are drawn for the eye, exemplifying the linear scaling of the molecular halogen complex frequency shifts. The peaks labeled with an asterisk, are known impurities. Vertical arrows point to the peaks which correspond to free C-H stretch HCN-X complexes.

complex. Our assignment is based on pick-up cell pressure dependence measurements (optimized 1:1 with HCN-Br_2), scaled harmonic frequency calculations, rotational band contour analysis, and pyrolysis source temperature dependence. A hydrogen bonded complex between molecular iodine and chlorine with HCN were also observed where as the corresponding isomer of fluorine was not. The survey scans for all cases are shown in Figure 6.6 as downward going peaks. The fact that a hydrogen bound F_2-HCN isomer is not formed might be attributed

to a smaller well depth, due to the smaller polarizability of fluorine compared with chlorine, bromine, and iodine, and larger zero-point energy effects allowing it to convert back to the global minimum linear nitrogen bound geometry, which is observed. The infrared spectra for these complexes taken under field-free conditions will be presented elsewhere. The dotted lines in Figure 6.6 illustrate the almost perfect linear scaling of the band origins for both the free stretch and the hydrogen bonded complexes.

6.4 The Br-HCN and I-HCN complexes

6.4.1 Br-HCN

Given the identification of the precursor complexes, we are now in a position to heat the pyrolysis source to produce the corresponding atoms. As found in our previous study of the X-HF systems, at sufficiently high pyrolysis source temperatures the signal levels associated with the molecular halogen complexes decrease, due to dissociation into atoms, and a complementary set of peaks grow in. The pendular survey scans performed with a hot pyrolysis source are shown in Figure 6.6, as upward going peaks. Each scan was taken at the appropriate pyrolysis source temperature for the dissociation of that particular precursor. Concentrating on the bromine spectra, two new peaks are observed with the hot source, namely at 3309.55 and 3284.61 cm^{-1}. Based on the frequency shifts of these two bands it is already apparent that both linear isomers of HCN - Br may be formed, with the hydrogen bonded isomer giving a much larger redshift on the C-H stretching frequency than the corresponding nitrogen bonded isomer, as one would expect. We choose to first focus on the peak we preliminarily assign to a hydrogen bonded complex since a direct comparison can be made with the corresponding X-HF complexes of Chapter 5.

A field-free spectrum of the pendular peak centered at 3284.61 cm^{-1} is shown in Figure 6.7. Again this band is only observed under conditions appropriate for bromine atom pickup. In agreement with that found for the Br-HF complex, P, Q, and R branches are observed consistent

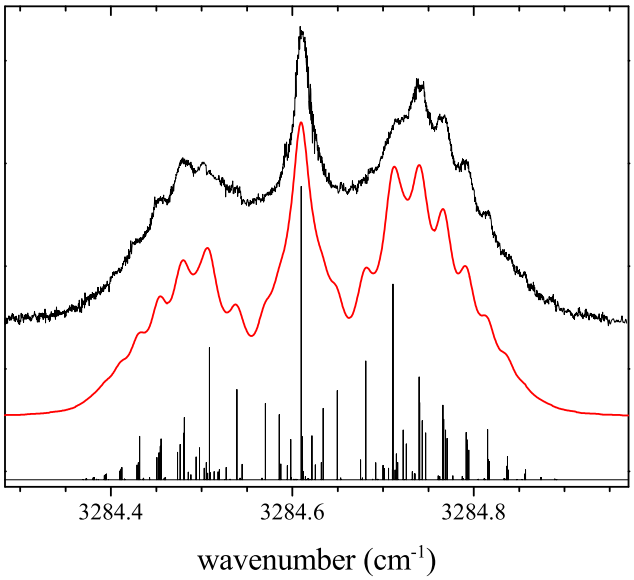

Figure 6.7: The rotationally resolved spectrum of the hydrogen bound Br-HCN isomer recorded under electric field-free conditions. The band shape is consistent with a $^2\Pi_{3/2}$ ground electronic state which is in agreement with theoretical predictions. The simulation includes a nuclear magnetic hyperfine interaction (I=3/2 for bromine) due to the large magnetic moment of the bromine nucleus.

with this being a linear complex in a Π ground electronic state. For Br-HF a distinct 5B gap was observed between the Q branch transitions and those arising from the first P and R branch transitions which confirmed the ground state is $^2\Pi_{3/2}$ consistent with the fact that the ground state of free bromine atoms is $^2P_{3/2}$. The smaller rotational constant of Br-HCN however, makes these gaps in the spectra more obscure, but due to the predicted weak coupling of the spin-orbit interaction upon complexation, we can say with confidence that this is also $^2\Pi_{3/2}$ band in analogy with Br-HF. A fit to the spectrum adopting the same Hamiltonian as used for Br-HF is also shown in Figure 6.7. A nuclear magnetic hyperfine perturbation of the form:

$$H' = a\Lambda(I \bullet k) + b(I \bullet S) + c(I \bullet k)(S \bullet k)$$

was also included in the Hamiltonian to reproduce the relative intensities of the P, Q, and R branches, in agreement with that observed for Br-HF, although here we do not resolve the individual hyperfine transitions. The $(I \bullet k)$ term represents the coupling of the nuclear spin with the axial magnetic field of the molecule, which is proportional to Λ, $(I \bullet S)$ is the direct coupling of the nuclear and electronic spin angular momenta, and $(I \bullet k)(S \bullet k)$ is a second order interaction of the nuclear and electronic spins due to both of their projections on the molecular axis. Assuming Hund's case (a), the expression for the interaction energy is:

$$W = [a\Lambda + (b+c)\Sigma]\frac{\Omega}{J(J+1)}I \bullet J$$

where

$$I \bullet J = \frac{F(F+1) - J(J+1) - I(I+1)}{2}$$

Note that quantum number representing nuclear spin (I) equals 3/2 for bromine atoms, and F (the quantum number representing the total angular momentum inclusive of nuclear spin) is the coupling of J and I. The relative transitions intensities were calculated using spherical tensor matrix elements similar to those already reported for the Stark effect for X-HF (Equation 5.1), and a Boltzmann distribution for the rotational state population at 0.37 K. The spectroscopic constants (ν, B, D, and [aΛ+ (b+c)Σ]) resulting from the fit are summarized in Table 6.5.

Constant	Br-HCN	I-HCN
ν_0 (cm^{-1})	3284.61(1)	3277.79(1)
B (cm^{-1})	0.0151(5)	0.0120(5)
D (cm^{-1})	1.5×10^{-4}	1.0×10^{-4}
[aΛ + (b+c)Σ] (cm^{-1})	0.04(1)	0.04(1)

Table 6.5: A summary of the experimental parameters for the linear X-HCN complexes obtained from a fit to the field-free spectra.

The experimental (helium) rotational constant is a factor of 2.7 smaller than that predicted from our *ab initio* calculations due to the fact that some of the helium follows the rotational

motion of the molecule, thus adding to the complexes moment of inertial. This magnitude of reduction is in good agreement with that observed for many other systems. The fact that Br-HCN is reduced by a factor of 2.7 while Br-HF is reduced by a factor of 2.2 is also in agreement that the rotational constant reduction factor is usually proportional to the magnitude of the B value in this range (See Figure 2.3). As shown in Section 5.9 for Cl-HF, the vibrational frequencies provide a very precise benchmark for theoretical calculations, and we hope to make this comparison once our 2D and 3D PESs are completed. The scaled harmonic vibrational frequency (RMP2/aug-cc-pVTZ) for this isomer is 3281.78 cm^{-1}, in good agreement with that observed (3284.61 cm^{-1}). Correcting for the helium induced shift (see Figure 2.2), one arrives at a predicted gas-phase origin of 3287.24 cm^{-1}. Although this makes the agreement somewhat worse, it is probably within the error of the *ab initio* calculations, and we await an estimate for the vibrational frequency from bound state calculations.

6.4.2 I-HCN

A similar study was carried out for the I-HCN complex, the infrared field-free spectrum being shown in Figure 6.8. The fit to the spectrum includes the hyperfine effects discussed above however I = 5/2 for iodine. The molecular constants derived from the fit are given in Table 6.5. Here again the experimental rotational constants are consistent with the *ab initio* calculations, corresponding to a ratio of 2.83. The frequency shift from HCN monomer is measured to be -33.41 cm^{-1} (-30.51 cm^{-1} estimated gas-phase), in excellent agreement with the calculations employing the ECP (-31.94 cm^{-1}). The nuclear magnetic hyperfine constant used in the fit is the same as for Br-HCN, namely 0.04 cm^{-1}. This is reasonable given that the magnetic moments for the atoms are quite similar [205, 206].

From the survey scans of Figure 6.6, peaks corresponding to the analogous Cl-HCN and F-HCN complexes are not observed. This is in contrast to the free stretch region where a new peak is observed for the HCN + Cl case, which will be discussed in Section 6.6.

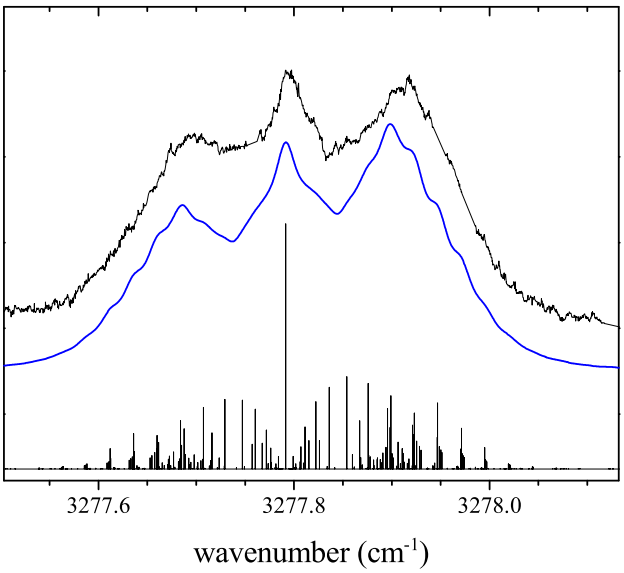

Figure 6.8: A field-free spectrum of the I-HCN complex in helium droplets. The fit to the spectrum, which includes the effects of nuclear hyperfine (I=5/2 for iodine), was used to derive the spectroscopic constants in Table 6.5.

6.5 The HCN-Br and HCN-I complexes

6.5.1 HCN-Br

We now turn our attention to the second set of new pendular peaks that grow in under the appropriate conditions for halogen atom pickup, namely those that exhibit a much smaller red-shift from HCN monomer. In the HCN + Br pendular survey scan (Figure 6.6), a peak is observed at 3309.55 cm^{-1} which is red-shifted from HCN monomer by -1.65 cm^{-1} in qualitative agreement with the calculations for a nitrogen bound HCN-Br isomer (-3.14 cm^{-1} at the RMP2/aug-cc-pVTZ level). Because the ground electronic state of this complex is predicted to be $^2\Sigma_{1/2}$, spin-orbit coupling could be important in this system, and thus harmonic frequency calculations (which are performed on the $^2\Sigma$ surface) are only semi-quantitative. From our 1D PES's which include spin-orbit coupling, we find that the binding energy of the complex is

increased by 1.61 cm^{-1} upon "vibrational excitation" of the HCN. Neglecting dynamical coupling of the different dimensions of the PES, this increase in the binding energy upon excitation necessitates a red-shift in the vibrational frequency of equal value, in excellent agreement with that observed, namely -1.65 cm^{-1}. Such excellent agreement could be fortuitous, and it will be interesting to compare this estimate with the results from higher dimensional calculations. An analogous comparison between the rCH v=0 and v=1 bound states for the non-relativistic curves gives a frequency shift of -2.66 cm^{-1}, which is in much poorer agreement with experiment.

To aid in the determination of this band to a second isomer of bromine atoms complexed with HCN, the pyrolysis source was altered such that a pressure gauge could be used to monitor the bromine pressure upstream of the pyrolysis region. In this way, pick-up "cell" pressure dependence measurements could made for the two bands. The resulting pressure dependence curves for the two peaks at 3309.54 and 3284.55 cm^{-1} are shown in Figure 6.9. Both bands

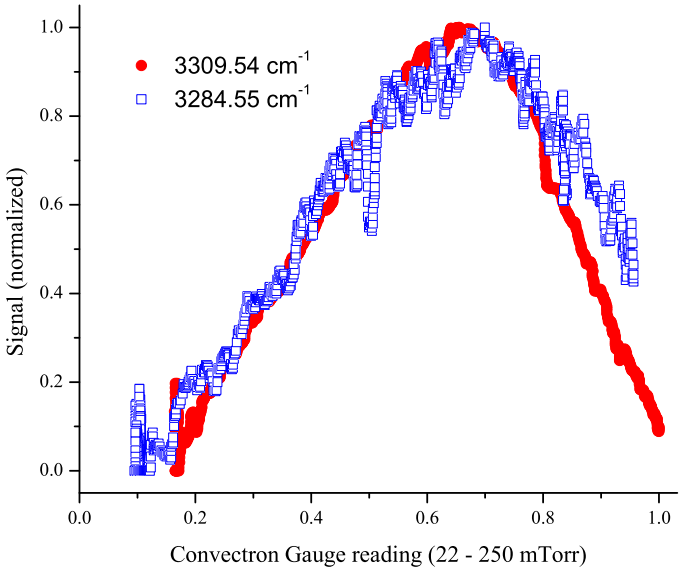

Figure 6.9: Br-HCN and HCN-Br pyrolysis source pressure dependence measurements which aid in the determination that both observed bands are due to 1:1 complexes.

are found to have exactly the same bromine pressure dependence, confirming that this new

band at 3309.54 cm^{-1} is also due to a 1:1 complex. The field-free and Stark spectra for this band are shown in Figure 6.10. The band shape is consistent with that of a linear rotor in a $^2\Sigma$ electronic state, as predicted by our earlier electrostatic arguments. In the field-free

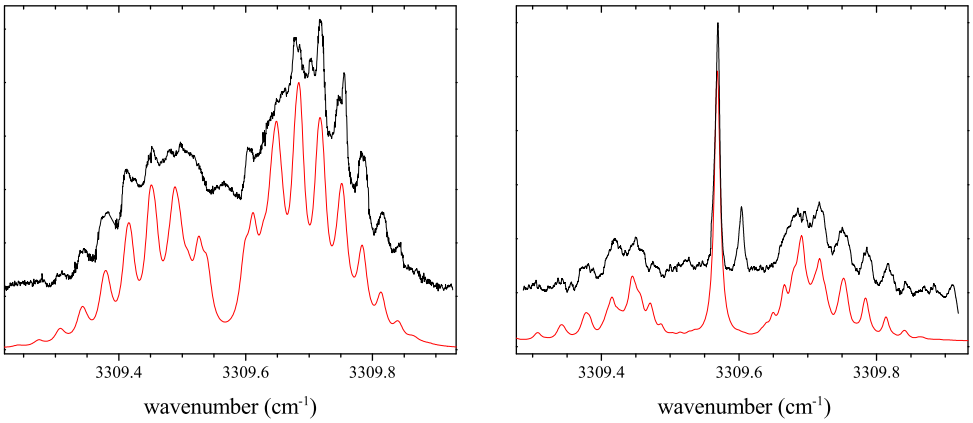

Figure 6.10: (Left panel) An infrared field-free spectrum for the C-H stretching vibration of the HCN-Br complex. Fine structure is observed which we preliminarily assign to a parity splitting induced by spin-orbit coupling of the $^2\Sigma_{1/2}$ and $^2\Pi_{1/2}$ states of the complex. A simulation of the band is also shown which includes the spin-orbit effects described in Chapter 12. (Right panel) The corresponding Stark spectrum for the HCN-Br complex recorded at an electric field strength of 2.25 kV cm^{-1}. The peak in between the field induced Q branch and the R branch is not predicted by the simulation and is assumed to be related to an impurity.

spectrum there appears to be fine structure, most notably as a splitting in the low rotational transitions. We tentatively ascribe this splitting to an interaction of the (relativistic) $^2\Sigma_{1/2}$ and $^2\Pi_{1/2}$ states, which are coupled by the off-diagonal spin-orbit perturbation. In addition to the lambda doubling expected for the $^2\Pi_{1/2}$ state, the $^2\Sigma_{1/2}$ state would exhibit a spin-rotation interaction identical in magnitude, but opposite in sign, to the $^2\Pi_{1/2}$ Λ doubling if plotted versus N(N+1)[4] rather than J(J+1) [244]. The simulation shown in Figure 6.10 was generated using an effective Hamiltonian which includes the off-diagonal spin-orbit interaction derived from one-dimensional calculations, however the splitting is not visible on this scale. The theory for

[4]The N quantum number typically arises in Hund's case (b) coupling and represents the rotational angular momentum apart from electron spin angular momentum. J = N + S = N $\pm$ 1/2.

this interaction is developed in Chapter 12, and in principle can be used to estimate the vertical energy separation between the $^2\Sigma_{1/2}$ and $^2\Pi_{1/2}$ states. The spectroscopic constants derived from the fit to the spectrum are collected in Table 6.6. The rotational constant obtained from the simulation is 0.019 cm^{-1}, which can be compared with the zero-point corrected (B_0) values derived from the bound states on both the non-relativistic ($^2\Sigma$) and relativistic ($^2\Sigma_{1/2}$) 1D potential energy surfaces, namely 0.0623 and 0.0538 cm^{-1} respectively. As shown in the 1D potentials, and reflected in the B values, the spin-orbit coupling shifts the potential minimum to slightly longer internuclear distance. Since a fully quantitative theory for the reduction of rotational constants due to the helium is still lacking, we cannot definitively say which of these calculated B values is in better agreement with experiment, since both reduction factors are within the range typically observed. By comparing the B reductions for the HCN-Cl, HCN-Br, and HCN-I complexes however we do gain some insight into the accuracy of our relativistic potentials. See below.

A Stark spectrum for HCN-Br is shown in Figure 6.10, recorded at an applied electric field strength of 2.25 kV cm^{-1}. The simulation includes the effects of the *e/f* symmetry splitting, however due to the mixing of J levels, its incorporation only slightly modifies the predicted spectrum. The peak that is not reproduced in the simulation is ascribed to an impurity complex and likely contributes slightly to the congestion in the field-free spectrum. The ground and excited state dipole moments obtained from the simulation are 3.78 D, in excellent agreement with that found at the RMP2/aug-cc-pVTZ level (3.77 D).

6.5.2 HCN-I

Based on the pendular survey scans shown in Figure 6.6, we observe a pendular peak at 3309.37 cm^{-1} , which we tentatively assign a free stretch complex between HCN and an iodine atom. The field-free spectrum for this band is shown in Figure 6.11. Again the band shape is consistent with a molecule with no net orbital angular momentum (a Σ state) in agreement with the results for the HCN-Br complex. The observed frequency shift from HCN monomer

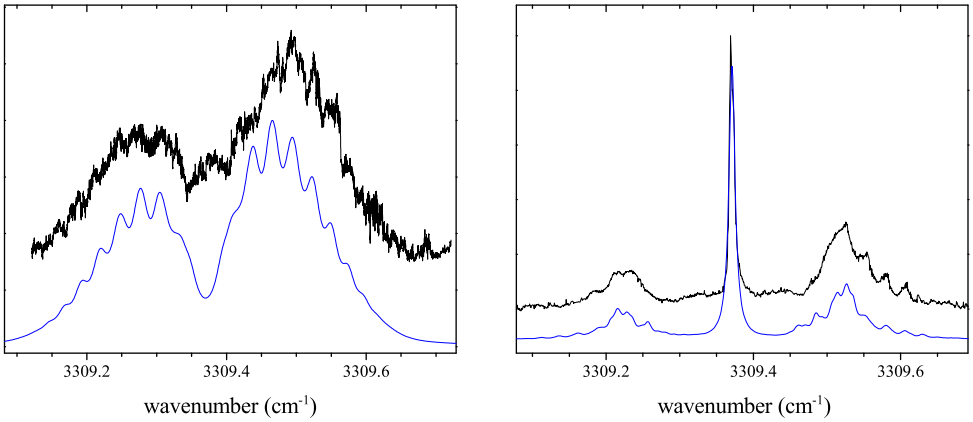

Figure 6.11: The field-free infrared spectrum of the HCN-I complex observed in helium droplets. The corresponding simulation was used to determine the molecular constants and includes an off-diagonal spin-orbit perturbation, which however only slightly modifies the band shape at this resolution.

is -1.83 cm^{-1}, which agrees nicely with the predicted increase in the binding energy upon vibrational excitation on the relativistic potentials, namely 1.63 cm^{-1}. The rotational constant derived from the simulation is B = 0.016 cm^{-1} which is consistent with the results for HCN-Br. The corresponding value of the rotational constant derived from the lowest bound state of the $^2\Sigma_{1/2}$ potential is B_0 = 0.04247 cm^{-1}. Figure 6.11 also shows a Stark spectrum for HCN-I. The lines in the Stark spectrum appear to be much narrower than in the corresponding field-free scan, which we attribute to considerable (unresolved) fine structure in field-free scan, which is decoupled by the field. Such fine structure is most likely caused by the spin-orbit coupling in this system, in analogy to that observed for HCN-Br. Unfortunately the electric field strength was not calibrated and so we do not have a measurement of its dipole moment.

6.6 The HCN-Cl complex

When flowing Cl_2 through the hot pyrolysis source, no bands were observed that could be assigned to a hydrogen bound Cl-HCN complex. In the free stretch region however, a new

peak is observed at 3309.33 cm^{-1} in good agreement with the previously observed bands for the HCN-Br (3309.55 cm^{-1}) and HCN-I (3309.37 cm^{-1}) complexes. The field-free and Stark spectra for HCN-Cl are shown in Figure 6.12. This new peak is only slightly shifted from the HCN-Cl_2 band, and thus the pyrolysis source was run at the highest possible temperatures to reduce the Cl_2 related signals. Unfortunately these conditions also lead to an increase in the amount of HCl produced in the source, presumably from the reaction of chlorine atoms with the quartz pyrolysis tube, and the HCN-HCl molecular complex is also observed. The assignment of this band to HCN-HCl was confirmed by a separate experiment in which HCl was intentionally introduced into the pick-up cell. Despite the overlap of two impurity complexes, we

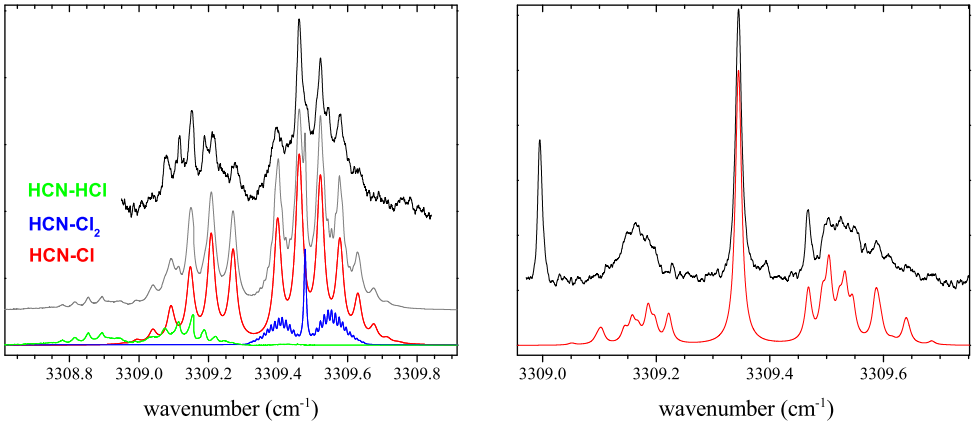

Figure 6.12: (Left panel) A rotationally resolved spectrum of the HCN-Cl complex in helium nanodroplets. The spectrum also has features due to both the HCN-HCl and HCN-Cl_2 complexes which overlap in this frequency region. (Right panel) A Stark spectrum of the corresponding band taken in the presence of a 2.833 kV cm^{-1} electric field.

are able to reproduce all of the features of the spectrum, and extract the molecular parameters which are listed in Table 6.6. In the analysis of the spectrum we were not able to identify any fine structure that could be attributed to a spin-orbit interaction, which we tentatively assigned in the bromine and iodine complexes. This is consistent with the much smaller spin-orbit coupling constant for atomic chlorine compared to bromine or iodine. Indeed a simulation of the

HCN-Cl spectra using the effective Hamiltonian developed for the HCN-Br, shows no such splittings at this resolution.

The vibrational band origin of HCN-Cl is shifted from HCN monomer by -1.87 cm^{-1}. The *ab initio* frequency calculations predict a shift of -2.09 cm^{-1} at the RMP2/aug-cc-pVTZ level (see Table 6.2) in good agreement with the experimental value. The shift predicted from the change in the binding energy upon vibrational excitation from 1D potential energy surfaces is -2.08 cm^{-1}. This value is nearly identical to the non-relativistic results due to the relatively small spin-orbit coupling constant for chlorine atoms. Bound state calculations predict that the isotope splitting between HCN-^{35}Cl and HCN-^{37}Cl is approximately 0.001 cm^{-1}, which is negligible for our resolution. In contrast, the two isotopes of Cl-HF were found to have a much larger splitting (0.038 cm^{-1}), due to the fact that it is hydrogen bound.

The rotational constant deduced from the fit to the spectrum is 0.032 cm^{-1}. Because the spin-orbit coupling is small in this case, the predicted rotational constants from the bound states on the $^2\Sigma$ and $^2\Sigma_{1/2}$ potentials are very similar, namely B_0= 0.08478 (0.08784) cm^{-1} for HCN-^{35}Cl on the $^2\Sigma_{1/2}$ ($^2\Sigma$) potential. The reduction of the rotational constant upon solvation is thus a factor of approximately 2.7. If we assume that the solvation behavior between the HCN-Cl, HCN-Br, and HCN-I complexes is the same, then this reduction factor also gives support to our earlier comparison of HCN-Br and HCN-I with the B values obtained from the spin-orbit corrected potentials. On these potentials the reduction factor was also determined to be ~2.75, however if we had compared the experimental value to the B value from the non-relativistic potentials, the B reduction would have been ~3.2.

Figure 6.12 also shows a Stark spectrum for HCN-Cl recorded at an applied field strength of 2.833 kV cm^{-1}. The dipole moment determined from the fit is 3.0(2) D, which is significantly smaller than the *ab initio* value of 3.66 D. The fact that the *ab initio* calculations are in poorer agreement for chlorine than for bromine is interesting, and could be due to vibrational averaging over the low frequency bending and stretching modes of the complex, which would be more important for Cl due to its lighter mass, which act to reduce the dipole moment from

its equilibrium value. Indeed a similar trend was also observed for the X-HF complexes.

Constant	HCN-Cl	HCN-Br	HCN-I
ν (cm^{-1})	3309.33	3309.55	3309.37
B (cm^{-1})	0.032	0.019	0.016
D (cm^{-1})	5.0×10^{-5}	1.2×10^{-5}	1.0×10^{-5}
μ(D)	3.0	3.78	-

Table 6.6: The experimental spectroscopic constants obtained from a fit to the infrared spectra for each of the pre-reactive HCN-X complexes. Fine structure is observed in the HCN-Br and HCN-I spectra, which is attributed to spin-orbit interaction. A more detailed theoretical treatment for this effect is given in Chapter 12.

6.7 Discussion

Extensive pendular survey scans have been performed in order to find evidence for the entrance channel complexes of fluorine atoms with HCN. From the *ab initio* calculations presented above, it is clear that the reaction to form the HFCN product is quite exothermic, and exhibits only a small barrier (if any) to the reaction. The calculated energies of the products and barrier relative to F + HCN are -34.05 and -2.45 kcal mol^{-1} (-28.44 and 3.05 kcal mol^{-1}) respectively at the G2 (UCCSD(T)/6-311++G(d,p)) level of theory. Two entrance channel complexes (F-HCN and HCN-F) were also found in the G2 calculations with energies -0.55 and -1.58 kcal mol^{-1} respectively. The unintuitive result that the transition state is calculated (at the G2 level) to be lower in energy than the corresponding van der Waals minima is simply an artifact of the calculation, and this small energy difference is within the estimated accuracy of the method. The fact that we do not observe a fluorine atom pre-reactive complex could be an indication that indeed the insertion reaction takes place, even at 0.37 K. This conclusion is also partially supported by the argon matrix work of Andrews [236] and Misochko [237] where the insertion product has been identified. No pre-reactive complexes were observed in these works. Guided by their observed frequency of the C-H stretching vibration of 3018 cm^{-1}, we searched for this complex in helium. No signals were observed, however this frequency range is at the edge of the tuning range of the FCL used in this work. The oscillator strength for this vibration

is also ~ 50 times weaker than the HCN fundamental (based on harmonic frequency calculations), and thus the argon matrix experiment has the big advantage of concentrating the product using longer deposition times. We hope to revisit this experiment using newer technology OPO lasers, which have enhanced tuning ranges and much greater powers.

In Chapter 11 we study the chemical reaction between an aluminum atom and HCN, which provides evidence that it should be possible to "tag" the HFCN product with another weakly bound molecule, which could then act as a stronger infrared chromophore. Shown in Figure 6.13 is a two-dimensional angular potential for HCN + HFCN calculated at the RMP2/aug-cc-pVDZ level, which shows that multiple van der Waals isomers may indeed exist. Since cluster formation in helium occurs sequentially and obeys Poisson statistics, these clusters should be formed when picking up HCN after the fluorine atom, given that the droplet is large enough to stabilize the HFCN. Based on the calculated exothermicity, the formation of HFCN would boil off approximately 2500 helium atoms (assuming 5 cm^{-1} per atom [56]).

The last remaining question in this study is the existence of a hydrogen bound Cl-HCN complex in analogy with that observed for bromine and iodine atoms. Due to the fact that the isomerization barriers between the hydrogen and nitrogen bound isomers are so small, one possible explanation is that this isomer is not formed due to a zero-point energy effect, and that the complex simply converts to the global minimum HCN-Cl isomer. To make any further analysis of this possibility we must await the spin-orbit corrected 2D potentials, to get a more realistic view of how the isomerization barrier is effected by spin-orbit coupling. A second possibility is that the reactivity is enhanced when the chlorine atom approaches the hydrogen end of HCN and it reacts, in analogy with that proposed for F + HCN.

Given the observation of the HCN-Br and Br-HCN complexes, it is interesting to consider the possibility of picking up two bromine atoms, to form a di-radical complex such as Br-HCN-Br, which utilizes the HCN as a stabilizer, preventing the recombination to form Br_2. Ofcourse this is completely analogous to using solid matrices to prevent reactive species from interacting with one another, however an example at such an atomic level is still lacking. Gordon *et al.*

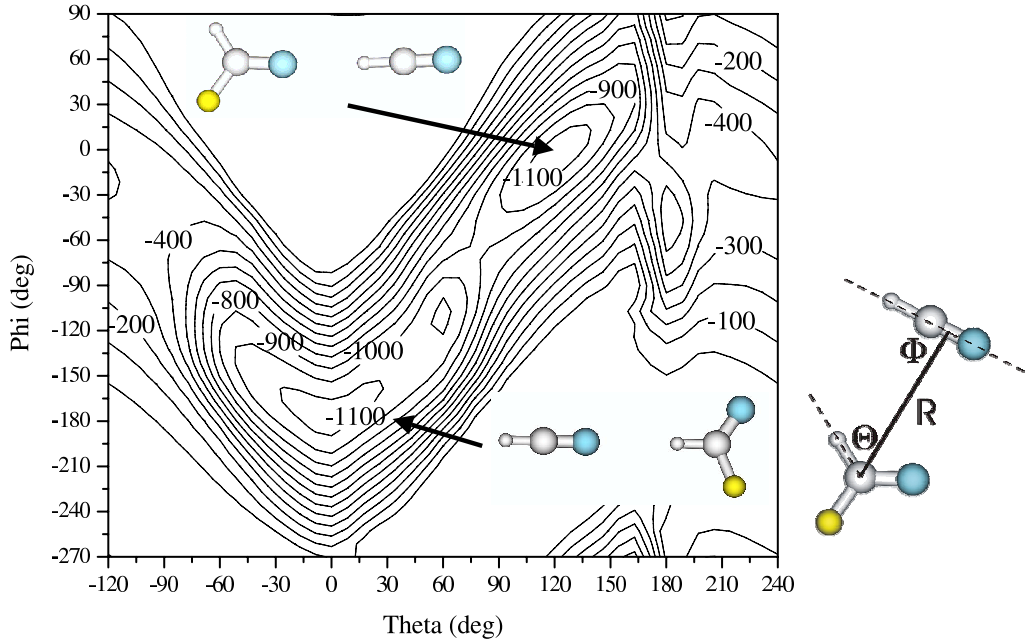

Figure 6.13: A two-dimensional interaction potential calculated at the RMP2/aug-cc-pVDZ level for the insertion product HFCN with a second HCN molecule. The second HCN molecule was assumed to lie in the plane of HFCN due to the fact that no non-planar geometries were observed in fully relaxed optimizations. The two angles were stepped in increments of 15^0 and only the intermolecular distance was allowed to optimize in the calculation. Counterpoise correction was applied and a spline interpolation used to generate the final surface. By tagging the F + HCN reaction product with a second HCN molecule, we regain a strong high-frequency C-H stretch which could be then probed experimentally.

proposed a similar mechanism was responsible for the stabilization of nitrogen atoms in a N_2 matrix (of up to 10% atomic concentration) frozen in bulk liquid helium [45–50]. While we have yet to perform extensive searches for HCN, we did explore this possibility for Br atoms and cyanoacetylene (HCCCN), where better signals are observed. Figure 6.14 shows a set of pendular survey scans covering the important frequency region. It is important to note that scans 6.14(A) - (C) were recorded by picking up the HCCCN first, but in 6.14D the order has been reversed, and we instead pickup from the pyrolysis source first. In Figure 6.14A, only HCCCN is added to the droplets, while in 6.14B, Br_2 is flowing through a room temperature pyrolysis source. The result of heating the pyrolysis to the appropriate temperatures for bromine atom pick-up are shown in 6.14C and 6.14D. In good agreement with the results of X + HCN, we find two peaks (labeled by a † in the figure) which we assign to the Br-HCCCN and

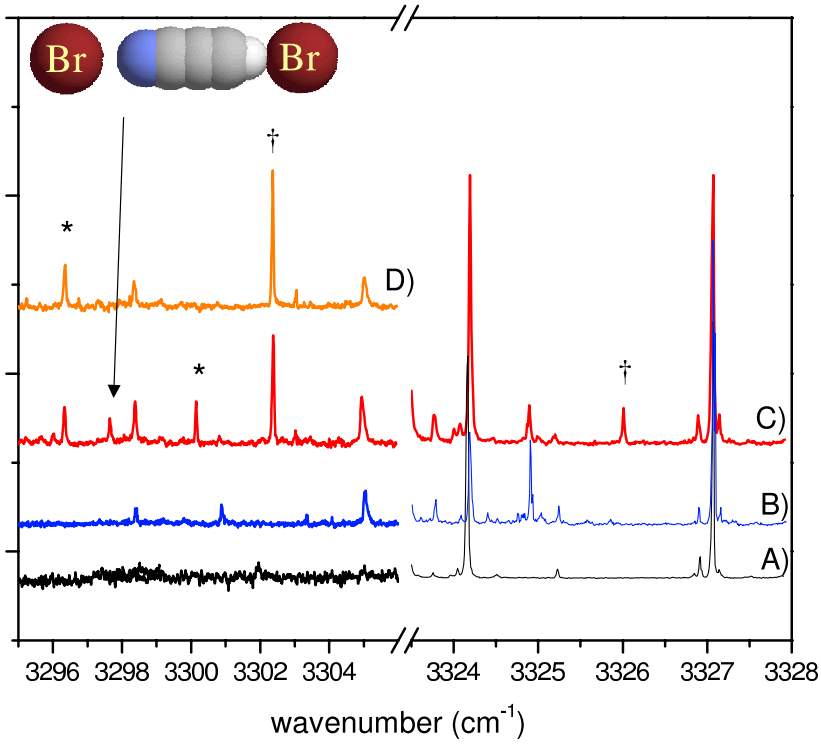

Figure 6.14: A series of pendular scans for Br + HCCCN where the bromine pressure is intentionally high to facilitate forming larger clusters. In (A) only HCCCN is picked up by the droplets and in (B) Br_2 is flowing through the cold pyrolysis source. Scans (C) and (D) were recorded with the pyrolysis source at the appropriate temperature for bromine atom production, but for (D) the bromine is picked up first. The peaks marked with a † are assigned to the linear Br-HCCCN and HCCCN-Br complexes. The two peaks marked with an * are found to optimize at higher HCCCN pressure and therefore correspond to more than one HCCCN. The peak at 3297.65 cm^{-1} optimizes at the same HCCCN pressure as the 1:1 complexes however is found to optimize at higher bromine pressure, suggesting that it is a complex containing two bromine radicals. The different behavior based on pick-up order is expected, since two bromine atoms will likely recombine to form Br_2 in the absence of the HCCCN.

HCCCN-Br complexes, based on their frequency shifts and signal strengths. The peaks labeled with an * were found to optimize at higher HCCCN pressure, so they correspond to complexes containing more than one HCCCN. The peak at 3297.65 cm^{-1} is a good candidate for being Br-HCCCN-Br because it only appears in the spectrum when the HCCCN is picked up first. This is to be expected since two bromine atoms will likely recombine to form Br_2 in the absence of the molecular spacer. To aid in this preliminary assignment we performed bromine pressure dependence measurements which are shown in Figure 6.15. This new peak is found

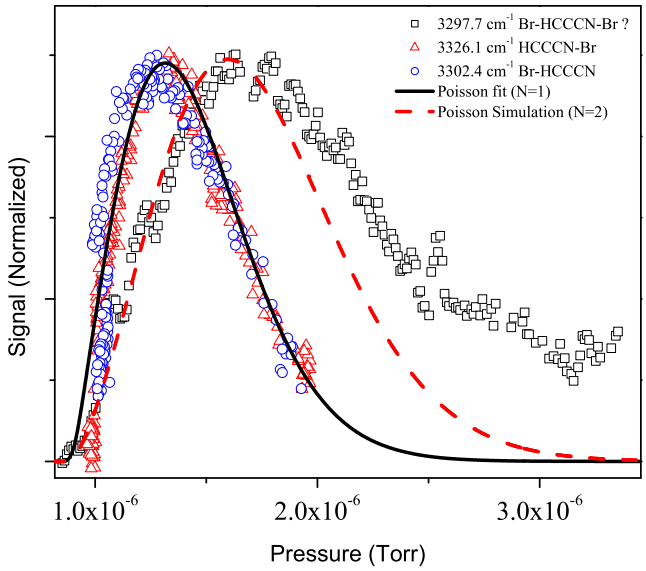

Figure 6.15: Bromine pressure dependencies for the peaks assigned to the Br-HCCCN, HCCCN-Br, and Br-HCCCN-Br complexes. The fact that the peak at 3297.65 cm^{-1} optimizes at higher bromine pressure than the 1:1 complexes lends supporting evidence to our claim that this is a di-radical complex. The smooth curves are the calculated pick-up probabilities obtained fitting a Poisson distribution to the 1:1 curve, and then re-simulating the curve for the dimer.

to optimize at higher bromine pressures than those peaks assigned to the 1:1 complexes, and agrees well with a simulation of a dimer using a Poisson distribution for the pick-up statistics. For these pick-up "cell" pressure dependence measurements the main chamber ion-gauge was used as the *x*-axis, however since this really monitors recombined Br_2 after collisions with the walls, instead of the local pressure of Br atoms in the pick-up zone, the pick-up curve for the dimer does not correspond to twice the optimum monomer pressure. Although we cannot rule out that a Br-HCCCN-Br_2, or similar complex might have such a pick-up cell pressure dependence, a double-resonance population transfer experiment (See Chapter 10) in which this new peak is pumped and the HCCCN-Br_2 complex is recovered would be definitive.

6.8 Summary

We have presented here a combined experimental and theoretical investigation of the halogen atom - HCN entrance channel complexes in order to compare with the X-HF complexes studied previously. The potential energy surfaces for X + HCN are found to be considerably more complex than for X+HX, due to the possibility of hydrogen atom abstraction and addition reactions. The lone pair on the nitrogen of HCN is also found to significantly alter the shape of the long-range potential energy surfaces, and for X + HCN, we find that the global minimum is a linear nitrogen bound geometry in contrast to the hydrogen bound global minimum for X-HF. A linear hydrogen bound X-HCN complex is also predicted to be stable however the isomerization barrier back to the global minimum is small. *Ab initio* calculations predict that for iodine and bromine significant barriers to the chemical reactions exist, and thus the entrance channel complexes should be quite stable when formed in a helium droplet. Both of the linear van der Waals isomers predicted by theory are observed experimentally for bromine and iodine atoms. Interestingly a HCN-Cl isomer was also observed however Cl-HCN was not. Since HCN-Cl is predicted to be the global minimum on the van der Waals potential, it could be that the isomerization barrier is simply too small to prevent Cl-HCN from rearranging back to HCN-Cl. A second possibility is that the reactivity is enhanced on the hydrogen end of HCN, and Cl-HCN goes on to react. No entrance channel complexes were observed in the fluorine experiments, and we preliminarily interpret this as a result of reaction. The intermediate reaction product HFCN has been recently observed in an argon matrix, however no pre-reactive complexes were observed in those works. Preliminary searches for HFCN, did not reveal this complex. The photon energy used to study the CH stretching vibration of the entrance channel complexes is greater than the predicted barriers, suggesting that photo-initiation of the corresponding reactions could be possible. The unique asymptotic degeneracy of the multiple electronic states in the region of the entrance and exit channels for free radical - molecule complexes is found to give rise to fine structure in the observed spectra for HCN-Br and HCN-I.

Chapter 7

The CH_3- HF Radical Molecule Complex

High-resolution infrared laser spectroscopy is used to study the CH_3-HF and CD_3-HF radical complexes, corresponding to the exit-channel complex in the F + CH_4 (CD_3H) $\rightarrow$ HF + CH_3 (CD_3) reactions. The rotationally resolved spectra presented here correspond to the fundamental v = 1$\leftarrow$0 H-F vibrational band, the analysis of which reveals a complex with C_{3v} symmetry. The vibrational band origin for the CH_3-HF complex (3797.00 cm^{-1}) is significantly red-shifted from that of the HF monomer (3959.19 cm^{-1}), consistent with the hydrogen bonded structure predicted by theory [E.Y. Misochko *et al.*, J. Am. Chem. Soc. **117**, 11997 (1995)] and suggested by previous matrix isolation experiments [M.E. Jacox, Chem. Phys. **42**, 133 (1979)]. The permanent electric dipole moment of this complex is experimentally determined by Stark spectroscopy to be 2.4 $\pm$ 0.3 D. The wide amplitude zero-point bending motion of this complex is revealed by the vibrational dependence of the A rotational constant. A six-fold reduction in the line broadening associated with the H-F vibrational mode is observed in going from CH_3-HF to CD_3-HF suggesting that fast relaxation in the former case results from near resonant intermolecular vibration - vibration (V-V) energy transfer. *Ab initio* calculations are also reported (at the MP2 level) for the various stationary points on the F + CH_4 surface, including geometry optimizations and vibrational frequency calculations for CH_3-HF.

7.1 Introduction

Of particular interest to the present study is the prototypical F + CH_4 $\rightarrow$$CH_3$ + HF reaction [248], a model system for the general class of corresponding hydrocarbon reactions. The rate constant for this highly exothermic reaction [242] (ΔE = -32.0 kcal mol^{-1}) has been determined to be (6.8 $\pm$ 1.4) $\times$ 10^{-11} cm^3 $molecule^{-1}$ s^{-1} at room temperature [249]. As recently reviewed by Harper *et al*. [248], there have been numerous state-to-state reactive scattering studies of this system, dating back to Nazar and Polanyi [250], who employed infrared chemiluminescence to measure the vibrational population distribution for HF(v') (v' = 3, 2, 1), namely, 0.10, 0.69, and 0.21, respectively, consistent with the large exothermicity of the reaction. These results were later confirmed by Wickramaaratchi *et al*. [251] employing arrested-relaxation techniques, and Harper *et al*. [248] using crossed supersonic jets, combined with high resolution infrared laser spectroscopy. The latter study yielded rotational distributions for the HF(v') product that were significantly hotter than those obtained previously, presumably due to the collision free nature of these experiments. Harper *et al*. [248] interpreted these results in terms of a bent C—H—F transition state. Most recently, Liu and coworkers [252–254] have also reported evidence for the existence of a reactive resonance in the F + CH_4 reaction.

7.1.1 F + CH_4 PES

A number of potential energy surfaces (PESs) have been developed for the fluorine atom-methane reaction and it is now known that this system has a small and early barrier, with a shallow entrance valley. The London-Eyring-Polanyi-Sato (LEPS) potential of Gauss [255] was adjusted to reproduce the experiments of the time, while two semiempirical surfaces have also been reported [256], namely the MJ1 surface, a modification of the J1 surface of Joseph *et al*. [257] for the H + CH_4 $\rightarrow$ CH_3 + H_2 reaction, and a surface obtained using PM3 semiempirical molecular orbital theory [258]. Kornweitz *et al*. [259] constructed a six-atom PES, which again is a modification of a H + CH_4 potential [260], which was fit to experimental thermal

rate constant data [261]. Classical trajectory calculations on this surface [259] indicate a direct reaction mechanism, with a preference for a collinear C—H—F geometry and bond switching occurring in less than an HF vibrational period. These results also indicate that very little of the available energy appears as internal excitation of the CH_3 radical product. Most recently, Troya *et al*. [262] reported dynamical studies of the reaction using quasiclassical trajectory methods, employing a three-atom analytical representation of the ground PES. The PES was obtained from *ab initio* points calculated at the PUMP4//UMP2/6-311+G(2df,2pd) level of theory, treating the CH_3 fragment as a pseudo-atom. The HF rovibrational state distributions obtained from these quasiclassical trajectory calculations were in good agreement with experiment. In view of the high dimensionality of the full atom potential, there is clearly need for further experimental results that probe specific regions of the potential surface.

7.1.2 Previous matrix isolation experiments

Although the CH_3-HF complex has not been observed in the gas-phase, some progress towards its characterization has been made using matrix isolation methods. Jacox [263] utilized microwave discharges of Ar/CF_4 and Ar/NF_3 mixtures to produce fluorine atoms prior to co-deposition with methane into an argon matrix. The resulting infrared spectra revealed the presence of isolated HF and CH_3 products, as well as vibrational bands that were assigned to the CH_3F-HF and CH_3-HF complexes. Johnson and Andrews [264] later performed a complementary photochemical study by co-depositing F_2 and CH_4 in solid argon. They found that CH_3F-HF was the primary photolysis product resulting from UV excitation of the CH_4-F_2 van der Waals complex. However, upon warming the matrix to 25 K they observed a band at 3764 cm^{-1}, which they assigned to the CH_3-HF complex, presumably formed by the reaction of the photo-generated fluorine atoms with methane. Misochko *et al*. [265, 266] confirmed many of these observations, identifying three distinct mechanisms for product formation, depending upon the matrix temperature. Once again, they found that the mechanism for stabilizing the CH_3-HF complex involved the diffusion of thermal F atoms. *Ab initio* calculations (at the

UMP4/6-311G(d,p)//UMP2/6-31G(d) level of theory), combined with hyperfine constants determined from their electron spin resonance (ESR) experiments, lead them to conclude that the CH_3-HF complex has C_{3v} symmetry. It is important to note that there is still some controversy concerning the structure of the transition state for this system. Indeed, early self-consistent field (SCF) calculations [267] and more recent MP2/cc-pVTZ calculations [268] suggest that the transition state is also C_{3v}, while recent work by Corchado and Espinosa-Garcia [269], at the MP2(full)/6-31G(d,p) level of theory, suggests a bent transition state, which is more consistent with the experimental results of Harper *et al*. [248]. In the present study we report a high-resolution infrared spectrum of the CH_3-HF exit channel complex and its CD_3-HF isotopomer.

7.2 *Ab initio* calculations

The experimental study reported here was supplemented by *ab initio* calculations designed to aid in both the initial search for the spectra and in the interpretation of the data. In particular, these calculations provide relative energies for the various stationary points on the potential energy surface, corresponding to the F + CH_4 $\rightarrow$ HF + CH_3 reaction, as well as vibrational frequencies, dipole moments and rotational constants. All calculations reported here were carried out using the GAUSSIAN 03 [194] package of programs. Closed and open shell species were treated using restricted and unrestricted Hartree-Fock self-consistent field (SCF) wavefunctions, respectively, while second order Moller-Plesset perturbation theory (MP2) was used in the geometry optimizations for the reagents, molecular complexes, transition state and products, using different basis sets. A full harmonic vibrational frequency calculation was also carried out for all of these species and all geometry optimizations were done with tight convergence criteria.

7.3 Helium droplet results

In the present study, ditertbutyl peroxide (DTBP) [$(CH_3)_3COOC(CH_3)_3$] and azomethane (CH_3NNCH_3) were used as precursors for the CH_3 radicals. Azomethane was synthesized using the procedure outlined by Renaud and Leitch [270–272] and stored in a stainless steel container. DTBP (95%) was obtained from Aldrich and placed in an evacuated glass bulb without further purification. The purity of these samples and their efficiencies for forming methyl radicals were estimated using electron impact mass spectrometry in a separate vacuum chamber, equipped with an SRS-RGA300 Residual Gas Analyzer. Pyrolysis was monitored by comparing mass spectra obtained at various source temperatures [273–275], which is shown in Figure 7.1 for DTBP. Thermal decomposition of DTBP (at 800 K) results in the formation of two

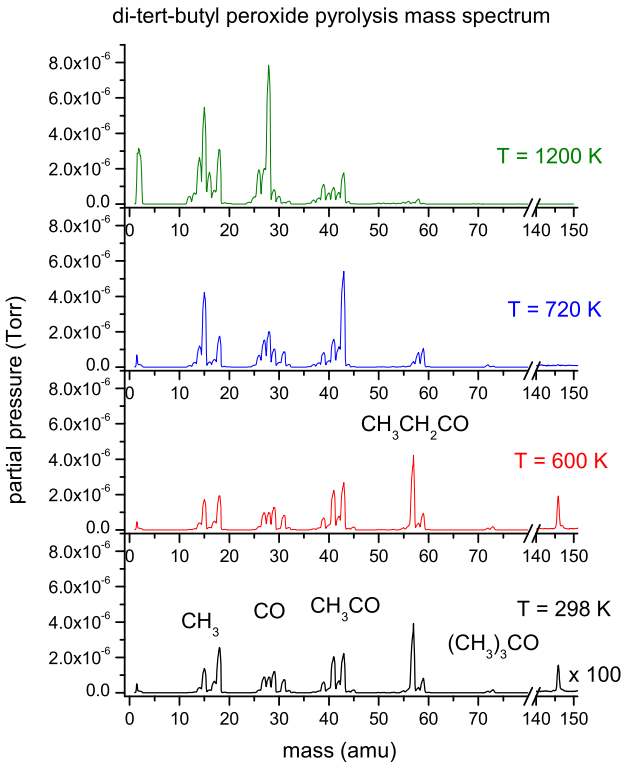

Figure 7.1: A series of mass spectra of DTBP recorded under different pyrolysis source temperatures. At temperatures higher than 700 K, CH_3 radicals are observed.

methyl radicals and two acetone molecules [275], while azomethane (at 1100 K) decomposes

into two methyl radicals and one nitrogen molecule [274]. Although this would suggest that azomethane would be a better choice for the present helium nanodroplet experiments, given the more favorable ratio of methyl radical to secondary products, the two precursors were found to give essential the same signal levels under optimal conditions. This is most likely due to the fact that at higher temperatures the acetone from DTBP can undergo further decomposition to form additional CH_3 radicals [275].

Several checks were performed to ensure that the measured spectra were indeed associated with the CH_3-HF radical complex. First, we scanned the C-H stretch region of the methyl radical (in the absence of the HF) and observed several transitions of the methyl radical monomer, which were only slightly shifted from those observed in previous gas-phase studies [127, 276]. In view of the large rotational constants associated with the methyl radical, we indeed expect that they will only be slightly changed by solvation in helium [277]. The signals levels for the methyl radical had precisely the same dependence on the pyrolysis source temperature and precursor pressure as those associated with the band assigned to CH_3-HF. Finally, we obtained the same spectrum for CH_3-HF when using methyl iodide (CH_3I) and dimethyl sulfoxide (CH_3SOCH_3) as precursors, although the associated signals were somewhat lower than those obtained with DTBP and azomethane. CD_3 radicals were produced by pyrolysis of CD_3I (99.8 % D Aldrich), which required substantially higher pyrolysis temperatures (1500 K).

Since HF has a relatively large dipole moment (1.826 D) [278, 279] it is clear that the CH_3-HF complex of interest here will be polar. This makes pendular spectroscopy an ideal starting point in the search for the associated spectrum, given the high sensitivity of this method [25, 129, 130]. This was accomplished by applying a 50 - 60 kV cm^{-1} electric field to the laser interaction region, while carrying out low resolution scans through the spectral region of interest. Appropriately scaled *ab initio* frequency calculations were used as a guide in this search. The rather large frequency shift expected for a hydrogen bonded complex ensures that the associated spectrum will be well separated from the other species formed in the droplets. In practice we carried out scans with the pyrolysis source both cold and hot, specifically looking

for new features that appeared in the latter case, particularly at temperatures appropriate for the formation of the methyl radical. The result was the observation of a single pendular peak in the region of the spectrum predicted by the *ab initio* calculations. The pyrolysis source pressure and temperature dependence of the associated signal, as well as the HF pressure dependence, strongly suggested that this band was indeed associated with the CH_3-HF complex. This band was also observed for all of the precursors discussed above, at the appropriate pyrolysis temperatures. Figure 7.2(A) shows the experimental spectrum obtained in the absence of an electric

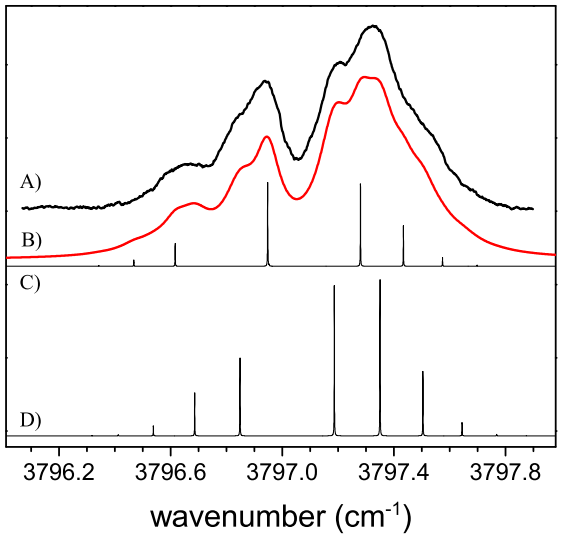

Figure 7.2: Electric field-free infrared spectrum (A) of the partially rotationally resolved H-F stretch of the CH_3-HF molecular complex in helium nanodroplets, along with the corresponding fit (B). The latter was obtained using a prolate symmetric top Hamiltonian, with a rotational temperature of 0.37 K. The appropriate 2:1 nuclear spin statistics were incorporated in the simulation (see text). Here we assume that the |K| = 1 states (C) do not cool to K = 0 (D). Molecular constants derived from the fit are presented in Table 7.2.

field, which we will go on to assign to the H-F stretch of the CH_3 -hydrogen fluoride complex.

We begin by noting that the *ab initio* calculations (at the MP2/6-311G(d,p) and MP2/aug-cc-pVTZ levels of theory) predict (see Table 7.1) that the CH_3-HF complex has C_{3v} symmetry, with the hydrogen atom of HF pointing toward the carbon atom of the methyl radical. Due to the fact that the unpaired electron resides mainly in a localized p orbital on the methyl

	CH_4	CH_4-F[a]	CH_3-H-F	CH_3-HF	HF	CH_3
r(CH)	1.0909	1.0903	1.0882	1.0806		1.0792
	(1.0862)		(1.0842)	(1.0765)		(1.0749)
r(CH')[b]		1.0896	1.1373	2.2285		
			(1.1239)	(2.1447)		
r(H'F)		2.8458	1.3920	0.9172	0.9128	
			(1.4598)	(0.9297)	(0.9218)	
∠HCH'[b]		109.52	107.05	93.83		
			(107.26)	(93.53)		
∠HCH	109.47	109.42	111.78	119.56		
	(109.47)		(111.59)	(119.62)		
∠CH'F		180.00	180.00	180.00		
			(180.00)	(180.00)		

[a]The CH_4-F complex was not found at the UMP2/aug-cc-pVTZ level.
[b]The abstracted hydrogen atom is denoted as H'

Table 7.1: Optimized geometrical parameters calculated at the MP2/6-311G(d,p) (MP2/aug-cc-pVTZ) level of theory of the reagents, molecular complexes, products, and transition state of the F + CH_4→HF + CH_3 reaction. Distances and angles are given in angstroms and degrees, respectively.

radical along the symmetry axis, the ground electronic state of this complex is predicted to be $^2A_1$. Calculated spectra, based upon a prolate symmetric top Hamiltonian, are shown in Figure 7.2(B, C (K = 0 band only), and D (K = 1 band only)), corresponding to a rotational temperature of 0.37 K. Given that the transition dipole moment associated with the H-F stretch is parallel to the *a*-axis, *a*-type selection rules apply, namely ΔK = 0, with ΔJ = $\pm$1 for K = 0 ←0 and ΔJ = 0, $\pm$1 for K $\neq$ 0 [280]. The presence of the transitions associated with the |K| = 1 levels, as evidenced by the presence of the Q-branch, lends strong support to the C_{3v} symmetry of this complex. Indeed, the large A rotational constant expected for this complex (predicted by the *ab initio* calculations to be approximately 4.8 cm^{-1}) would normally make thermal population of the |K| = 1 levels negligible at the temperature of the droplets. Nevertheless, the C_{3v} symmetry ensures that states with |K| $\neq$ 3n, where n is an integer $\geq$1 (E symmetry), cannot cool to those with K = 0 or |K| = 3n (A symmetry). In addition, the latter states have twice the nuclear statistical weight of the former [281]. One would not expect the relative populations of nuclear-spin isomers to relax on the timescale of the experiment (~1 ms) due

to the slow rate of interconversion [175], and thus the ratio of spin isomers should resemble that of room temperature (approximately 1:2 A:E, where we assume equilibrium). Therefore, to calculate the intensities in the simulation, the ratio of A:E population is first calculated at room temperature and then cooled into the lowest K = 0 (A symmetry) or K = |1| (E symmetry) state adiabatically. The final intensity ratio of the K = 0 and K = |1| bands is thus governed by the ~1:2 A:E population times the 2:1 A:E spin statistics yielding ~1:1. For clarity, the K = 0 and |K| = 1 bands of the simulation have been plotted separately in Figure 7.2 (D and C respectively).

Constant	Helium droplet	MP2 6-311G(d,p)	MP2 6-311++G(d,p)	MP2 aug-cc-pVTZ	Ar matrix
ν_0 (cm^{-1})	3797.00(3)	4144.01	4062.40	3931.35	3764[a]
A" (cm^{-1})	4.74275[b]	4.796	4.791	4.830	-
ΔA (cm^{-1})	-0.06(1)	-	-	-	-
B (cm^{-1})	0.090(10)	0.197	0.193	0.206	-
D_J (cm^{-1})	$2.5(10) \times 10^{-4}$	-	-	-	-
μ" (D)	2.4(3)	2.49	2.58	2.54	-
$\Delta\mu$ (D)	0.2(2)	-	-	-	-
HF molecule					
ν_0 (cm^{-1})	3959.19(1)	4251.90	4198.72	4122.87 (3961.42)[d]	3962 and 3955[c]
μ" (D)	-	1.90	1.97	1.81 (1.826)[f]	-

[a] See Refs. [263, 264]
[b] Fixed as the C rotational constant of CH_3 monomer. See Refs. [127, 276, 282]
[c] See Ref. [76]
[d] See Ref. [278]
[e] See Ref. [264]
[f] See Ref. [279]

Table 7.2: A summary of the experimental and calculated molecular constants for the CH_3-HF complex. The corresponding data for the HF monomer (including the gas-phase values given in parentheses) are also provided for comparison.

Table 7.2 contains a summary of the experimental constants determined from the fit to the zero-field spectrum, namely the H-F stretch vibrational band origin and the rotational constants, along with the corresponding values obtained from the *ab initio* calculations. The vibrational band origin obtained from matrix isolation studies of this complex [264] is also given for com-

parison with the present results. The magnitude of the A rotational constant is not determined from this fit, given that the band is *a*-type and that the relative populations of the K = 0 and 1 levels are controlled by the symmetry rather than the temperature. Thus the determination of the A rotational constant will have to await future experiments designed to study the asymmetric C-H stretch of the methyl radical. Indeed, the associated perpendicular band will provide an accurate determination of this constant. Nevertheless, we expect that rotation of CH_3-HF about its *a*-axis will be relatively unhindered by the helium, given that the associated motion is in the non-following regime. In particular, rotational motion corresponding to a rotational constant of 4.8 cm^{-1} is too fast for the helium to follow and it is now well documented that the associated constants are only slightly changed from the gas-phase [84, 283]. In addition, the A rotational constant of the complex should be approximately equal to the C rotational constant of the isolated methyl radical, given that it will be only slightly modified by vibrational averaging.

Given the limited number of transitions and their broad linewidth in the present spectrum, it was necessary to assume that the rotational (B) and centrifugal distortion (D_J) constants in the ground and vibrationally excited states are the same. The experimental B rotational constant (0.090(10) cm^{-1}) is a factor of approximately 2 smaller than that predicted from the *ab initio* calculations, which is typical of molecules solvated in liquid helium droplets [283]. A Lorentzian linewidth of 0.16 cm^{-1} was used in the simulation of each of the calculated transitions in the spectrum.

Although the parallel band in Figure 7.2 is not sensitive to the absolute magnitude of the A rotational constant, it does provide an accurate value for ΔA = A' - A", namely -0.06(1) cm^{-1}. The most obvious effect of this difference is on the relative positions of the P, Q, and R branches in the spectrum. In particular, the Q branch does not appear at the midpoint between the P and R branches of the K = 0 band. As discussed below, this rather large change in the A rotational constant upon excitation of the H-F stretching vibration results from effects associated with the wide amplitude bending of this complex. The H-F stretching frequency of

CH_3-HF is measured to be 3797.00(3) cm^{-1} in helium, corresponding to a red-shift of 162.19 cm^{-1} from the H-F stretch of the monomer in helium nanodroplets. Such a large frequency shift is consistent with a hydrogen bonded CH_3-HF radical-molecule complex.

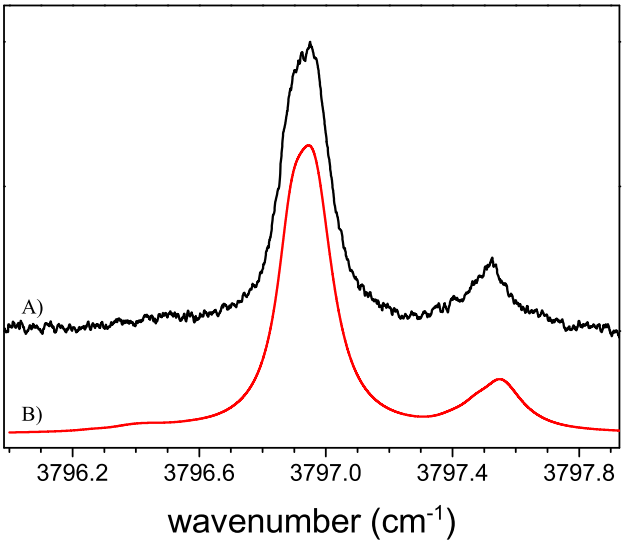

Figure 7.3: The experimental (A) and calculated (B) Stark spectra of the H-F stretch of the CH_3-HF molecular complex in helium nanodroplets. The calculated spectrum is again based upon a prolate symmetric top Hamiltonian, including the effects of the 15.42 kV cm^{-1} electric field. The fit is also done with a fixed rotational temperature of 0.37 K, including the appropriate symmetry effects. The dipole moment determined from this fit is 2.6 $\pm$ 0.3 D.

Figure 7.3(A) shows a Stark spectrum for CH_3-HF recorded at an electric field of 15.42 kV cm^{-1}. The simulation shown in Figure 7.3(B) was generated using the rotational constants determined from the field-free spectrum and a ground-state dipole moment of 2.4 D. A change in the dipole moment upon vibrational excitation of 0.2 D was also used in generating the best fit; however the broad linewidths observed here make the uncertainty of the associated fits rather large ($\pm$0.3 D). *Ab initio* calculations (Table 7.1) predict the dipole moment for this complex to be 2.5 D, which is within the error bars of our fit.

7.3.1 Vibration-vibration resonance

Given that the resolution obtained in the infrared spectra of many molecules solvated in helium is quite high [283, 284], due to the lack of elementary excitations in the bulk superfluid to which the molecule can couple, the broad linewidths observed here for CH_3-HF are somewhat anomalous. It is interesting to note that spectra recorded with the OPO (70 mW) laser had the same linewidth as those obtained with the FCL (5 mW), suggesting that power broadening is not important in this system.

Previous studies on the isotopomers of the H_2-HF complex have revealed the importance of intermolecular vibration-to-vibration (V-V) resonances in shortening the excited state lifetimes [285, 286]. In this system, the excited vibrational states of HD (and D_2) lie just below that of the H-F stretch, so that rapid V-V energy transfer can occur upon H-F vibrational excitation. We propose a similar vibration-vibration resonance is responsible for the broadening in the CH_3-HF spectrum, presumably involving the C-H stretching vibrations of the methyl radical.

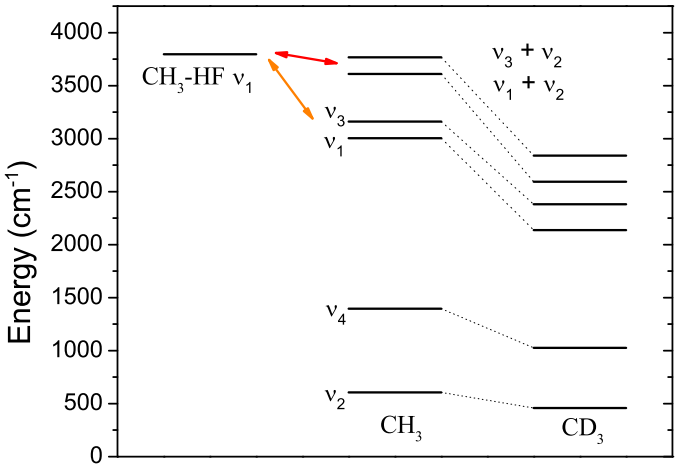

Figure 7.4: An energy level diagram showing the relative energies of the monomer fragments to the H-F vibrationally excited state of the CH_3-HF (CD_3-HF) complex. Since no experimental data exists for the combination bands of the methyl radical, their energies are simply the sum of the corresponding fundamentals. The near degeneracy between the H-F stretching vibration in the complex and the isolated methyl radical combination bands suggests that a vibrational resonance could indeed be the source of the broadening in the CH_3-HF spectra.

Figure 7.4 shows a vibrational energy level diagram, comparing the vibrational energy of the H-F stretch excited CH_3-HF complex with that of the methyl radical fragments (CH_3 and CD_3). Since experimental data does not exist for the combination bands of the methyl radical, the corresponding energies are simply the sum of the fundamental energies. It is unclear whether the coupling is to one of the fundamental C-H stretches of the methyl (a rather large energy gap, but possibility a large matrix element) or to a combination band, for example involving either the symmetric (ν_1) or asymmetric (ν_3) C-H stretching vibration and the umbrella mode (ν_2) of CH_3. The importance of the ν_2 umbrella mode is postulated given that *ab initio* calculations predict that the CH_3 molecule distorts slightly from planarity (see Table 7.1) upon formation of the complex, suggesting that this mode may be coupled.

Constant	Helium droplet
ν_0 (cm^{-1})	3787.14(1)
ΔA (cm^{-1})	-0.026(5)
B$''$ (cm^{-1})	0.0826(5)
B$'$ (cm^{-1})	0.0849(5)
$D_J^{''}$ (cm^{-1})	$2.7(3) \times 10^{-4}$
$D_J^{'}$ (cm^{-1})	$2.3(3) \times 10^{-4}$
$\mu^{''}$ (D)	2.6(1)
$\mu^{'}$ (D)	2.9(1)

Table 7.3: A summary of the experimental molecular constants for the CD_3-HF complex.

In light of the above discussion, deuterium substitution on the methyl should detune the associated vibrational modes from resonance (as shown in Figure 7.4), resulting in a longer lifetime for the H-F stretch excited state. Figure 7.5A shows the field-free spectrum obtained for the CD_3-HF complex. The fit to the experimental spectrum (Figure 7.5B) is based upon a symmetric top Hamiltonian (C_{3v} symmetry), the resulting constants being summarized in Table 7.3. The widths of the observed transitions are clearly much smaller than for CH_3-HF, in agreement with our expectations. The fit to the CD_3-HF spectrum employs a 0.025 cm^{-1} Lorentzian linewidth for each of the transitions and also takes into account the 11:8 A:E nuclear spin statistics.

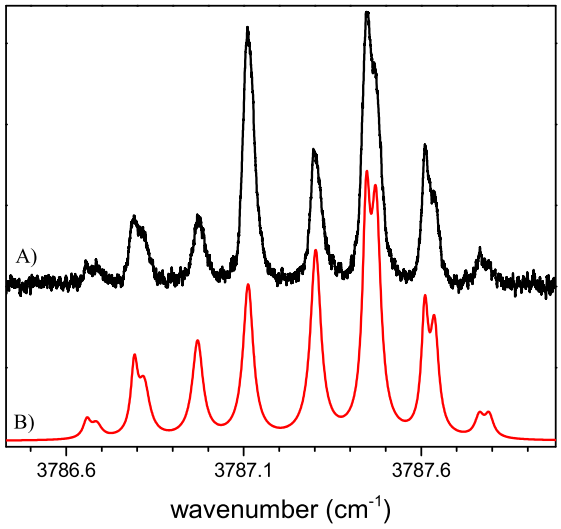

Figure 7.5: The electric field-free spectrum of CD_3-HF in helium droplets. The linewidths observed in this spectrum are considerably smaller than those in the CH_3-HF complex due to quenching the V-V resonance. Molecular constants derived from this fit are shown in Table 7.3. The fit to the experimental data includes the 11:8 nuclear spin statistics for C_{3v} symmetry.

The H-F stretch of CD_3-HF has a significantly larger red-shift (by 9.86 cm^{-1}) than the corresponding band of CH_3-HF, a point we will discuss further below. The higher resolution of the CD_3-HF complex allows for more precise determinations of the corresponding molecular constants. In this case it is possible to determine the vibrational dependence of the B rotational constant (B' = 0.0849(5) cm^{-1} and B" = 0.0826(5) cm^{-1}). The *ab initio* calculations give a reduction in B by a factor of 1.13 upon deuterium substitution, and this difference is within the error bars associated with the fit to the CH_3-HF spectrum. It is interesting to note that ΔA is much smaller for CD_3-HF (-0.026(5) cm^{-1}) than for CH_3-HF (-0.06(1) cm^{-1}). The direct mass effect of substitution requires ΔA (for CD_3-HF) to be reduced by a factor of 2 when compared with CH_3-HF. Based on the fact that our measured ΔA is reduced by slightly more than this, again leads us to the conclusion that the magnitude of ΔA is related to the wide amplitude intermolecular bending motion in these systems, which is expected to be considerably smaller for CD_3-HF.

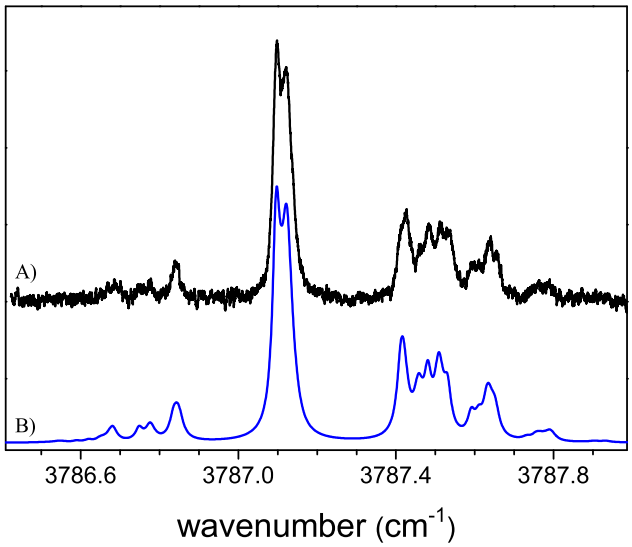

Figure 7.6: A Stark spectrum of CD_3-HF, recorded at an electric field of 5.073 kV cm^{-1}. The fit was obtained by holding fixed all of the molecular constants determined from the zero-field spectrum. The resolution in this spectrum was sufficient to provide significant values for the dipole moments in both the ground and vibrationally excited states (See Table 7.3).

Figure 7.6A shows a Stark spectrum of the CD_3-HF complex, recorded at an electric field of 5.073 kV cm^{-1}. The fit shown in Figure 7.6B yields ground and vibrationally excited dipole moments of μ" = 2.6(1) D and μ' = 2.9(1) D, respectively. The large change upon H-F vibrational excitation is likely due to the associated change in the intermolecular bending motion.

7.4 Discussion

Figure 7.7 presents an energy level diagram for the F + CH_4 reaction system, showing the reagents, molecular complexes, transition state, and products, all calculated at the MP2/6-311G(d,p) level of theory. The relative energies of these stationary points on the potential energy surface are also summarized in Table 7.4, calculated at MP2 level of theory using 6-311G(d,p), aug-cc-pVDZ, and aug-cc-pVTZ basis sets. It is clear from this figure that the lowest energy configuration along the reaction coordinate is the CH_3-HF molecular complex

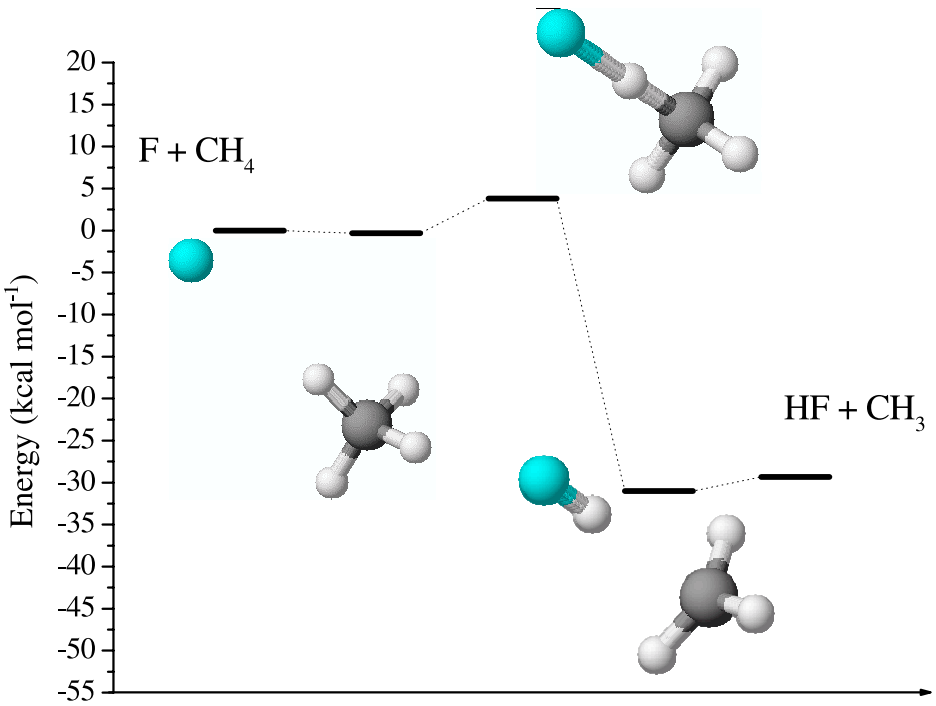

Figure 7.7: A reaction path energy level diagram based on computed energies and optimized structures (also shown) of the reagents, intermediate molecular complexes, transition state and products for the hydrogen abstraction reaction, F + CH_4 $\rightarrow$ HF + CH_3. The energies and geometries were calculated at the MP2/6-311G(d,p) level of theory and the former include the zero-point energies.

observed here, which lies 31.02 kcal mol^{-1} below the reagents and 1.69 kcal mol^{-1} below the products at the MP2/6-311G(d,p) level of theory. In addition to this exit channel complex, a very weakly bound entrance channel complex exists, namely CH_4-F. This complex is bound by only 0.32 kcal mol^{-1} and has an optimized C_{3v} structure, corresponding to the F atom weakly bound to a hydrogen atom of the methane, at an equilibrium distance of 2.85 Å. As a result, the methane molecule is only slightly perturbed by this weak interaction.

It is important to point out that the equilibrium geometry of this F-CH_4 complex is predicted to lie only 4.13 kcal mol^{-1} below the reaction barrier, which is less than the energy associated with the C-H vibrational modes of methane. This system is therefore an ideal candidate for studying vibrationally induced reaction dynamics. Future studies will aim to provide high-resolution infrared spectra of this entrance channel complex, formed by pick-up of an F atom

Level of theory	CH_4-F	CH_3-H-F	CH_3-HF	CH_3+ HF
MP2/6-311G(d,p)	-0.32	3.81	-31.02	-29.33
MP2/aug-cc-pVDZ	-0.10	1.44	-36.88	-35.26
MP2/aug-cc-pVTZ	-[a]	1.50	-38.25	-36.66
Exp.	-	-	-	-32.00

[a]The pre-reaction molecular complex stationary point on the PES was not located using aug-cc-pVTZ basis set.

Table 7.4: A summary of the relative *ab initio* energies including zero-point energy (in kcal mol^{-1}), with respect to the separated F + CH_4 reagents, for the stationary points on the PES, calculated at different levels of theory. The experimental value of the reaction enthalpy (at 0 K), derived from enthalpies of formation at 0 K (see Ref [287]) is also given.

and a methane molecule. The early transition state associated with this system is linear in all but the MP2(full)/6-31G(d) calculations [269], with C–H and H–F bond lengths of 1.14 and 1.39 Å respectively, at the MP2/6-311G(d,p) level of theory.

The H_3C–H and H-F bond lengths in the CH_3-HF complex are 2.23 and 0.92 Å respectively, indicating that the CH_3 and HF molecules are only slightly perturbed, relative to the free molecules. The rather strong hydrogen bond between the methyl radical and HF is evident from the large red-shift of the H-F vibrational mode upon complex formation. The *ab initio* harmonic frequency shifts obtained from the MP2/6-311G(d,p) (-107.89 cm^{-1}) and MP2/aug-cc-pVTZ (-191.52 cm^{-1}) calculations bracket the experimental value (-162.17 cm^{-1}). The hydrogen bond shift observed in conventional matrices is somewhat larger than observed for helium, namely -198 cm^{-1}, presumably due to stronger matrix effects. A simple harmonic *ab initio* vibrational frequency calculation predicts that the isotopic dependence of the HF stretch (in going from CH_3 to CD_3) is only -0.02 cm^{-1}, compared to -9.86 cm^{-1} observed experimentally. This qualitative disagreement again suggests that this is quite a dynamic system and that simple equilibrium calculations do not capture many of the important aspects of this system.

The experimental and theoretical results presented here both suggest that the equilibrium structure for the CH_3-HF complex has C_{3v} symmetry, in agreement with observations by Misochko *et al*. [265]. Nevertheless, the wide amplitude intermolecular bending and stretching motion that is apparent in this system can provide important and new information on the nature of

the potential energy surface in the exit channel of this reaction. Such interactions are important in determining the final state distributions of the products from this reaction. It is instructive to note that the lowest frequency, intermolecular bending modes of this complex correspond to two degenerate vibrations, associated with the HF and CH_3 bending motions, having calculated harmonic frequencies of 425 cm^{-1} and 128 cm^{-1} respectively, at the MP2/aug-cc-pVTZ level of theory. The corresponding intermolecular stretching frequency is 137 cm^{-1}. We expect that the rather large changes in the HF stretching frequency upon deuterium isotope substitution on the methyl, as well as the changes of the A rotational constants and dipole moments upon vibrational excitation, can be understood in terms of these wide amplitude intermolecular motions.

7.4.1 Vibrational averaging

Since both of the monomer constituents in the methyl-HF complex are quite light, and therefore undergo rather wide amplitude motions within the complex, it is difficult to say *a priori* which of the corresponding low frequency vibrational modes will be most important, or if both will have significant effects on the observed molecular constants. It is interesting to note that in the T-shaped C_2H_2-HF [288, 289] complex, gas-phase studies have shown that A" of the complex (1.13168 cm^{-1}) is smaller than B" of the acetylene monomer (1.1766 cm^{-1}). This effect cannot be attributed to a geometric change upon complexation, instead it is the result of vibrational averaging over the low frequency vibrations. Since bending of the HF sub-unit away from T-shaped decreases the A value, while bending of the acetylene makes the complex more linear, thus increasing A, this is a system for which the HF bending clearly overwhelms the effects from the acetylene bending. This makes sense given that the HF has a much larger rotational constant than the acetylene, making the wide amplitude motion of the former much larger. In contrast, the opposite trend is observed for C_2H_2-HCN [85], which can be understood by the fact that the rotational constants of the two monomers are much more similar, so that the intermolecular bending of the HCN does not overwhelm that of the

acetylene. Unfortunately, as mentioned above, the parallel band observed here for the methyl-HF complex does not provide an accurate A" value to compare with the C" rotational constant of CH_3. This nevertheless shows the importance of future studies of the methyl stretches of this complex, which can provide this information.

We now consider the effects of vibrational excitation on the A rotational constants of these complexes. It is again interesting to note that both acetylene-HF and acetylene-HCN have negative ΔA's (ΔA = A' - A") (upon vibrational excitation of the H-X stretch, both of which are approximately 0.001 cm^{-1}), while for CH_3-HF the change is much larger (-0.06 cm^{-1}), but also negative in sign. The effect of intermolecular bending of the CH_3 molecule in the CH_3-HF complex is to increase the A rotational constant of the complex, relative to that of the C_{3v} structure, whereas the bending of HF will decrease A The increase in the H-F bond length upon H-F vibrational excitation results in a slight shortening of the intermolecular bond and an increase in the interaction between the two molecules. In general the associated stiffening of the intermolecular bond will result in a decrease in the intermolecular bending amplitudes for both the HF and the CH_3 bending modes. Neglecting the effect of the increase in HF bond length upon vibrational excitation on the A' rotational constant, the stiffening of the intermolecular bond would necessarily cause A' > A" for the HF bending mode. This effect gives the wrong sign of ΔA, when compared with our experimental results. The lengthening of the HF bond length however, reduces A' (when not in C_{3v} symmetry), and thus may cancel the effects of the stiffening intermolecular bond. Indeed, numerical calculations reveal that this is in fact the case, and even in the case of the HF bending, A' < A".

A quantitative understanding of the vibrational averaging in the CH_3-HF complex will require a calculation that includes all of the low frequency intermolecular modes of the systems. This is beyond the scope of the present study and we instead focus on the HF and CH_3 bending vibrations, treating each of them independently. First, let us consider the case where the CH_3 bending mode is assumed to dominate. For simplicity, we have restricted the CH_3 to remain planar during the bending coordinate. The corresponding one-dimensional bending potential

was calculated at the MP2/6-311++G(d,p) level, as a function of the angle theta in increments of 5^0, defined as $\angle$(H'C–F) - 90^0 (where H' denotes one of the hydrogens of CH_3, such that at 0^0 the C_{3v} structure is recovered). Inasmuch as the potential was found to be only weakly dependent upon the azimuthal angle, corresponding to the rotation of the methyl group about the *a* axis, we assume here that the potential is isotropic in this coordinate. This assumption also requires that the energies for positive and negative values of theta be equal. For each fixed value of theta, the angle between the HF bond axis and the carbon atom was constrained to be zero, while the remaining geometric parameters were optimized and a harmonic frequency calculation was then performed. Although the resulting structures do not correspond to a global minimum on the surface, so that some of the harmonic frequencies cannot be trusted, the high frequency HF stretch is likely still to be reliable as this coordinate was optimized.

The resulting one-dimensional potential shown in Figure 7.8 was used to calculate the corresponding bending wavefunction, using the Numerov-Cooley method [176]. The B rotational constant of CH_3 was used in the calculation, providing an estimate of the reduced mass associated with this bending motion. The vibrationally averaged rotational constant and HF vibrational frequency were then determined by averaging the corresponding *ab initio* values over the calculated wavefunction.

The vibrationally averaged constants obtained from this calculation, <A"> = 4.902 cm^{-1} and $<\nu_{HF}>$ = 4088.00 cm^{-1}, may be compared directly with those obtained from the equilibrium structure, namely A = 4.726 cm^{-1} and ν = 4081.14 cm^{-1}. One can see that vibrational averaging results in a reduction in the red-shift of the HF stretching vibration (compared to that for the equilibrium structure) by 6.86 cm^{-1}. Similarly the <A"> rotational constant is increased by 0.176 cm^{-1} as a result of vibrational averaging. It is interesting to note that the measured change in A upon vibrational excitation (ΔA = -0.06 cm^{-1}) is approximately 1/3 of the change calculated, (between the equilibrium and zero-point structures) using this one dimensional (1D) model for the vibrational averaging. Thus it is reasonable to suggest that the source of the ΔA is the change in the bending potential upon vibrational excitation, as discussed above. Similarly,

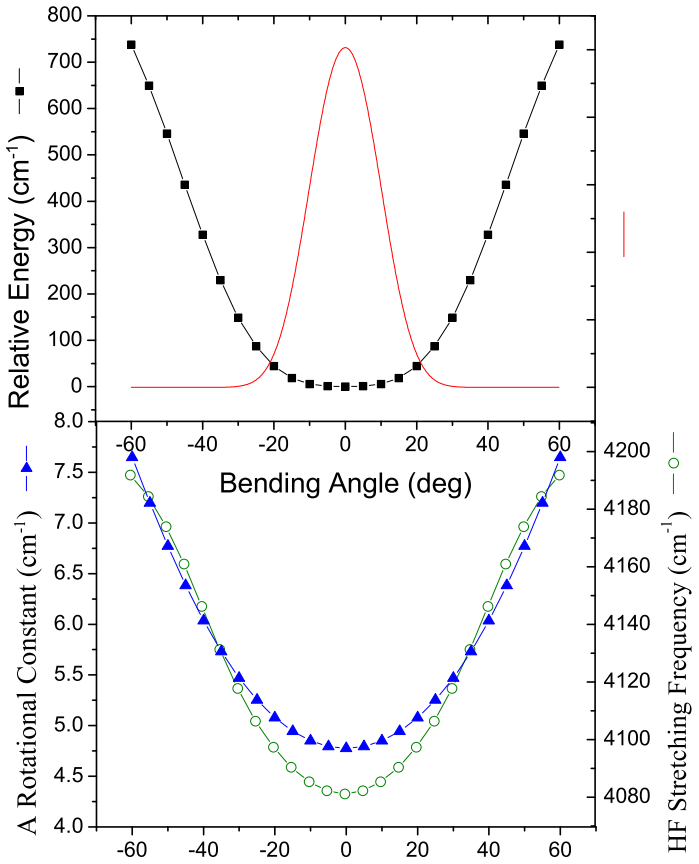

Figure 7.8: Bending potential associated with the ($\angle$H'C–F - 90^0) angle (H' denotes one hydrogen atom of CH_3) of the CH_3-HF molecular complex. In addition the vibrational dependence of the A rotational constant and HF stretching frequency are plotted. The wavefunction was calculated using the Numerov-Cooley method (Ψ^2 shown for reference) and was used to estimate the effects of vibrational averaging on the above molecular parameters.

the vibrational band origin shift is in the right direction for explaining the CD_3-HF isotopic shift, given that the latter complex is observed to have a vibrational frequency shift from the HF monomer that is approximately 10 cm^{-1} larger than that of the CH_3-HF complex. The heavier complex bends less and thus gives a larger red-shift. Although the agreement is not quantitative, it does provide at least some understanding of these large changes.

In an attempt to provide further insights into the changes in vibrational averaging upon vibrational excitation of HF in these systems, we also carried out 1D averages, by generating

ab initio 1D bending potential energy surfaces, holding the HF bond length frozen at either the ground or first excited state values. The ground state, vibrationally averaged HF bond length was obtained from a fully optimized calculation of the complex, while the first excited vibrationally averaged bond length was calculated from the elongation observed in the gas-phase for HF monomer. The vibrationally averaged $\langle\Delta A\rangle = \langle A'\rangle - \langle A''\rangle$ resulting from this 1D calculation is $\langle\Delta A\rangle$ = -0.006 cm^{-1}, which substantially underestimates that observed experimentally. This again suggests that such a simple model does not capture the essence of the problem. It is interesting to note, however, that this is the magnitude of the ΔA for the C_2H_2-HF and C_2H_2-HCN systems, indicating also that the ΔA in CH_3-HF is anomalously large.

As noted above, the HF bending mode may also be important in determining the vibrationally averaged structure. Therefore, additional one-dimensional vibrational averaging calculations were undertaken on this coordinate to estimate its effect on the A rotational constants. In contrast to the CH_3 bending mode, $\langle A''\rangle$ is found to be lowered from the equilibrium geometry, as expected from the interpretation of the acetylene-HF data, however ΔA is found to be of the correct sign when compared with experiment. Unfortunately the magnitude of ΔA is still predicted to be on the order of -0.003 cm^{-1}, which is much smaller than that observed experimentally.

The experimentally determined ground state dipole moment is in good agreement with the *ab initio* value, namely 2.54 D obtained at the MP2/aug-cc-pVTZ level of theory. In previous studies of open shell systems [290], we showed that the increase in the anisotropy of the bending potential upon vibrational excitation of the H-F stretching vibration also lead to a corresponding increase in the dipole moment. The large change in dipole moments for CH_3-HF and CD_3-HF upon vibrational excitation is attributed to this effect. We have also calculated the change in dipole moment upon vibrational excitation based upon our CH_3 and HF one-dimensional vibrational averaging models, namely $\langle\Delta\mu\rangle = \langle\mu'\rangle - \langle\mu''\rangle$ = 0.06 D, and find that it is much smaller than that observed experimentally, namely, 0.3(1) D for CD_3-HF. This

disagreement is not totally surprising as it likely stems from the model's underestimation of the anisotropy of the potential surface, which also predicts ΔA to be too small.

7.5 Conclusions

The CH_3-HF and CD_3-HF molecular complexes, corresponding to the exit channel complexes of the F + CH_4 (CD_3H) reaction have been stabilized in helium droplets. The infrared spectra indicate that the complexes have a hydrogen bonded, C_{3v} structure, in agreement with both *ab initio* theory and previous ESR studies [265]. The rotationally resolved spectrum provides detailed information concerning the intermolecular potential and vibrational dynamics. A sixfold difference is observed in the vibrational relaxation times for the H-F stretch excited states of the CH_3-HF and CD_3-HF complexes, which we attribute to a near resonance between the H-F and CH_3 vibrational modes, which is missing for H-F and CD_3, making relaxation in this latter complex much slower. This resonance could be facilitated by the ν_2 umbrella mode of CH_3, which may be coupled to the intermolecular coordinate. The intermolecular bending motion of the complex is also seen to have a significant effect on the vibrational frequency shift associated with the H-F stretch, which is qualitatively related to the substantial difference between the equilibrium and vibrationally averaged structures of this complex. These effects are clearly observed from the changes in the A rotational constants, dipole moments, and vibrational band origins with both vibrational excitation and isotope substitution. A one-dimensional model is presented, based on the intermolecular bending of the CH_3 and HF monomers in the complex, which gives only qualitative agreement with experiment. We conclude that quantitative agreement will only be possible with theoretical calculations that simultaneously include several degrees of freedom. Only in this way will it be possible to extract detailed information on the potential energy surface of this reactive system, in the corresponding reaction channel.

The twofold reduction of the experimentally measured B rotational constant, relative to the

ab initio value, is typical of what has been observed previously for many different molecules in helium, which all suggest that the effective moment of inertia of a helium solvated complex is larger than the gas-phase value, owing to the adiabatic following of the molecular rotational motion by some of the helium atoms. *Ab initio* calculations indicate that the binding energy of the complex is less than 2 kcal mol^{-1}, relative to the separated CH_3 and HF products.

Future experiments on this system will include the measurement of the asymmetric C-H stretch on the methyl sub-unit. The associated perpendicular band will provide accurate values for the ground and excited state A rotational constants. These studies will provide detailed information for comparison with future multi-dimensional dynamics calculations. When taken together, these will in turn provide detailed information on the potential energy surface in the exit channel of the F + CH_4 reaction.

Chapter 8

The CH_3- HCN Molecular Complex

In the previous chapter we found that the complex between a methyl radical and a HF molecule exhibits several unusual properties, including a strong vibration-vibration resonance which acts to depopulate the HF stretch excited state. The dark states which are important in this coupling were postulated to have asymmetric and symmetric CH stretching vibration character, or possibly a combination band of CH stretch plus umbrella bend. Dueteration of the methyl was found to quench the coupling (resulting in narrow linewidths for the CD_3-HF complex) in agreement with our hypothesis. In this chapter we further explore this phenomenon by changing the infrared chromophore, namely by replacing HF with HCN, which may also act to influence the V-V resonance. As we shall see, the CH_3-HCN complex is quite interesting in its own right, and also helps lend further insight into the vibrational averaging dynamics observed for CH_3-HF.

8.1 Introduction

The studies of CN radical reactions with hydrogen and hydrocarbons have generated substantial interest over the years, because of their importance in atmospheric reactions of other planets [30, 291], their role in combustion [27, 292–294], as well as the basic interest in understanding the dynamics of reactions between polyatomic molecules [295–298]. It has also been postulated that the long range forces in the entrance channel are responsible for "complex" formation, which lead to observed negative temperature dependences of the reaction rates for CN radicals with secondary and tertiary C-H bonds [15, 297, 299]. Indeed, CN radical reactions span a wide range of reactivity, with barriers predicted for reactions with H_2 [297, 300], HCN [301], and CH_4 [296], whereas the reaction of CN with C_2H_6 [302, 303] and larger saturated and unsaturated hydrocarbons appear to be barrierless [304]. In all of these reactions it has been observed that most of the reaction exothermicity is channeled into vibrational excitation of the HCN product [295, 305]. The CN radical is often viewed as a pseudo halogen atom, which has led to investigations of the similarities of these two classes of reactions, particularly focusing on whether or not the CN radical can be treated as a spectator to the reaction.

The reaction of interest for the current chapter is between CN and CH_4, which can proceed via a number of abstraction channels with the CN + CH_4 $\rightarrow$ HCN + CH_3 channel being the most exothermic (-20.40 kcal mol^{-1} at 0 K [242]). Reaction kinetics studies [296–298, 305–307] showed that rate constant increases monotonically with temperature and can well be described with the modified Arrhenius equation k(CN + CH_4) = 5.11 $\times$ 10^{-17} T$^{1.84}$ e$^{-332/T}$ in the T $\in$183 - 1500 K temperature range [308]. Indeed the curvature in the experimental Arrhenius plot suggests that a small barrier exists along the reaction coordinate [309]. This is in agreement with the *ab initio* calculations of Shreedhara Rao and Chandra [304] (performed at the MP2(full)/6-31G**//UHF/6-31G** level) which also pointed out the formation of a very weak pre-reactive CH_4-CN complex. Furthermore their calculations predicted that the transition state has a linear CH_3–H–CN geometry and is located early in the entrance channel portion on the potential energy surface (PES). Bethardy *et al.* [295] investigated the dynamics of the reaction by probing

the HCN and CH_3 reaction products by time-resolved infrared absorption spectroscopy and found that only about 20% of the HCN products were initially produced in the HCN(ν_1, ν_2 = 0, ν_3) vibrational levels with ν_1 and ν_3 = 0, 1, 2, while the rest must contain significant bend excitation, most likely in combination with the stretching modes. Such high degree of bending excitation is somewhat surprising in view of the linear transition state geometry predicted by the earlier *ab initio* calculations. The CH_3 radicals on the other hand were found to be produced predominantly in the ground state. Interestingly Bethardy *et al*. [295] did not observe significant correlation between CN(ν) reagent and HCN(ν_1, ν_2 = 0, ν_3) product vibrational level distributions which is indicative of the non-adiabaticity in the CN vibrational motion. This is in contrast with the conclusion that the CN is a spectator as derived from the rate constant measurements [310, 311] which showed similar values for the reaction of CN(v = 1) and CN(v = 0) with CH_4. This spectator hypothesis was also supported by *ab initio* calculations [296] of the CN vibrational frequency along the reaction coordinate as the system evolves from reagents toward the products. Thus it is still not clear how appropriate it is to treat CN as a spectator in the reaction of CN radicals with methane.

While the above mentioned results provide information on the overall picture about the reagents and products, the detailed knowledge about other stationary points such as the pre-reaction CH_4-CN, post-reaction CH_3-HCN complexes, and other possible insertion products along the PES, remains scarce due to the inherent difficulties associated with stabilizing such short lived and weakly bound species.

8.2 Computational details

Previous theoretical calculations [296, 304, 312–314] on the reaction between CN radicals and methane (CH_4) have revealed many of the important stationary points on the corresponding potential energy surface. The energies of the reactants and products, along with some of the transition states and pre and post reactive complexes have appeared in the literature previously,

albeit with different levels of theory. We present here a common set (at the MP2/6-311++G(d,p) level) of calculations for the relevant stationary points leading to the HCN and CH_3 products. For the CH_3-HCN complex we present calculations at the UMP2/6-311++G(d,p) and UMP2/aug-cc-pVTZ levels which focus on the molecular parameters, including vibrational frequencies, rotational constants, and dipole moments which are then compared with our experimental results. *Ab initio* calculations were performed using the GAUSSIAN 03 software package [194]. The effects of vibrational averaging on the observed molecular parameters were also estimated at the UMP2/aug-cc-pVTZ level of theory using numerical integration of the wide amplitude bending wavefunctions found for both CH_3 and HCN subgroups.

8.3 Experimental

Given our previous characterization of the CH_3-HF complex [315], the search for CH_3-HCN was straightforward. In practice, the pyrolysis source was optimized on CH_3-HF signal and then the HF was removed and replaced with HCN. Pendular survey scans were then performed in the region predicted by appropriately scaled *ab initio* calculations. Only a single peak at 3265.70 cm^{-1} was found in the region predicted by scaled *ab initio* calculations, which we assign to the CH_3-HCN complex. As in the case of the CH_3-HF molecular complex, several checks were performed in order to conclusively determine the identity of the new spectral features, including pyrolysis temperature and pressure dependencies. Identical spectra were obtained, although with differing signal to noise ratios, with the DTBP, azomethane, and CH_3I precursors.

The vibrational band origin shift for CH_3-HCN (from HCN monomer in helium) is measured to be -45.51 cm^{-1}, in excellent agreement with the *ab initio* calculations of Solimannejad and Alikhani [314], at the UCCSD(T)/6-311++G(2d,2p) level (-48 cm^{-1}). The calculated frequency shift at the UMP2/6-311++G(2d,2p) level is -38 cm^{-1} [314], compared to the UMP2/6-311++G(d,p) result of -23 cm^{-1} presented below. It is apparent that even in this relatively small

system, large basis sets with high levels of electron correlation are needed to quantitatively reproduce the frequency shift. Nevertheless, such a large frequency shift is in agreement with the hydrogen bonded structure predicted by theory.

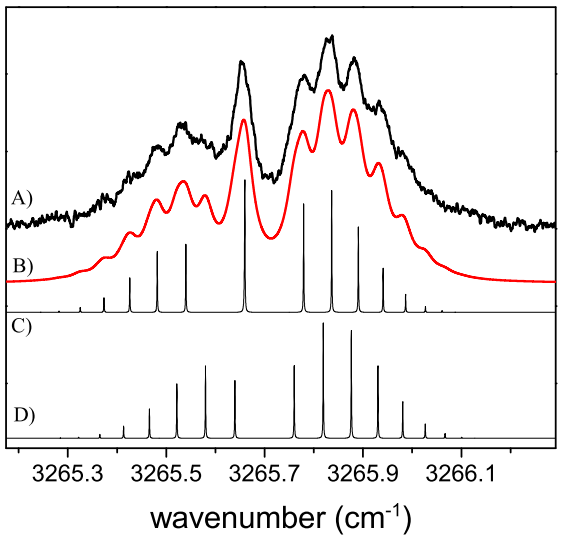

Figure 8.1: Electric field-free infrared spectrum (A) of the rotationally resolved H-CN stretch of the CH_3-HCN molecular complex in helium nanodroplets. The calculated spectra (B, C (|K| = 1 band only), and D (K = 0 band only)) are the result of a simulation employing a prolate symmetric top Hamiltonian at a temperature of 0.37 K and incorporating the appropriate symmetry. The |K| = 1 states (C) cannot cool to K = 0 (D) states, giving rise to the intense Q-branch, and are shown separately in the figure for clarity. The inertial parameters derived from the simulation are shown in Table 8.1.

Figure 8.1(A) shows the observed electric field-free spectrum for the peak assigned to the CH_3-HCN complex. *Ab initio* calculations predict that the CH_3-HCN complex has C_{3v} symmetry with the hydrogen atom of HCN pointing towards the carbon atom of the methyl radical at a distance of 2.55 Å (at the UMP2/6-311++G(d,p) level). Simulated spectra, based on a prolate symmetric top Hamiltonian are shown in Figure 8.1(B, C (|K| = 1 band only), and D (K = 0 band only)). The rotational temperature was fixed at 0.37 K in accord with the temperature of the droplets [56]. The selection rules and symmetry properties (nuclear spin statistics) for this band are the same as those already detailed for CH_3-HF, and thus will not be repeated here.

Constant	Helium droplet	MP2/6-311++G(d,p)	MP2/aug-cc-pVTZ
ν_0 (cm^{-1})	3265.70(1)	3459.81	3425.56
A" (cm^{-1})	4.74275*	4.785	4.825
ΔA(A'-A") (cm^{-1})	-0.040(5)	-	-
B (cm^{-1})	0.030(2)	0.086	0.093
D_J (cm^{-1})	$3.6(5) \times 10^{-5}$	-	-
μ" (D)	3.1(2)	3.42	3.53
$\Delta\mu$ (D)	0.2(1)	-	-
HCN molecule			
ν_0 (cm^{-1})	3311.21	3482.96	3466.57
μ" (D)	2.985*	3.00	3.02
$\Delta\mu$ (D)	0.032*	-	-

Table 8.1: A summary of the experimental and calculated molecular constants for the CH_3-HCN complex. The corresponding data for the HCN monomer are also provided for comparison. Values marked with an asterisk are taken from the gas-phase, while those in parentheses are one estimated standard deviation.

Table 8.1 contains the parameters used to simulate the field-free spectrum. Similar to that found for CH_3-HF (ΔA = -0.07 cm^{-1}), a significant change in the A rotational constant, ΔA = -0.04 cm^{-1}, is observed upon vibrational excitation of the H-CN stretch of the CH_3-HCN molecular complex. As argued in the CH_3-HF case, this is likely a result of the wide amplitude bending motions of the complex, and will be discussed below. The B rotational constant used in the simulation, B = 0.030 cm^{-1}, is found to be reduced from the *ab initio* value by a factor of 2.9, which accounts for the effects of the helium, in good agreement with previous studies on systems of this size [316]. The fit to the spectrum was performed using a 0.04 cm^{-1} Lorentzian linewidth for all of the transitions in both the K = 0 and |K| = 1 bands.

Stark spectra, shown in Figure 8.2(A), recorded at an electric field strength of 6.122 kV cm^{-1}, were used to determine the dipole moment of the complex. Since K is still a good quantum number in the field, the nuclear spin statistics also rigorously hold. The Stark spectrum clearly shows the effects of the change in A rotational constant upon vibrational excitation, most notably the two Q branch peaks arising from the K = 0 and |K| = 1 bands, which are separated by ΔA. For the fitted Stark spectrum shown in Figure 8.2(B), all molecular parameters determined from the electric field-free fit were held fixed, so that only the dipole moment

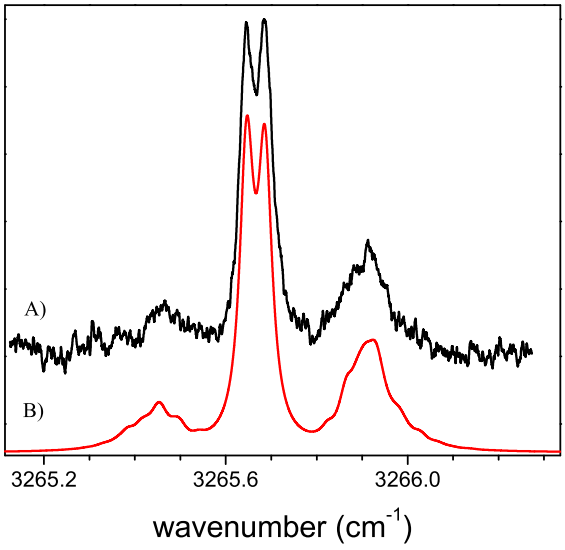

Figure 8.2: The experimental (A) and calculated (B) Stark spectra of the H-CN stretch of the CH_3-HCN molecular complex in helium nanodroplets. The calculated spectrum includes the effects of a 6.122 kV cm^{-1} applied electric field and the appropriate nuclear spin symmetry. The ground and excited dipole moments of 3.1 and 3.3 D were derived from the simulation.

and were used as adjustable parameters. In this manner the ground and excited state dipole moments of the CH_3-HCN complex are determined to be 3.1(2) and 3.3(2) Debye respectively.

In the previous chapter on the CH_3-HF complex [315] we observed that the rotational linewidth was quite broad, leading us to hypothesize that fast vibration-vibration energy transfer resulting from the near resonant coupling of the HF stretch to the modes of CH_3 was taking place. This vibrational resonance was confirmed by deuterium substitution of the methyl radical, which broke the resonance, resulting in much narrower lines. In that work it was proposed that the HF stretch coupled directly to the CH stretches of the methyl, or to a combination band of CH stretch plus one quantum of the umbrella mode. The importance of the umbrella mode was postulated because of the slight distortion of the CH_3 away from planarity due to complexation, and due to its predicted near resonance. The observation of CH_3-HCN now allows us to further explore this resonance phenomenon.

The energy level diagram for CH_3 and CD_3 monomers are shown in Figure 8.3, along with

the experimentally determined vibrational frequencies for the H-F and H-CN stretching vibrations for their respective complexes with CH_3. One can see that while excitation of the H-F

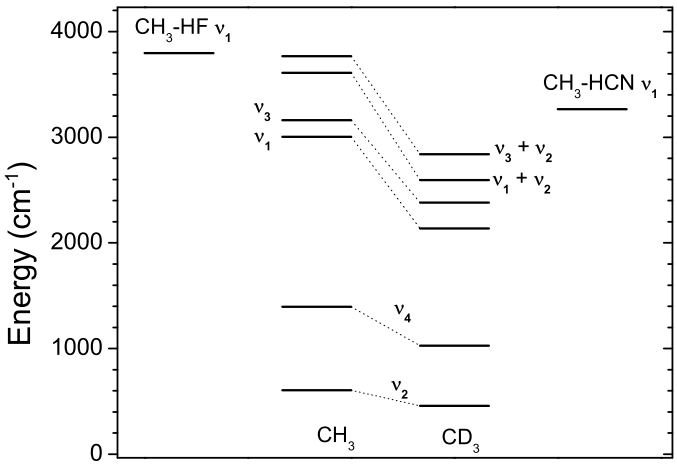

Figure 8.3: An energy level diagram showing the relative energies of the monomer fragments to the H-CN and H-F vibrationally excited states of the CH_3-HCN (CD_3-HCN) and CH_3-HF (CD_3-HF) complexes. The lower vibrational frequency of HCN compared to HF is found to quench much of the vibration-vibration resonance found in the CH_3-HF complex. The effect of dueteration of the methyl radical in the CH_3-HCN complex is found to increase the vibrationally excited state lifetime, just as observed in the HF case, however the effect is somewhat smaller.

stretch of the CH_3-HF complex can couple directly to combination bands, these excitations are not energetically available in the case of CH_3-HCN. However, the lower vibrational frequency of HCN compared to HF is much closer to the CH stretching vibrations of the methyl radical (CH_3) monomer, possibly facilitating a coupling to these vibrational modes. By comparing the linewidths observed for the HF and HCN complexes with CH_3 we find that the lifetime of the HCN complex is approximately four times longer than that with HF. This evidence supports the hypothesis that the coupling to the combination mode is indeed dominant in the CH_3-HF complex. The linewidths observed for the CH_3-HCN spectrum are comparable to other spectra measured in helium droplets, therefore it was not initially clear if a vibrational resonance was occurring in this case. Interestingly, the effect of dueteration on the methyl radical, is to lower

the combination band frequencies below that of the CH_3–H-CN stretching frequency, and that could possibly enhance any vibrational resonance.

To explore the effects of dueteration on the vibrational dynamics, further experiments were undertaken to observe the CD_3-HCN complex. Figure 8.4A shows the field-free spectrum

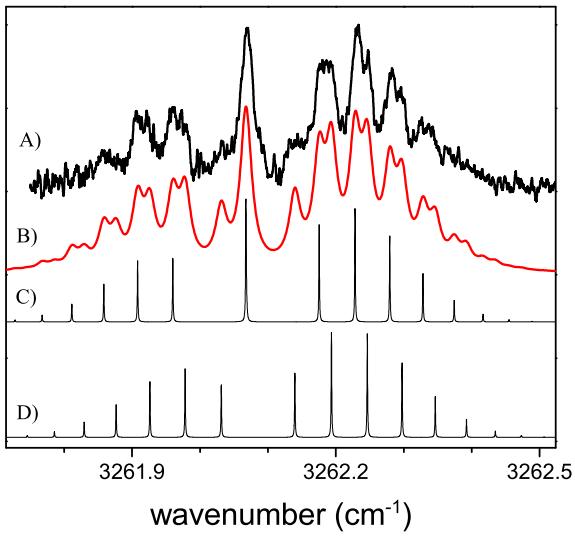

Figure 8.4: The electric field-free spectrum (A) of CD_3-HCN in helium droplets. The linewidths observed in this spectrum are smaller than those in the CH_3-HCN complex indicating the presence of a vibration-vibration resonance in the latter. Molecular constants derived from a fit to the spectrum (B) are shown in Table 8.2. The fit includes the 11:8 nuclear spin statistics for C_{3v} symmetry. The K = 0 (D) and |K| = 1 (C) bands are shown separately to illustrate the effect of the symmetry.

whereas Figure 8.5A shows the corresponding Stark spectrum recorded at an electric field strength of 6.122 kV cm^{-1}. The fits assume C_{3v} symmetry as before, but included the 11:8 nuclear spin statistics appropriate for deuterium atoms. The resulting molecular parameters from the fits to the spectra (Figures 8.4B and 8.5B) are listed in Table 8.2. The linewidth used in the simulations is 0.02 cm^{-1}, reduced from that of CH_3-HCN by a factor of two. Clearly the effect of dueteration is to enhance the vibrational lifetime compared to CH_3-HCN, indicating that a vibrational resonance is indeed occurring, most likely with the asymmetric or symmetric C-H stretching vibrations of the methyl radical. Note that the combination bands do not directly

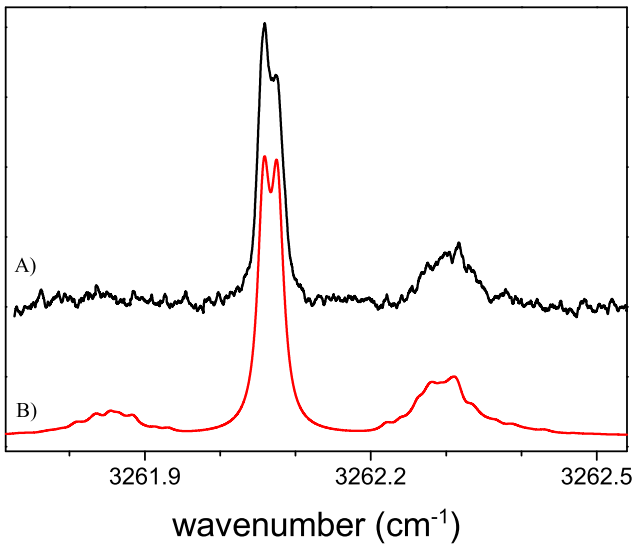

Figure 8.5: A Stark spectrum (A) of CD_3-HCN, recorded at an electric field of 6.122 kV cm^{-1}. The fit (B) was obtained by holding fixed all of the molecular constants determined from the zero-field spectrum, leaving μ and $\Delta\mu$ as the only adjustable parameters. A dipole moment of 3.1 D is derived from the fit.

Constant	Helium droplet
ν_0 (cm^{-1})	3262.09(1)
ΔA (A'-A") (cm^{-1})	-0.018(2)
B (cm^{-1})	0.027(2)
D_J (cm^{-1})	$2.6(5) \times 10^{-5}$
μ" (D)	3.1(2)
$\Delta\mu$ (D)	0.2(1)

Table 8.2: A summary of the experimentally determined molecular constants for the CD_3-HCN complex.

represent an intermediate state in which to facilitate relaxation, however we cannot rule out a coupling with the ν_4 bending fundamental alone. This would be rather unlikely however due to the large energy mismatch. Perhaps using careful selection of the chromophore, and partial dueteration of the methyl radical one could more accurately tune the V-V resonance to further explore these dynamical effects. Furthermore these effects could possibly be explored using time resolved pump-probe methods.

The vibrational band origin of CD_3-HCN is significantly red-shifted from that of CH_3-HCN, namely by -3.61(1) cm^{-1}, although not as dramatically as the corresponding shift observed for CH_3-HF of -9.88 cm^{-1}. This large isotopic shift is the result of a significant change in the vibrational averaging dynamics upon dueteration. In agreement with that found for CD_3-HF, the ΔA of CD_3-HCN is found to be -0.018 cm^{-1}, nearly a factor of two times smaller than that of CH_3-HCN, which is due to the direct mass effect of the substitution.

A direct comparison can be made of the molecular parameters for CH_3-HCN and CD_3-HCN, due to the high-resolution observed in both cases. The measured B rotational constant (B = 0.027 cm^{-1}) is found to be reduced by a factor of 1.11 upon deuterium substitution, in good agreement with the *ab initio* ratio of 1.125. The dipole moments of the two complexes are measured to be the same, within the experimental uncertainty.

8.4 Discussion

Figure 8.6 summarizes the various stationary points on the potential energy surface for the CN + CH_4 reaction, calculated at the UMP2/6-311++G(d,p) level of theory. In order to obtain geometry convergence for some of the stationary points, it was necessary that the full Hessian matrix be constructed at each optimization point. Tight convergence criteria were employed in all of the optimizations to ensure that the local minima and transition states had exactly zero or one imaginary frequency, respectively.

In agreement with previous experimental and theoretical studies we found that the reaction is highly exothermic, exhibiting only a small barrier to reaction. The overall exothermicity is predicted, at the UMP2/6-311++G(d,p) level, to be -39.38 kcal mol^{-1}. Compared to the experimentally determined value of -20.40 kcal mol^{-1} [242] we see that our calculations significantly overestimate this quantity. This trend has been previously reported for other CN radical reactions and most likely stems from the large degree of spin contamination in CN at the UMP2 level [317]. The predicted bond lengths, angles, vibrational frequencies and dipole moments

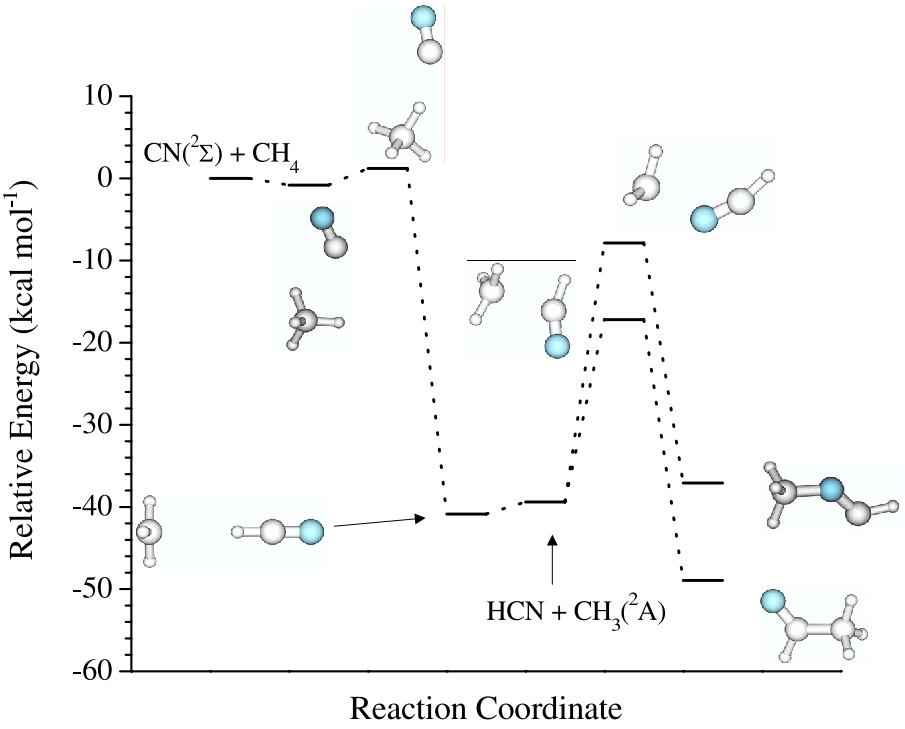

Figure 8.6: A relative energy profile based on computed energies and optimized geometries (also shown) of reagents, intermediate molecular complexes, transition states and products of the hydrogen abstraction reaction of CN radical with CH_4. The energies and geometries are calculated at the UMP2/6-311++G(d,p) level of theory.

however are still found to be quite accurate. The reaction of CN and CH_4 proceeds through the entrance channel of the potential exhibiting a weakly bound complex between the CN radical and a methane molecule. The binding energy of this complex is predicted to be less than 1 kcal mol^{-1} with respect to the reactants. The optimized geometry of the complex is found to have C_1 symmetry with the carbon atom (of CN) pointing towards a tetrahedral face of CH_4 at a carbon-carbon distance of 3.24 Å. The barrier to the hydrogen abstraction reaction is predicted to lie 1.20 kcal mol^{-1} above the separated reactants. In the transition state geometry, the carbon atom of CN has moved to interact with a single C-H bond of methane. The distance between the abstracted hydrogen and the carbon atom of CN is 1.826 Å, in agreement with that found previously [304]. Interestingly, the transition state geometry at the UMP2/6-311++G(d,p) level is not linear in the NC–H–CH_3 moiety, in contrast to calculations at the UHF/6-31G(d,p) [304] level. The angles of the N-C–H and C–H–C parts are predicted to be 155 and 157 degrees re-

spectively, which could rationalize the high degree of bending excitation of the HCN products measured experimentally [295]. The harmonic frequency for the reaction coordinate is calculated to be 266*i* cm^{-1}. The lowest frequency bending vibrations which are orthogonal to the reaction coordinate are calculated to be 17 and 42 cm^{-1} indicating a somewhat loose transition state.

Our experimental investigation of this reactive potential starts with the exit channel valley, corresponding to the HCN and CH_3 products. As noted above, the products of the reaction are predicted to lie 39.38 kcal mol^{-1} lower than the reactants. The complex between HCN and a methyl radical is predicted to be bound by 1.47 kcal mol^{-1} with respect to the separated products and is found to have a hydrogen bonded C_{3v} geometry. Our binding energy is also in very good agreement with that calculated at the UCCSD(T)/6-311++G(2d,2p) and ROMP2/6-311++G(2d,2p) (~1.27 kcal mol^{-1}) levels, which are corrected for the effects of basis set superposition error [314].

In addition to the formation of a weakly bound CH_3-HCN van der Waals complex, two insertion products are also calculated to be stable, open shell intermediates, with the methyl covalently binding to either the nitrogen or carbon atom of HCN. Interestingly the side on attack of the methyl radical at the carbon atom (of HCN) appears to be more reactive than at the nitrogen end, based on the calculated energetics. Given the large barriers associated with all three possible reactions however, the weakly bound complex should be the only product formed in our helium nanodroplet studies. Indeed, no evidence was found for other complexes being formed in our experiment. Nevertheless, these other reactive intermediates could still play a role when starting with the CN and CH_4 reactants.

The experimental results presented here definitively prove that the equilibrium structure for the CH_3-HCN complex has C_{3v} symmetry. Nevertheless, the wide amplitude intermolecular bending and stretching motions are likely to strongly affect the observed properties due to vibrational averaging. The large changes in the A rotational constants and dipole moments upon vibrational excitation of the H-CN stretch, along with the isotopic dependence of the

vibrational origin are likely the result of this vibrational averaging. Indeed, the calculated harmonic frequencies for the methyl and HCN bending vibrations in the complex are 136 and 65 cm^{-1} at the UMP2/aug-cc-pVTZ level respectively, revealing its quite floppy behavior. Since the vibrational averaging is a sensitive probe of the surrounding potential, it can provide important clues on the nature of the potential energy surface in the exit channel of this reaction.

8.4.1 Vibrational averaging

Our previous work on the CH_3-HF system illustrated that the two lowest frequency bending vibrations (CH_3 and HF bending) are most likely responsible for the observed changes in the A rotational constants, dipole moments and isotopic dependence of the vibrational band origin in that case [315]. Because of the similarity between the observed properties for CH_3-HF and CH_3-HCN, it is reasonable to assume that these low frequency vibrations are also responsible in the CH_3-HCN case. In an analogous manner to that performed in our investigation of CH_3-HF, the effects of vibrational averaging on the observed properties of CH_3-HCN were estimated by averaging the properties over one-dimensional bending wavefunctions obtained numerically by the Numerov-Cooley method [176].

To calculate the effect of bending on the A rotational constants in both the ground and excited vibrational states of HCN, four different one dimensional bending potentials were calculated at the UMP2/aug-cc-pVTZ level. For the HCN bending potential, the HCN was fixed in a geometry corresponding to the either the v = 0 or v = 1 vibrational level (taken from gas-phase rotational constants) and rotated about its center of mass in increments of five degrees. All other geometric parameters (other than the C-H bond length of HCN, which was elongated in the v = 1 geometry to simulate the effect of vibrational excitation) were constrained to their equilibrium values found for the complex. The gas-phase rotational constants of HCN (in v = 0 and v = 1) were used as estimates of the reduced mass in each case. The bending potential corresponding to HCN in its ground vibrational state is shown in Figure 8.7, along with the calculated wavefunction (Ψ^2 shown) and the resulting dependence of the A rotational constant

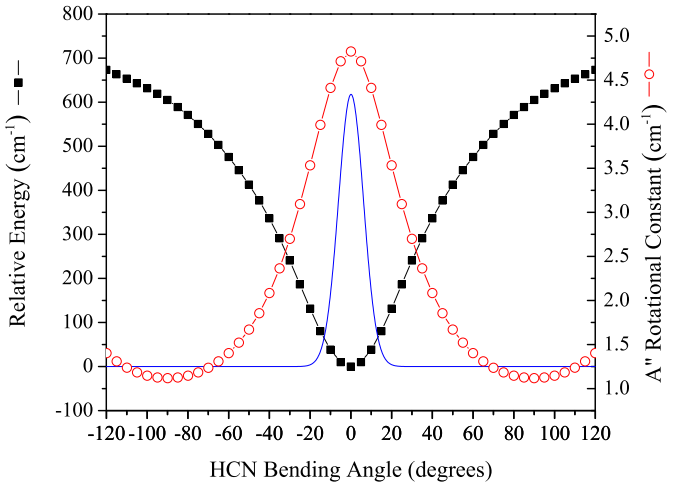

Figure 8.7: Bending potential associated with the (H'C-C - 90^0) angle (H' denotes one hydrogen atom of CH_3) of the CH_3-HCN molecular complex. The wavefunction was calculated using the Numerov-Cooley method [ψ^2 shown for reference] and was used to estimate the effects of vibrational averaging on the A rotational constants.

on bending angle. The expectation value for A" is given by:

$$< A >= \frac{\int_0^\pi \Psi A \Psi sin\theta \partial\theta}{\int_0^\pi \Psi \Psi sin\theta \partial\theta}$$

yielding 4.509 cm^{-1}, reduced from the equilibrium value of 4.825 cm^{-1}. A similar treatment for the vibrationally excited state yields <A'> = 4.498 cm^{-1} or a ΔA of -0.011 cm^{-1}.

Additional one dimensional potentials were calculated to estimate the effects of the CH_3 bending within the complex. In this calculation the angle defined as (H'C–C) where H' denotes one of the hydrogens of CH_3, was varied while constraining the rest of the complex. The methyl radical was assumed to remain planar during this bending motion and its gas-phase B rotational constant was used as an estimate of its reduced mass. This bending motion is observed to raise <A"> compared to the equilibrium structure, an opposite trend to that calculated for the HCN bending motion. However, the value of ΔA is of the same sign when compared with the HCN bending effect, but its magnitude is much smaller (ΔA = -0.002 cm^{-1}).

Comparison of the calculated change in A due to both of the bending motions with the

experimentally determined value of ΔA = -0.04 cm^{-1} shows qualitative agreement, while the calculations further emphasize that the effects of the HCN bending coordinate should be dominant. Nevertheless it is clear that the ΔA is rather large in both the HF and HCN systems, and thus a more fully dimensional analysis will be needed to in order to make quantitative predictions about the anisotropy of this region of the potential energy surface.

8.5 Conclusions

The CH_3-HF and CH_3-HCN complexes detailed in the last two chapters serve as prototypical models for hydrogen abstraction reactions. Despite their fundamental nature, a complete knowledge of the ensuing reaction dynamics is still lacking. While it is clear that most (~60% [318]) of the available energy is channeled into H-F (H-CN) vibration, relatively little (< 10%) population has been observed in the CH_3 umbrella mode despite methyl's change from pyramidal to planar geometry along the reaction coordinate. Recently K. Liu *et al.* have reported direct observation of excitation of the ν_1 vibration of CH_3 (symmetric C-H stretch) only when the reaction is conducted near threshold, however due to uncertainties in the relative intensities of their 2+1 REMPI experiments, the branching ratios could not be determined [253]. The authors attribute this observation to a reactive resonance, which we believe also manifests itself as a V-V coupling in our experiment. By changing the relative energetics of the resonant states (by dueteration and by changing the chromophore) we attributed the short lifetime of CH_3-HF to a significant coupling to the combination band of the C-H stretches and the umbrella mode of the methyl, not just a coupling with the C-H stretches alone. It would therefore be interesting to search for these product states in the crossed molecular beam experiments. Nevertheless, this result emphasizes the fact that the exit channel region of the potential can have a significant influence on the ensuing reaction dynamics.

Chapter 9

IR-IR Double Resonance Spectroscopy of Cyanoacetylene

Anticipating that a two laser experiment will be necessary to explore the photo-induced dynamics of the entrance and exit channel complexes detailed in previous chapters, this chapter serves to illustrate the double resonance technique in helium droplets. While cyanoacetylene monomer is not one that is immediately thought of being related to work described thus far, it does serve as a benchmark system to explore these two laser experiments where we know that no chemical (or isomerization) reactions can take place upon vibrational excitation. As it turns out, these experiments also serve as a sensitive probe of the vibrational relaxation dynamics in helium given that HCCCN is well characterized in both the gas-phase [319] and in helium [79,199]. The technique described here allows us to burn a hole in the inhomogeneously broadened transitions of cyanoacetylene and we find that the distribution of droplet sizes in the beam is a significant source of broadening. Although the source of the remaining broadening in the double resonance experiments cannot be assigned conclusively, the data is consistent with a broadening mechanism resulting from the coupling of the rotations and vibrations of the molecule to the elementary excitations of the helium.

9.1 Introduction

Despite the growing number of studies of molecules and clusters in helium, the spectra of which show a wide range of line shapes, a detailed understanding of the associated broadening mechanisms is still lacking [74]. This is in part due to the fact that there are a number of homogeneous and inhomogeneous broadening sources that typically have comparable contributions to the overall linewidth [94]. Some progress has been made in separating these contributions by making use of microwave-microwave [320] and infrared-microwave [79,321,322] double resonance spectroscopies, although even here the results are not conclusive. New experimental and theoretical approaches are therefore still needed if we are to develop a detailed understanding of the associated processes.

9.2 Experimental

Since the experimental apparatus was modified to perform two laser experiments, a brief description of the changes will be presented here. A schematic of the experiment is shown in Figure 9.1. After formation of the helium droplet beam, a 3.5 cm long gas pick-up cell is used to dope the droplets with cyanoacetylene, which is maintained at a pressure that is optimized so that the droplets on average capture a single molecule. The captured molecules are then cooled to the internal temperature of the helium droplet, (0.37 K). As shown in the figure, two spherical mirror multi-pass cells [323] are used to focus multiple passes of the infrared lasers onto the droplet beam. The two laser interaction regions (pump / probe) are separated by approximately 8 cm, corresponding to a droplet flight time of approximately 175 μs. The probe laser (the downstream multi-pass cell) is the cw F-center laser, whereas the pump laser (the upstream multi-pass cell) is the Linos PPLN-OPO.

Each spherical multipass cell is equipped with independent Stark electrodes, which for the current experiments are used to apply a large, static DC electric field (~ 30 kV cm^{-1}) to the laser interaction region. As pointed out in section 3.3.1, for a polar molecule like cyanoacetylene, the

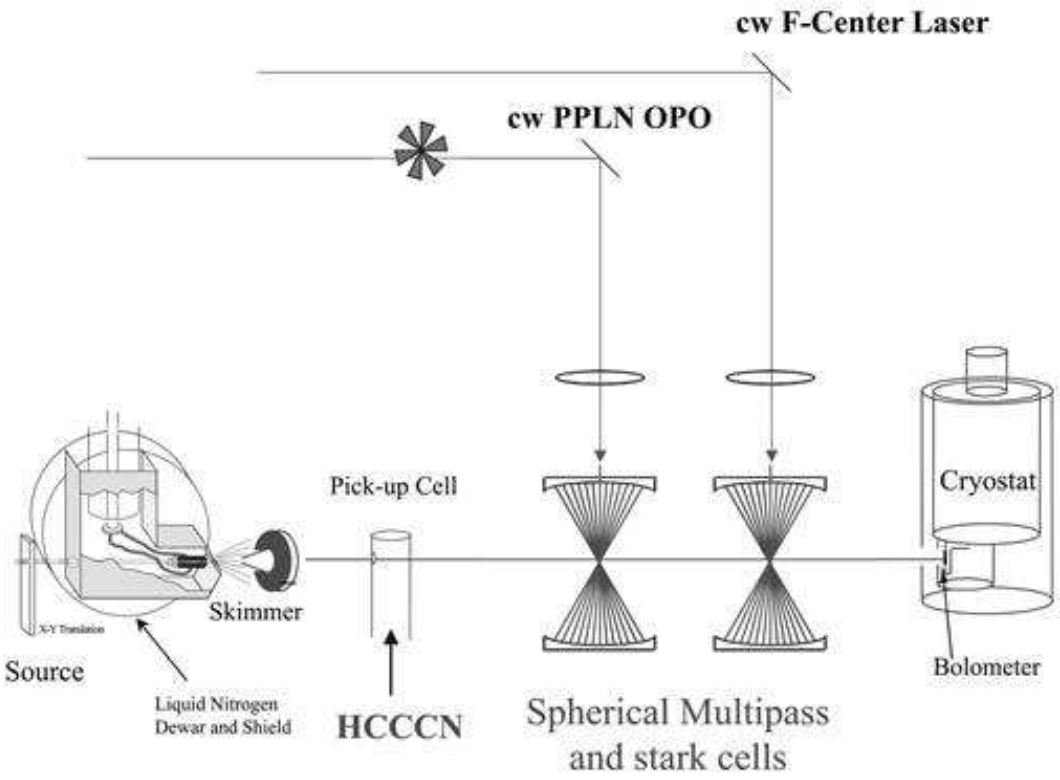

Figure 9.1: A schematic of the helium droplet apparatus modified for double resonance experiments. Two spherical multi-pass cells were used to separate the pump and probe laser interaction regions by 8 cm. Both multi-pass cells were equipped with Stark plates so that a large DC field could be applied to each laser interaction region. The fields in both interaction regions were determined to be the same, within $\pm$ 1kV cm^{-1}.

resulting pendular spectrum [129, 130, 199] is characteristic of the orientation of the permanent dipole moment with the DC field. With the laser polarization aligned parallel to the applied field the entire P and R branch spectrum collapses into a single peak (owing to the fact that the rotational constants and dipole moments of cyanoacetylene are rather similar in the ground and excited vibrational states).

Assuming the time required for vibrational relaxation of cyanoacetylene in helium is short compared to the flight time between the pump and probe laser interaction regions (this assumption is confirmed by the present experiment), the molecules excited by the pump laser will be cooled back to the ground vibrational state prior to entering the probe laser multipass cell. The present experiments were performed by amplitude modulating the (fixed frequency) pump

laser (tuned into resonance with the pendular transition), while the cw probe laser was scanned through the same transition. The result is a double resonance spectrum that rides on top of the single resonance signal from the pump laser. The effect of this modulation scheme is to measure a difference spectrum, corresponding to the change in the infrared spectrum between the pump laser being on and off. The pump laser was locked to a 150 MHz confocal etalon to prevent frequency drift.

9.3 HCCCN single-resonance results

The zero-field spectrum of the ν_1 fundamental of cyanoacetylene (HCCCN) in helium droplets has been described in detail previously [79] and is well represented by a linear rotor spectrum. This is in agreement with the general observation that the symmetry of the molecule is unaffected by helium solvation [35, 57, 74]. On the other hand, the anisotropy associated with the He-HCCCN interaction potential [324] results in an increase in the effective moment of inertia of the solvated molecule, corresponding to a decrease in the rotational constant by a factor of approximately 3 relative to the gas-phase value [74].

In the present study we focus on the pendular spectra of HCCCN, shown in Figure 9.2, as a function of the mean droplet size (varied by changing the source temperature). The droplet sizes listed in the figure caption were obtained from the nozzle diameter, source temperature and stagnation pressure, using the results published previously by Knuth and coworkers [88]. For each pendular spectrum corresponding to each source condition, the pressure in the pick-up cell was optimized for the pick-up of one HCCCN molecule. It is clear from Figure 9.2 that the pendular transition shifts to the red and narrows with increasing droplet size. These results are quantified in Figure 9.3, which shows a plot of the peak frequencies and the FWHM linewidths as a function of the nozzle temperature. It is interesting to note that the tail to the blue side of the resonance shown in Figure 9.2, which becomes more prominent in the spectra corresponding to small mean droplet sizes, is quite common in helium droplet spectra, having

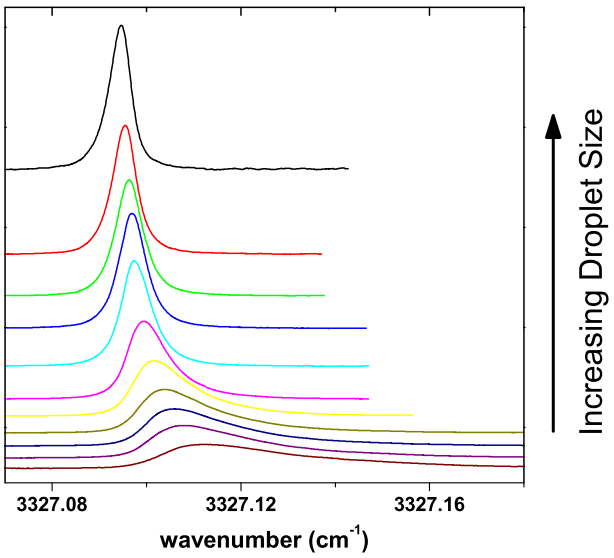

Figure 9.2: Droplet size dependence of the single resonance pendular spectrum of HCCCN in helium droplets, obtained with a 30 kV cm^{-1} electric field applied to the laser interaction region. The mean droplet sizes decrease from top to bottom, ($\overline{N}$ = 11570, 7200, 4610, 3730, 2480, 2050, 1700, 1400, 1200, 600). The helium backing pressure was fixed at 60 atm. and the nozzle temperature was varied from 16 K to 30 K.

been reported in previous infrared [57, 277] and visible [325] studies.

The vibrational frequency shift associated with helium solvation has been the subject of considerable discussion and is generally thought to be the result of two competing effects [74, 326, 327]. On the one hand, there are short-range repulsive interactions between the solute and the helium, which for the C-H stretch considered here, come from the helium atoms located near the hydrogen end of the molecule. The repulsive interactions with these helium atoms result in a blue-shift of the corresponding vibrational mode. In addition, the long-range attractive interactions between the surrounding helium atoms and the molecule, which become stronger upon excitation of the C-H stretching vibration, cause a red-shift. For example, the dipole-induced dipole attraction increases upon vibrational excitation, owing to the associated increase in the dipole moment of the molecule. As a result, the increasing red-shift with droplet size comes from the fact that the additional helium atoms are at long range and therefore only

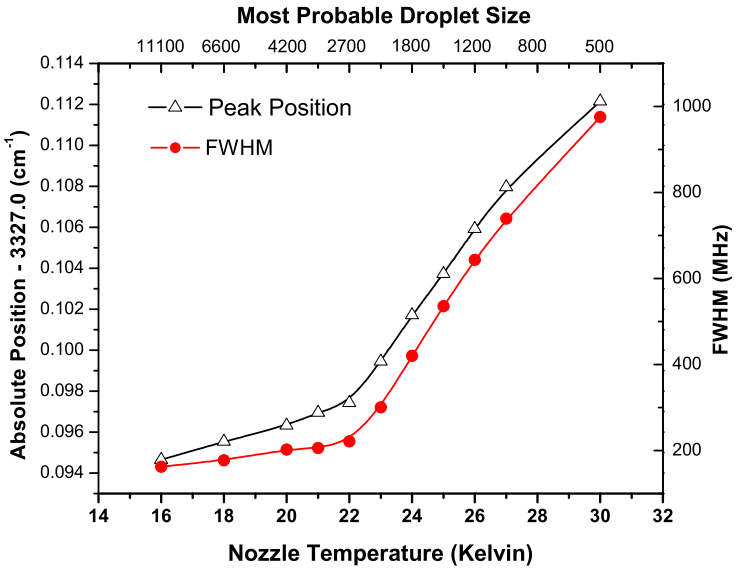

Figure 9.3: Peak frequency and Full Width at Half Maximum (FWHM) of the pendular transition (the ν_1 vibrational band of HCCCN), as a function of nozzle temperature. With increasing nozzle temperature the spectra shift to the blue and broaden.

contribute to the red-shift. The saturation of the vibrational frequency shift for the largest droplets reflects the fact that the added solvent is now too far from the molecule to have a significant influence on its vibrational frequency (corresponding to the bulk limit).

The above data suggest that the asymmetric line shapes observed in Figure 9.2 result from inhomogeneous broadening associated with the droplet size distribution. It is important to point out, however, that there are other mechanisms for inhomogeneous broadening in helium nanodroplets that have been previously discussed [57, 94, 325, 328]. For example, quantum confinement of the dopant molecule in the droplet results in particle-in-a-box type levels (in this case a spherical box) that are thermally populated even at the low temperatures considered here. The distribution over these "translational" states can therefore contribute to the inhomogeneous broadening. These states can also have orbital angular momenta, which can be coupled to the molecular rotation, through the anisotropic interaction between the dopant and the helium, resulting in additional line broadening. In a previous study, the observation of a splitting in the R(0) line of HCN in helium was attributed to this kind of solvent-solute interaction [329].

Additionally, the coupling of the molecular rotations to the thermally populated surface wave excitations (ripplons) [56] have been considered as probable broadening mechanisms [94]. In previous MW-MW and IR-MW double resonance experiments on HCCCN [79, 320], it was suggested that the molecule undergoes rapid transitions between the "particle-in-a-box" type substates, the associated time scale being similar to that of rotational relaxation. This inhomogeneous broadening mechanism is considered dynamic, so that a double resonance scheme cannot be used to burn a hole in the distribution of translational states. In contrast, a distribution over pendular states provides a source of static inhomogeneous broadening. However, a calculation of the pendular spectrum [25] of cyanoacetylene, assuming a thermal distribution [198] over pendular states, reveals that this broadening is small for the field strengths used here, owing to the fact that the dipole moments are rather similar in the ground and excited vibrational states [134].

The broadening associated with the droplet size distribution is also static, since a given molecule is confined to a single droplet and does not sample the overall distribution. Assuming the droplet size distribution is the dominant source of static inhomogeneous broadening, a suitable double resonance scheme should be capable of "tagging" molecules that reside in a narrow range of droplet sizes. Consequently, the broadening associated with the distribution of sizes in the beam can be reduced or eliminated using such a hole burning technique. Indeed, the width of the hole can then be used to obtain information on other broadening mechanisms, as discussed below.

For the case where the widths of the pendular spectra are limited by the static inhomogeneity resulting from the droplet size distribution, these widths are directly correlated to the droplet size dependence of the center frequency. As a result, the line shapes can be estimated by averaging the curve representing the variation in the transition frequency as a function of the droplet size (Figure 9.3) over the relevant log-normal distribution [91], which has been further weighted to account for the appropriate pick-up statistics [102]. The inset in Figure 9.4 shows a fit to the experimental pendular peak frequency versus most probable droplet size,

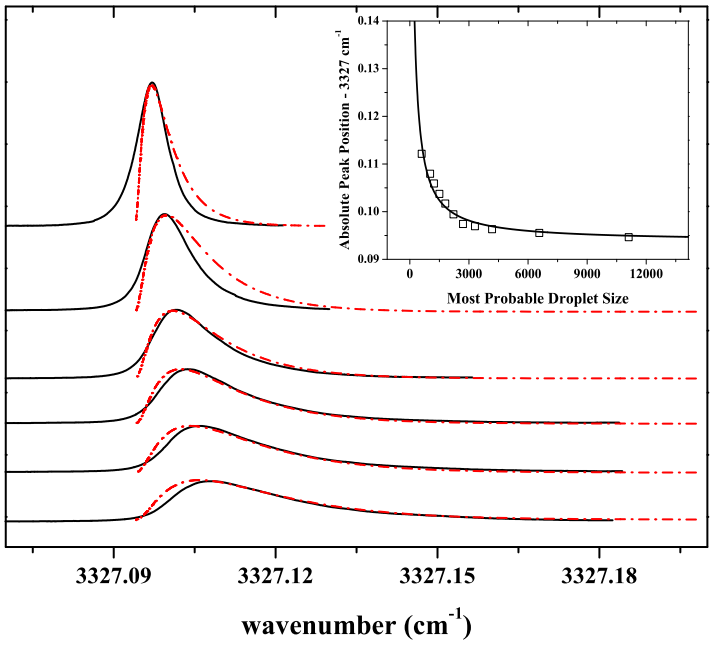

Figure 9.4: A comparison of the experimental (solid lines) and simulated (dashed lines) pendular spectra of HCCCN in helium droplets, assuming the distribution of droplet sizes is the sole source of inhomogeneous broadening. The inset shows the variation of the single resonance peak frequency with the most probable droplet size and the best fit to the "excluded volume" model described in the text. The most probable size is the maximum in the distribution resulting from the product of the log-normal distribution of droplets sizes and the Poisson distribution for the pick-up of a single HCCCN molecule.

based upon the "excluded volume" model [330], for which the transition frequency approaches an asymptotic value for large N. An additional constraint is imposed to ensure that the gas-phase frequency (3327.371 cm^{-1}) [331] is reproduced at N = 0. The constants obtained from the fit are ν_0 = 3327.0938 $\pm$ 0.0007 cm^{-1}, a = 13(1) cm^{-1}, and b = 48(4) [91]. The simulated pendular spectra are shown in Figure 9.4 for six different source conditions (dashed lines), along with the corresponding experimental spectra (solid lines). The excellent agreement between the simulated and experimental spectra provides considerable support to the assignment of the primary source of inhomogeneous broadening in these pendular spectra to the droplet size distribution.

It is interesting to note that Callegari *et al.* [330] carried out a similar analysis to the one

presented here, for the first overtone zero-field spectrum of hydrogen cyanide (C-H stretch), from which they concluded that the droplet size distribution was not the limiting source of broadening. Nevertheless, the corresponding spectra were much broader than those reported here, which is indeed suggestive of different broadening sources. Having obtained reasonably firm evidence that the primary source of broadening in the pendular spectra of cyanoacetylene is static inhomogeneity associated with the droplet size distribution, we can anticipate that it will be possible to burn a hole in the spectrum using an IR-IR pump/probe method.

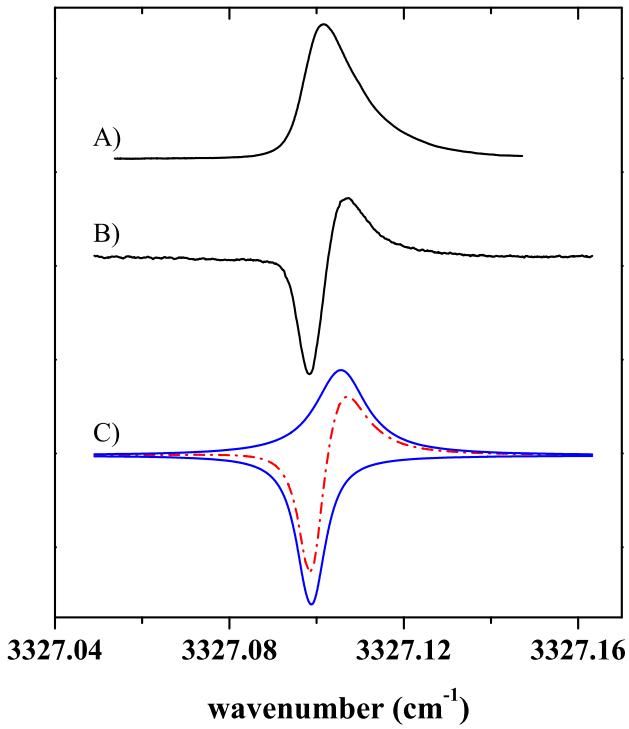

Figure 9.5: A) An infrared single resonance pendular spectrum of HCCCN in helium droplets, obtained at a backing pressure of 60 atm and a nozzle temperature of 23 K, corresponding to a mean droplet size of 2500 helium atoms. B) Infrared-Infrared double resonance spectrum of HCCCN obtained under the same source conditions. C) The dashed curve is a fit of the above experimental spectrum to two Lorentzians of opposite sign, with FWHM linewidths for the hole and pile of 208 MHz and 406 MHz, respectively.

Figure 9.5B shows an IR-IR double resonance spectrum recorded using source conditions

that yielded a mean droplet size of approximately 2500 helium atoms (~3.0 nm radius) [88]. The spectrum in Figure 9.5A is the corresponding pendular spectrum obtained without the pump (single-resonance). As noted above, the pump laser was amplitude modulated, while its frequency was fixed on resonance with the HCCCN pendular transition. A lock-in amplifier was used to process the laser induced bolometer signal. In the absence of the probe laser, the modulated pump gives a constant bolometer signal. The cw probe laser was then scanned through the pendular transition, resulting in the double resonance signal shown in Figure 9.5B, which is riding on top of the constant background from the pump. The double resonance spectrum represents the difference between the probe laser spectra that could be independently recorded with the pump on and off. The negative contribution to the spectrum is a conventional "hole", corresponding to the fact that the probe laser excites fewer molecules in this frequency range when the pump is on, compared to when it is off. The implication is that molecules that would normally have absorbed in this spectral region (when the pump was off) are depleted by the pump. If there were no mechanism for returning the molecule to the ground state, such that the excited molecules were no longer available to the probe, only the depletion would be observed. In the gas-phase, for example, the excited state molecule might dissociate, or simply remain for a long period of time in some intermediate excited state, making it unavailable to the probe laser. In the helium droplet experiments, however, the molecules can relax back to the ground state, due to quenching by the helium, on a time scale that is competitive with the flight time between the two lasers, making them once again available for excitation by the probe laser. Indeed, this relaxation gives rise to the positive signal in the double resonance experiment, which we will hereafter refer to as the "pile". The existence of the pile confirms our earlier assumption that the vibrational relaxation occurs on a time scale that is fast compared with the flight time of the droplets between the two laser interaction regions (175 μs).

The fact that the "hole" and "pile" appear at different frequencies can be understood by considering that excitation by the pump laser, and subsequent relaxation to the ground vibrational state, results in the evaporation of approximately 660 helium atoms (5 cm^{-1} per atom) [56].

Thus, molecules that are cooled to the ground state, following the pump excitation, are now in a smaller droplet than they would have been in the absence of the pump laser. As noted above, smaller droplets have a slightly blue-shifted pendular spectrum (compared to larger ones), explaining the position of the pile relative to the hole.

Given that the hole is narrower than the overall width of the pendular spectrum recorded under the same source conditions, we conclude that the pump laser is burning a hole in the droplet size distribution. Subsequent vibrational relaxation of the molecules results in the production of more droplets that are approximately 660 atoms smaller than those originally excited by the laser. The effects of this size selection become even more important for smaller average sizes, where the broadening from the corresponding distribution is considerably larger.

The dashed line shown in Figure 9.5C is a fit to the experimental double resonance spectrum, using two Lorentzians of opposite sign (also shown in Figure 9.5C), whose centers are separated by 205 MHz. The fit is excellent and gives us a way of determining the widths and areas of the positive and negative features in the double resonance spectrum. The quality of the fits to a Lorentzian line shape gives at least some support to the idea that the remaining broadening is due to a homogeneous mechanism. Nevertheless, it is again important to point out that this broadening could come from a number of different sources, including the dynamic inhomogeneous broadening processes discussed above. The Lorentzian FWHM linewidths for the hole and pile are 208 MHz and 406 MHz, respectively, compared to FWHM linewidth of 300 MHz for the corresponding pendular spectrum in Figure 9.5A. The fact that the hole and pile have different linewidths is of considerable interest. Qualitatively, the implication is that the corresponding broadening mechanism is strongly size dependent, an issue we will now examine in some detail.

This IR-IR double resonance scheme clearly provides us with a way of probing broadening mechanisms that are normally obscured by the static inhomogeneous broadening that appears to result from the droplet size distribution. Double resonance spectra were recorded for a wide range of source conditions and in all cases the line shape was well reproduced by a

fit to two Lorentzians of opposite sign. Figure 9.6 shows a plot of the corresponding FWHM

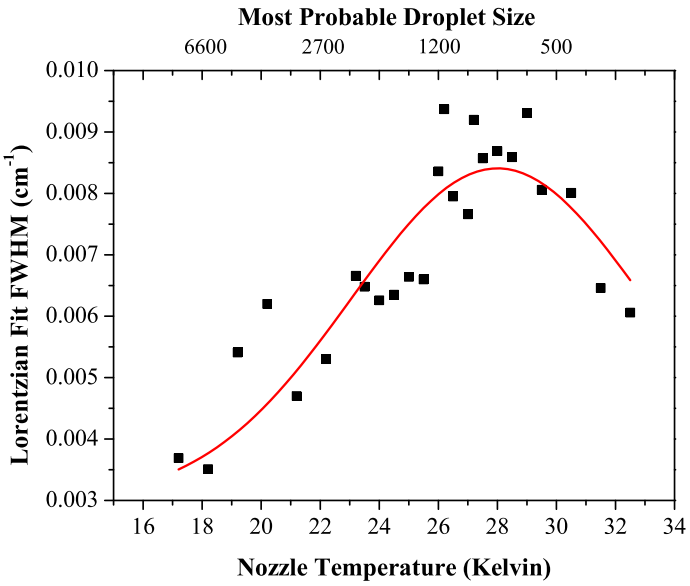

Figure 9.6: A plot of the FWHM Lorentzian linewidths for the holes, as a function of nozzle temperature (the smooth line being a guide for the eye). The nozzle temperatures correspond to droplets with a most probable size ranging from 8500 helium atoms to less than 500 atoms.

linewidths for the holes as a function of the nozzle temperature. The corresponding data for the piles was more limited, owing to the fact that for the smaller initial droplet sizes (high source temperatures) the piles became too broad to observe. The data in Figure 9.6 was obtained by tuning the pump laser to the maximum in the pendular spectrum. As a result, the nozzle temperatures in the figure can be approximately correlated with the droplet size, corresponding to the maximum in the distribution for a given mean size. The droplet size dependence of the linewidth is interesting, becoming broader with decreasing droplet size (down to approximately 1000 atoms) and then decreasing for even smaller droplets. Although we cannot provide a definitive interpretation of this data, it is consistent with what might be expected from the homogeneous broadening associated with relaxation to the helium excitations, as discussed below.

Another way of probing droplets of different size is to tune the pump laser through the pendular spectrum, recording the corresponding double resonance spectra for each case. The

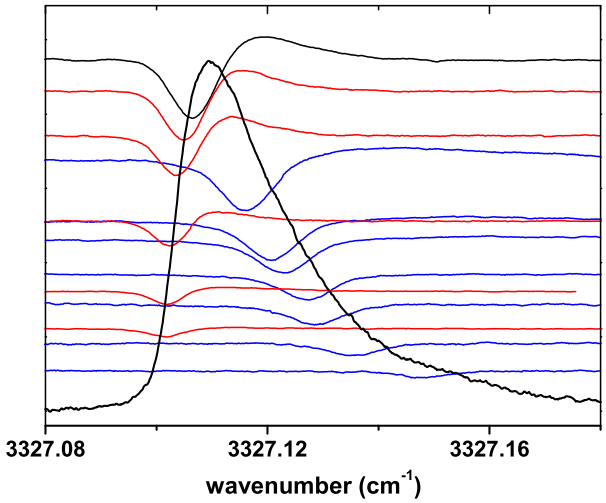

Figure 9.7: A series of double resonance spectra obtained at different pump laser frequencies. The double resonance spectra are superimposed on the single resonance spectrum, obtained using identical source conditions (60 atm., 28 K ($\overline{N}$ = 1000 helium atoms)).

corresponding spectra are shown in Figure 9.7, where the vertical offset of the spectra and the position of the resonance relative to the pendular spectrum indicate the frequency of the pump laser. Assuming the blue tail in this spectrum is due to the small droplets in the distribution, we would expect that the linewidth of the hole would depend upon the pump laser frequency in a manner similar to that seen in Figure 9.6. Figure 9.7 shows a plot of the linewidth of the hole as a function of the pump laser frequency, where again we see that the linewidth first increases as the pump is tuned to the blue (smaller droplets) and then decreases for even smaller droplets. In this case, we are able to sample much smaller droplets, to the point where the linewidth becomes as narrow as that observed for the largest droplets.

9.4 Discussion

The results presented in the previous section give convincing evidence that the asymmetric line shapes observed for the pendular spectra of cyanoacetylene in helium nanodroplets

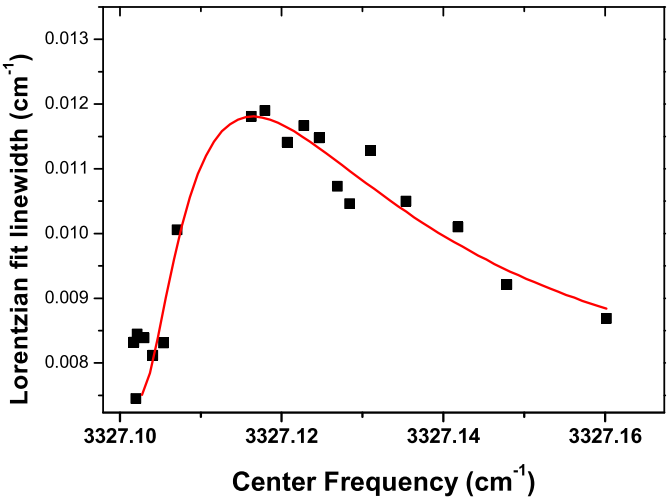

Figure 9.8: A plot of the widths of the holes vs the pump laser frequency (the smooth line being a guide for the eye). The linewidths of the holes ere obtained by fitting each double resonance spectrum to two Lorentzians of opposite sign. When the pump frequency was tuned to the blue tail of the spectrum, the pile disappears entirely, and the linewidths of the corresponding holes were obtained from fits to a single Lorentzian.

originate from the distribution of droplet sizes. The fact that we can burn a hole in these line shapes indicates that this inhomogeneous broadening is indeed static, in agreement with what would be expected from the droplet size distribution. In fact, the frequency shifts observed from the hole to the pile are consistent with the loss of approximately 660 helium atoms from the droplet, due to excitation by the pump laser. This can be approximately illustrated by taking two different single resonance pendular spectra with mean droplet sizes that differ by approximately 600 atoms, and subtracting one from the other. The result is a simulated double resonance spectrum, which is compared with the corresponding experimental result in Figure 9.9. When the simulated double resonance spectrum is fit to two Lorentzians, the corresponding centers are separated by 310 MHz, compared to the experimental separation of 205 MHz. Actually, we do not expect better than qualitative agreement here given that the hole burning experiment only samples a portion of the droplet size distribution, while the difference in the pendular spectra has contributions from the entire distribution. Nevertheless, the qualitative

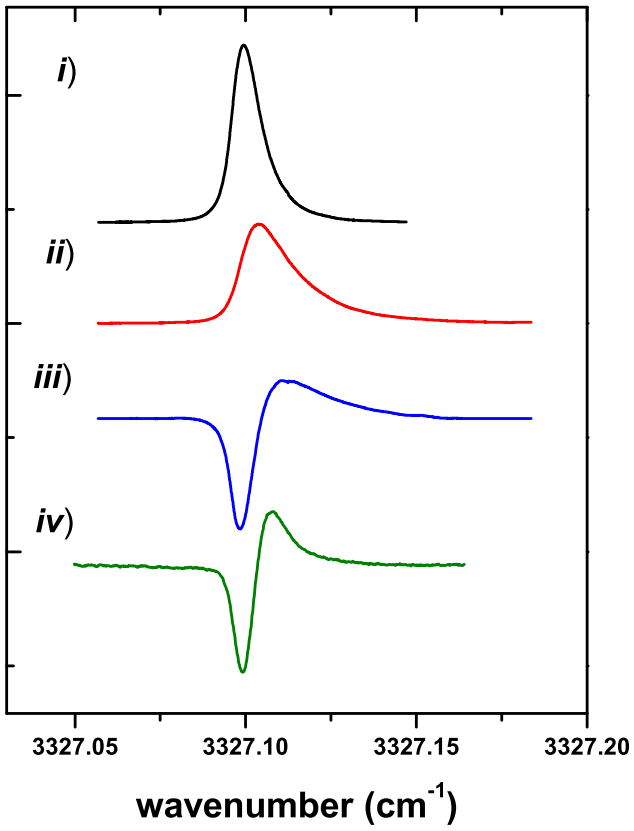

Figure 9.9: Pendular spectra of HCCCN, corresponding to droplets with mean sizes of (i) 2500 and (ii) 2000 helium atoms. The difference between the two pendular spectra (iii) is in qualitative agreement with the double resonance spectrum (iv) obtained under source conditions similar to those used in the upper pendular spectrum.

agreement again supports the idea that the shift between the hole and the pile results from the photo-induced evaporation of helium from the "pumped" droplets.

It is interesting to note that under source conditions resulting in the formation of very large droplets (>15,000 atoms) the double resonance signals disappear altogether. This is expected for large droplets, where the loss of 660 helium atoms does not significantly shift the vibrational frequency of the solvated molecule, such that the hole and the pile overlap and cancel one another. Indeed, we find that in all of the double resonance spectra recorded for this system,

the integrated areas of the hole and pile are very nearly the same, namely within 5%. In actual fact, the area of the pile is consistently slightly smaller than that of the hole, suggesting that some of the pumped molecules are missing from the probe. There are a number of possible explanations for this small difference. First, if some of the excited molecules do not cool to the ground state on the time scale of the flight time between the laser interaction regions, the pump laser would miss these molecules. Alternatively, the droplet recoil resulting from the evaporation of 660 helium atoms could cause a small fraction of the helium droplets to miss the probe laser interaction volume, reducing the probe laser signal. To obtain an estimate of this effect, we modeled the evaporation by assuming that each helium atom that evaporates from the surface of the droplet has 5 cm^{-1} of translational energy [56]. Treating the evaporation events as uncorrelated, we calculated that approximately 3% of the droplets were sufficiently deflected (for a mean droplet size of 3000) so that they would miss the probe laser interaction region, in good agreement with experiment.

As shown above, the linewidths of the holes in the double resonance experiments depend strongly upon the helium droplet source conditions, as well as the pump frequency, providing us with clues concerning the source of this broadening. In the former case, we observe an approximately linear increase in the linewidth of the hole for conditions that produce mean droplet sizes from approximately 10,000 to 800 helium atoms. For even smaller droplets we observe that the linewidths once again become narrower.

In light of the previous work on cyanoacetylene in helium, which suggests that the surface ripplon modes are important for the rotational relaxation of the molecules [79] (as well as perhaps contributing to the vibrational quenching), the increase in the linewidth with decreasing droplet size can be justified by the fact that the molecule is on average closer to the surface in smaller droplets. This in turn could increase the coupling to the ripplons and thus decrease the lifetime of the molecular states. This mechanism might also explain the decrease in the linewidth for the smallest droplets. Indeed, in a Fermi golden rule treatment of relaxation, the rate depends upon both the coupling matrix elements and the density of states. It is well known

that the ripplon density of states decreases rapidly with decreasing droplet size [56]. The rapid decrease in the density of states might therefore overwhelm the increasing coupling strength, causing the linewidth to become narrow for the smallest droplets. Unfortunately, we still do not have a quantitative theory for the relevant coupling in these systems, so we are left to speculate concerning the source of this broadening. Indeed, these simple ideas are in need of further testing by both experiment and theory.

Given the relatively high power (60 mW) of the pump laser used in the present study, it is important to estimate the effects of power broadening in these experiments. Using an *ab initio* value for the C-H stretch transition moment (0.1 Debye) and estimates of the focal volume of the laser, we estimate that the power broadening due to the pump laser is approximately 50 MHz. Although this value could easily be a factor of two in error, we expect that it is not the dominant source of broadening for the holes, given that power broadening would not be strongly droplet size dependent.

9.5 Summary

In the present study we reported a new IR-IR double resonance approach for studying the dynamics of molecules in helium nanodroplets. By choosing a simple molecule that cannot undergo chemical modifications upon vibrational excitation, we are able to explore the capabilities of the method for probing the associated vibrational dynamics. The method is used to reduce the static inhomogeneous broadening, which appears to result from the droplet size distribution, uncovering another broadening source that is strongly and non-monotonically dependent upon the droplets size. The frequency shift between the hole and the pile observed in these double resonance experiments is consistent with the fact that the pump laser causes the evaporation of approximately 660 helium atoms, making the droplets smaller when they enter the probe laser interaction region.

The potential of this experimental method can be appreciated if one considers its application

to systems where the pump laser can initiate a reaction or a conformation change. The ability to observe both the hole (depletion of the reactant) and the pile (the product) make this method particularly powerful. For example, in a double resonance experiment where the area of the hole is measured to be much larger than that of the pile, we might conclude that the missing molecules correspond to those that have undergone reaction or isomerization. This would then motivate the more time consuming search for the spectrum of the products of the photo-initiated reaction. On the other hand, if the areas of the hole and pile are approximately the same, we can immediately conclude that reaction has not occurred, saving us the time required to search for products.

Chapter 10

Photo-Induced Isomerization of HF-HCN

Having first applied the IR-IR double resonance technique to a stable molecule in helium, namely cyanoacetylene monomer (Chapter 9), we can now turn our attention to a system in which dissociation or isomerization may be possible after the absorption of an infrared photon. The HF-HCN complex is an ideal system for this study given than two isomers have been observed in helium and their single resonance spectra have been fully characterized. In the gas-phase, the HF-HCN complex undergoes vibrational predissociation, and thus the role of the solvent is likely to be very important in determining the relaxation dynamics of such weakly bound complexes.

10.1 Introduction

The vibrational dynamics of helium solvated molecules that follows infrared laser excitation is poorly understood. The ultimate fate of the vibrational excitation is generally known, namely resulting in the evaporation of several hundred helium atoms from the droplet [332], however, the detailed mechanisms associated with these relaxation processes are not known. Some indirect evidence for how the molecules are relaxed has come from studies of diatomic HF in helium [76], which has been shown to remain vibrationally excited for the entire flight time (~1ms) of the droplets through the apparatus [333]. This is determined by the fact that laser induced excitation of the HF results in an increase in the energy of the droplet beam, as measured by a bolometer detector [334]. The implication is that for a diatomic molecule, where there are no intermediate states between the ground and excited vibrational levels, vibrational energy transfer to the helium is very slow. In contrast, polyatomic molecules typically have a whole ladder of vibrational levels, which allows the system to relax in a sequential set of smaller energy steps, corresponding to a cascading of the molecule through at least some of these intermediate levels. To date, however, experiments have not been done which directly probe the transient population in these intermediate levels.

In the present chapter we report results obtained using an infrared pump-infrared probe technique which could ultimately be used to probe these intermediate levels. However, since the time resolution of the present experiments is limited by the use of continuous wave lasers, we begin by considering the application of the method to the study of photo-induced isomerization of a hydrogen-bonded complex, due to vibrational excitation. gas-phase complexes are well known to undergo vibrational pre-dissociation when the excited intra-molecular vibrational mode has an energy that is greater than the hydrogen bonding energy [26, 335–338]. Indeed, much is already known about the associated energy transfer processes that funnel energy from the intra-molecular vibrational coordinate into the intermolecular bond. The solvation of a complex in helium introduces a range of other possible dynamical pathways. For example, if the vibrational pre-dissociation lifetime is long with respect to the relaxation rate to the he-

lium, it is possible that intra-molecular vibrational excitation will not result in dissociation of the complex, even when the latter channel is energetically open.

The IR-IR double resonance method was explained in detail in Chapter 9, where cyanoacetylene was vibrationally excited in helium droplets and then probed again after vibrational cooling was complete [332]. In that study, where isomerization of the molecule is not possible, the results clearly show that the effect of the first photon is simply to reduce the size of the droplet, due to helium evaporation. The resulting area of the hole (representative of the population in bigger droplets which is lost due to vibrational excitation) and pile (population in smaller droplets which is gained due to the evaporation of Helium atoms from the pumped droplet) were found to be approximately the same indicating that the population is conserved. This has important implications in that if population is being transfered between isomers, the relative areas of the hole and pile will be different, motivating the search for the isomerization / reaction products. In the present chapter we apply this method to the hydrogen bonded HCN-HF binary complex, which has two well characterized isomers in helium droplets [339]. This system is thus ideally suited to studying photo-induced isomerization, particularly given that the energies of these two isomers are quite different.

10.2 Results

In a recent paper on the infrared spectra of hydrogen cyanide-hydrogen fluoride complexes in helium droplets [339], the first high resolution infrared spectra of the bent HF-HCN isomer, as well as helium nanodroplet spectra for the well studied (in the gas-phase) HCN-HF linear isomer, the latter corresponding to the global minimum on the potential energy surface, were obtained. The zero-field and Stark spectra of these two isomers of HCN-HF provide us with the rotational constants and dipole moments needed to understand the pendular spectra of these species. From an analysis of the spectral intensities and computed oscillator strengths, we conclude that the the linear HCN-HF isomer is formed approximately twice as often as the

higher energy bent HF-HCN complex. The relative populations of these two isomers in helium are controlled more by the approach geometries of the two molecules than by their relative energies [36,316,339]. Figure 10.1 (i) shows four pendular spectra recorded using the F-center

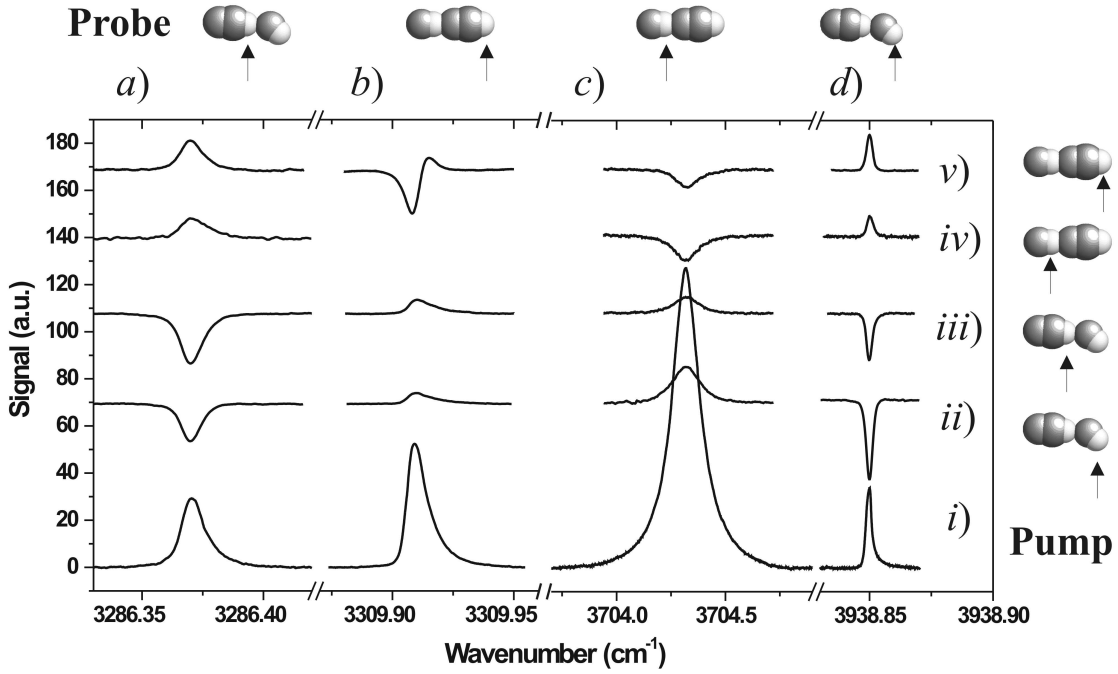

Figure 10.1: Pendular spectra (i) of the C-H and H-F stretching vibrations of the bent and linear isomers of HCN-HF in helium droplets. The probe laser was scanned over each of the transitions associated with the vibrational modes indicated along the top of the figure. The double resonance spectra (ii)-(v) were obtained by fixing the OPO pump to the frequency corresponding to the peak in the pendular spectrum (the pumped vibration is shown to the right of the figure) and then scanning the F-center probe laser through each pendular transition. A negative (positive) signal in the double resonance spectrum corresponds to a reduction (increase) in the population of the pumped isomer. The source conditions were held fixed for all single and double resonance spectra at 60 Bar, 22.5 K producing a mean droplet size of approximately 3000 helium atoms. [88]

laser, with a large DC electric field applied to the corresponding interaction region. These four spectra correspond to the C-H and H-F vibrations of the two isomers. The pendular spectra show only a single peak since in parallel polarization, all of the corresponding transitions occur at the same frequency.

It is clear from this series of pendular spectra that the linewidth associated with the hydrogen bonded vibrational mode of the linear isomer is significantly larger than the corresponding

free C-H stretch. (Note that the frequency scale associated with the bonded H-F stretch of the linear isomer is ten times that for the other modes, indicative of the much greater broadening in this band.) This is consistent with what has been observed previously in the gas-phase, where the difference is even larger. Indeed, the width of the gas-phase ν_1 band (H-F stretch) of the linear isomer is 230 times larger than that of the ν_2 band (C-H stretch) [338], which is rationalized by the fact that the H-F stretch is much more strongly coupled to the intermolecular degrees of freedom, compared with that of the C-H stretch, making the vibrational pre-dissociation rate for the H-F stretch correspondingly larger. In the helium nanodroplet pendular spectra the linewidth of the H-F stretch is 15 times that of the C-H stretch. The smaller difference is at least in part due to the fact that the broadening associated with the C-H stretch of the linear isomer has a significant contribution from inhomogeneous broadening, due to the droplet size distribution [91]. Indeed, the asymmetric line shape of the corresponding pendular spectrum shows a tail to the blue, which is characteristic of broadening due to the distribution of droplet sizes in the beam [332].

It is also interesting to note that the linewidth associated with the ν_1 band of the linear isomer is 1.6 times that obtained in the gas-phase [338], the implication being that the vibrational relaxation rate (corresponding to vibrational pre-dissociation in the gas-phase) is enhanced by the presence of the helium solvent. This effect has been observed previously for HCN dimer [277], where the vibrational relaxation rate in helium was found to be 40 times faster than in the gas-phase. This makes qualitative sense given that gas-phase vibrational predissociation of small complexes is quite often in the sparse density of states regime. Thus the presence of the elementary excitations of the helium can provide the additional density of states needed to allow for more nearly resonant, and therefore faster, vibrational relaxation.

The two bands of the bent isomer, corresponding to the free H-F stretch and the bonded C-H stretch, both appear to be inhomogeneously broadened, as indicated by the tails to the blue side of the spectra. In this case the FWHM linewidth of the bonded C-H stretch (335 MHz) is only slightly broader than the free C-H stretch of the linear complex (291 MHz). This

small difference is consistent with the fact that the intermolecular bond in the bent isomer is rather weak, making the associated intra-molecular coupling also weak and the corresponding lifetime rather long. The free H-F stretch of the bent isomer is particularly narrow, with a FWHM linewidth of only 77 MHz, again reflective of the weak coupling in this complex.

We now turn our attention to the pump-probe experiments that are shown in Figure 10.1(ii)-(v). As in the previous chapter, the pump and probe regions are separated by 8 cm, corresponding to a droplet flight time of 175 μs. These spectra were all obtained with a large DC electric field applied to the upstream, pump laser interaction region and fixing the pump laser at the peak of the pendular spectra, corresponding to the modes indicated to the right of the figure. These spectra were obtained by amplitude modulating the pump laser, while the downstream probe laser was scanned through the pendular transitions indicated above.

Figure 10.1(v)(b) shows a double resonance spectrum resulting from pumping and probing the same C-H stretch of the linear isomer. This spectrum has both a negative "hole" and positive "pile", which previously have been shown to arise from the fact that the pumped molecules that have returned to the same ground state are now in a smaller droplet, which shifts the spectrum to the blue (the pile) [332], depicted schematically in Figure 10.2. A fit to this double resonance spectrum consisting of two Lorentzians of opposite sign, separated by 162 MHz, yields linewidths for the hole and pile of 231 MHz and 258 MHz, respectively, which are both narrower than the overall linewidth of the single resonance pendular spectrum.

In our previous study of the vibrational relaxation of a stable molecule in helium, namely cyanoacetylene, we found that the areas of the hole and pile were approximately the same (within 8%), indicative of the fact that the system has no where else to go but back to the ground state, following vibrational excitation. The small difference was attributed to the fact that the pump process results in a small deflection of the droplet beam, due to helium evaporation, meaning that some of the pumped molecules miss the downstream interaction region and the detector. In contrast, the areas for the linear HCN-HF complex are quite different when pumping and probing the free C-H stretch. Indeed, the signal for the pile only accounts for

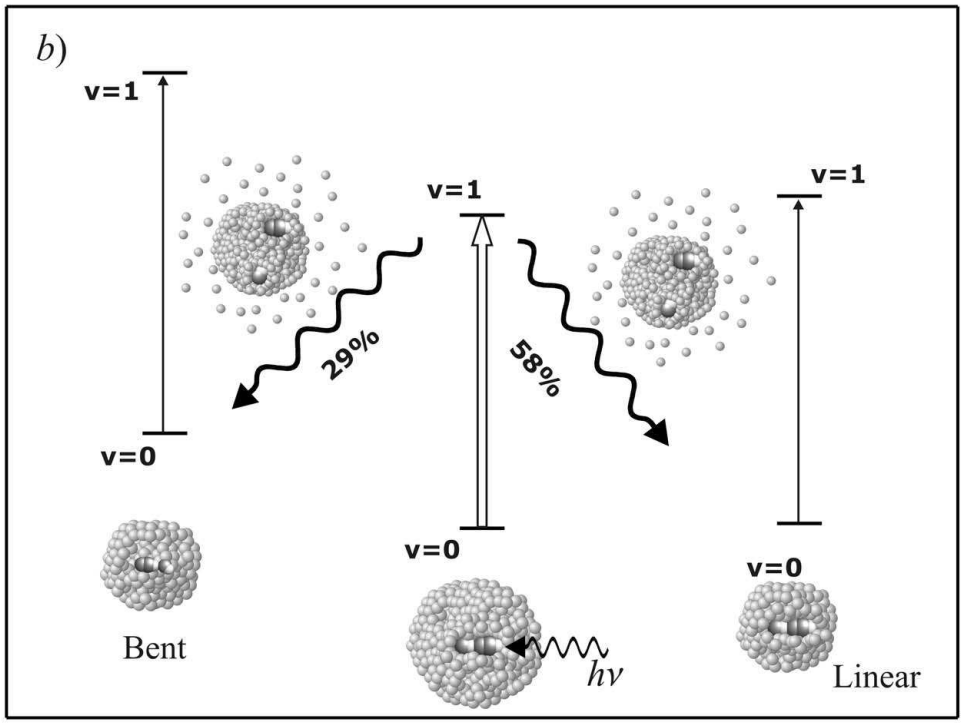

Figure 10.2: A schematic diagram showing the photo-induced droplet evaporation and cluster isomerization resulting from pumping the linear HCN-HF complex.

58% of the total depletion, indicated by the area of the hole, as is immediately apparent from the spectrum in Figure 10.1(v)(b). The same situation is evident in Figure 10.1(v)(c) where the H-F stretch of the linear isomer is probed after pumping the corresponding C-H stretch. In this case, the broadening is sufficient to blur the hole and pile into a single peak. The net negative signal clearly indicates that the hole has more intensity than the corresponding pile. So the obvious question is, where is the missing intensity? This question can be answered directly by tuning the probe laser through the C-H and H-F vibrational bands of the bent isomers, as shown in Figures 10.1(v)(a) and 10.1(v)(d), respectively. The positive going signals observed for these two bands clearly show that vibrational excitation of the C-H stretch of the linear isomer results in population transfer to the bent isomer. This photo-induced isomerization process is clearly feasible given the excitation of the C-H stretch of the linear isomer puts the complex approximately 1750 cm^{-1} above the isomerization barrier [339].

A quantitative analysis of the areas for these various processes can provide detailed information on the efficiency of this isomerization process. After correcting for the different transition moments for the various vibrations, using *ab initio* results [339], as well as for changes in the probe laser intensities for the different spectra, we obtain the results reported in Table 10.1. These results indicate that 29% of the C-H excited linear complexes find their way into

Pump / Probe	L(C-H)	L(H-F)	B(C-H)	B(H-F)
L(C-H)	2.4 / 1.4 (hole / pile)	0.9	0.7	0.7
L(H-F)	-	1.3	0.8	0.4
B(C-H)	1.5	2.2	2.8	2.0
B(H-F)	1.4	3.7	1.9	3.3

Table 10.1: Integrated areas of the double resonance spectra for the two isomers of the HCN-HF complex. The areas are corrected for the initial population ratio observed in helium, the *ab initio* intensities, and the pump and probe laser intensities. The relative areas were determined by fitting the spectra to Lorentzians, and in the case of pumping and probing the C-H stretch of the linear isomer, two Lorentzians of opposite sign were used.

the bent isomer during the relaxation process. When combined with the 58% that cool back into the linear isomer, we have accounted for 87% of the overall population. Excitation of the H-F stretch of the linear isomer gives essentially the same results. At least some of the missing population is indicative of the droplet deflection referred to above [332]. The fact that this value is somewhat larger than that observed previously for cyanoacetylene [332] could be due to the fact that the droplets used here are on average somewhat smaller, due to the additional evaporation that comes with the formation of the HCN-HF complexes within the droplets. In addition, the use of the approximate *ab initio* intensities in determining the integrated areas may introduce an error that becomes important when comparing the double resonance spectra for the different isomers. The other possibility is that there is some other minor species that is formed during this photo-excitation process that we have not yet spectroscopically identified. In fact, it is important to note that this approach of pumping and probing the same species can provide us with clues with regards to whether or not a photo-induced process has occurred. Indeed, if the hole is significantly deeper than the pile, we immediately know that there must be some other relaxation channel that is then worth looking for.

One channel we did explore corresponds to the possibility that vibrational pre-dissociation of the complex results in the loss of one of the fragments from the droplet, which would obviously prevent the re-formation of the complex. Indeed, recent studies of CH_3I and CF_3I [340] in helium droplets have revealed (at least in this high energy dissociation process) that escape from the droplet is possible. We looked for this channel by tuning the probe laser to the C-H stretch and H-F stretch transitions of the HCN and HF monomers in helium droplets. No double resonance signals were observed in either case, regardless of the isomer pumped. Presumably, the low translational recoil associated with vibrational pre-dissociation [341, 342] is insufficient to eject the fragments from the droplets. This makes sense given that the solvation energy of a molecule in helium [94] is much greater than the translational energies typical of a vibrational pre-dissociation process [341]. In contrast, 266 nm photo-dissociation of CH_3I gives rise to 1.3 eV of translational energy [343], suggesting a more ballistic ejection process.

It is interesting to point out that the above results indicate that the linear isomer is formed twice as often as the bent upon excitation of either the C-H or H-F stretch of the linear isomer, namely the same isomer ratio observed in the initial formation of the complexes within the droplets. This result provides a significant clue concerning the mechanism of the population transfer. As shown in Figure 10.3, the excitation energy of the linear isomer is 1340 cm^{-1} above its dissociation limit (given that D_0 = 1970 cm^{-1} [341]), making it reasonable to expect that the complex might undergo vibrational pre-dissociation (similar to that observed in the gas-phase) before the energy is transferred to the helium. Subsequent geminate recombination, due to the collision of the fragments with the helium solvent cage, could then result in the re-formation of the complexes with the same isomer ratio as observed in the original pick-up process (see Figure 10.2). Indeed, provided that the fragments separate to a large enough distance such that they lose all memory of their relative orientations (the intermolecular interactions become negligible), they will re-condense with the same isomer ratio as obtained from pick-up, assuming they are also internally cold. This seems possible since the diameter of a 3000 helium atom droplet is approximately 6.4 nm (R = 2.22 $\sqrt[3]{N}$), while the interaction energy of the two

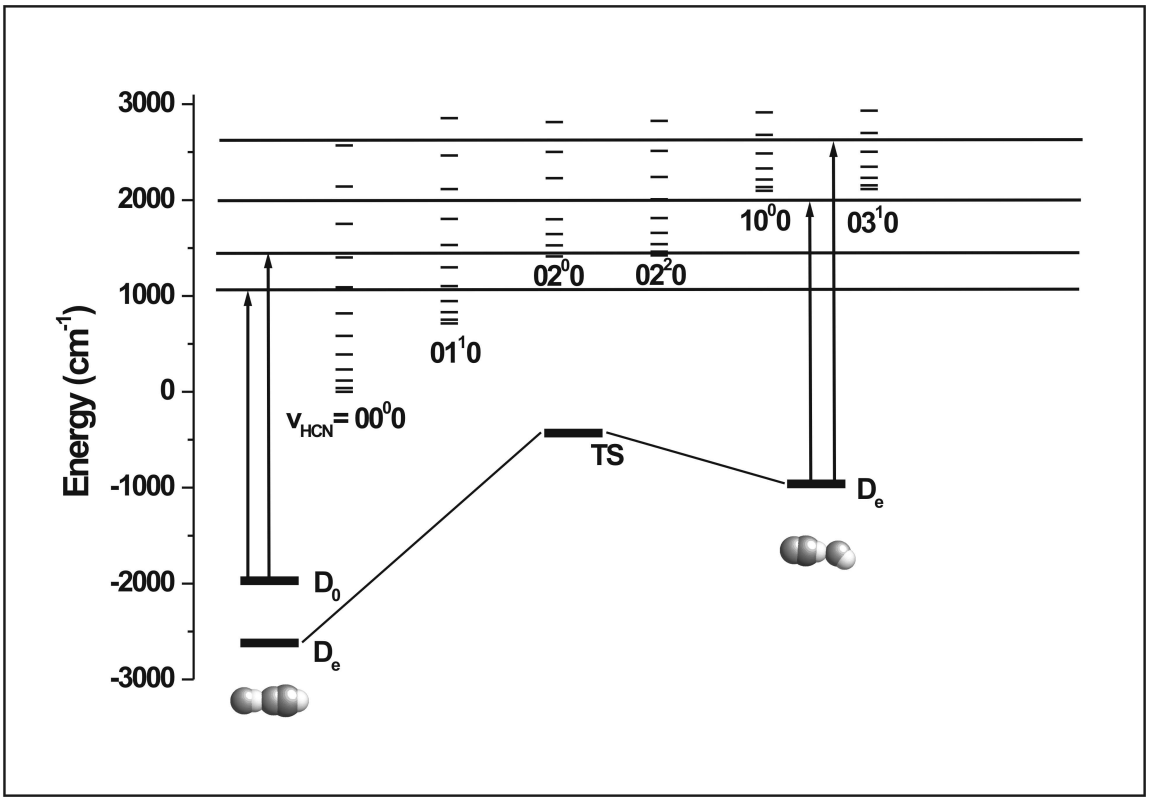

Figure 10.3: An energy level diagram showing the relative energies of the two HCN-HF isomers and the corresponding transition state, obtained at the MP2/aug-cc-pVTZ level of theory. The arrows indicate the vibrational excitation energy of the C-H and H-F stretching vibrations, while the horizontal bars indicate the available energy. The rotational states of HF are built on top of the vibrational states of HCN, representing the open photo-fragment channels for the binary complex, assuming vibrational excitation is followed by dissociation.

fragments at 4 nm is approximately 0.4 K (with the dipole moments of the fragments aligned), as determined from the *ab initio* results. Ofcourse, the results reported here are only suggestive of the mechanism, and we cannot rule out the possibility that isomerization occurs without dissociation and that the 2:1 isomer ratio observed for the photo-induced processes is purely a coincidence.

We now turn our attention to the double resonance spectra shown in Figure 10.1(ii-iii), corresponding to pumping the H-F and C-H stretching vibrations of the higher energy bent isomer. The vibrational energy associated with H-F excitation puts the bent complex 3400 cm^{-1} above the isomerization barrier and 3000 cm^{-1} above the dissociation limit (see Figure 10.3), while the corresponding values for C-H stretch excitation are 2800 cm^{-1} and 2400 cm^{-1}. These

values are considerably larger than those for the linear isomer, which might result in different dynamical processes. It is evident from these double resonance spectra that photo-induced population transfer between the two isomers is again occurring, although the associated dynamics are qualitatively different than those discussed above. The most obvious difference is that only the depletion signal (the "hole") is observed when pumping and probing the modes of the bent isomer. This is despite the fact that the corresponding double resonance spectra are sharp, suggesting that the depletion signal is not simply the sum of the hole and pile (as is the case for the results in Figure 10.1(iv)(c) and 10.1(v)(c)). The implication is that none of the excited bent complexes make it back into the ground state of the bent complex. Instead, the entire pumped population appears to have been transferred to the linear isomer upon vibrational excitation. This is confirmed by probing the linear isomer, following pumping of the bent isomer, where the corresponding signals are now all positive. The quantitative results are given in Table 10.1. These isomer specific processes are clearly of considerable interest, even though we do not yet have a complete understanding of them. Indeed, further experimental and theoretical work will be needed to reveal the details associated with these dynamical processes.

10.3 Discussion

We have presented here the first observation of photo-induced isomerization of a weakly bound, hydrogen bonded complex embedded in helium droplets. The vibrational excitation energies in the present study are well above the barriers to isomerization between the two isomers of HCN-HF, as well as the dissociation energies of the complexes. The results clearly show that the helium solvent does not quench the excited molecules fast enough to prevent isomerization. While the dynamical processes appear to be mode independent, there is a strong dependence upon which isomer is initially excited. Indeed, excitation of either the H-F or C-H stretches of the linear isomer results in the same ratio of isomer populations that is obtained from the initial pick-up process. This at least suggests that complex dissociation is occurring

before the helium can fully quench the system, followed by geminate recombination of the cooled fragments. In contrast, pumping the C-H and H-F stretches of the bent isomer results in complete population transfer to the lower energy, linear isomer. As shown in Figure 10.3, the energy difference between the two isomers is quite large, making the energetics associated with isomerization in the two directions quite different. The available energy is considerably larger when pumping the bent isomers, which could very well be the determining factor in controlling the dynamics. Indeed, the higher density of states in this region could result in faster intra-molecular vibrational redistribution (IVR), compared to that associated with pumping the linear isomer. Higher IVR rates would compete with vibrational pre-dissociation, effectively heating the molecule internally, allowing it to equilibrate into the lower energy isomer structure. IVR would also improve the coupling of the intra-molecular vibrational energy to the helium solvent (since the lower frequency vibrations associated with the corresponding dark states [344, 345] are more easily quenched by the helium [77]).

It is interesting to note that final state distributions of the photo-fragments resulting from C-H stretch and H-F stretch excitation have been measured for the linear complex in the gas-phase [341]. In both cases it is found that the majority of the available energy appears as HF rotation (ie. V-R transfer), with the HCN fragment produced in the ground vibrational state. This is despite the fact that the bending excited state of HCN is energetically accessible. If the early time dynamics of the linear isomer are similar in liquid helium, the rotationally excited HF fragment will likely be quenched rapidly by the helium. Indeed, in an earlier study of the HF monomer in helium [76], we found that the J=1 level was quenched in approximately 12 psec. Thus the production of ground state HCN and rotationally excited HF, which is rapidly quenched (assuming the higher HF rotational states are similarly quenched by the helium), could then give rise to geminate recombination of the cold molecules, producing the same isomer ratio as resulting from pick-up. Alternatively, if the HCN were produced in a vibrationally excited state, the slow vibrational relaxation of this molecule might mean that recombination occurred before the molecule was fully relaxed. In this case, there would be no reason to

think that the isomer ratio would be the same as that obtained by the pick-up of ground state molecules.

As noted above, and apparent from Figure 10.3, the available energy upon excitation of the bent isomer is much higher than in the case of the linear complex. In the above scenario we propose that faster IVR rates effectively heat the molecule internally, allowing it to rearrange and cool at a slow enough rate so that complete population transfer results. Alternatively, the complex could still vibrationally pre-dissociate, but due to the higher excess energy, result in the population of vibrationally excited states of the HCN fragment. If geminate recombination occurs more rapidly than vibrational relaxation of the HCN fragment (which seems likely given that the typical vibrational relaxation lifetimes in helium are on the nanosecond time scale [277]), the result would still be the formation of a hot cluster, which could then go on to isomerize into the linear complex. The mechanisms proposed here provide a reasonable explanation for the observed isomer ratios, resulting from pumping the two isomers of HCN-HF. Nevertheless, further experimental and theoretical work will be needed to test these ideas and to glean deeper insights into these interesting phenomena. For example, time resolved pump-probe experiments could be used to observe the transient monomers that result from vibrational pre-dissociation, if it is indeed occurring. Alternately, the transient development of hot bands in the spectrum of the complex could provide insights into IVR mechanisms that might be important.

10.4 Summary

Infrared-Infrared double resonance spectroscopy has been used as a tool to study the vibrational dynamics of the hydrogen bonded HCN-HF isomers in helium nanodroplets. Following the absorption of the first infrared photon, population transfer is observed from the excited complex to a second stable isomer. Pumping the lower energy linear isomer results in the production of both isomers upon cooling by the helium. In this case the isomer ratio is essentially

the same as that obtained following the initial pick-up and complexation in the helium droplets. We tentatively explain these results in terms of vibrational pre-dissociation of the linear complex, followed by geminate recombination due to interaction with the solvent cage. The results also suggest that the fragments are cooled by the solvent on a time scale that is fast with respect to geminate recombination. In contrast, vibrational excitation of the metastable, bent isomer results in complete population transfer to the linear complex. The implication seems to be that the complex either does not dissociate, but undergoes IVR to produce a hot cluster, which slowly cools into the more stable linear isomer, or dissociates to produce vibrationally excited fragments that do not cool before recombination occurs, again producing a hot complex which can then isomerize.

The IR-IR double resonance method presented here could also be used to study the photo-initiation of a reaction from a metastable entrance channel complex [301]. In this case, the spectral signature of the reaction would be the appearance of a product complex, with the hole associated with the reactant complex having more intensity than the pile. In systems where the hole and the pile in the double resonance spectrum have approximately the same intensity, it would be immediately obvious that reaction has not occurred. Chapter 11 will expand upon our efforts to study photo-induced chemical reactions.

Chapter 11

Gallium, Aluminum, and Indium Atom Complexes with HCN

Group IIIA elements of the periodic table (Boron, Aluminum, Gallium, etc ...) represent the metal atom analogues of the halogen atoms, in which there is one unpaired electron in a p orbital. Unlike the halogen atoms, which are only missing one electron from an otherwise closed shell however, group IIIA atoms have three electrons in the valence shell, two being paired in an s orbital, which leads to their tendency to form multiple bonds. This property strongly influences the reactivity of these metals as single atoms as well as in the small cluster regime. In this chapter we explore the interactions between a single gallium, aluminum, or indium atom with HCN. Theoretical calculations are presented which show that these metal atoms have the capability to undergo low barrier insertion reactions. With the double resonance techniques detailed in Chapters 9 and 10, we present compelling evidence for photo-induced reaction of the entrance channel complex (HCN-Ga) at 0.37 K initiated with a single infrared photon.

11.1 Introduction

A detailed experimental investigation of the reactions of laser ablated B, Al, Ga, In, and Tl atoms with HCN has been performed in argon matrices by the group of Andrews [346, 347]. For each of the metal atom (M) reactions; the MCN, MNC, and MH product species were identified upon codeposition in the matrix. For Ga, In, and Th + HCN, broad-band UV photolysis was found to increase the population of MCN at the expense of MNC, and this was reasoned by assuming that MNC was initially favored in the deposition due to its lower energy, and UV photolysis equilibrates the two isomers, given that the photon has sufficient energy to overcome the barrier to interconversion. That the MNC isomer is lower in energy, is in agreement with their electronic structure calculations (at the DFT/BP86/6-311G*/LANL2DZ level) which place the MCN isomer 1846, 1010, 457, and 114 cm^{-1} higher in energy than MNC, for M = B, Al, Ga, and In respectively. Interestingly for thallium, the energies of the two isomers are predicted to invert, with TlCN 552 cm^{-1} lower in energy than TlNC, which is somewhat contradictory to the above reasoning. In the Al + HCN experiments, both the cyanide and isocyanide peaks grew upon photolysis, and so an additional mechanism for their formation was postulated, namely that the populations could also be influenced by photolytic decomposition of a intermediate reaction product [MHCN]:

$$\begin{aligned} M + HCN &\rightarrow [MHCN] \\ [MHCN] + h\nu &\rightarrow MNC/MCN + H \end{aligned}$$

Indeed, from their work on the reactions between boron atoms and HCN [347], Andrews identified the HBCN, HBNC, and HB(CN) products, which could then go on to produce MCN and MNC, however such species were not assigned in the aluminum work. The HBCN product represents an insertion of the boron atom into the C-H bond of HCN, while HBNC is the

corresponding iso-cyano complex. HB(CN)[1] was determined to be a cyclic isomer, with the hydrogen bound to boron. The calculated energies of these complexes have been adapted[2] from reference [347] and are shown in Table 11.1. In their experiment, no evidence for N-H or C-H

Species	Relative energy (kcal mol^{-1})
HBCN	-75.70
HBNC	-75.70
HB(CN)	-71.20
HC(NB)	-55.78
HN(CB)	-23.19
B + HCN	0.0
H + BCN	19.59
H + BNC	6.84
BH + CN	51.27

Table 11.1: Calculated energies of the insertion products in the boron atom - HCN reaction at the DFT-B3LYP / D95*level, adapted from Reference [347].

containing complexes were found, illustrating that the barriers to isomerization to the lower energy products can be surmounted. Clearly these systems would be ideal test cases for helium droplet study, given that the associated reaction dynamics could be significantly altered, such that the HC(NB) and HN(CB) isomers may be trapped behind their respective barriers.

11.2 Non-relativistic HCN + Ga calculations

In analogy with our calculations for the X + HCN reactions and those for B + HCN by Andrews [347], we have carried out a survey of the stationary points on the gallium - HCN potential with the composite CBS-Q and G2 methods and also at the UCCSD(T)/6-311++G(d,p) level. All of the computed energies are collected in Table 11.2, which include a zero-point energy correction. Because of the significant disagreement among the three methods, which is

[1]Note that parentheses will be used to denote cyclic products, and the atom not included in the parentheses is bonded to the hydrogen atom.

[2]In their original work only the total energy was given. In order to relate the insertion products to B + HCN, H + BCN, H + BNC, and BH + CN the energies for B, HCN, BH, CN, and H were recomputed at the original level of theory.

Species	CBS-Q	G2	UCCSD(T) / 6-311++G(d,p)
HCN + Ga (^{2}P)	0.0	0.0	0.0
GaH + CN ($^2\Sigma$)	52.00	53.67	59.07
H + GaCN	9.50	12.75	20.11
H + GaNC	8.63	23.38	22.86
HCN-Ga	-5.30	-3.84	-2.88
Ga-HCN	-4.17	-1.99	-[a]
HGaCN	-17.88	-15.16	-8.42
HGaNC	-13.94	-0.61	-0.91
HC(GaN)	-14.04	-[a]	-[a]
HCNGa	-12.02	-[a]	2.45
TS1	-9.13	-3.91	-[a]
TS2	-[a]	15.68	-[a]
TS3	-6.27	-3.25	-[a]

[a]No Convergence

Table 11.2: Calculated energetics (in kcal mol^{-1}) for the stationary points on the Ga + HCN PES including zero-point energy.

most likely due to the unconventional bonding present in several of the species, the calculations should be interpreted only in a qualitative fashion. In agreement with the previous calculations for B + HCN, we find several insertion products which lie lower in energy than Ga + HCN. The HGaCN reaction product is found by all three methods to be the global minimum, being bound by -15.16 kcal mol^{-1} at the G2 level. The barrier to this reaction (TS2) is predicted to be 15.68 kcal mol^{-1} (again at the G2 level), which is the largest of the three calculated barriers. While the reaction to form HGaCN could proceed in a single step (inserting into the C-H bond), the reaction to form HGaNC most likely occurs in two steps, in which gallium first reacts on the nitrogen end of HCN followed by a hydrogen atom migration. Although we have not attempted to calculate this barrier, given the rather high energy of H + GaNC, it is likely that the barrier should be similar to TS2. Two products from the gallium attack on the nitrogen end of HCN are also calculated, which could be intermediates to HGaNC formation, in agreement with our proposed two step reaction mechanism. The gallium analog of HB(CN), which was observed in the argon matrix work, could not be converged in our calculations.

In addition to the chemically bound species, the calculations also predict two linear van der Waals complexes, which represent the entrance channel complexes to the associated reactions.

In Figure 11.1, we draw a representative reaction diagram for Ga + HCN which summarizes

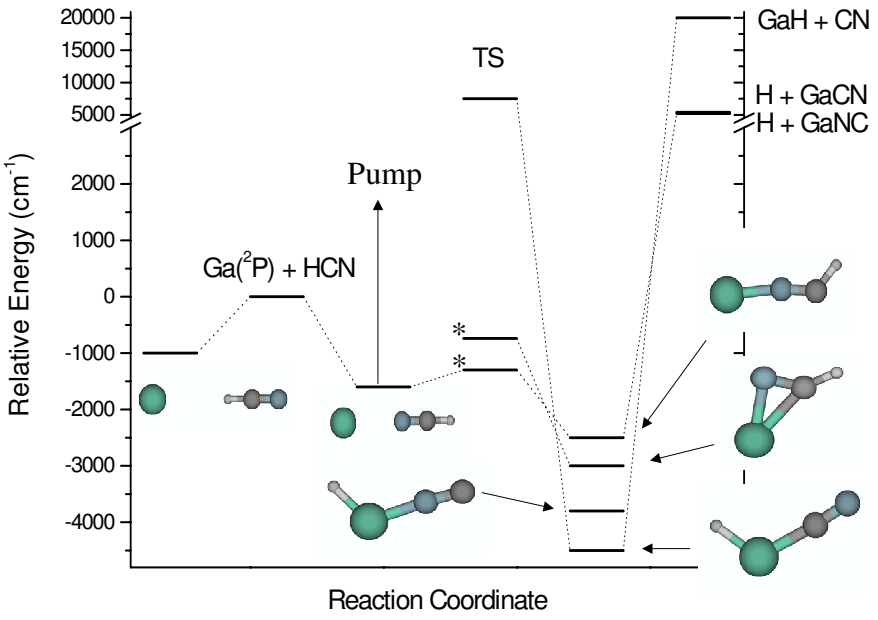

Figure 11.1: A gallium atom - HCN potential, based on *ab initio* calculations and our experimental results. Due to the disagreement between different levels of theory, the energies depicted in this figure should be regarded as qualitative in nature. In addition to two weakly bound van der Waals complexes, four insertion reaction products are calculated to be stable. The transition states connecting the entrance channel to the reaction products are also shown for three of the products, and two of these might be surmounted with a vibrational photon, as illustrated by the (pump) arrow. The two transition states labeled with an asterisk are calculated (at the G2 and CBS-Q levels) to lie below the entrance channel complexes, however we have experimental evidence to the contrary (see text).

the qualitative features of the PES inferred from the calculations. The important features of the PES are that several reaction products may be stable intermediates and that each may have a low barrier transition state which connects to the entrance channel valley. Due to the low energies of the barriers, vibrational excitation of the HCN (denoted by the vertical arrow in the figure) might be used to initiate the corresponding reactions. Clearly higher-level calculations are needed to further quantify the energetics of this potential.

Calculations have also been performed for the corresponding aluminum bearing complexes, which are in general similar to those found with gallium. One interesting difference is that

we could not stabilize a nitrogen bound van der Waals complex at higher levels of theory, suggestive that the barrier to this reaction is very low. Indeed, at the G2 level, the reaction to form HCNAl is found to be barrierless.

11.2.1 HCN - Ga 2D PES

To further quantify the long-range potential we have calculated two-dimensional PES's for the three spin-free adiabatic potentials (1A", 1A', 2A') at the RCCSD(T)/aug-cc-pVDZ+{332} level using MOLPRO [172], which are shown in Figure 11.2. The calculations incorporate Jacobi coordinates where R is the HCN center of mass - gallium distance and Theta is the angle between R and the HCN symmetry axis. $\theta = 0$ corresponds to the nitrogen bound HCN-Ga geometry. R and θ were incremented in steps of 0.1 Å and 20^0 respectively and a spline interpolation was used to smooth the surface. The HCN bond lengths; rCN = 1.1532 and rCH = 1.0655 Å were held fixed during the scans. In the application of the counterpoise correction procedure outlined by Boys and Bernardi [195], the default active space for electron correlation needed to be modified to achieve a consistent treatment of the basis set superposition error (BSSE). The problem arises because when calculating the energy of the cluster, the HCN (2σ) molecular orbital lies lower in energy than the highest Ga 3d orbital, which is shown in Table 11.3 for a sample RHF calculation. The default settings in MOLPRO were set to include the lowest 12 A' and 4 A" orbitals into the core (not correlated), which did not correspond to the same active space for a gallium atom calculation which does include all of the Ga 3d orbitals in the core. To correct this behavior, the calculation was restricted to always exclude the gallium $4s^2 3d^{10} 4p^1$ electrons from the core. Furthermore, as noted by Fishchuk *et al.* for Cl-HF [222], there is some choice in how counterpoise correction is applied due to the two A' states of the free gallium atom. Our procedure is the same as that reported for Cl-HF, in that the lowest RCCSD(T) energy of the free gallium atom was subtracted from both A' dimer energies which preserves the double degeneracy of the Π state for both linear geometries.

Symmetry label	RHF/cc-pVDZ orbital energy (Hartree)	Description
1.1	-378.8732	Ga 1s
2.1	-48.2173	Ga 2s
3.1	-42.5449	Ga 2p
4.1	-42.5449	Ga 2p
1.2	-42.5439	Ga 2p
5.1	-15.6113	N 1s
6.1	-11.3062	C 1s
7.1	-6.4116	Ga 3s
8.1	-4.5003	Ga 3p
9.1	-4.5003	Ga 3p
2.2	-4.4945	Ga 3p
10.1	-1.2379	HCN 2σ
11.1	-1.2039	Ga 3d
12.1	-1.2039	Ga 3d
13.1	-1.1966	Ga 3d
3.2	-1.1965	Ga 3d
4.2	-1.1941	Ga 3d
14.1	-0.8130	HCN 3σ
15.1	-0.5841	HCN $2\sigma^*$
16.1	-0.4952	HCN π_y
5.2	-0.4951	HCN π_x
17.1	-0.4113	Ga 4s
6.2	-0.1955	Ga 4p

Table 11.3: A summary of the energies of each of the resulting molecular orbitals taken from an RHF/cc-pVDZ calculation on HCN-Ga. The symmetry notation is taken from MOLPRO (X.1 = A', X.2 = A"). Since the HCN (3σ) orbital lies lower in energy than the molecular orbital which represents the highest Gallium 3d orbital, the default electron correlation parameters had to be changed to obtain a consistent treatment of the energy when performing counterpoise correction. In our calculations the active space for electron correlation was restricted to always exclude the gallium $4s^2 3d^{10} 4p^1$ electrons from the core.

In the linear HCN-Ga geometry ($\theta = 0^0$) the 1A" and 1A' states are found to correlate with the doubly degenerate $^2\Pi$ state and the 2A' state corresponds to the $^2\Sigma$ state, whereas for Ga-HCN the 1A" and 2A' correlate with $^2\Pi$ and 1A' is the $^2\Sigma$ state. This state correlation is exactly opposite to that observed in our HCN-Cl calculations (see Figure 6.3) due to the swap in electronic symmetry. Again that this is true is easily rationalized by simple electrostatics. Two linear isomers are predicted from the 2D surfaces, with calculated binding energies (D_e) of 1380 and 970 cm^{-1} for the HCN-Ga and Ga-HCN isomers respectively, in good agreement

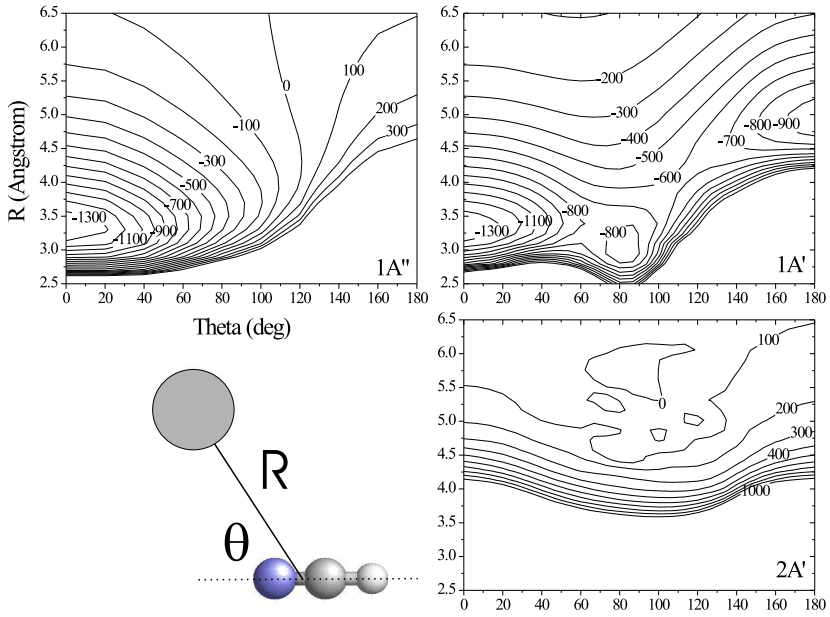

Figure 11.2: 2D Potential energy surfaces for the 1A", 1A', and 2A' symmetries of HCN-gallium calculated at the RCCSD(T)/aug-cc-pVDZ+{332} level. Basis set superposition error has been removed using counterpoise correction.

with the CBS-Q results. The transition state for isomerization between the two isomers is found at θ = 109^0, R = 4.01 Å at an energy of -610 cm^{-1}. Fully relaxed geometry optimizations were undertaken for the linear complexes, and the resulting molecular parameters are given in Table 11.4. A detailed comparison of these calculations with our experimental results will be presented in the next section. In addition to the two linear minima on the 1A' surface, a third well is observed which corresponds to a T-shaped isomer, in analogy with that observed in halogen-HX calculations [184, 186]. The barrier connecting the T-shaped and nitrogen bound minima is quite small, ~65 cm^{-1}, however it is this T-shaped geometry which corresponds to the HC(GaN) reaction product. In the T-shaped minimum the carbon-gallium distance is found to be ~3.0 Å , compared to ~2.0 Å in the reacted product. We have not been able to stabilize this weakly bound T-shaped isomer in subsequent geometry optimizations however.

Figure 11.3 shows a higher-level (RCCSD(T)/aug-cc-pVTZ+{332}) 1D cut of our 2D PES

HCN-Ga (Ga-HCN)	RCCSD(T) aug-cc-pVTZ	RMP2 aug-cc-pVTZ	RMP2 aug-cc-pVDZ
D_e (cm^{-1})	1380[a]	-	-
	(970[a])	-	-
R_{N-Ga} (Å)	2.707	2.641	2.732
(R_{H-Ga})	(3.250)	(3.238)	(3.216)
B_e (cm^{-1})	0.0753	0.0781	0.0737
	(0.0355)	(0.0356)	(0.0355)
ν_{shift} (cm^{-1})	-2.47	+0.09	+6.15
	(-95.94)	(-99.19)	(-118.62)
Intensity (km mol^{-1})	-	133.50	129.57
	-	(367.35)	(419.47)
μ (D)	4.50[b]	5.17	4.98
	(3.77[b])	(4.00)	(4.08)

[a]Taken from the 2D PES in Figure 11.2
[b]Finite field approximation [348]

Table 11.4: A summary of molecular properties for the HCN-Ga and Ga-HCN complexes from *ab initio* theory.

corresponding to the HCN-Ga geometry and includes a few more points at shorter internuclear distances. A discontinuity is observed in the $^2\Sigma$ surface at R = 2.6 Å which is a result of a switch in the electronic structure of the complex when covalent bonding of the gallium atom to the nitrogen atom occurs. Using the molecular orbitals for the reacted complex as a starting guess in subsequent single point energy calculations[3], we were able to partially map out this reacted potential to longer intermolecular distance, as shown in the figure. The point at which the van der Waals complex reacts (R $\leq$2.6 Å) is found at much higher energy than in our previous G2 calculations (see Table 11.2) which is due to the fact that the HCN geometry has been restricted. Also, that the $^2\Sigma$ state reacts at larger internuclear separation than the $^2\Pi$ state makes qualitative sense given that the unpaired orbital is in a more favorable orientation to interact with the HCN.

[3]The default setting in MOLPRO was to use the atomic densities.

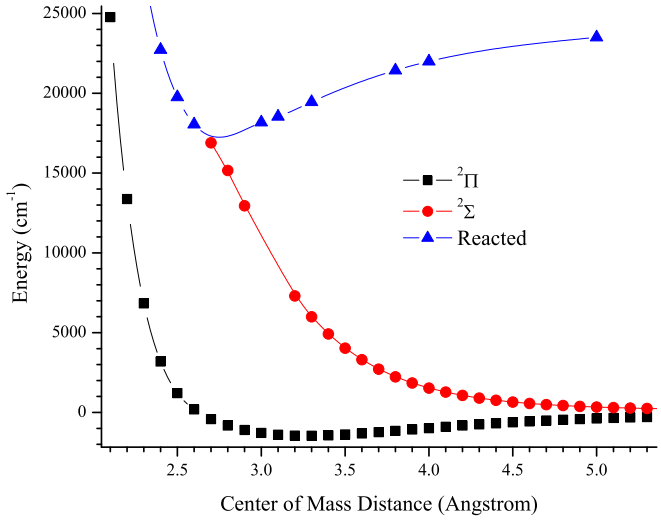

Figure 11.3: One-dimensional RCCSD(T)/aug-cc-pVTZ+{332} (non relativistic adiabatic) potentials for HCN - Ga . The three different curves are representative of the $^2\Sigma$ and $^2\Pi$ states, as well as a reacted complex.

11.3 Relativistic HCN + Ga calculations

In order to make quantitative comparisons with our experimental results we must include spin-orbit coupling into our potential energy surfaces. Using the theory laid out in Section 6.2.1, the relativistic potentials for HCN + Ga may be found by diagonalizing the (R dependent) matrix:

$$\begin{bmatrix} {}^2\Sigma & (2^{-1/2}A) & 0 \\ (2^{-1/2}A) & {}^2\Pi - A/2 & 0 \\ 0 & 0 & {}^2\Pi + A/2 \end{bmatrix}$$

The diagonalized relativistic and non-relativistic potentials for HCN + Ga are shown together in Figure 11.4 for both linear geometries of HCN+Ga. The legend on the graph for the $^2\Sigma_{1/2}$ and $^2\Pi_{1/2}$ states corresponds to the basis function with the largest mixing coefficient. Interestingly, the electronic character for the mixed states of the hydrogen bound isomer actually invert as the distance is decreased, and thus for the lowest energy potential at long range this state is mostly $^2\Pi$ like, but in the region of the minimum it is $^2\Sigma$ like. The bound states of these

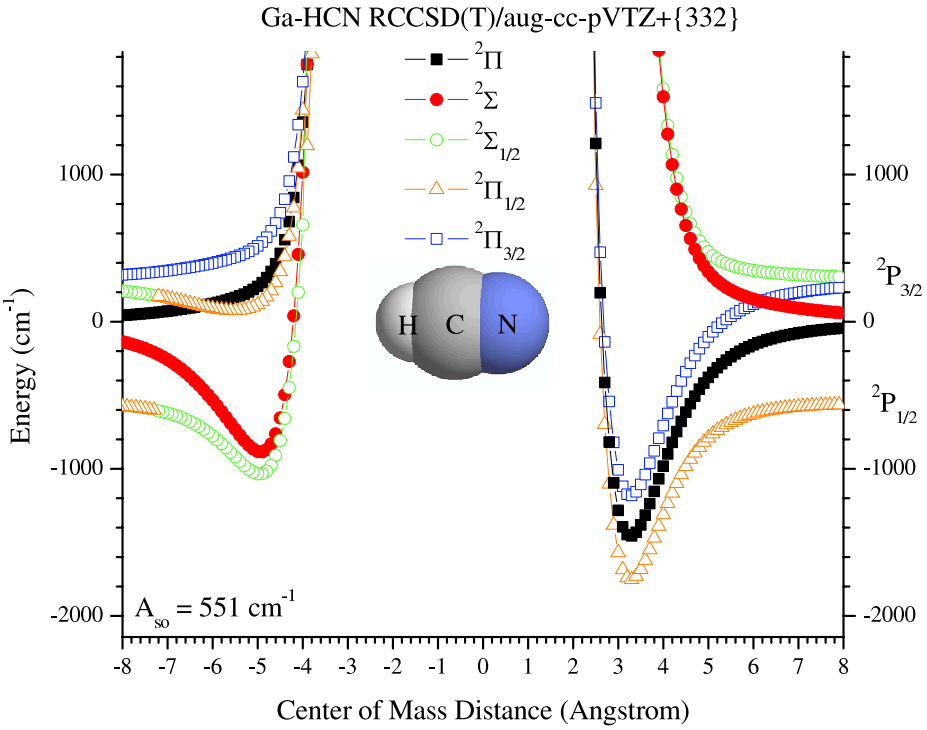

Figure 11.4: Relativistic adiabatic potential energy curves for the HCN-Ga complex derived from the *ab initio* results. (See text)

potentials were calculated numerically using the program Level [247] and the binding energies, rotational constants, and the van der Waals stretching frequencies are summarized in Table 11.5. To estimate the effects of CH stretching of HCN on the potentials, computations were also performed in which the HCN geometry was constrained to have a CH bond length of rCH = 1.09 Å, which is close to the equilibrium bond length for the v=1 state. In general, the excitation of HCN results in a slight increase in the binding energy of the complex which we attribute to an increased dipole - induced dipole interaction. As noted above, spin-orbit coupling can strongly influence the potentials, and indeed the dissociation energies of the complexes are significantly lowered due to the asymptotic degeneracy of the $^2\Sigma$ and $^2\Pi$ states. However the positions of the minima, which are reflected by the B values, are not greatly affected due to the large energy separation in the region of the minimum. Also, the spin-orbit interaction for the hydrogen bound isomer is sufficiently large that a small well develops in the upper $^2\Pi_{1/2}$ state. But since this state correlates with the excited spin-orbit component of the atom, we would not

Constant (cm^{-1})		Ga-HCN	
HCN $\nu_1 = 0$ ($\nu_1 = 1$)	$^2\Sigma$	$^2\Sigma_{1/2}$	$^2\Pi_{1/2}$
D_0	790.61	401.27 (439.16)	97.97
B_0	0.03549	0.03496 (0.03540)	0.02822
ν_{vdws}	46.81	43.13 (44.22)	17.40
		HCN-Ga	
	$^2\Pi$		$^2\Pi_{1/2}$
D_0	1403.91		1147.51 (1152.66)
B_0	0.08101		0.08057 (0.08059)
ν_{vdws}	76.59		74.96 (75.16)

Table 11.5: A summary of the computed properties for the HCN-Ga and Ga-HCN isomers from bound state calculations on our one-dimensional relativistic-adiabatic potentials. Note that the computed bound states for the $^2\Pi_{3/2}$ state are the same as those for the non-relativistic $^2\Pi$ state.

expect this isomer to be produced in helium.

11.4 Experimental results

From an *ab initio* calculation of the vibrational frequencies of the various reaction products (See Figure 11.12), we find that for the isomers which preserve a C-H stretching vibration, the frequency is strongly affected by the reaction, being shifted down to ~ 2700 - 2900 cm^{-1}. The helium droplet however, may be able to quench the corresponding reactions, and trap the species in the entrance channel, and thus we start our search in frequency region around 3300 cm^{-1} where the *ab initio* calculations (in Table 11.4) predict vibrational transitions for the pre-reactive complexes. Our experimental investigation starts with the pendular survey scan shown in Figure 11.5, taken with the FCL. The scan was recorded with the gallium oven heated to approximately 1200 K, at which point the signal associated with HCN monomer was significantly reduced, presumably due to the droplets picking-up gallium atoms. At this temperature the local pressure of gallium is estimated to be approximately 1×10^{-4} Torr from published vapor pressure curves [349]. This pick-up "cell" pressure is slightly larger than that usually needed to optimize for the pick-up of just one impurity, however in this case it is

reasonable given the relatively short effective path length of the oven. The nozzle conditions (40 Bar, 15 K) were such that a mean droplet size of 10000 helium atoms (before pickup) were produced. As is typically the case, several peaks in the survey scans can be attributed to the linear chains of HCN [36], including both free and bonded fundamentals of the C-H stretching vibrations. The peaks which grow in as the gallium oven is raised in temperature are highlighted in the figure. Initially, only the sharp peaks at 3301 and 3282 cm^{-1} were observed however after repeated scans, the other weaker features were determined to be related to gallium also. Since the *ab initio* calculations predict that at most 3 isomers (assuming that the

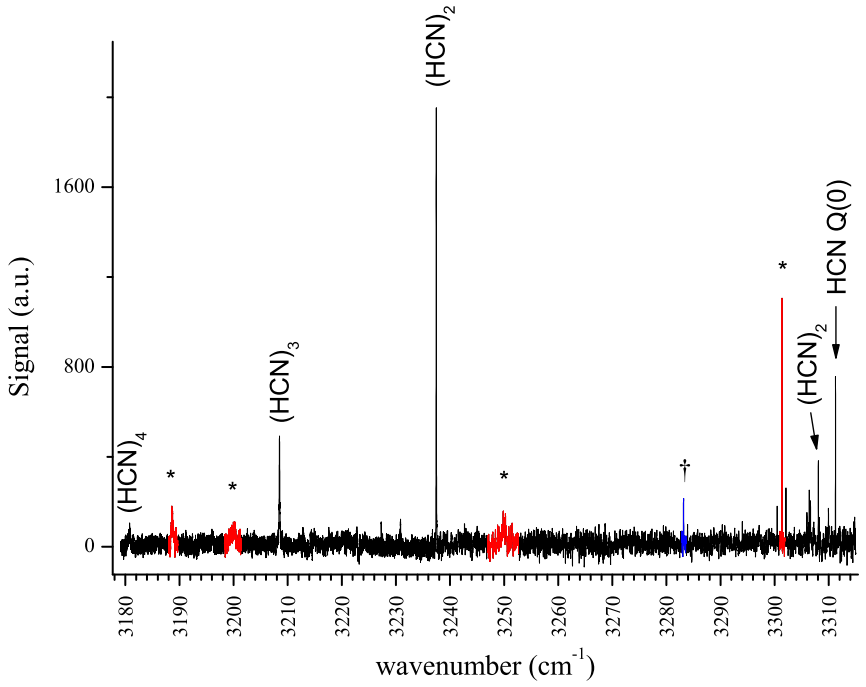

Figure 11.5: A pendular survey scan indicating the presence of gallium related complexes (marked with an asterisk). The peak marked with a † optimized for the pickup of a gallium atom, however also increased when air was introduced into the pickup cell and so it is related to an impurity. We assign the peak at 3301 cm^{-1} to the nitrogen bound HCN-Ga complex.

T-shaped isomer could be stabilized) should absorb in this frequency region, the observation of 5 new peaks hints that higher order clusters are being formed. To sort out the contributions to higher order HCN clusters, pick-up cell pressure dependence measurements were performed

and the results are shown in Figure 11.6. The peaks at 3301.30, 3249.88, and 3199.77 cm^{-1}

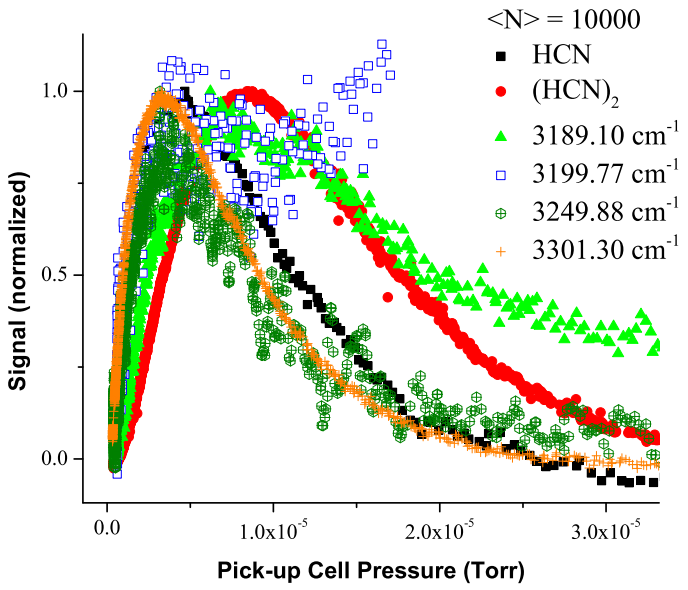

Figure 11.6: HCN Pick-up cell pressure dependencies of the peaks attributed to gallium related complexes in the pendular survey scan of Figure 11.5. The intensities of three of the peaks are observed to optimize at the same pressure as HCN monomer, suggesting they are all related to 1:1 complexes.

are found to optimize at the same pressure as HCN monomer confirming they are related to just one HCN. The peak at 3199.77 cm^{-1} is observed to decrease in intensity at pressures slightly higher than optimum for one HCN, but then increase again as the HCN pressure is raised further (going off scale in the figure), which is the result of an overlapping multimer band. The band at 3189.10 cm^{-1} optimizes at nearly double the pressure of HCN monomer, in good agreement with the PUC curve for the dimer. Not included in Figure 11.6, is the peak at 3283 cm^{-1} (marked by an † in the pendular scan) which was also found to optimize for 1 HCN. However we found that this peak also grew in intensity when air was introduced into the pickup cell, and thus we preliminarily assign it to an N_2-HCN-Ga complex. All of the peaks were found to optimize at the same oven temperature. Since our focus is on identifying the 1:1 complexes we will not discuss the higher order HCN clusters further.

We assign the most intense peak in the survey scan at 3301.29 cm^{-1} to the nitrogen bound HCN-Ga complex based on the observed frequency shift of -9.91 cm^{-1} from the HCN monomer. Although this frequency shift is somewhat larger than that predicted by the *ab initio* calculations presented in Table 11.4, it is clearly not in the region predicted for the Ga-HCN complex. In fact, it appears that the calculated vibrational frequency shift might not be converged given that the agreement gets increasingly better at higher levels of theory. Because spin-orbit coupling is likely to be important in this system, these harmonic frequency calculations are only semi-quantitative. From our 1D PES's which include SO coupling we found that the binding energy of the complex is increased by 5.14 cm^{-1} upon vibrational excitation of the HCN. Neglecting dynamical coupling of the different dimensions of the PES, this change in the binding energy upon excitation would result in a red-shift in the vibrational frequency of the same value, in qualitative agreement with our observation. A field-free spectrum of this band is shown in Figure 11.7A, along with simulations using two different $^2\Pi_{1/2}$ Hamiltonians, where the rotational temperature has been fixed at 0.37 K. In the first simulation (B), we assume a

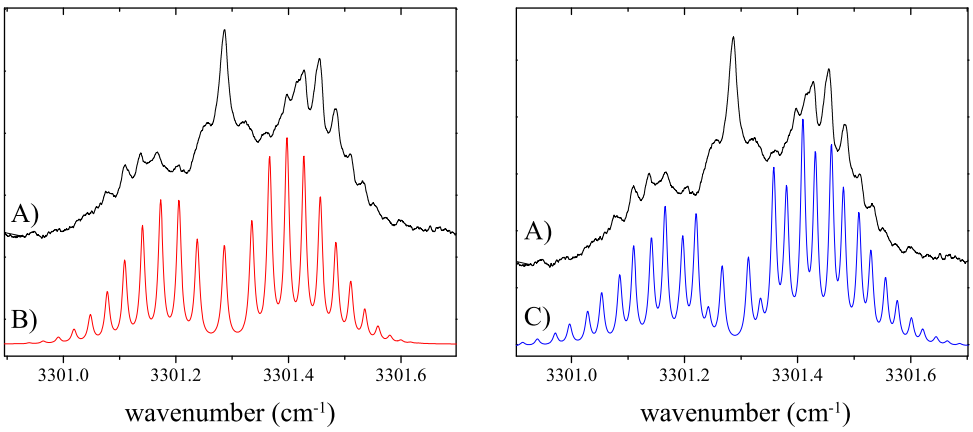

Figure 11.7: A field-free spectrum (A) of the band at 3301 cm^{-1} which we assign to the HCN-Ga complex. In the left panel (B) the spectrum is simulated using a pure $^2\Pi_{1/2}$ model, where as on the right (C), spin-orbit coupling has been taken into account. The later simulation shows large parity splittings which may resolve the discrepancy in the rotational constant reduction factor observed. (See text)

pure $^2\Pi_{1/2}$ model, and that the fine structure in the band is due to each of the different rotational transitions. Clearly the simulation is not in very good agreement with the experimental spectrum, most notably in the Q-branch intensity and the peak in the P and R branches. The rotational constant, B and centrifugal distortion constant, D for this simulation are given in Table 11.6. The rotational constant obtained from the simulation, B = 0.016(1) cm^{-1}, is a factor of 4.6 smaller than the *ab initio* calculations (B = 0.0753 cm^{-1} at the RCCSD(T)/aug-cc-pVTZ level), which is somewhat larger than that observed for most systems in helium (a typical value for the reduction factor on system of this size being 2.5 - 3.5) although a reduction of this magnitude is not unprecedented [69, 350].

HCN-Ga	Pure $^2\Pi_{1/2}$	Perturbed $^2\Pi_{1/2}$
ν_{shift} (cm^{-1})	-9.86	-9.86
B (cm^{-1})	0.0163	0.0270
D (cm^{-1})	7×10^{-6}	5×10^{-6}
μ (D)	5.3 ± 0.4	3.5 ± 0.4

Table 11.6: A summary of the fitted molecular constants for the HCN-Ga complex using two different model Hamiltonians. In the first a pure $^2\Pi_{1/2}$ complex is assumed, whereas in the second the $^2\Pi_{1/2}$ state is perturbed by the $^2\Sigma_{1/2}$ state by off-diagonal spin-orbit coupling. The large discrepancy in the rotational constants is due to a large parity splitting in the perturbed model. See text for details. Note that the dipole moment measurements come from fitting Stark spectra which are shown in Chapter 12.

What remains to be discussed now is the effect of the off-diagonal spin-orbit coupling on the infrared spectrum. Although we defer a full treatment of this interaction until Chapter 12, the simulated band structure for such a case is shown in Figure 11.7C. Qualitatively, the interaction of the $^2\Sigma_{1/2}$ state removes the degeneracy associated with the two $^2\Pi_{\pm 1/2}$ states, resulting in parity (lambda) doubling. The magnitude of the parity splitting incorporated into the simulation is based on a physically realistic model, and has a strong impact on the optimal rotational constant used to simulate the spectrum. For the simulation shown in Figure 11.7C, B = 0.0270 cm^{-1}. If one compares this rotational constant with the *ab initio* value we find that it is a factor of 2.79 smaller, which is in much better agreement with that observed for the majority of molecules in helium droplets. The unsatisfying feature of the new simulation is that the

Q-branch transitions are also split, and no longer stack up at the band origin, where substantial intensity is observed experimentally. The possibility that the vibrational band may also take on some $^2\Sigma_{1/2} \leftrightarrow ^2\Pi_{1/2}$ character should be considered due to the spin-orbit mixing, however we estimate (in Chapter 12) that these effects are negligibly small. A more in-depth discussion of these effects, and the resulting Stark spectrum for this band are deferred to Chapter 12. Despite the less than definitive rotational assignment, we are confident that the band at 3301.29 cm^{-1} is due to the HCN-Ga complex.

Given our preliminary characterization of HCN-Ga we now turn our attention to the Ga-HCN isomer. That this isomer could be formed is reasonable given that the barrier to isomerization (back to HCN-Ga) is approximately 350 cm^{-1} on the spin-free adiabatic 1A' surface. Indeed, many examples now exist where barriers of this magnitude have been observed to quench condensation of the complex to the global minimum in helium droplets [36, 39, 339]. In the frequency region of the bonded stretch of the linear HCN trimer (3208.54 cm^{-1}), a new peak is observed at 3200.0 cm^{-1} which matches up quite well with the *ab initio* vibrational frequency calculations for this isomer. The observed frequency shift for this peak from HCN monomer in helium is -111.4 cm^{-1} while *ab initio* calculations predict a shift of -95.94 (-99.19) cm^{-1} at the RCCSD(T) (RMP2) /aug-cc-pVTZ level. The approximate correction factor for the vibrational frequency due to the helium solvent is 5.97 cm^{-1} (based upon Figure 2.2) which again, further improves the agreement with theory. Due to the rather large linewidth observed for this peak a rotational analysis in not possible, however as mentioned above we have determined that this peak optimizes at nearly the same HCN pressure and Ga oven temperature as the peak we assign to HCN-Ga, which is suggestive of another 1:1 complex.

Close examination of several pendular survey scans revealed a broad feature at ~3250 cm^{-1}. HCN pressure and Ga oven temperature dependence measurements clearly show that this band optimizes at exactly the same gallium oven temperature, and nearly the same HCN pressure as that of the other two Ga related peaks. The fact that the HCN pressure dependencies for these peaks are not exactly the same is explained in Section 11.7.1. The frequency shift of this

band from the HCN monomer is measured to be -61.3 cm^{-1}, which is considerably different from both the predicted free and bonded stretches of the two linear complexes. It is tempting to assign this peak to the T-shaped complex for which our potential showed a very shallow minimum, however more telling is the frequency shift of this band from the peak we assign to the hydrogen bound complex. The energy separation between these two peaks is 49.80 cm^{-1} which agrees quite well with the van der Waals stretching frequency from the 1D bound state calculations presented above, namely 43.13 cm^{-1}. We preliminarily assign the peak at 3249.87 cm^{-1} to a combination band of the Ga-HCN isomer consisting of the CH and the intermolecular stretches. Given the very weak signals associated with these peaks, we need more supporting evidence for the assignment, which will come in the form of double resonance experiments, and in comparison with aluminum and indium results presented below.

11.5 Comparisons with aluminum and indium

To aid in our interpretation of the gallium results, experiments were performed with aluminum and indium atoms, in an attempt to observe their respective entrance channel complexes with HCN. The pendular survey scans in Figure 11.8 show Al, Ga, and In + HCN related peaks, and the 1:1 complexes have been marked with an asterisk.

11.5.1 Al-HCN and In-HCN

First let us focus on the hydrogen bonded region where we assigned the Ga-HCN complex at 3200 cm^{-1}. In the aluminum experiments a strong peak at 3192.07 cm^{-1} is observed which is in good agreement with the *ab initio* vibrational frequency of 3208.12 cm^{-1} at the RMP2/aug-cc-pVTZ level, which has been scaled to the HCN monomer frequency in helium droplets. Of each of the metal atom experiments, aluminum should be the most accurately described by the *ab initio* calculations due to the relatively small spin-orbit coupling constant (A = 74.7 cm^{-1}). Correcting for the effects of helium solvation on the vibrational band origin

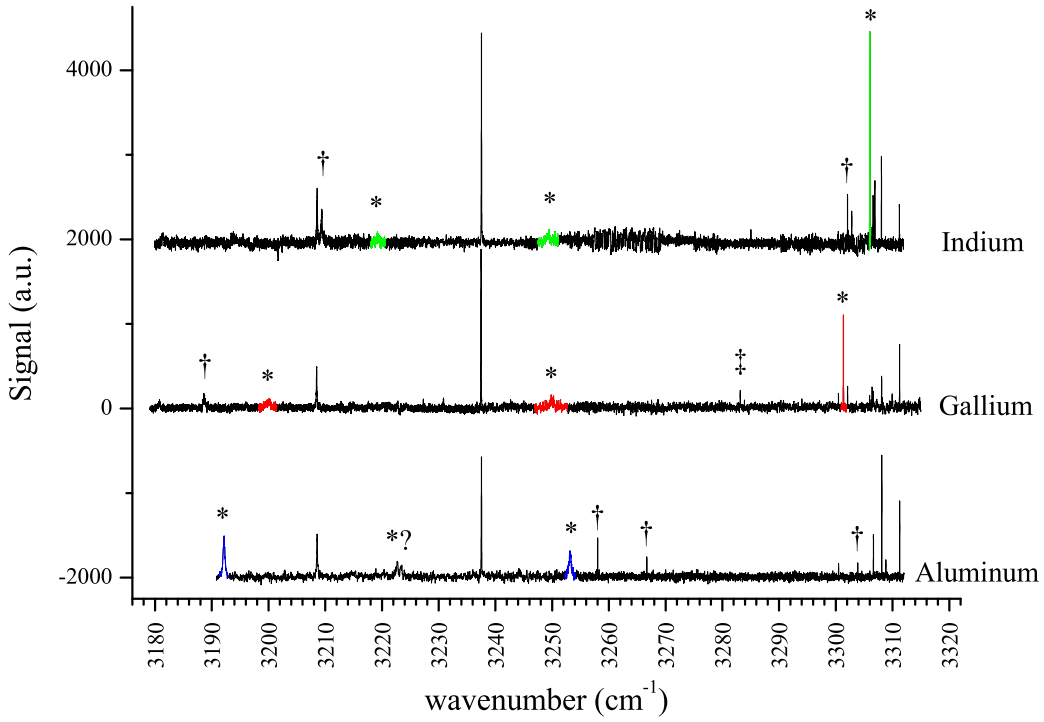

Figure 11.8: Three pendular survey scans corresponding to separate indium, gallium, and aluminum + HCN experiments. New peaks which are related to the oven are highlighted and those marked with an asterisk correspond to 1:1 complexes. Peaks marked with a † are higher order HCN clusters.

we estimate a gas-phase origin of 3198.32 cm^{-1}, in good agreement with the *ab initio* calculations. A second strong peak is observed at 3254 cm^{-1} which we again assign to a combination band of the C-H and intermolecular stretches. From the energy separation between this band and the fundamental, the van der Waals stretching frequency is determined to be 60.96 cm^{-1}. The calculated harmonic frequency (RMP2/aug-cc-pVTZ) for this vibrational mode is 69.14 cm^{-1}, in qualitative agreement with that observed. To obtain a more accurate representation of the potential, 1D potential surfaces were calculated for this isomer at the RCCSD(T)/aug-cc-pVTZ+{332} level, incorporating the effects of spin-orbit coupling as done above for gallium. The molecular parameters determined from the bound states of this potential and those from separate geometry optimizations (which neglect spin-orbit coupling) are presented in Table

11.7. From bound states of the 1D potentials, the intermolecular stretching frequency is cal-

RCCSD(T)/aug-cc-pVTZ	Al-HCN	Ga-HCN	In-HCN (ECP)
ν_{CH} (cm^{-1})	3339.27	3337.71	
$\nu_{CH-scaled}$ (cm^{-1})	3220.70	3219.20	
ν_{vdws} (cm^{-1})	69.14 (59.19[a])	54.58 (43.13[a])	(30.52[a])
D_e[a] $^2\Sigma$ (cm^{-1})	798.29	813.31	823.75
D_e[a] (D_0[a]) $^2\Sigma_{1/2}$ (cm^{-1})	726.36 (695.83)	423.89 (401.27)	238.86 (223.12)
R_{X-H} (Å)	3.303	3.250	3.461

[a)] Taken from bound state calculations on 1-D PESs similar to Figure 11.4.

Table 11.7: A summary of the molecular properties for Al, Ga, and In-HCN computed at the RCCSD(T)/aug-cc-pVTZ level. The calculations labeled (ECP) incorporated a small core relativistic pseudopotential (aug-cc-pVTZPP [196]) for the indium atom in which 28 core electrons were replaced by the ECP. Binding energies have been counterpoise corrected and the scaled frequencies obtained by comparing a separate HCN calculation with the band origin observed in helium droplets. The effects of spin-orbit have been taken into account to yield the $^2\Sigma_{1/2}$ binding energies with the theory developed in this work.

culated to be 59.88 cm^{-1}, substantially improving the agreement with that observed, thereby lending further support to our assignment.

A third set of experiments was carried out with indium. Extensive searching led to the identification of the peaks highlighted (in green) in Figure 11.8, identified as 1:1 complexes, which are barely visible in the initial survey scan. By comparison with our earlier assignments, the peak at 3219.1 cm^{-1} is assigned to the fundamental CH stretching vibration of In-HCN, and the peak at 3249.11 cm^{-1} to the combination band. From the separation between these peaks the intermolecular stretching frequency is determined to be 30.01 cm^{-1} which is in excellent agreement with that determined from our bound state calculations, namely 30.52 cm^{-1}. It is important to point out that the experiment really probes the van der Waals stretching frequency in the excited H-CN vibrational state, whereas strictly speaking our calculations were for the ground state. The calculated intermolecular stretching frequency on the "excited" 1D In-HCN surface is 31.72 cm^{-1}, which although yields slightly worse agreement with experiment, gives the important physical picture that the effect of the excitation is quite small.

11.5.2 HCN-Al and HCN-In

Next let us first focus our attention on the free CH stretching region around 3300 cm^{-1}, where we expect the nitrogen bound complexes to absorb. In agreement with the gallium experiment, a strong peak is observed in the indium survey scan which we assign to a HCN-In complex. The band origin of this complex is 3306.01 cm^{-1}, red-shifted from HCN monomer by 5.19 cm^{-1}. The calculated frequency shift from the bound states on the 1D potentials is 4.73 cm^{-1} in excellent agreement with that observed. The field-free and Stark spectra for this band are shown in Figure 11.9 (A) and (E) respectively. In analogy with the HCN-Ga

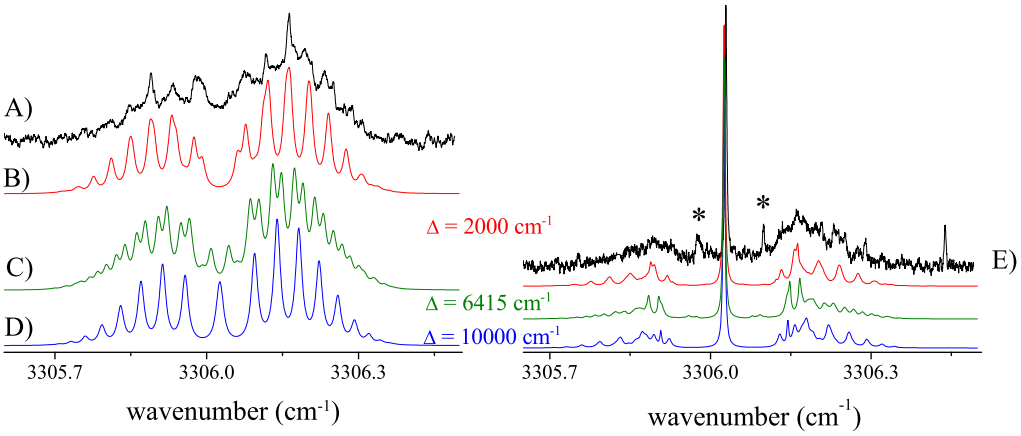

Figure 11.9: Rotationally resolved field-free (A) and Stark spectra (E) for the HCN-Indium complex observed in helium droplets. A series of simulations (B-D) are also shown which illustrate the effect of the transition from Hund's case (a) to case (c) on the possible spectra. The peaks marked with an asterisk correspond to higher order clusters. See Chapter 12 for further details on the simulations. The Stark spectrum was recorded under the presence of a 2.542 kV cm^{-1} electric field.

spectrum, we find that the field-free spectrum of HCN-In does not fit well to a pure $^2\Pi_{1/2}$ model (Figure 11.9D) which is the result of strong off-diagonal spin-orbit coupling. Instead, the spectrum more appropriately conforms to Hund's case (c) rather than case (a). A simulation using intermediate coupling is shown in Figure 11.9B. For details on the simulations the reader is referred to Chapter 12. The rotational constant obtained from the simulation is B = 0.023

cm^{-1} which is a factor of 2.64 smaller than that predicted from our 1D potentials (including SO coupling), namely B_{calc} = 0.0608 cm^{-1}. This value for the B reduction lends supporting evidence for that used for gallium, where there is some discrepancy in the experimentally observed and predicted spectra.

From the comparison of the three survey scans in Figure 11.8, it is apparent that there is no peak that corresponds to a nitrogen bound aluminum complex. Instead, several weaker features were observed, which could be assigned to higher-order complexes. One possible explanation for this observation is that the HCN-Al complex simply reacts even in the helium droplet. This is reasonable given that MP2/aug-cc-pVTZ calculations did not find a stable HCN-Al isomer, instead it always spontaneously fell directly into the HCNAl product well. Since we have yet to scan the region of the infrared spectrum where the reaction products are predicted to absorb, we do not have a definitive identification of these complexes. As noted above however, in the survey scans other weaker peaks are observed which can be attributed to aluminum bearing complexes with more than one HCN. One possibility is that these peaks are the result of a barrierless reaction (to form one of the 4 different products), and then a second HCN is added to the droplet to form a new complex. That this may be possible is due to the unique growth process in helium. Due to the multitude of possible reaction products and the multi-dimensional potential associated with the second HCN, there are many possible weakly bound complexes. For the pendular peak at 3266 cm^{-1} we were able to record field-free and Stark spectra, which are shown in Figure 11.10. The Stark spectrum was recorded under the presence of a 5.103 kV cm^{-1} electric field. Based on the fact that the spectrum resembles a linear rotor, and that the spectrum is in the hydrogen bonded frequency region of HCN, we searched via *ab initio* calculations for possible products which may exhibit these properties. A reaction product which shows good agreement with experiment is drawn in the figure and its properties are summarized in Table 11.8. Although the complex is not exactly linear, the resulting A rotational constant would be too large to allow significant population in the excited K states at the temperature of the droplets, and thus the resulting K = 0 $\leftarrow$ 0 band would be

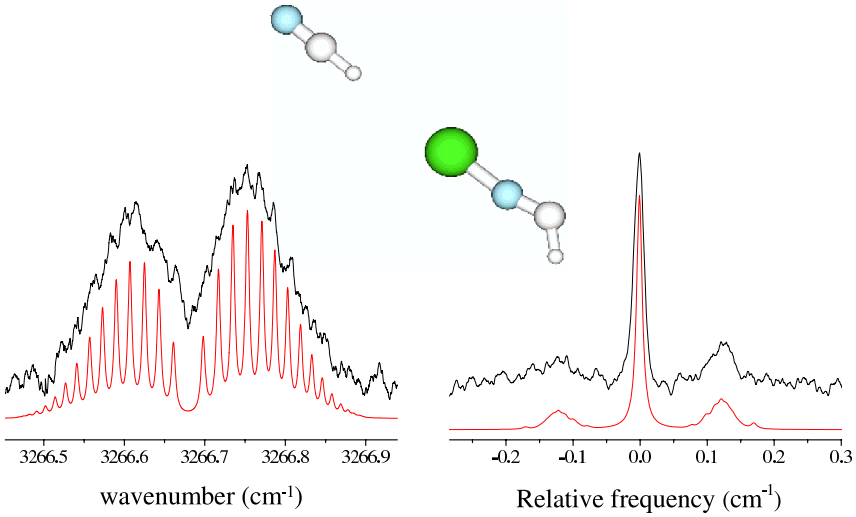

Figure 11.10: Field-free (A) and Stark spectra (C) for a band that we preliminarily assign to a complex between a HCNAl reaction product with a second HCN. Pickup cell pressure dependence measurements indicate that this band corresponds to 2 HCN's and MP2 calculations for the drawn structure are in qualitative agreement with the molecular constants derived from the simulations of the spectra. See Table 11.8.

indistinguishable from that of a linear rotor. One can see that the agreement with theory is

Constant	UMP2/aug-cc-pVDZ	Experiment
ν_0 (cm^{-1})	3260.56	3266.68
B (cm^{-1})	0.0223	0.0093
μ (D)	3.54	3.5(3)

Table 11.8: A summary of the experimental and UMP2 molecular properties of the complex between HCNAl and a second HCN which is weakly bound to the Al in a hydrogen bonded arrangement. The calculated band origin has been scaled to the HCN monomer band origin in helium. The experimental rotational constant is reduced by a factor of 2.4 compared to the calculations, which is necessary to account for the effects of the helium, providing additional support for our assignment.

quite good lending support to this preliminary assignment. There are also several other small peaks which could be related to structures of this type. Apparently the barrier in this system is low enough that the reaction takes place for aluminum, but is too large for gallium and indium, thus stabilizing the nitrogen bound pre-reactive complex in those cases.

11.6 Double resonance experiments

The double resonance (DR) technique discussed in Chapters 9 and 10 showed that it was possible to transfer population between two weakly bound isomers, namely HF-HCN and HCN-HF, upon absorption of an infrared photon [40]. For systems in which the reaction barriers are smaller than the vibrational energy, it then may also be possible to photo-induce the corresponding reaction to generate novel reaction intermediates and to study the associated orientational effects of initiating the reaction from a well defined starting point.

The IR-IR DR experiments performed here are nearly identical to those described in Chapters 9 and 10 however a home built PPLN-OPO was used as the pump laser (for details see Appendix A), which is fixed in resonance with the maximum of a pendular peak, while the FCL was used to scan for the products. Since our previous results indicate that aluminum reacts with HCN when approaching from the nitrogen end, and gallium and indium do not, the barrier to reaction might be quite small, making these complexes ideal for this study. Figure 11.11 shows the single (A,B) and double (C,D) resonance pendular spectra for pumping and probing the HCN-Ga and HCN-In complexes. It is immediately obvious from the DR spectra that there is a qualitative difference in the dynamics of these two complexes following vibrational excitation. The DR spectrum for HCN-In is reminiscent of that observed for HCCCN monomer, which tells us that all of the population which is excited simply cools back down to the ground state. Indeed, when we integrate the areas of the hole and pile[4], we find that the pile has 96% of the area of the hole, where this small percentage of lost population is in agreement with that estimated for loss by droplet deflection. In contrast for HCN-Ga, we are able to completely burn away the signal to baseline, indicating that 100% of the population has been lost.

These results raise the question about the fate of the excited HCN-Ga population. As

[4]The hole corresponds to a loss of population and the pile is the recovery of this population but in a smaller droplet size. That these two contributions do not lie on top of one another is due to an inhomogeneous broadening effect due to the droplet size distribution.

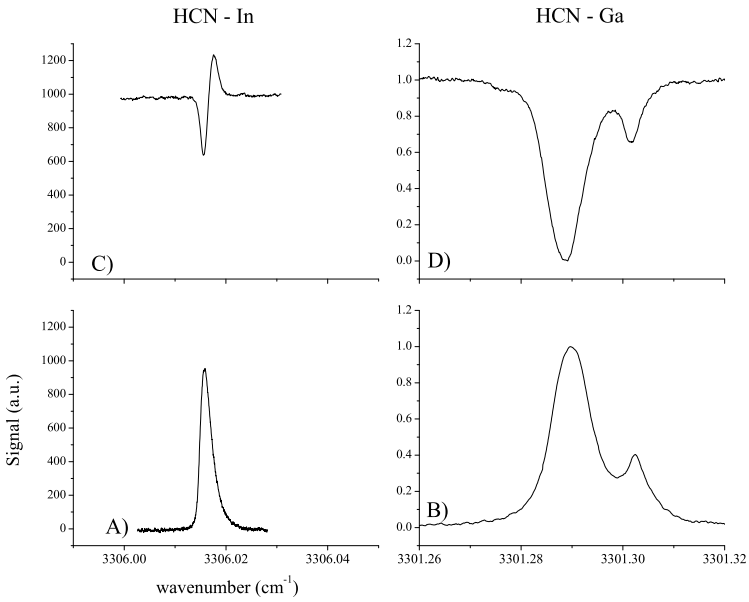

Figure 11.11: Single (A,B) and double (C,D) resonance pendular spectra for the HCN-In and HCN-Ga complexes respectively. The double resonance spectra correspond to the pump laser tuned to the maximum of the band and probing with the FCL. A striking difference in the dynamics of these two complexes upon vibrational excitation is revealed, namely that 100% of the HCN-Ga population is depleted, whereas 96% percent of the excited HCN-In returns back to the ground state. The small percentage of population loss for HCN-In can be attributed to the effects of droplet deflection as shown in Chapter 9, however the complete loss of HCN-Ga is attributed to photo-induced reaction.

we saw in Chapter 10, one possibility is that the complex simply isomerizes to the Ga-HCN isomer. We have performed complementary double resonance experiments in which HCN-Ga is pumped and the probe laser set to monitor Ga-HCN. Although the associated signal to noise ratio of the Ga-HCN spectrum limits our sensitivity to detect the population transfer, we estimate that it must be less than 25%. Clearly, a significant fraction of population is unaccounted for. To rule out any possibility of ejection of one or more of the fragments from the droplet, which would certainly result in lost population of HCN-Ga, DR experiments were also performed by pumping HCN-Ga and probing both gas-phase, and helium HCN monomer transitions. Again, no transfered population was observed for these species, ruling out this possibility. The most interesting possibility is that upon vibrational excitation the complex

reacts, which is very reasonable given that the calculated barriers are predicted to be smaller than our photon energy of 3301 cm^{-1}. The key experiment to prove this hypothesis will be a pump-probe study in which the HCN-Ga complex is pumped to initiate the reaction, and the probe laser is scanned to identify the reaction products. Shown in Figure 11.12 are the scaled harmonic vibrational frequencies for the reacted HCN+Ga products at the RMP2/aug-cc-pVDZ level. For the isomers which preserve the C-H bond, the C-H stretching frequency is predicted

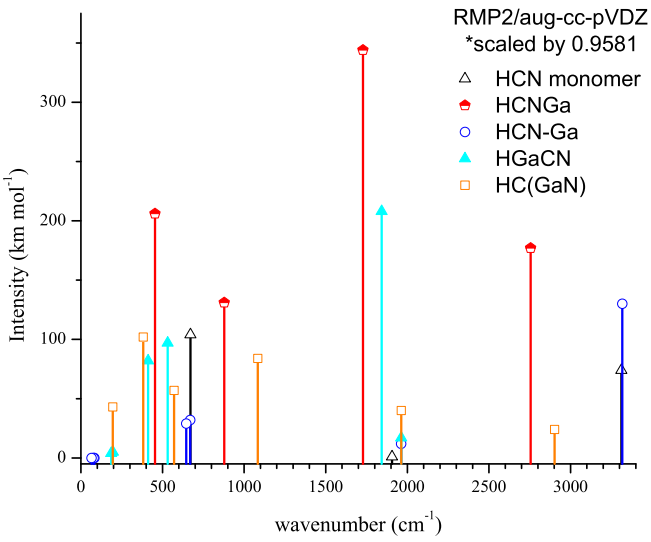

Figure 11.12: Calculated vibrational frequencies of the possible HCN + Gallium reaction products. Also included for comparison are HCN monomer and the van der Waals HCN-Ga complex calculated at the same level of theory. The scaling factor was derived by comparing the HCN monomer C-H vibrational harmonic frequency with that observed in helium.

to shift strongly to the red because the hybridization on the carbon atom changes substantially. The reaction products are predicted to absorb in a totally different spectral region, which we have not yet probed. If these complexes are observed it will be particularly interesting to see whether any reacted products are formed without the vibrational excitation, such as predicted for the aluminum case.

We next turn our attention to the vibrational / reaction dynamics of the hydrogen bound Ga-HCN complex. Figure 11.13, shows the single (B, F, and D) and double (A, E, and C) resonance spectra for selectively pumping HCN-Ga, Ga-HCN, or the combination band of the Ga-HCN

isomer and probing HCN-Ga respectively. The signal to noise ratio of the single resonance

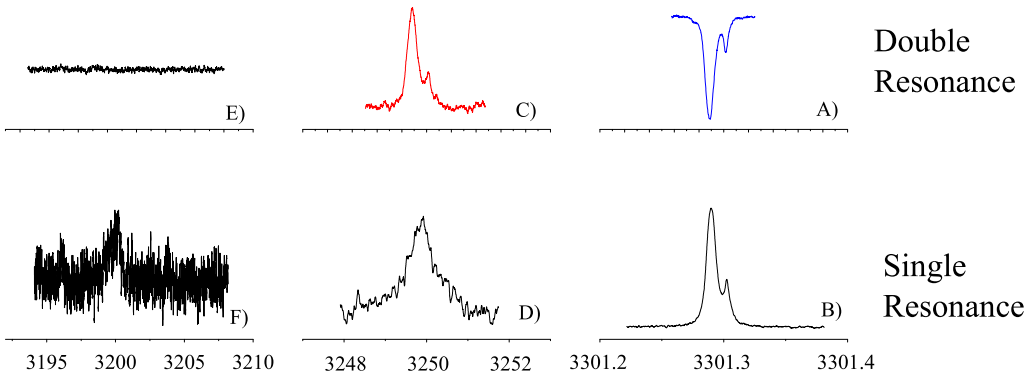

Figure 11.13: Single resonance infrared spectra for HCN-Ga (B), Ga-HCN (F), and the combination band of Ga-HCN (D). Double resonance spectra are also shown for pumping HCN-Ga and probing HCN-Ga (A), pumping Ga-HCN and probing HCN-Ga (E), and pumping the combination band of Ga-HCN and probing HCN-Ga (C). All spectra were recorded under pendular conditions to maximize the pumping efficiency. The results show that some degree of population transfer is observed when pumping the combination band, however no transfer is observed when pumping the fundamental.

scans for the fundamental and combination bands of Ga-HCN are a bit misleading because the combination band has been averaged with much longer integration times. In fact, the peak signal levels on the fundamental and combination band are approximately equal as seen from the initial survey scan, so that our pumping efficiency in the double resonance experiment should be approximately the same in these two cases. Figure 11.13A shows the result of pumping and probing the CH vibration of HCN-Ga which was already shown in Figure 11.11. This double resonance spectrum tells us that 100% of the initial HCN-Ga population is lost by the excitation process. Figure 11.13C was recorded by pumping the combination band of Ga-HCN, and probing HCN-Ga which shows some degree of population transfer. Finally, Figure 11.13E shows the result of pumping the fundamental CH vibration of Ga-HCN, and probing HCN-Ga, showing no transfer of population. It is interesting that population transfer (to HCN-Ga) is observed when pumping the combination band of Ga-HCN, however none

is observed when pumping the fundamental. This could be the result of the intermolecular stretching coordinate, which lies directly on the dissociation coordinate and thus could facilitate the rearrangement. Because the ultimate fate of excited weakly bound complexes in the gas-phase is often vibrational predissociation, pumping the fundamental band of Ga-HCN should, on some timescale, also result in dissociation if this complex were in the gas-phase. This is especially true for a hydrogen bonded species where strong coupling between rCH and R might be expected. The DR results indicate that the rate of cooling provided by the helium is competitive with the dissociation, and so localizing the energy in the intermolecular vibration enhances the likelihood that the two fragments come apart before the helium acts to quench the available energy. Additional DR experiments were carried out pumping and probing both vibrational modes of the Ga-HCN complex (not shown) in order to observe the corresponding depletion of Ga-HCN (upon excitation of the combination band), given that it is clear that some population is transfered to HCN-Ga. No DR depletion signals were observed for either case of pumping and probing the bands at 3200 or 3250 cm^{-1}. Based on our sensitivity, we estimate that the degree of population transfer must be smaller than 25%, which indicates that most of the molecules cool back down to their original ground state. Thus it is clear that when pumping the Ga-HCN isomer, a significant amount of population does not go on to react, in contrast to that observed for HCN-Ga, suggesting that the nitrogen end of HCN is indeed more reactive as predicted from our calculations.

11.7 Discussion

We begin this discussion by examining several observations for the hydrogen bound M-HCN complexes. When one compares the vibrational frequencies of the fundamentals in each of the Al, Ga, and In-HCN complexes (3192, 3200, and 3219 cm^{-1}) we see that the band origin is strongly shifting to the blue as one goes down the periodic table, a trend that is opposite to that observed in our earlier halogen work (X-HCN and X-HF), where a greater red-shift in

frequency was observed for the heavier atoms. A large red-shift in frequency for a hydrogen bound HCN complex can be shown to be a result of an interaction that weakens the C-H bond, which for this atom-molecule system results mostly from a dipole-induced dipole interaction of the form [351]:

$$V = -\frac{4\mu^2\alpha}{(4\pi\epsilon_0)^2\, r^6} \tag{11.1}$$

Ab initio calculations on the X-HCN and X-HF complexes reveal that the complexes have increasingly larger binding energies as one goes down the periodic table, which we attribute to the increasing halogen atom polarizabilities, α. Note that the distance between the halogen atom and the HCN center of mass also increases as one goes down the periodic table however the increase in α overwhelms this effect. A similar argument may be applied for the metal atom complexes and one might predict that the heavier metal atoms would also have larger binding energies, and a correspondingly larger red-shift of the HCN vibrational frequency. These trends are predicted in our non-relativistic *ab initio* calculations for gallium and aluminum, which is again opposite to that observed. While it is certainly true that gallium atoms are more polarizable than aluminum atoms, the dominant interaction here is the spin-orbit coupling, which actually makes the overall interaction weaker as we go down the periodic table (See Table 11.9), producing a smaller effect on the H-CN vibrational frequency as the spin-orbit coupling increases. For the halogen atom complexes this interaction is not as important because the ground state configuration is $^2\Pi_{3/2}$ which does not interact (via a first order process) with the $^2\Sigma_{1/2}$ state.

In order to estimate the contribution to the frequency shift resulting from an increase in the binding energy of the complex one can compare the bound states from the 1D potential energy surfaces with the HCN restricted in a v = 0 or v = 1 like geometry, as we did for the nitrogen bound complexes. A summary of the lowest calculated bound state energies is given in Table 11.9 for both the non-relativistic ($^2\Sigma$) and relativistic ($^2\Sigma_{1/2}$) potentials. One can see the spin-orbit corrected binding energies of the complexes decrease in the order of Al > Ga > In, in good agreement with the ordering predicted on the basis of the frequency

Energy (cm^{-1})	In-HCN	Ga-HCN	Al-HCN
$^2\Sigma$ ($\nu_{CH} = 0$)	800.52	790.61	767.72
$^2\Sigma$ ($\nu_{CH} = 1$)	845.59	837.03	811.73
$^2\Sigma_{1/2}$ ($\nu_{CH} = 0$)	223.12	401.27	695.83
$^2\Sigma_{1/2}$ ($\nu_{CH} = 1$)	244.25	439.16	739.69
ν_{exp}	3219.1	3200.0	3192.07

Table 11.9: A summary of calculated binding energies (D_0) for the In, Ga, and Al-HCN complexes determined from bound states of 1D potential energy surfaces at the RCCSD(T)/aug-cc-pVTZ+{332} level. The states labeled by $^2\Sigma$ represent non-relativistic adiabatic potentials taken directly from *ab initio* whereas those labeled by $^2\Sigma_{1/2}$ incorporate spin-orbit coupling. The excitation of HCN to the first excited CH stretching vibration was simulated using two different CH bond lengths in the calculations, namely rCH = 1.0655 and 1.090 Å, and the difference in binding energies between these two states closely parallels the experimental frequency shift.

shifts. Based solely on the differences in binding energies, the calculations predict red-shifts of 45.07 (21.13), 46.42 (37.89), and 44.01 (43.86) cm^{-1} for the (spin-orbit corrected) potentials of In, Ga, and Al-HCN respectively. Clearly these frequency shifts are much smaller than that observed experimentally illustrating that the coupling of R and rCH is quite strong, as one might expect for a hydrogen bound isomer. Since the bound states of Ga-HCN are currently being computed by the group of Avoird on a 2D potential, it will be instructive to compare their results with our 1D model. Interestingly, our model which includes spin-orbit coupling does predict the relative spacing of the different metal atom complexes, namely ν_{Ga-HCN}- ν_{Al-HCN} = 6.12 cm^{-1} and ν_{In-HCN}- ν_{Ga-HCN} = 16.76 cm^{-1}, compared with the 7.93 and 19.1 cm^{-1} shifts observed experimentally.

In order to interpret all of the observed features in our spectra, we have assigned three peaks to combination bands based on their agreement with theoretical calculations. What is slightly unusual about this assignment is that the combination band intensities are found to be comparable with those found for the fundamentals, whereas typical combination bands are much weaker. For these open shell complexes however, an additional source of mechanical anharmonicity [351] may come from state mixing induced by the spin-orbit coupling, possibly resulting in intensity borrowing from the fundamental C-H stretching vibration to the combina-

tion band. Clearly a theoretical prediction of the intensities for these combination bands would be helpful in assigning our spectra, and to further our understanding of the couplings present in these multi-dimensional potential energy surfaces.

The observation of combination bands is also of substantial interest in helium droplet spectroscopy due to their role in facilitating vibrational relaxation to the fundamental modes of the droplets (phonons, ripplons, etc...). To our knowledge, only one other example of a low frequency combination band has been observed in helium, namely that of HF dimer [166]. In that study, the $\nu_2 + \nu_5$ "geared bend" and $\nu_1 + \nu_4$ "van der Waals stretch" were observed and when compared with the gas-phase, a 4% increase in the vibrational frequencies ($\nu_4 = 132.98$, $\nu_5 = 185.77$ cm^{-1}) was determined. Such a small influence of the helium solvent again allows us to make direct comparisons with our calculations. The linewidth of these bands were Lorentzian and are much broader than observed in the gas-phase (0.8 and 1.7 cm^{-1} for the $\nu_2 + \nu_5$ and $\nu_1 + \nu_4$ bands respectively), suggestive that the droplet somehow facilitates relaxation. The broader linewidth of the latter was attributed to a stronger coupling of the helium to the ν_4 state due to its lower energy. Despite the low signal to noise observed for indium and gallium, using signal averaging we were able to extract quantitative values for the linewidths (and thus the lifetimes) of these states, which are plotted against the van der Waals stretching frequency in Figure 11.14. Note that the error bars in the figure correspond to the linewidth axis. As one can see there is a strong increase in the lifetime as the intermolecular stretching frequency is increased. Unfortunately we do not have gas-phase data available to compare this behavior with the isolated complex, however the trend is consistent with a vibrational relaxation time that is determined by the energy of the low frequency mode in the combination band, and the lower this vibrational frequency the easier it is to excite the fundamental modes of the droplet due to the higher density of states at these energies (See Section 2.3.3).

Next we focus our attention back to HCN-Ga which did not fit well to our simulations. A high-resolution scan of the pendular spectrum for HCN-Ga is shown in Figure 11.13, showing two partially resolved peaks which are separated by 0.0132 cm^{-1} with an intensity ratio of

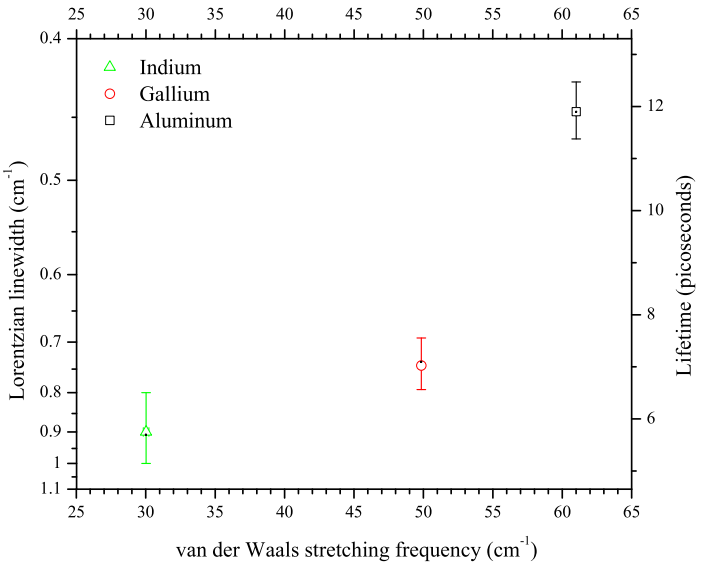

Figure 11.14: A plot of the excited combination band (CH stretch plus intermolecular stretch) vibrational state lifetime of the Al, Ga, and In-HCN complexes as a function of the van der Waals stretching frequency. The trend in lifetime is consistent with the idea that the presence of the low lying vibration acts to strongly couple the excited state to the fundamental modes of the droplet. The error bars are relative to the linewidth axis. axis.

7.3:1. As described in Section 3.3.1 for closed shell molecules, a splitting of the pendular Q branch into individual transitions may be the result of a large change in the dipole moment or rotational constant ($\Delta\mu$ or ΔB) upon vibrational excitation. From hypothetical simulations of the band structure, we can rule out both of these contributions to the splitting. For instance, a large ΔB would also be visible in the field-free spectrum presented above. Also, while it is possible obtain qualitative agreement with the band when a $\Delta\mu$ = 0.5 D is introduced in the simulation, such a large $\Delta\mu$ would also strongly shift the position of the field induced Q branch relative to the field-free band origin. Since this is not observed experimentally, we can also rule out $\Delta\mu$. It is also important to consider that a splitting of this type could be the result of the two possible isotopes of gallium, in analogy to that observed in Chapter 5 for Br-HF [290]. The natural abundance ratio of ^{69}Ga : ^{71}Ga, is 1.5:1 [352], and since we have not used an isotopically enriched sample, it is unlikely that these two isotopes are the cause of the splitting. Furthermore, in analogy with the OSMS measurements of Cl-HF (Section 5.7.1), our double

resonance experiment could be used to separate out these two isotopic contributions to the infrared spectrum. As seen in Figure 11.13A, where the pump laser was tuned atop the larger peak, and the probe laser scanned through the entire band, both peaks are observed with the same intensity ratio as in the single resonance spectrum. If the splitting were a result of two different isotopomers, we should be able to burn a hole in only one isotopomer's population, and the resulting DR spectrum would only contain contributions from that single species. Because this is clearly not the case, we can definitively conclude that the origin of both peaks is that of a single complex, with no contribution from other impurities. Attempts to simulate the pendular spectra numerically using the effective Hamiltonian approach used for the field-free spectrum did not reproduce such a splitting. Ruling out all of the other obvious possibilities, we conclude that the origin of the splitting must be due to an effect related to the open shell nature of the complex or a helium droplet interaction that we have not taken into account. This perturbation is also likely the culprit for the poor agreement in the field-free spectrum as well.

Given the rather large uncertainty in the *ab initio* calculations of the energies for both minima and transition states, the observation of photo-induced reaction places an upper limit to the reaction barrier of one (or both) of these products, namely 3301.30 cm^{-1} for HCN-Ga, which is larger than that calculated for the HC(GaN) and HCNGa products. Since HCN-In is observed not to react, either the barrier is larger than 3306 cm^{-1} or the helium is able to quench the vibrational energy before reaction occurs. Although the lower limit of the reaction barrier is much harder to estimate, it is clear that in helium the barrier is large enough to stabilize the HCN-Ga and HCN-In complexes in the entrance channel. Given our recent work on the sequential ring insertion mechanisms of water [37] and HF [39] clusters, this barrier could be as low as 10's of wavenumbers. The lack of a nitrogen bound HCN-Al complex hints that this reaction takes place on the ground potential energy surface, despite the cooling power of a helium droplet. Data of this type will help to gain new insights into the nature of these reactions, in particular regarding the associated steric effects. For example, the fact that excitation of the hydrogen bonded Ga-HCN complex results in isomerization rather than

reaction suggests that only the nitrogen end of the HCN is reactive, and by the time the gallium atom rearranges to this position, the system has already cooled to the point where reaction can no longer occur. Clearly this behavior is likely to be strongly dependent on the interactions with the solvent. Indeed, this situation is somewhat analogous to the competition between reaction and vibrational predissociation in the gas-phase.

11.7.1 Pick-up cell (PUC) pressure dependencies

In a recent preliminary report [75] for HCN-Ga, evidence for the photo-induced reaction was argued based on PUC pressure dependence measurements for this system, which are shown in Figure 11.15 for two different droplet sizes. In both droplet sizes the HCN-Gallium com-

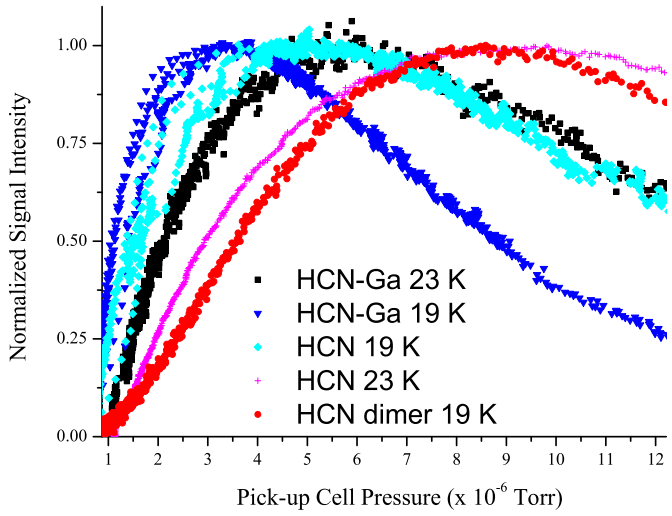

Figure 11.15: A series of pick-up cell pressure dependence curves for the HCN-Ga complex, HCN monomer and HCN dimer taken at two different droplet sizes: 23 K = 1900 Helium atoms, 19 K = 4600 atoms. The signal for HCN-Ga peaks at a pressure which is much lower than HCN monomer, which would indicate a preference for much larger droplets. This behavior was thought to be an indicator for a photo-induced reaction mechanism due to the fact that there is more helium to contribute to a depletion signal, than in a typical van der Waals complex.

plex optimizes at much lower HCN PUC pressure that the corresponding experiment for HCN monomer, which is typically not the case. It should be noted that the HCN monomer PUC

curve was recorded with the gallium oven hot, otherwise this would slightly change the distribution of droplets which just pick up one HCN. As a check, we also recorded the PUC pressure dependence of the HCN-Mg complex for which no reaction would be expected. Indeed, in this case, HCN and HCN-Mg [353] signals optimize at exactly the same HCN pressure. In our original argument, we proposed that in order for the HCN-Ga signal to optimize at a substantially lower pressures, there must be a preference for larger droplets sizes, due to their larger pick-up cross-sections, despite their fewer numbers compared with smaller droplets. If photo-induced reaction were occurring, considerably more helium evaporation might be expected if the exothermicity of the reaction is greater than the photon energy. As a result, larger droplets will contribute more to the associated signals, given that they can take advantage of this extra evaporation, whereas the smaller droplets will completely evaporate and thus have a reduced signal level. That this might be true is also indicated by the "shift" in the optimum HCN pressure, which is more pronounced for the nozzle conditions which produce (on average) smaller droplet sizes, due to the fact that they will be more sensitive to this effect. This hypothesis could also be used to justify why the pressure dependencies of the Ga-HCN and HCN-Ga complexes were not exactly the same, presuming that photo-induced reaction only occurred for the HCN-Ga isomer.

PUC pressure dependencies for the HCN-In and In-HCN complexes have also been recorded and these are shown in Figure 11.16. Since we have experimentally verified that no photo-induced reaction occurs using the double resonance technique, these curves may be used to test our observations for gallium. Interestingly the two peaks we assign to HCN-In and the combination band of In-HCN optimize at significantly lower HCN pressures than HCN monomer, in agreement with that found for HCN-Ga. In contrast, the peak we assign to the fundamental band of In-HCN optimizes at exactly the same pressure as HCN. Clearly this new observation casts doubt on our earlier hypothesis that the shift in the PUC curves results solely from photo-induced reaction.

As the HCN pressure is adjusted in our PUC pressure dependence measurements, the real

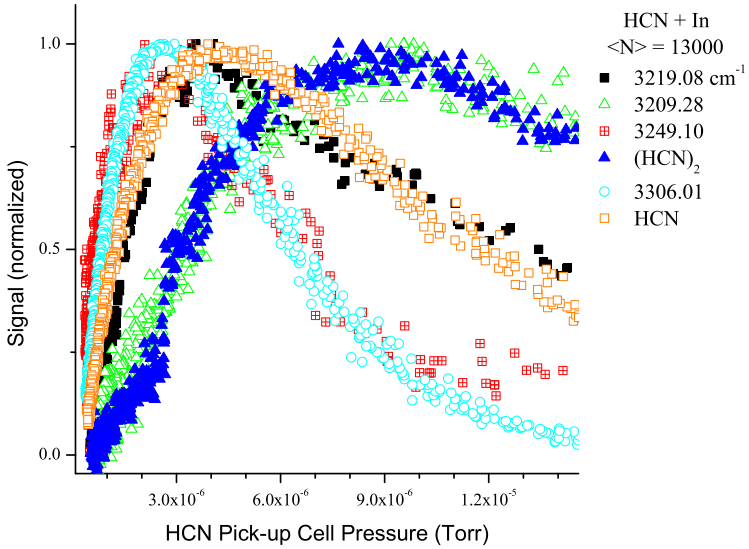

Figure 11.16: A series of pick-up cell pressure dependence curves for HCN-In , In-HCN, HCN monomer, and HCN dimer taken at a mean droplet size of 10000 helium atoms. The signal for HCN-In peaks at a pressure which is much lower than HCN monomer, in agreement with that found for HCN-Ga, which was suggestive of photo-induced reaction. However from the double resonance experiments we can rule this scenario out conclusively.

measurement is the change in probability that only the absorbing molecule (or complex) is picked up. At high pressures the PUC curve is reflective of small droplets since larger ones, with their correspondingly larger pickup cross sections, will have already picked up more than one HCN. At low pressure the situation is reversed, and the bigger droplets make a larger contribution. As we have shown previously that the width and center frequency of narrow pendular lines can be influenced by droplet size [332], it is clear that by simply parking the laser at the peak of the absorption (at optimal conditions) and recording the PUC curve, we ignore these effects. To properly account for these effects one must measure the integrated band strength for each HCN pressure. One might expect then that comparing PUC curves for narrow bands which exhibit these droplet size effects would cause some discrepancies. However it is somewhat surprising that the combination band of In-HCN also optimizes at much lower HCN pressure, despite having a large homogeneous linewidth and that the fundamental (again having a large homogeneous linewidth) lies right on top of HCN. Clearly a deeper understanding of

these effects must be achieved before the modeled PUC pressure dependencies can be used to perform calorimetry on a microscopic scale.

11.8 Summary

In this study helium nanodroplets have been applied to the stabilization of the highly reactive entrance channel complexes between aluminum, gallium, and indium atoms and a single HCN molecule. Theoretical calculations predict two linear van der Waals complexes for gallium and indium whereas for aluminum the nitrogen bound isomer was predicted to always fall into a reaction product well (HCNAl). Experimentally the HCN-(Ga, In) and the (Al, Ga, In)-HCN complexes were observed in good agreement with theory. The lack of the corresponding HCN-Al isomer is attributed to reaction, even at 0.37 K. The rotationally resolved spectra of HCN-Ga and HCN-In do not fit well to a standard Hund's case (a) $^2\Pi_{1/2}$ model, and we attribute this to an off-diagonal spin-orbit interaction, which gives rise to large parity splittings. In the indium spectrum, the spin-orbit coupling is so large that the spectrum is best described using a Hund's case (c) formalism. Using a one-dimensional treatment (presented in Chapter 12) we can qualitatively reproduce the parity splitting, which brings the agreement of the observed rotational constant into good agreement with theoretical calculations. The HCN-Ga spectrum has a large Q branch feature at the band origin, which is not reproduced by the simulations and we attribute this to a helium droplet interaction. Using double resonance techniques we provide nearly conclusive evidence for photo-induced reaction of HCN-Ga when the HCN is vibrationally excited to the v=1 (CH stretching) level. While we have yet to scan to low enough frequency to observe the corresponding reaction products, the initiation of the reaction is based on the 100% loss of population of the HCN-Ga complex. The corresponding experiment on HCN-In shows no depletion, indicating that the barrier to reaction must be larger than the photon energy (3306 cm^{-1}), or that the helium is able to quench the energy on a timescale faster than reaction.

Two vibrational modes of the Al, Ga, and In-HCN complexes are observed consisting of the fundamental C-H stretching and a combination band of C-H plus intermolecular stretch. Bound states on spin-orbit corrected 1D (intermolecular stretch) potential energy surfaces are presented, and are in excellent agreement with the experimental frequencies for the van der Waals stretch. Pumping Ga-HCN to a state corresponding with the combination band is found to result in some population transfer ($< 25\%$) to the HCN-Ga isomer, while the rest must cool back down to the ground state. This suggests that the nitrogen end of HCN is more reactive, and that the helium is able to quench the vibrational energy on a timescale greater than that needed for reaction of the hydrogen bound isomer.

Chapter 12

Spin-Orbit Coupling in HCN-Ga and HCN-Br

It was pointed out in the previous chapter that the infrared spectrum (for the CH stretching vibration) of the nitrogen bound HCN-Ga and HCN-In isomers do not fit well to a standard $^2\Pi_{1/2}$ model. In this chapter an effective Hamiltonian will be developed which aims to take into account the open shell nature of the complex, and will be used to simulate the infrared spectra. In addition, this model has been applied to the spectra of HCN-Halogen atom complexes presented in Chapter 6, which qualitatively reproduced some of the fine structure observed for those bands as well.

12.1 Gallium and bromine atoms

Before considering the HCN-Ga and HCN-Br complexes, it is prudent to first review what is known about the atoms themselves. The ground electronic state configuration of gallium is: [Ar] $4s^2 3d^{10} 4p^1$ which shows that it has one unpaired electron in a p type orbital outside of a quasi-closed shell core. Similarly the configuration for bromine is: [Ar] $4s^2 3d^{10} 4p^5$. Because the unpaired electrons can be described as being in an orbital with nonzero orbital angular momentum (specifically L = 1 for p orbitals), its motion is in effect a circulating current, creating a magnetic field which can interact with the electron spin angular momentum (S = 1/2 for Ga and Br). The two orientations of S relative to L produce levels with slightly different energies, represented by the total angular momentum J = L + S, which can take on the values of 1/2 or 3/2. The energy difference of these two states is given by [200]:

$$E_{l,s,j} = \frac{1}{2} hcA\{j(j+1) - l(l+1) - s(s+1)\}$$

where A is the spin-orbit coupling constant, in wavenumbers. The experimentally determined splittings in the gas-phase for gallium and bromine atoms are 826.19 cm^{-1} [244] and 3685.24 cm^{-1} [354], giving spin-orbit coupling constants of 551 cm^{-1} and 2457 cm^{-1} respectively. It is also important to point out that the $^2P_{1/2}$ state lies below the $^2P_{3/2}$ state for gallium, and thus A is positive. The opposite is true however for the halogen atoms, and the spin-orbit coupling is said to be inverted. The magnitude of the spin-orbit splitting is proportional to the magnetic field at the electron caused by the relative motion of the nucleus, where as its sign is related to core-polarization [355]. The influence of this spin-orbit coupling in the complexes will be discussed below.

12.2 HCN-Ga

The generalized angular momentum coupling schemes for diatomic molecules were first described by Hund, who described 5 limiting cases, labeled (a) through (e), which may be generalized for our linear complex. For Hund's case (a) (a good starting point for gallium and bromine), L and S interact strongly with the axial field of the molecule, and therefore their projections on the internuclear axis (Λ and Σ respectively) are well defined. The projection of the total electronic angular momentum along the nuclear axis is given by $\Omega = \Lambda + \Sigma$ and has a similar significance with the projection quantum number K of symmetric top molecules. If we assume that the atomic spin-orbit coupling is not strongly affected by complexation (See Section 11.3), then for the HCN-Ga complex, the Ω = 1/2 state will be lower in energy than Ω = 3/2 , in an analogous fashion to the atom. Since $J \geq \Omega$, the lowest (rotationless) state is J = 1/2 ($^2\Pi_{1/2}$). Since Ω is nonzero, the selection rules for the infrared transitions are $\Delta J = 0, \pm 1$, giving rise to P, Q, and R branches. In analogy with the X-HF spectra of Chapter 5, the first P and R branch transitions are spaced by 3B from the origin, while the spacing between successive P and R branch transitions is 2B in a $^2\Pi_{1/2}$ band. A simulation of such a band for HCN-Ga is given in Figure 11.7B.

The spectroscopy of weakly bound complexes involving open shell atoms and molecules requires that particular attention be paid to the asymptotic degeneracy associated with the different electronic states, which can lead to strong perturbations in the optical spectrum. While such effects have been observed in the electronic spectroscopy of diatomic molecules [244] where different electronic states are found to be accidentally degenerate, very few examples exist for complexes with open shell atoms and molecules. The most well studied exceptions are HX (X = O, N, and S) molecules complexed with rare gas atoms [356].

Let us first derive how the coupling of different electronic states comes about. We are interested in simulating the HCN-Ga spectrum so we start by creating an effective Hamiltonian which will describe the rotational structure of the vibrational band including the effects of spin-orbit coupling. The rotational Hamiltonian may be written as $H^{rot} = B(r)\, R^2$ where B(r) is

the rotational "constant" operator $\left(\frac{1}{2\mu r^2}\right)$ and R is the nuclear rotational angular momentum. In our pseudo-diatomic molecule treatment, r would be the Gallium-HCN center of mass distance and μ its reduced mass. Expressed in a form appropriate for Hund's case (a):

$$\begin{aligned} J &= R + L + S \\ H^{rot} &= B(r)\,(J - L - S)^2 \end{aligned} \tag{12.1}$$

Note that although we derive the necessary machinery in a Hund's case (a) form, the calculations will be numerical and the choice of proper Hund's case simply changes the labeling of states. Since we are interested in the rotation of a linear molecule, the rotation operator may be simplified to $R^2 = R_x^2 + R_y^2$. Substituting this into Equation 12.1 with the aid of the algebraic identities:

$$\begin{aligned} J^2 - J_z^2 &= J_x^2 + J_y^2 \\ J^{\pm} &= J_x \pm iJ_y \end{aligned}$$

(which can be generalized for each of the different angular momenta) one finds:

$$\begin{aligned} H^{rot} &= B(r)[J^2 - J_z^2 + S^2 - S_z^2 + (L^2 - L_z^2) \\ &\quad -\{(J^+L^- + J^-L^+) + (J^+S^- + J^-S^+) - (L^+S^- + L^-S^+)\}] \end{aligned} \tag{12.2}$$

In general the orbital angular momentum of molecules is not quantized due to the non-spherical nature of the potential and thus $(L^2 - L_z^2)$ is usually absorbed into the electronic band origin [244]. The effect of the raising and lowering operators in Equation 12.2 is to couple the different electronic states, which is what we set out to derive. If one neglects all of the off-diagonal coupling, the familiar (rigid-rotor) rotational energy is regained:

$$E^{rot} = B(r)[J(J+1) - \Omega^2 + S(S+1) - \Sigma^2]$$

Since the centrifugal distortion constants of rotors solvated in helium are often quite large, one adjustable parameter, D, has been incorporated into the simulation to account for these effects.

$$\left\langle J,\Omega,\Lambda,S,\Sigma|H^{cd}|J,\Omega,\Lambda,S,\Sigma\right\rangle = -D[J(J+1)-\Omega^2+S(S+1)-\Sigma^2]^2$$

The spin-orbit Hamiltonian also consists of diagonal and off-diagonal elements and may be written as:

$$H^{so} = A(L\cdot S) = A[L_zS_z + \frac{L^+S^- + L^-S^+}{2}]$$

Collecting the diagonal terms and writing them in bra-ket notation one attains:

$$\begin{aligned}\left\langle J,\Omega,\Lambda,S,\Sigma|H^{rot}+H^{so}+H^{cd}|J,\Omega,\Lambda,S,\Sigma\right\rangle &= B[J(J+1)-\Omega^2+S(S+1)-\Sigma^2]\\ &+ A\Lambda\Sigma\\ &- D[J(J+1)-\Omega^2+S(S+1)-\Sigma^2]^2\end{aligned}$$

where A and B are the spin-orbit and rotational constants respectively and D is a centrifugal distortion constant.

The detailed form of the off-diagonal coupling matrix elements has been given previously [244], however a brief description of each of the pertinent matrix elements will be given here for completeness. The $J^{\pm}S^{\mp}$ "S-uncoupling" operator has the perturbation selection rules $\Delta\Lambda = \Delta S = 0$, and $\Delta\Omega = \Delta\Sigma = \pm 1$. As the name implies, the operator represents the uncoupling of the electron spin angular momentum from the molecular axis and is responsible for the evolution from Hund's case (a) to case (b). It has the following relevant matrix elements:

$$\begin{aligned}\left\langle {}^2\Sigma_{1/2}|B(r)J^-S^+|{}^2\Sigma_{-1/2}\right\rangle &= B(J+1/2)\\ \left\langle {}^2\Pi_{3/2}|B(r)J^-S^+|{}^2\Pi_{1/2}\right\rangle &= -B[(J+1/2)^2-1]^{1/2}\end{aligned}$$

The $J^{\pm}L^{\mp}$ "L-uncoupling" operator has the perturbation selection rules $\Delta\Omega = \pm 1$ and $\Delta\Sigma = 0$, and is responsible for the evolution from Hund's case (a) to case (d). Again the important matrix elements are:

$$\begin{aligned} \left\langle {}^2\Pi_{1/2}|B(r)J^-L^+|{}^2\Sigma_{-1/2}\right\rangle &= -2^{1/2}B(J+1/2) \\ \left\langle {}^2\Pi_{-3/2}|B(r)J^+L^-|{}^2\Sigma_{-1/2}\right\rangle &= -2^{1/2}B[(J-1/2)(J+3/2)]^{1/2} \end{aligned}$$

The rotational $L^{\pm}S^{\mp}$ "Spin-electronic" term has selection rules, $\Delta\Omega = \Delta S$ = 0, $\Delta\Lambda = \Delta\Sigma = \pm 1$, and the relevant matrix element is given by:

$$\left\langle {}^2\Pi_{1/2}|B(r)L^+S^-|{}^2\Sigma_{1/2}\right\rangle = 2^{1/2}B$$

Finally, the off-diagonal spin-orbit matrix element is:

$$\left\langle {}^2\Pi_{1/2}|\frac{A}{2}L^+S^-|{}^2\Sigma_{1/2}\right\rangle = 2^{1/2}(A_{so}/2) \tag{12.3}$$

Since for all of the cases considered here A >> B, the rotational contribution to $L^{\pm}S^{\mp}$ may be ignored.

Before we leave this section it is important to define the meaning of rotational and spin-orbit "constants" when multiple electronic states are coupled together. In the absence of coupling, these constants have their usual meanings. The rotational constant, B, is defined for a linear molecule as:

$$B = \frac{h^2}{8\pi^2 I} = \frac{h^2}{8\pi^2\mu}\left\langle\frac{1}{r^2}\right\rangle$$

where I is the moment of inertia, μ is the reduced mass and r is the HCN (center of mass) - Ga distance in a pseudo-diatomic treatment. The $\left\langle\frac{1}{r^2}\right\rangle$ operator acts on the vibrational part of the total wavefunction, $\langle v|B(r)|v'\rangle$. Thus for the matrix elements which are diagonal in

the electronic and vibrational wavefunctions, we may define separate rotational constants for the Π and Σ states, B_Π and B_Σ. The off diagonal matrix elements of identical (interacting) potential energy curves are given by $B_{vv'} = \langle v|B(r)|v'\rangle \approx B_v\delta_{vv'}$, while for nearly identical potentials the $B_{vv'}$ matrix elements behave similarly to vibrational overlap integrals and must be either estimated or calculated numerically [244]. An example calculation will be shown below. Similarly, the relation of the atomic spin-orbit coupling constant to the off-diagonal matrix element involves the assumption that the orbital that contains the unpaired electron is not strongly affected by the complexation, which was argued in Section 11.3.

12.2.1 Application to HCN-Ga

The expectation value of $\frac{1}{r^2}$ for the various matrix elements can be determined from the resulting bound states on the spin-orbit corrected potentials given in Figure 11.4. Using Level [247] we find that the $\left\langle {}^2\Pi_{3/2}(v=0)|\frac{-\hbar^2}{2\mu r^2}|{}^2\Pi_{1/2}(v=0)\right\rangle$ matrix element is 0.08032 cm^{-1} which is approximately $\frac{B_{\Pi_{3/2}}+B_{\Pi_{1/2}}}{2}$. To calculate the $1/r^2$ expectation value connecting the ${}^2\Sigma_{1/2}$ and ${}^2\Pi_{3/2}$ states, we must take a different approach because of the continuum nature of the Σ wavefunctions. What we require is the calculation of the matrix element:

$$\left\langle {}^2\Sigma_{1/2}\right| B(r)J^+L^-\left|{}^2\Pi_{3/2}\right\rangle = -\sqrt{2}[(J-\frac{1}{2})(J+\frac{3}{2})]^{1/2}*\frac{\hbar^2}{2\mu}\left\langle \Psi_{\Sigma_{1/2}}(v=0)\right|\frac{1}{r^2}\left|\Psi_{\Pi_{3/2}}(v=0)\right\rangle \tag{12.4}$$

Using the results of our previous matrix diagonalization for the coupling of ${}^2\Sigma_{1/2}$ and ${}^2\Pi_{1/2}$ (See Section 11.3) we may rewrite the expectation value in Equation 12.4 as:

$$\left\langle \Psi_{^2\Sigma_{1/2}}\right|\frac{1}{r^2}\left|\Psi_{^2\Pi_{3/2}}\right\rangle = \frac{\hbar^2}{2\mu}[a\left\langle \Phi_{^2\Sigma_{1/2}}\right|\frac{1}{r^2}\left|\Phi_{^2\Pi_{3/2}}\right\rangle + (1-a^2)^{1/2}\left\langle \Phi_{^2\Pi_{1/2}}\right|\frac{1}{r^2}\left|\Phi_{^2\Pi_{3/2}}\right\rangle]$$

where a is the (R dependent) basis function coefficient obtained from the diagonalization. Since the $\left\langle \Phi_{^2\Sigma_{1/2}}\right|\frac{1}{r^2}\left|\Phi_{^2\Pi_{3/2}}\right\rangle$ matrix element still contains continuum wavefunctions, we will assume that they only contribute a continuous background to the spectrum and thus ignore

them. The $\left\langle \Phi_{^2\Pi_{1/2}} \right| \frac{1}{r^2} \left| \Phi_{^2\Pi_{3/2}} \right\rangle$ matrix element is easily computed in analogy to that described earlier. Using the $a(R)$ value at the average equilibrium distance for the two Π wavefunctions, we obtain $\frac{\hbar^2}{2\mu} \left\langle \Psi_{^2\Sigma_{1/2}} \right| \frac{1}{r^2} \left| \Psi_{^2\Pi_{3/2}} \right\rangle = 0.005$ cm^{-1}.

The simulation of the HCN-Ga spectrum begins by formulating the Hamiltonian matrix (distinct for each vibrational level) using Hund's case (a) basis functions which act as the basis set. Because the matrix elements described above are only dependent on the quantum number labels that describe the rotational wavefunction, the basis functions are just a set of labels that describe the state. The total number of basis functions to be included will be determined by eigenvalue convergence in the diagonalization. As we are interested in coupling the Σ and Π states, we include all possible basis functions containing $\Lambda = 0, \pm 1$, $\Sigma = \pm 1/2$ and $\Omega = \Lambda + \Sigma = \pm 1/2, \pm 3/2$. The total angular momentum quantum number J, is the sum of rotational and electronic angular momenta, (J = R + Ω), and thus J $\geq$ |Ω| is imposed. The mixing program is also written to include the effects of electric fields, whose effect is to mix basis functions off-diagonal in J [25]. The Stark matrix elements are identical to those of the symmetric top case, in which K is replaced with Ω, and these are given elsewhere [25]. M_J, the quantum number associated with the projection of J on the lab fixed z-axis (determined by the electric field), takes on the values $-M_J \leq$ J $\leq M_J$. Since M_J is a good quantum number in the field, the Hamiltonian is block diagonal in this dimension. For the pendular spectra here, a basis set of [J, M_J] $\geq$ [10, 10] was sufficient for convergence.

When the effects of lambda doubling cannot be ignored, it is necessary to adopt a parity adapted basis set of the form:

$$|J, |\Omega|, |\Lambda|, |\Sigma|, M_J, e/f\rangle = \frac{1}{\sqrt{2}} \left[|J, \Omega, \Lambda, \Sigma, M_J\rangle \pm |J, -\Omega, -\Lambda, -\Sigma, M_J\rangle \right]$$

The existence of parity as a good quantum number is due to the isotropy of free space, meaning that basis functions with + or - projection quantum numbers are not properly symmetrized with respect to the molecular inversion operator *i* [244]. We choose here to work with *e/f*

symmetry which factors out the J dependence of the total parity [200]. The matrix elements of the parity adapted basis are the same as those above, with the exception of the $\left\langle {}^2\Pi_{1/2}\right| \left|{}^2\Sigma_{1/2}\right\rangle$ and $\left\langle {}^2\Sigma_{1/2}\right| \left|{}^2\Sigma_{1/2}\right\rangle$ elements. Specifically these are given as [244]:

$$\begin{aligned}
\left\langle {}^2\Pi^{e/f}_{1/2}|H^{SO}+H^{SE}|{}^2\Sigma^{e/f}_{1/2}\right\rangle &= 2^{1/2}(\frac{A}{2})+[1\mp(J+\frac{1}{2})]*2^{1/2}B \\
\left\langle {}^2\Sigma^{e/f}_{1/2}|B(R)J^+S^-|{}^2\Sigma^{e/f}_{1/2}\right\rangle &= B_\Sigma[(J+\frac{1}{2})^2\mp(J+\frac{1}{2})]
\end{aligned}$$

where the top (bottom) sign is for *e* (*f*) symmetry. The perturbation selection rules in the parity basis couple states of the same parity, ie $\langle J,e/f|\,H^{rot}+H^{so}\,|J,f/e\rangle=0$, however the Stark Hamiltonian does couple the *e* and *f* states. In particular $\langle J,e/f|\,H^{Stark}\,|J,e/f\rangle = 0$ and $\langle J,e/f|\,H^{Stark}\,|J\pm1,f/e\rangle=0$ [357]. Otherwise these matrix elements are the same as those for the symmetric top. The last piece of information which goes into the simulation is the energy spacing between the Π and Σ states, which will control the amount of mixing between them. In the simulations the Σ state is artificially tuned in energy by adding a constant, Δ, to the diagonal $\left\langle {}^2\Sigma_{1/2}\,|H^{rot}|\,{}^2\Sigma_{1/2}\right\rangle$ matrix elements. Thus Δ is the the energy spacing between the ${}^2\Sigma_{1/2}$ state and ${}^2\Pi$ (ie (${}^2\Pi_{1/2}+{}^2\Pi_{3/2}$)/2). In principle this artificial tuning of Δ also would require a re-evaluation of the $\left\langle {}^2\Sigma_{1/2}\right| B(r)J^+L^-\left|{}^2\Pi_{3/2}\right\rangle$ matrix elements due to the fact that it is dependent on the amount of mixing between states, however in practice we found that the spectrum was not sensitive to a change of this parameter by one order of magnitude, and thus it was simply held fixed while Δ was adjusted.

12.2.2 Energy levels

Using the constants listed in Table 12.1, we performed the matrix diagonalization and extracted the energy levels for the first few rotational states in the ground and first excited vibrational manifolds of the nominally ${}^2\Pi_{1/2}$ state, which are shown in Figure 12.1, as a function of the Σ - Π separation, Δ. In order to make a comparison with our helium droplet spectra, we make the assumption that the diagonal and off-diagonal rotational constants can be reduced

Constant	(cm^{-1})
ν_0	3301.29
$\left\langle {}^2\Pi_{3/2}\left\vert\frac{-\hbar^2}{2\mu r^2}\right\vert{}^2\Pi_{1/2}\right\rangle$	0.027
$\left\langle {}^2\Sigma_{1/2}\left\vert\frac{-\hbar^2}{2\mu r^2}\right\vert{}^2\Pi_{1/2}\right\rangle$	0.005
$\left\langle {}^2\Sigma_{1/2}\left\vert\frac{-\hbar^2}{2\mu r^2}\right\vert{}^2\Sigma_{1/2}\right\rangle$	0.027
$\left\langle {}^2\Pi\left\vert\frac{-\hbar^2}{2\mu r^2}\right\vert{}^2\Pi\right\rangle$	0.027
D_J	5×10^{-6}
A	551

Table 12.1: A summary of the effective parameters used in the simulation of the HCN-Ga spectrum. The centrifugal distortion constant is defined as $-D[J(J+1)-\Omega^2+S(S+1)-\Sigma^2]^2$, and was assumed to be the same for both of the ${}^2\Sigma_{1/2}$ and ${}^2\Pi$ states.

in a similar manner to that observed for previous systems. When the Σ state is infinitely high

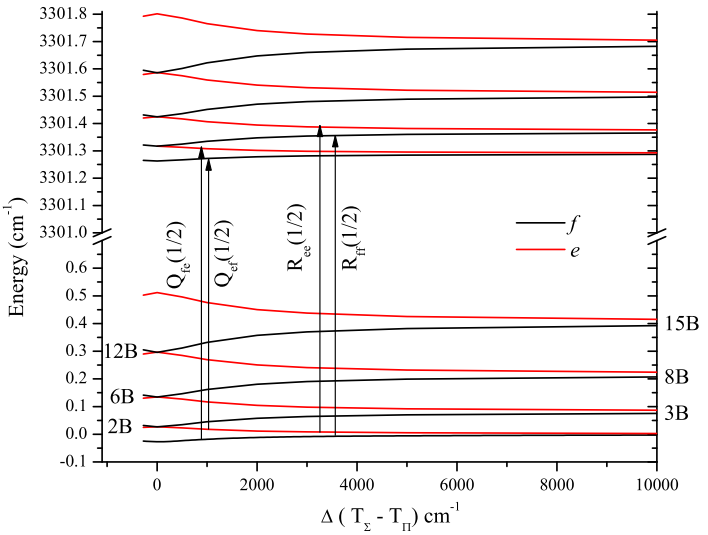

Figure 12.1: A correlation diagram representing the energy levels of HCN-Ga as a function of the spin-orbit induced mixing between ${}^2\Sigma_{1/2}$ and ${}^2\Pi_{1/2}$ states. As the ${}^2\Sigma_{1/2}$ state is lowered in energy, large parity splittings are observed in the ${}^2\Pi_{1/2}$ state. At the point where the ${}^2\Sigma_{1/2}$ and ${}^2\Pi$ states are degenerate (Δ = 0), the pattern of rotational states simplifies considerably, and we attribute this to a change in the appropriate angular momentum coupling scheme (Hund's case (c)). The arrows are representative of four possible transitions between the levels.

above the Π state, the energy levels fit to the expression B*J(J+1) where J is half integer (the lowest level being J = 1/2), as expected for a ${}^2\Pi_{1/2}$ state described by Hund's case (a), and

the two parity states are degenerate. As the $^2\Sigma_{1/2}$ state is lowered in energy, parity splittings are clearly observed and grow as Δ is lowered. At the point where the $^2\Sigma_{1/2}$ and $^2\Pi$ states are heavily mixed ($\Delta \sim 0$), the interaction between them is so large that the LS (spin-orbit) interaction is larger than the interaction between L and the molecular axis, which gives Hund's case (c). Under this description Λ and Σ are no longer good quantum numbers, but L and S still add vectorially to form a resultant angular momentum (typically labeled J_a) which has a projection of Ω on the internuclear axis. At this point a simplified (but different) pattern of energy levels is regained.

Figure 12.2 shows the full calculated spectrum for five representative values of Δ, where each transition has been convoluted with a single Lorentzian lineshape function. The rotational

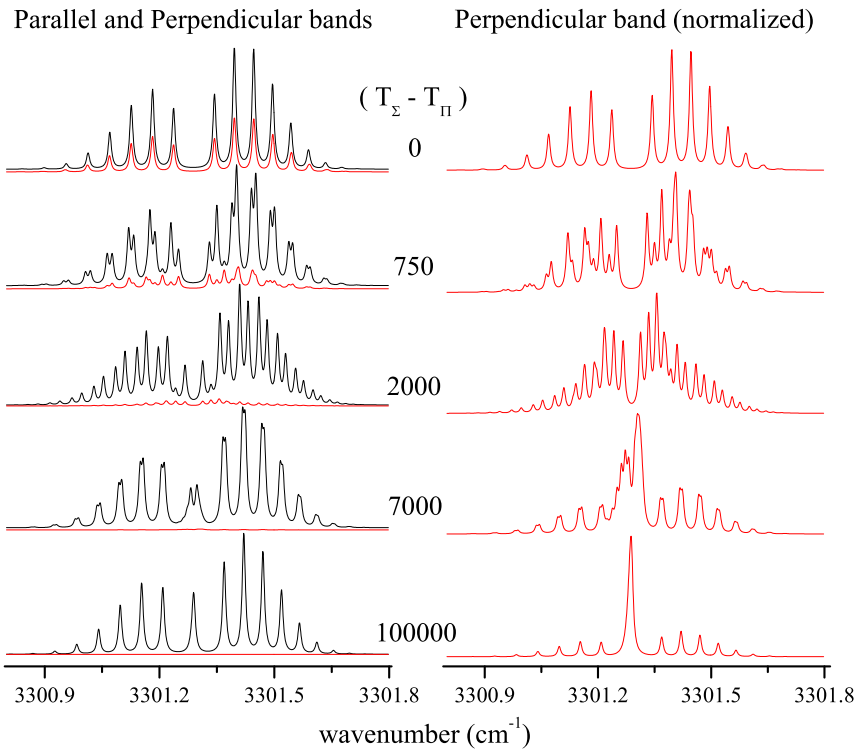

Figure 12.2: A series of simulations of the HCN-Ga spectrum as a function of the Σ - Π mixing. In the left panel the parallel and perpendicular are presented on a common vertical scale, such that the perpendicular band intensity can clearly be seen to grow in with the mixing. The right panel shows the corresponding perpendicular bands where the intensity has been normalized. The observed spectrum would be the sum of parallel and perpendicular components.

temperature has been fixed to 0.37 K, and the spectrum for $\Delta = 100000$ cm^{-1} is used to represent the limit as $\Delta \rightarrow \infty$. Due to the mixing of $^2\Pi_{1/2}$ and $^2\Sigma_{1/2}$ states, the observed band may be regarded as being made up of both parallel type transitions ($^2\Pi_{1/2} \leftarrow {}^2\Pi_{1/2}$) shown in black in the figure, and perpendicular type transitions ($^2\Pi_{1/2} \leftrightarrow {}^2\Sigma_{1/2}$) shown in red. Also, for the left panel the relative intensity between the parallel and perpendicular transitions is dictated by the amount of mixing, and on the right panel we zoom in on the perpendicular band only. In the absence of an electric field, the only rigorous selection rules are for J and *e/f* symmetry, which dictate that for $\Delta J = 0$, $f \leftrightarrow e$ while for $\Delta J = \pm 1$ $e \leftrightarrow e$ and $f \leftrightarrow f$ are allowed. As expected from the correlation diagram, for the two limiting cases of delta, simple spectra are observed corresponding to the idealized Hund's cases. For intermediate values of Δ, each of the transitions are split which is the result of breaking the degeneracy of the *e* and *f* symmetry substates. Also from the spectra we can immediately see that the strength of the perpendicular band transitions grow in intensity as the mixing increases.

12.2.3 Perpendicular band intensities

What we have not discussed thus far is what controls the relative intensities between the parallel and perpendicular components of the band. In the above simulations, the oscillator strength of the perpendicular band is derived from a vibrational type transition moment, which gains strength due to the mixing. The perpendicular band however is really an electronic transition, and the corresponding electronic transition moment needs to be evaluated with respect to the vibrational transition moment of the parallel band. The intensity of a band is proportional to the square of the transition moment integral:

$$I \propto \langle \Psi_{ev} \left| \mu \right| \Psi'_{ev} \rangle^2$$

where Ψ_{ev} is an electronic-vibronic wavefunction. Assuming Born-Oppenheimer separation of nuclear and electronic degrees of freedom, we may write $\Psi_{ev} = \psi\chi$ where $\psi(r, R)$ and $\chi(R)$

are separate electronic and nuclear wavefunctions respectively. r (R) will be used to denote the generalized electron (nuclear) coordinates and Z the nuclear charge. The dipole moment operator, μ, may also be factored into electronic and nuclear parts yielding:

$$\mu = -e\sum r_i + e\sum R_s Z_s = \mu_e + \mu_n$$

The transition moment integral, μ_T, is thus:

$$\begin{aligned}
\mu_T &= \langle \Psi_{ev} \left| \mu \right| \Psi'_{ev} \rangle \\
&= \int\int \psi(r,R)\chi(R)\left(\mu_e(r,R) + \mu_n(R)\right)\psi'(r,R)\chi'(R)\partial r \partial R \\
&= \int \chi(R)\left(\int \psi(r,R)\mu_e(r,R)\psi'(r,R)\partial r\right)\chi'(R)\partial R \\
&+ \int \psi(r,R)\psi'(r,R)\partial r * \int \chi(R)\mu_n(R)\chi'(R)\partial R
\end{aligned} \tag{12.5}$$

For the vibrational transition considered here, $\psi = \psi'$ which implies (by the Born-Oppenheimer approximation) that the vibronic transition does not induce a change in the electronic wavefunction. If this is true then the only terms which survive in Equation 12.5 are those of the dipole derivatives with respect to the vibrational states, $\int \chi(R)(\mu_n + \mu_e)\chi'(R)\partial R$. Thus within this framework there cannot be intensity for perpendicular type electronic transitions in this vibronic band. In reality, HCN-Ga does not have to satisfy the Born-Oppenheimer approximation, and if the electronic and vibrational wavefunctions are coupled, there can be intensities in these electronic transitions. That this could be true is easily seen by noting that the electronic mixing coefficient a (Equation 6.2), is indeed dependent on R.

From the diagonalization of the spin-orbit interaction (Equation 6.2), we find that in the region of the van der Waals well, the mixing coefficient is small (a = 0.05), which is consistent with the large energy spacing of the $^2\Sigma_{1/2}$ and $^2\Pi_{1/2}$ states at this internuclear separation (~8000 cm^{-1}). Since $a << 1$ we can simplify Equation 6.2 as:

$$\Psi_{^2\Pi_{1/2}} = a(R)\Phi_{^2\Sigma} + \Phi_{^2\Pi_{1/2}}$$

Substituting this form of the wavefunction into the equation (12.5) for the transition moment integral yields the rather lengthy expression:

$$\begin{aligned}
\mu_T &= \int\int \psi_\Pi(r,R)\chi(R)(\mu_e(r,R)+\mu_n(R))\psi'_\Pi(r,R)\chi'(R)\partial r\partial R \\
&+ \int\int \psi_\Pi(r,R)\chi(R)(\mu_e(r,R)+\mu_n(R))a(R)\psi'_\Sigma(r,R)\chi'(R)\partial r\partial R \\
&+ \int\int a(R)\psi_\Sigma(r,R)\chi(R)(\mu_e(r,R)+\mu_n(R))\psi'_\Pi(r,R)\chi'(R)\partial r\partial R \\
&+ \int\int a(R)\psi_\Sigma(r,R)\chi(R)(\mu_e(r,R)+\mu_n(R))a(R)\psi'_\Sigma(r,R)\chi'(R)\partial r\partial R \\
&= A1 + A2 + A3 + A4 + B1 + B2 + B3 + B4 \qquad (12.6)
\end{aligned}$$

where the A and B labels represent the electronic and nuclear dipole moment integrals respectively. This transition moment is for the vibrational mode of interest, namely the CH stretch. Thus $a(R)$ is not the same function derived from Figure 11.4, which was computed as function of the HCN-Ga separation. The coupling as a function of the C-H normal mode is shown in Figure 12.3, which was approximately determined by varying only the C-H bond length of HCN. To begin to simplify Equation 12.6, we define:

$$M(R) = \int \psi(r,R)\mu\psi'(r,R)\partial r$$

so that A1 becomes:

$$\int \chi(R)M^\Pi(R)\chi'(R)\partial R \qquad (12.7)$$

Performing a Taylor series expansion about R=R_e:

$$M(R) = M(R_e) + \left.\frac{\partial M}{\partial R}\right|_{R=R_e}(R-R_e)$$

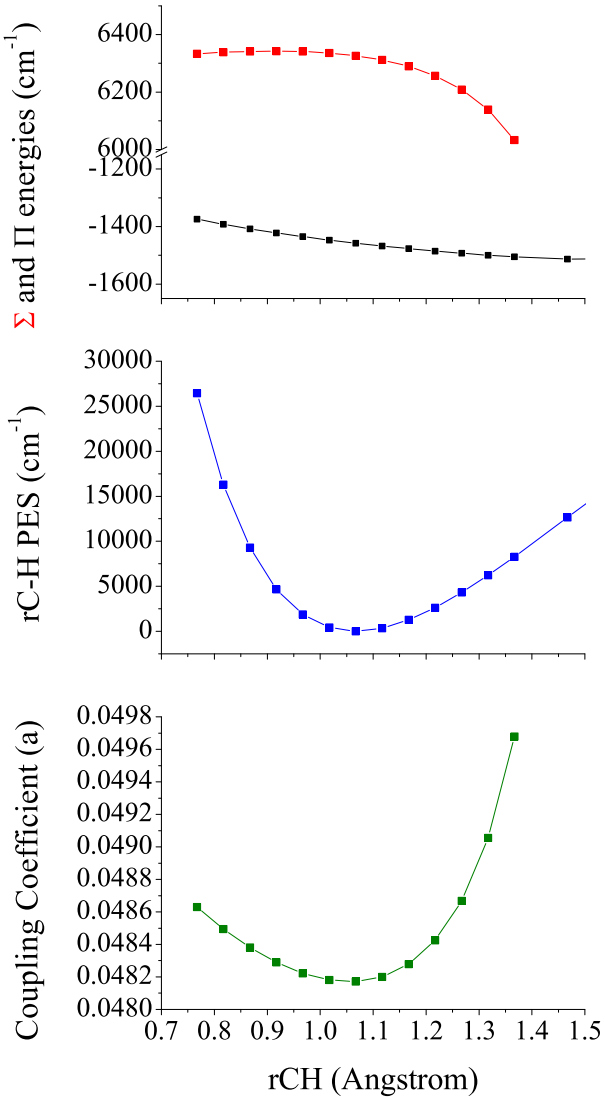

Figure 12.3: A series of plots showing the relative energies of the Π and Σ states of HCN-Ga and their coupling as a function of the rCH bond length. The energies were calculated at the RCCSD(T)/aug-cc-pVTZ+{332} level and for the Σ and Π states counterpoise correction relative to HCN + Ga was included. The mixing coefficient was generated by numerically diagonalizing the two states ($^2\Pi - A/2$ and $^2\Sigma$) using Equation 12.3 for the off-diagonal coupling. The C-H stretching potential is also shown for reference.

$$= \quad M_0 + M_1 Q$$

and thus:

$$\begin{aligned} A1 &= M_0^{\Pi} \int \chi(R)\chi'(R)\partial R + M_1^{\Pi} \int \chi(R) Q \chi'(R)\partial R \\ &= M_1^{\Pi} \int \chi(R) Q \chi'(R)\partial R \end{aligned}$$

where the first integral vanishes due to the orthogonality of vibrational wavefunctions. B1 is the analogous integral for the nuclear dipole moment operator and we find:

$$\begin{aligned} A1 + B1 &= \left.\frac{\partial \mu}{\partial R}\right|_{R=R_e} \int \chi(R) Q \chi'(R)\partial R \\ &= M_1^{\Pi} \int \chi(R) Q \chi'(R)\partial R \end{aligned}$$

where μ and M_1^{Π} now refer to the total dipole moment. Thus the A1 + B1 term represents the normal dipole derivative term of the parallel band ($\Pi \leftarrow \Pi$) intensity.

For the remaining integrals we make the further simplification:

$$\begin{aligned} a(R) &= a(R_e) + \left.\frac{\partial a}{\partial R}\right|_{R=R_e} (R - R_e) \\ &= a_0 + a_1 Q \end{aligned}$$

The perpendicular band intensity which we are after is contained in the A2 and A3 terms. For A2 we find:

$$\begin{aligned} A2 &= \int\int \psi_{\Pi}(r,R)\chi(R)\mu_e(r,R)a(R)\psi'_{\Sigma}(r,R)\chi'(R)\partial r \partial R \\ &= a_0 M_0^{\Pi\Sigma} \int \chi(R)\chi'(R)\partial R \\ &+ a_1 M_0^{\Pi\Sigma} \int \chi(R) Q \chi'(R)\partial R \\ &+ a_0 M_1^{\Pi\Sigma} \int \chi(R) Q \chi'(R)\partial R \\ &= (a_1 M_0^{\Pi\Sigma} + a_0 M_1^{\Pi\Sigma}) \int \chi(R) Q \chi'(R)\partial R \end{aligned}$$

$$A2 \;=\; A3$$

where we have neglected terms which contain Q^2. It can also be easily shown that the analogous B2 and B3 integrals which contain the nuclear dipole moment operator are zero due to the orthogonality of the electronic wavefunctions in the $\int \psi_\Pi \psi_\Sigma \partial r$ integrals. That these integrals are zero makes sense given that our perpendicular band arises not from the vibration, but only from the electronic mixing. The remaining integrals A4 and B4 are analogous to A1 and B1 and represent the parallel components of $\Sigma \leftarrow \Sigma$ type. Since we are in the weak mixing limit however, these terms will be much smaller than those above and we shall not derive them here. Also since $\int \chi(R) Q \chi'(R) \partial R$ is a common factor in all of the simplifications the actual evaluation of this integral is not necessary.

From the derivations above we now have an estimate for the ratio of the parallel to perpendicular transition intensity, namely:

$$\frac{I_\parallel}{I_\perp} \;=\; \frac{M_1^\Pi}{2 * (a_1 M_0^{\Pi\Sigma} + a_0 M_1^{\Pi\Sigma})} \tag{12.8}$$

To re-emphasize, M_1^Π is a typical dipole derivative term for the Π state, $\frac{\partial \mu_\Pi}{\partial R}\big|_{R=R_e}$, $a_1 M_0^{\Pi\Sigma}$ is the electronic transition dipole moment integral, $\int \psi_\Pi(r, R_e) \mu_e(r, R_e) \psi_\Sigma(r, R_e) \partial r$ scaled by the derivative of the ($^2\Sigma$ ~ $^2\Pi - A/2$) mixing coefficient along the normal mode, $\frac{\partial a}{\partial R}\big|_{R=R_e}$, and $a_0 M_1^{\Pi\Sigma}$ is the derivative of $\int \psi_\Pi(r, R) \mu_e(r, R) \psi_\Sigma(r, R) \partial r$ with respect to R (evaluated at R=R$_e$) multiplied by the coupling coefficient $a(R_e)$.

In order to estimate the electronic transition dipole moments, CASSCF(1,3)-MRCI calculations were performed using the aug-cc-pVDZ+{332} basis set. A simple 1D grid of C-H bond lengths was used to find the equilibrium value and to perform the numerical differentiation while R and rCN were held fixed at 3.273 and 1.1601 Å respectively. The values for the transition dipole moments and the energy spacing between Π and Σ states are shown in Table 12.2 for three representative values of the C-H bond length (R$_e$ = 1.074967 Å) where the z axis defines the molecular symmetry axis. The computed values for Δ and $\langle \Pi \,|\mu_z|\, \Pi \rangle$ are found

to agree well with our previous RCCSD(T) results of 7784.40 cm^{-1} and 4.50 D respectively lending support to this theoretical method. From the data in the table the needed parameters

	rCH (Å)		
	1.074967	1.075967	1.084967
$\Delta(E_\Sigma - E_\Pi)$ (cm^{-1})	7927.85	7927.92	7928.47
$\langle \Pi \left\| \mu_z \right\| \Pi \rangle$ (D)	4.73571	4.73737	4.75233
$\langle \Sigma \left\| \mu_z \right\| \Sigma \rangle$ (D)	6.87349	6.87488	6.88731
$\langle \Pi \left\| \mu_x \right\| \Sigma \rangle$ (D)	0.14203	0.14207	0.14247
$\langle \Pi \left\| \mu_z \right\| \Sigma \rangle$ (D)	-0.0001	-0.0001	-0.0001

Table 12.2: Computed transition dipole moments and energy separation of the Σ and Π states of the HCN-Ga complex. By symmetry $\langle \Pi \left\| \mu_x \right\| \Sigma \rangle = \langle \Pi \left\| \mu_y \right\| \Sigma \rangle$ and thus $\mu = \sqrt{\mu_x^2 + \mu_y^2}$.

in our simulation can now be evaluated: $\frac{\partial \mu_\Pi}{\partial R}\big|_{R=R_e}$ = 1.66 D $Å^{-1}$, $\frac{\partial \mu_{\Pi\Sigma}}{\partial R}\big|_{R=R_e}$ = 0.063 D $Å^{-1}$, $a(R_e)$= 0.047, and $\frac{\partial a}{\partial R}\big|_{R=R_e}$ = 0.0004 $Å^{-1}$. As might have been expected from Figure 12.3 both the magnitude of the electronic coupling coefficient and its derivative with respect to rCH are small and from Equation 12.8 we estimate that the ratio of parallel to perpendicular intensity is ~250, clearly negligible for our spectrum.

Figure 12.4 shows the experimentally observed spectrum for HCN-Ga and a simulation for Δ = 2000 cm^{-1} and B = 0.027 cm^{-1}. It is clear from trying to fit our spectrum that both Δ and the rotational constant (B) are highly correlated parameters due to the parity splitting and thus we have concentrated on achieving better agreement with the peaks of the P and R branches using a rotational constant reduction factor which is more typical of molecules in helium. Indeed by fitting the spectrum using a pure $^2\Pi_{1/2}$ model (See Figure 11.7) assuming that each of the peaks in the experimental spectrum were individual rotational transitions, we obtained a reduction factor of 4.62 which is much larger than that typically observed. For the current simulations, which include parity doubling, Δ and B have been set to 2000 and 0.027 cm^{-1} respectively, bringing the rotational constant reduction factor back down to 2.79 in much better agreement with most molecules solvated in helium. It becomes apparent that our simulations do not predict an enhancement of intensity for a Q-branch feature at the band

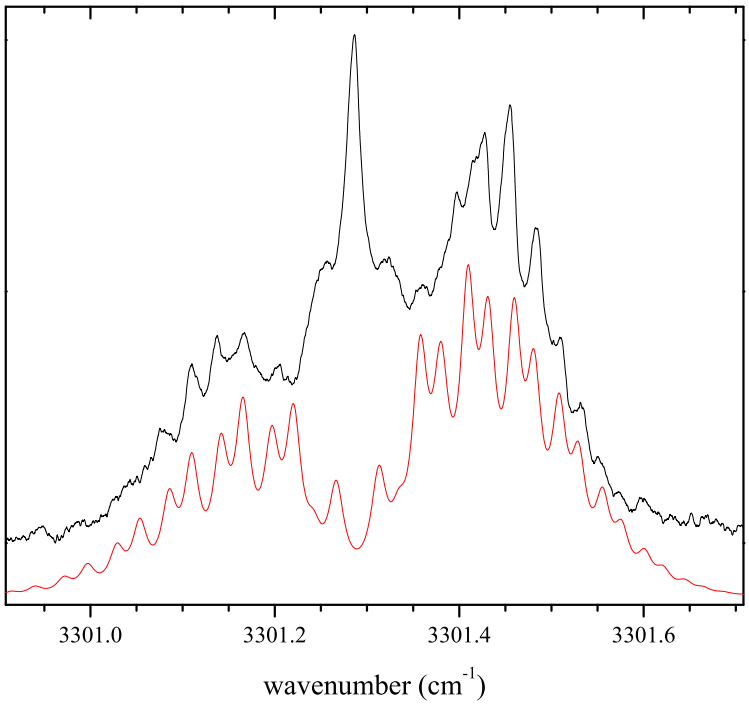

Figure 12.4: The experimental spectrum of HCN-Ga accompanied by a simulation employing a effective Hamiltonian to include the effects of parity doubling due to the low lying $^2\Sigma_{1/2}$ state. The effective parameters$\Delta$and B have been optimized to 2000 and 0.027 cm^{-1} respectively. Clearly differences between our model and the experimental spectrum are observed, most notably the strong Q branch feature at the band origin. (see text)

origin and we conclude that it must be related to a helium droplet interaction or other open shell effect.

In order to compare our results with future bound state calculations and experimental studies, we have calculated the lambda doubling parameter, p (from our simulation with B = 0.027 and Δ = 2000 cm^{-1}) by fitting the J dependence of the parity splitting to [244]:

$$\Delta\nu_{ef} = p(J + \frac{1}{2})$$

yielding p = 0.024 cm^{-1}. This value agrees quite nicely with the perturbation theory result of Van Vleck [200] which gives p as:

$$p = \frac{4AB}{\Delta}$$

or 0.0298 cm^{-1} for our constants.

12.2.4 Interpretation of delta

Up to this point we have treated Δ as a variational parameter in the fit to our experimental spectrum, however we find that our best fit value of 2000 cm^{-1} is clearly much smaller than the energy spacing between the $^2\Pi_{1/2}$ and $^2\Sigma_{1/2}$ states around the vicinity of the $^2\Pi_{1/2}$ minimum in our RCCSD(T) calculations (~7800 cm^{-1}). To gain insight into this issue we briefly discuss the results of von Haeften *et al.* who have observed NO (nitrous oxide) doped in helium droplets [358] for which a quantitative comparison has been made with previous gas-phase results [359]. For NO a 55% increase in the lambda doubling was observed upon solvation while the rotational constant amounts to 76% of that of the gas-phase. An approximate expression for the lambda doubling parameter p has been proposed which takes into account only the $^2\Sigma$ valence and Rydberg excited states [360].

$$p = 4\sum(-1)^s \frac{\langle \Pi | H^{so} | \Sigma \rangle \langle \Sigma | BL_y | \Pi \rangle}{E_\Sigma - E_\Pi} \tag{12.9}$$

According to Equation 12.9, p is proportional to the rotational constant B, and since B was reduced upon solvation this gives an opposite contribution to that observed. Secondly, p is also proportional to the energy denominators which depend on the energies of the excited Σ states. While we expect that the valence states will be only weakly effected by solvation, much larger effects are predicted for Rydberg states. Because the interaction between the Rydberg electron of NO and a helium atom is repulsive we expect a large blue-shift in their energy in agreement with that observed in a H_2 matrix [361]. Since the energy denominators will then increase in Equation 12.9, this would again lead to the opposite behavior observed. In

numerical calculations by de Vivie and Peyerimhoff [362], 90% of the lambda doubling in NO is attributed to the valence excited $G^2\Sigma^-$ and $I^2\Sigma^+$ states, and only about 10% of p is due to the Rydberg states. Thus a blue-shift of the Rydberg states should only cause a small decrease in p. Thirdly the off-diagonal matrix elements may also be modified. According to von Haeften *et al.*, "The changes in the H^{so} matrix elements are expected to be small, since the $1/r^3$ weighting in the microscopic spin-orbit Hamiltonian implies that only the inner parts of the wavefunctions are probed." This hypothesis was also supported by the fact that the nuclear hyperfine splittings of NO were not changed from the gas-phase, an interaction which also scales as $1/r^3$. On the other hand the L_y matrix elements probe the outer parts of the orbitals which could be more strongly affected due to a confinement of the unpaired electron by the helium. Finally an additional source for the increased Λ doubling was postulated to be a result of helium density fluctuations which result from the fact the helium density would be different in the nodal plane of the Π orbital than perpendicular to it. Without a fully quantitative understanding of these effects we are left to suggest that the effect of the helium on the HCN-Ga spectrum could also increase the parity splitting, which would then give rise to a smaller Δ in our simulations when compared with *ab initio* theory. If we assume that Δ and B are correctly predicted by the *ab initio* calculations, the lambda doubling constant from our simulation for a "gas-phase" HCN-Ga complex is p = 0.0215 cm^{-1}. Compared to our helium droplet value of p = 0.0240 cm^{-1}, this would be a 12% increase upon solvation. In analogy with NO, this increase in the lambda doubling is surprising given that the rotational constant reduction should decrease p by a factor of ~ 2.8, neglecting the other contributions.

12.3 HCN-In

The infrared field-free and Stark spectra for HCN-In were presented in Chapter 11 however we will briefly review the important parameters used to fit the field-free spectrum here. For indium, the spin-orbit coupling constant is 1475 cm^{-1} and this provides an even stronger off-

diagonal mixing between the $^2\Sigma_{1/2}$ and $^2\Pi_{1/2}$ states when compared with gallium (A = 551 cm^{-1}). The best fit to the field-free spectrum was found for Δ= 2000 $\pm$1000 cm^{-1} and B = 0.023 cm^{-1} and when compared to the spin-orbit corrected RCCSD(T) values (taken from 1D PES calculations, not shown) of Δ= 6415 and B = 0.0608 cm^{-1}, we see that the rotational constant is reduced by a factor of 2.64 and that our measured Δ is again much smaller than the calculated value. Both of these observations are consistent with our gallium data, lending further support to the method used to fit the gallium data. Interestingly the simulations agree much better for HCN-In than HCN-Ga, in that no Q branch feature is predicted and none is observed.

12.4 Dipole moments

Stark spectra have been recorded for the HCN-In and HCN-Ga complexes and these are shown in Figures 11.9 and 12.5 respectively. The simulations employ the effective Hamiltonian model developed in this chapter to take into account the off-diagonal spin-orbit coupling. Holding all of the parameters derived from the fit to the field-free spectra fixed, we can simulate the Stark spectra using only μ and $\Delta\mu$ as adjustable parameters. Both the HCN-Ga and HCN-In spectra exhibit the best agreement with the simulation incorporating μ = 3.5 D ($\Delta\mu$ = 0), which is considerably smaller than the calculated values of 4.50 D (for HCN-Ga at the RCCSD(T)/aug-cc-pVTZ level) and 4.54 D (for HCN-In at the RMP2/aug-cc-pVTZPP level) respectively. Note that both of the calculations for the dipole moments employed the Finite-Field approximation [348]. That the experimental dipole moment is less than the calculated value could be a result of several factors including vibrational averaging, a helium droplet interaction (see Section 3.3.1.3), and / or spin-orbit coupling.

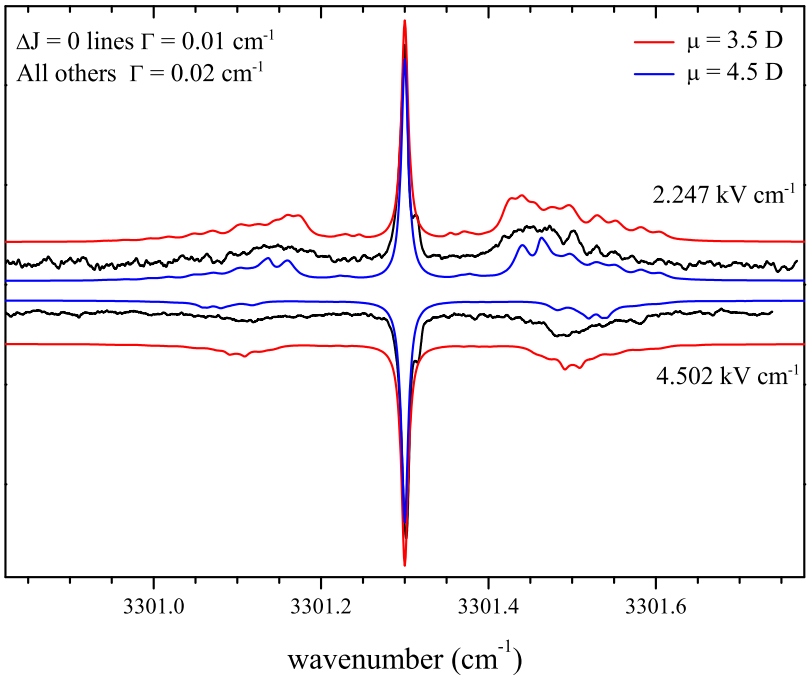

Figure 12.5: Stark spectra of HCN-Ga recorded in the presence of 2.247 and 4.502 kV cm^{-1} electric fields. The simulations employ the effective Hamiltonian model developed in this chapter to take into account the off-diagonal spin-orbit coupling. For each value of the electric field, a simulation was performed with μ = 4.5 D and μ = 3.5 D with the latter having better agreement with the observed spectrum, despite the *ab initio* prediction of $\mu_{RCCSD(T)}$ = 4.50 D. The large discrepancy between the *ab initio* calculations and that observed experimentally could be related to vibrational averaging, a helium droplet interaction, or the spin-orbit coupling.

Chapter 13

Summary and Outlook

What is lacking in the study of reactive species is a detailed understanding of their corresponding potential energy surfaces. Their reactivity, the very property which we wish to investigate, ultimately limits their study due to the associated short lifetimes and low concentrations one can achieve in the laboratory. A great deal of progress has been made experimentally in the study of isolated radicals, however what we are really after is an understanding of their interactions with other species. While particular attention has been focused on elucidating the structure and dynamics of the transition state region of the potential energy surface, it is the longer range attractive region, characterized by the entrance and exit channel valleys, which has recently been shown to strongly influence the reaction dynamics in several experiments. Helium droplets are very well suited to the study of reactive species due to their cold temperatures and fast cooling rates, allowing one to trap reactive species behind even very small reaction barriers. The biggest experimental challenge to studying radicals in helium droplets is producing the radicals with sufficient purity so as not to contaminate the droplets. Extending our work on the CH_3 radical to many other small hydrocarbon radicals is straightforward and Figure 13.1 shows an unpublished spectrum corresponding to a HF-ethyl radical complex. Clearly there is much that could be done to further explore the reactivity of metal atoms, which is very interesting in light of the known catalytic properties of small metal clusters. The experiments described within this thesis illustrate the power of helium nanodroplets to study the

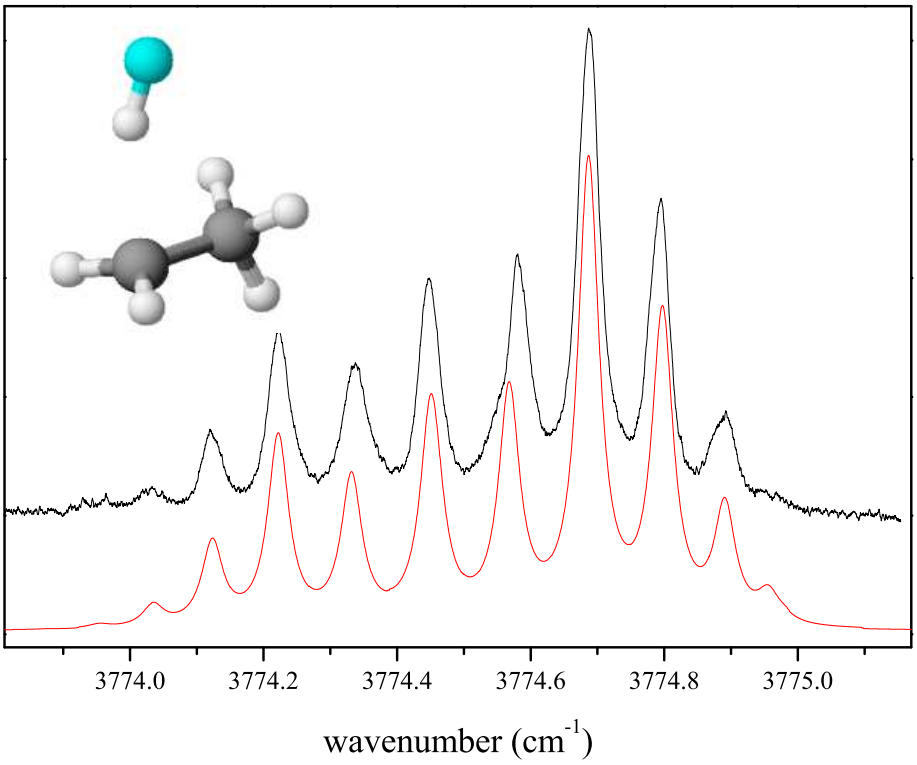

Figure 13.1: An experimental spectrum of the HF-Ethyl radical (C_2H_5) complex stabilized in helium droplets.

potential energy surfaces and dynamics of these entrance and exit channel complexes. The technique is completely general, and due to the unique growth process in helium, species with much smaller barriers to reaction can be stabilized. We have really only just scratched the surface of what is possible, and the future is sure to hold many surprises.

Appendix A

Optical Parametric Oscillators

All of the single resonance work presented in this thesis was recorded with an F-center laser, which was described in Chapter 3. Our double resonance studies used the FCL as a probe laser and the OPO's detailed in this appendix were used as the pump laser. Our groups interest for exploring these OPO laser sources was the desire to generate much longer wavelength radiation than is capable with the F-center, and the much larger powers that are available with these sources, in hopes to explore a wide variety of new spectroscopic probes. Two new laser systems have been developed in our laboratory for such use, and this appendix is meant to serve as a brief reference on the theory and realized performance of these systems.

A.1 Optical parametric oscillation (OPO)

The heart of any OPO is an active medium (usually a birefringent crystal) which has a non-linear susceptibility. Another way of saying this is that the interaction of the electromagnetic radiation and matter creates an electric field polarization, P, within the material which can be described as:

$$P = \chi^1 E + \chi^2 E^2 + \dots$$

where χ^k is a k-th order susceptibility tensor and E is the magnitude of the electric field strength. With the advent of the laser, very intense sources of radiation can take advantage

of these higher order terms in the polarization expansion, which can lead to frequency mixing, as we shall see. Suppose two different frequencies of light are collinearly propagated through a nonlinear material ($\chi^2 \neq 0$). Their wave equation may be written as:

$$E = E_1 cos(\omega_1 t) + E_2 cos(\omega_2 t)$$

The first order susceptibility gives a DC polarization wave. The second order (quadratic term) may be expanded to yield:

$$P^{(2)} = \chi^2 E^2 = \chi^2 [E_1^2 cos^2(\omega_1 t) + E_2^2 cos^2(\omega_2 t) + 2E_1 E_2 cos(\omega_1 t) cos(\omega_2 t)]$$

which, with the aid of the trigonometric identity:

$$cos(a) * cos(b) = \frac{cos(a+b) + cos(a-b)}{2}$$

can be arranged into the following:

$$P^{(2)} = \chi^2 [\frac{E_1^2 + E_2^2}{2} + \frac{E_1^2 cos^2(2\omega_1 t)}{2} + \frac{E_2^2 cos^2(2\omega_2 t)}{2} + E_1 E_2 [cos((\omega_1 + \omega_2)t) + cos((\omega_1 - \omega_2)t)]]$$

Thus there is an additional DC polarization, waves resonating at the second harmonics of each of the component light frequencies (2ω), and the sum or difference of these frequencies ($\omega_1 \pm \omega_2$). These equations also work in reverse, meaning that it is possible to "split" a photon into two different frequencies, given conservation of energy. The extent to which each of these possible frequency mixing conditions is important can be controlled by design. Given the wide range of frequencies which can be produced, it is obvious why the OPO is becoming a widely used tool in spectroscopy.

A.2 Phase-matching

For the OPO's used in this thesis, the photons from a pump laser (~1 μm) can be thought of being split into two parts, a signal photon (1.5 - 2.0 μm) and an idler photon (2.5 - 4.0 μm). As the waves of different frequency travel in the nonlinear crystal, they will not in general have the same phase velocity due to natural dispersion ($n_p \neq n_s \neq n_i$ where n_x is the corresponding index of refraction at a specific wavelength). This phase slip causes an oscillation in the direction of power flow from one wave to another due to constructive and destructive interference. The distance over which the relative phase of the waves changes by π (180^0 out of phase) is termed the coherence length, Λ. A typical value for the coherence length in the OPO's used here is ~25 μm. If one wishes to build up intensity in one or more of the frequencies (at the expense of the pump power), phase-matching must occur.

A.2.1 Birefringent phase-matching

Taking advantage of the natural birefringence[1] of some materials, the generated waves of two different frequencies can be made to travel at the same velocity. This is usually achieved by rotating the angle between the optical axis of the crystal and the propagation directions of the beams. The pump, signal, and idler beams all mix in the crystal and their interaction as a function of traveling distance in the crystal (z) is given by [363, 364]:

$$\frac{\partial E_s}{\partial z} = i\omega_s \frac{d_{eff}}{n_s c} E_P E_i \exp(i\Delta k z)$$

$$\frac{\partial E_i}{\partial z} = i\omega_i \frac{d_{eff}}{n_i c} E_P E_s \exp(i\Delta k z)$$

[1] Birefringence is characterized by a material having different indicies of refraction based upon the propagation direction and polarization angle that light makes with the crystallographic axis.

$$\frac{\partial E_p}{\partial z} = i\omega_p \frac{d_{eff}}{n_p c} E_s E_i \exp(i\Delta k z)$$

where E_x is the amplitude of the waves, n_x are their corresponding indicies of refraction and d_{eff} is the effective nonlinear coefficient. The three wave vectors (k) add together giving rise to the vector mismatch Δk, however in perfect phase-matching this is always zero. These three equations are coupled differential equations and their solution is non trivial. However, if the simplifying assumption is made that $\frac{\partial E_p}{\partial z} = \frac{\partial E_s}{\partial z} = 0$, then the amplitude of the idler wave (as a function of distance traveled in the crystal) is calculated to be:

$$E_i(L) = i\omega_i \frac{d_{eff}}{n_i c} E_p E_s L$$

The generated idler intensity is then:

$$I_i(L) = \frac{2}{n_i c \epsilon_0} E_i(L)^2 = 2\omega_i^2 \frac{d_{eff}^2 L^2}{n_i^3 c^3 \epsilon_0} I_p I_s$$

When Δk is not zero, E_i(L) can be written as:

$$E_i(L) = i\omega_i \frac{d_{eff}}{n_i c} E_p E_s \frac{sin(\Delta k L)}{\Delta k}$$

and the intensity is now :

$$I_i(L) = 2\omega_i^2 \frac{d_{eff}^2 L^2}{n_i^3 c^3 \epsilon_0} I_p I_s \frac{sin^2(\Delta k L)}{(\Delta k L)^2}$$

The idler intensity as a function of distance traveled in the crystal is shown graphically in Figure A.1. As one can see, when birefringent phase-matching exists the idler intensity grows as L^2, where as without phase-matching the idler power simply oscillates around zero.

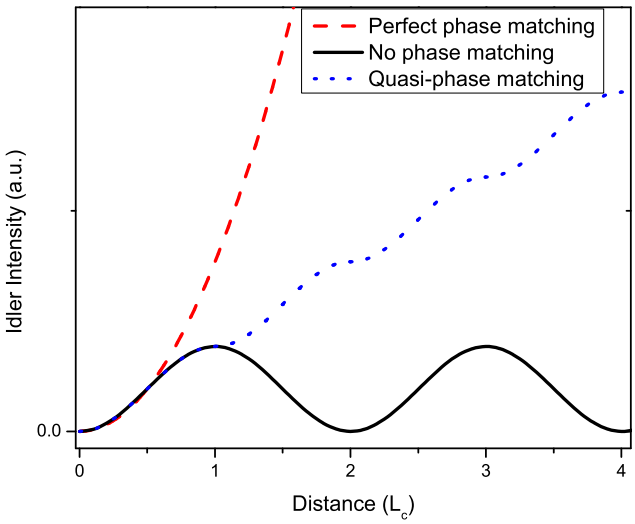

Figure A.1: Calculated phase matching curves for generating idler radiation.

A.2.2 Quasi Phase-matching

If the sign of the nonlinear coefficient of the crystal could be changed every odd multiple of the coherence length, then the areas of destructive interference would be changed to constructive interference. This type of phase matching is termed quasi phase-matching and was first proposed by Armstrong in 1962 [365]. The first realization of quasi phase-matching used thin crystal wafers which the optic axis could be oriented 180^0 with respect to one another. The gain in idler intensity for quasi phase-matching is shown in Figure A.1 and can be compared directly with perfect phase-matching. Despite the apparent lower efficiency of quasi phase-matching compared to birefringent phase-matching, quasi phase-matching has several advantages which in general leads to much higher efficiency.

The main advantage of quasi phase-matching when compared with birefringent phase-matching is that the pump, signal, and idler beams may propagate collinearly through the crystal. In birefringent phase-matching, the angle of the pump and signal beams is adjusted relative to the crystallographic axis, which in general means that they will have different paths thought the crystal limiting their overlap. Thus quasi phase-matching allows the use of much

longer crystals, to increase the interaction path length of the beams, and can take better advantage of the crystal direction which has the highest nonlinear coefficient. Also crystals that have nonlinear coefficients can be used that do not exhibit birefringence.

The effect of quasi phase-matching is a partial compensation of the k vector mismatch, which can be written as:

$$\Delta k = k_p - k_s - k_i - \frac{2\pi}{\Lambda}$$

where Λ is the poling period (coherence length) of the crystal. Thus for any desired set of generated idler frequencies, one must only fulfill the requirement of conservation of energy between the pump, signal, and idler photons, because in principle, the wave-vector mismatch can always be chosen to be zero, by simply adjusting Λ.

A.3 Periodically Poled Lithium Niobate (PPLN)

Lithium niobate ($LiNbO_3$) is the nonlinear medium used in our OPO's, and dominates the market of quasi phase-matched OPO's due to its wide transparency (0.33 - 4.5 μm), high nonlinear coefficient, and ease of periodic domain inversion[2]. Given that only a narrow tuning range (typically < 100 cm^{-1}) can be achieved with a single poling length, crystals can be manufactured having multiple poling regions on a single crystal. For the Linos OPO used in our studies, the PPLN crystal has 33 different polings needed to cover the 2 - 4 μm range. Course tuning of the OPO is achieved by translating the crystal to select out the desired poling (Λ). The discrete frequency steps that the different poling regions impose can be eliminated with a "fan out" design [366], in which the poling distance is continuously varied as the crystal is translated perpendicular to the laser beams. The degree to which the polings can be fanned out is limited by domain overlap, and thus smaller total tuning ranges have been achieved using standard dimension crystals. The discrete frequency regions of the periodically poled crystal

[2]Lithium niobate is a ferroelectric material, so its growth under electric fields can be used to create the domain inversion.

can be make to overlap by temperature tuning, removing the need for the fan out design. The crystals used in our OPO's had dimensions of 50 mm $\times$ 12 mm $\times$ 0.5 mm and are of the discrete periodic structure type.

A.4 PPLN Temperature Tuning

Because lithium niobate has a relatively large thermal expansion coefficient, the poling length can be varied by changing its temperature. Because of the importance in predicting the generated signal and idler frequencies from a specific grating period, a great deal of work has been focused on fitting the observed temperature dependence of the OPO frequencies to multi-parameter fits, which are given by the Sellmeier equations of Jundt [367]. Fully quantitative comparisons can be made of the observed and calculated OPO frequencies in the whole transparency region of lithium niobate. When comparing frequency calculations at several different temperatures of the crystal, typically only the grating period at room temperature is given.

One of the drawbacks of lithium niobate is its relatively low damage threshold and the fact that it suffers from photorefractive effects. Photorefractive effects can cause permanent damage, however they also play an important role in disrupting phasematching. At elevated temperatures these effects are found to be minimized and for this reason the PPLN crystals are mounted in an oven which is operated above 130 ^{0}C. For the Linos OPO with 33 poling regions, tuning the temperature from 150 - 180 ^{0}C gives ~10% overlap in frequency between 2 poling regions.

A.5 Linos photonics OS-4000

A schematic of the OS-4000 purchased from Linos photonics is shown in Figure A.2. The PPLN crystal is placed in a cavity made to resonate both the signal and pump beams in order to reduce the threshold for parametric gain. The side of the PPLN crystal facing the pump laser is coated to be highly reflective for the pump (R~92%) and signal (R~99.5%) beams and

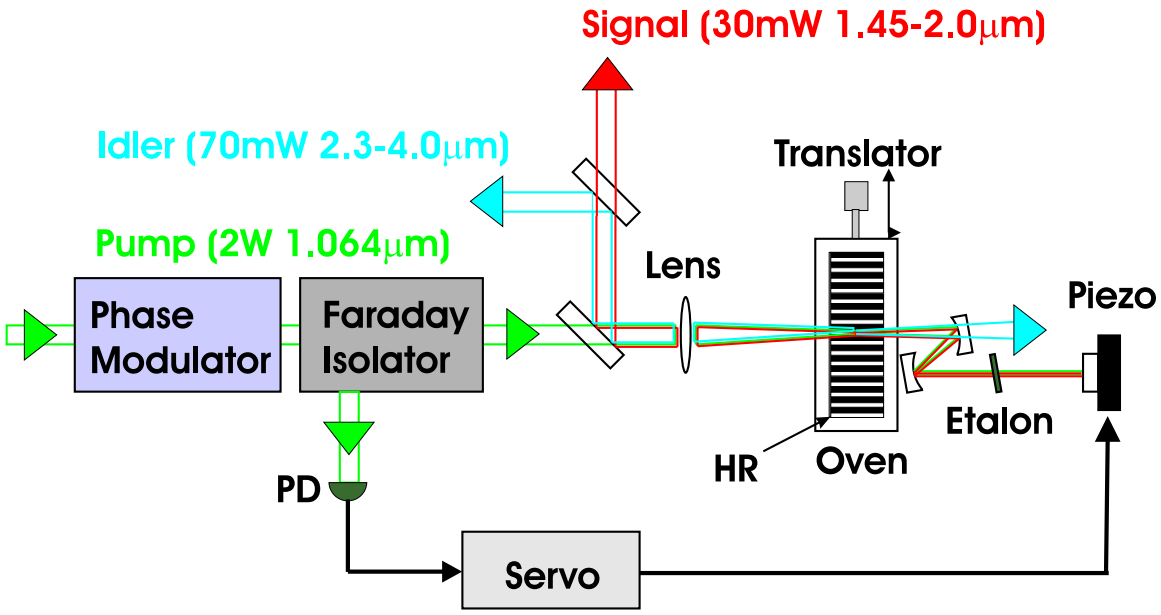

Figure A.2: A schematic diagram of the OS-4000 OPO produced by Linos Photonics. The OPO has a tuning range of 1.45 - 2.0 μm in the signal beam and 2.3 - 4.0 μm in the idler beam in a doubly resonant oscillator configuration.

anti-reflection coated for the idler (R~3%). This makes one of the mirrors of the cavity. The other side of the crystal is anti-reflection coated for all three frequencies. The other end mirror is mounted on a piezo element in order to vary the cavity length, which is needed to maintain the pump resonance. The pump laser is a 1064 nm diode pumped CW Nd:YAG laser which is continuously tunable over ~7 GHz by tuning the temperature of the YAG crystal. Two watts of power from the pump is focused into the center of the PPLN crystal. The intensity of the back-reflected pump is separated out from the incoming beam using a Faraday isolator, and is used as the error signal for cavity resonance [368]. The signal beam produced by the OPO must also be resonant in the cavity and the idler beam will simply fulfill the conservation of energy requirement. The two mirrors which make the cavity a Z-configuration are used to couple the idler beam out of the cavity, which is necessary for single frequency stability due to idler feedback from trying to becoming resonant in the cavity. A solid undoped YAG etalon (50% R for the signal, <1% R for the pump, with 0.19 - 1.0 mm thickness) may also be placed in the cavity, and is used to select a particular signal cavity mode. Course frequency selection of the OPO is achieved by translating one of the 33 poling regions of the crystal into the pump beam,

typically resulting in jumps of 50 - 100 cm^{-1} in the idler. As mentioned above, the frequencies in between these jumps can be reached by changing the temperature of the crystal, which was typically kept in the range of 155 - 180 ^{0}C.

The OS-4000 produces idler powers of approximately 50-70 mW and signal powers of approximately 20 mW, which are found to vary only slightly from poling to poling. The natural linewidth is approximately 150 kHz (from the manufacturer) due to the narrow bandwidth pump source used and the frequency drift is on the order of 50 MHz / hour. The cavity mode spacing is ~450 MHz. Mode-hop scanning is accomplished by keeping the pump frequency fixed, and scanning the signal frequency by rotating the solid etalon with a galvo (Cambridge Technologies - model 6210). The idler frequency makes equal in magnitude frequency hops but opposite in direction in order to maintain conservation of energy ($\omega_{pump} = \omega_{signal} + \omega_{idler}$). To scan more than a few wavenumbers, the PPLN temperature must also be adjusted to keep the OPO resonating on the correct etalon mode, otherwise it will hop back by 1 free spectral range of the etalon. Due to walk off loses, the zero position for the etalon is at normal incidence to the signal beam and the etalon is tilted just far enough to scan one free spectral range before being reset. The frequency tuning with angle is nearly quadratic, so calibration tables are used to linearize the scan in time. Because the temperature tuning of the PPLN crystal and the rotation of the etalon would normally change the cavity length, the locking scheme to the pump frequency actively counteracts these changes.

Continuous tuning of the signal and idler frequencies is made possible by changing the pump frequency. Due to the fact that the signal and pump beams must stay resonant in the cavity, the tuning of the three beams is given by:

$$\frac{\Delta\omega_{idler}}{\omega_{idler}} = \frac{\Delta\omega_{signal}}{\omega_{signal}} = \frac{\Delta\omega_{pump}}{\omega_{pump}}$$

Since the pump laser can be tuned approximately 7 GHz before a mode hop occurs, this amounts to only a ~2 GHz change in the idler frequency. While in principle it is then pos-

sible to reset the pump laser frequency, and use the etalon to stay on the current mode, this method of scanning was found to be very slow, and typically resulted in frequency jumps when resetting the pump. Thus we have mainly used this laser source for lower resolution mode-hop scanning, and as a pump source in the double resonance studies.

A.6 Home built OPO's

Doubly resonant oscillators (DRO) like the Linos OPO have typically been plagued with difficulties to achieve long continuous scans due to the fact that both the pump and the signal frequencies need to stay resonant in the same cavity. This problem can be addressed by making two separate cavities, which allows the pump and signal frequencies to be tuned independently. This has a considerable advantage given that if the signal frequency is made to stay fixed, the tuning behavior of the idler beam is exactly the same as that of the pump. Another way of achieving this tuning behavior is to resonate the signal frequency only (SRO). Indeed, this setup is the easiest to build, however due to the lack of pump enhancement, a much higher oscillation threshold is observed and so higher power pump sources must be used. For comparison the oscillation threshold of the Linos OPO is on the order of 200 mW, where as in a single resonant design the threshold is typically > 3 Watts. Interestingly the output powers of the idler beams are found to be much larger in the single resonant design than in the DRO, despite similar effective pump power in the crystal.

The design of our SRO-PPLN-OPO is shown schematically in Figure A.3, and is modeled after the design of Bisson and van Herpen [225, 369]. An excellent guide to the workings of these OPO's is given in the thesis of Maarten van Herpen (Katholieke Universiteit Nijmegen - 2004). The pump source is a Versadisk-1030-20 (ELS) which provides 20 Watts at 1030 nm. Tuning of the pump frequency is controlled by an etalon and birefringent filter and over the range of 1025 - 1035 nm, a minimum of 10 W of power is produced. At the current time there is no option for automated tuning so this has been developed in house. The pump is focused

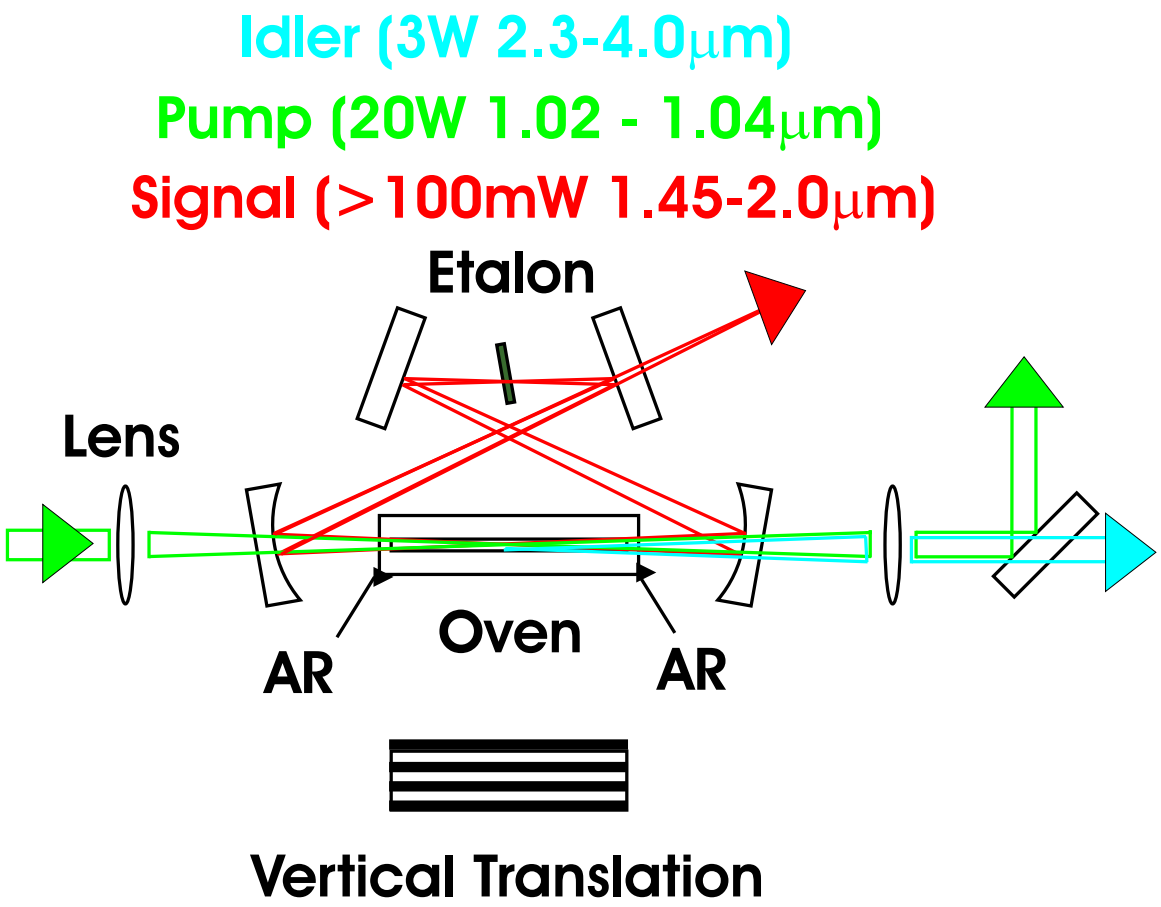

Figure A.3: A schematic diagram of an OPO built in our laboratory. The idler tuning range covers 2 - 5μm utilizing only two different crystals and mirror sets, and produces up to 3W.

into the center of the PPLN crystal (0.5 mm $\times$ 12 mm $\times$ 50 mm - Crystal Technologies) which is in the center of a bowtie ring cavity, made to resonate the signal frequency only. The PPLN crystal has been anti-reflection coated on both surfaces for all three wavelengths. In contrast to the OS-4000, there are only 8 poling regions and they run down the long axis of the crystal. The need for fewer polings is due to the much wider tuning of the pump source. The crystal is mounted in an oven, and a translation stage is used to select out the desired poling. Using two different crystals and cavity optics sets, the idler frequency can be tuned from ~2 - 5 μm. The idler power of this setup is very high, generating up to 3 Watts in the range of ~2 - 4 μm. Since there is no output coupler in the cavity for the signal beam, four equal power beams are found exiting each of the cavity mirrors, however we have not measured their actual power. For longer wavelengths the idler power decreases significantly due to an absorption of the PPLN

itself, and van Herpen has measured a power of ~100 mW at 4.7 μm using a very similar setup to ours [369]. When fully aligned, the OPO exhibited an oscillation threshold of ~3 watts and a pump depletion of approximately 80%, which agrees with those previously reported. While the OPO tended to lase on a single longitudinal cavity mode, a solid etalon (an uncoated 0.4 mm thick piece of YAG - VLOC) was placed in the OPO resonator to enhance the signal frequency stability. The etalon is also needed in order to keep the signal frequency constant when tuning the pump laser. Due to the very wide tuning of the pump laser, the signal frequency will eventually jump by 1 free spectral range of the etalon however this can be prevented by also changing the temperature of the PPLN crystal. At the present time this OPO has only been used as a pump laser in our double-resonance experiments and has not been fully automated.

BIBLIOGRAPHY

[1] M. I. Lester et al., Faraday Disc. **118**, 373 (2001).

[2] D. M. Neumark, Phys. Chem. Comm. **5**, 76 (2002).

[3] T. Takayanagi and A. Wada, Chem. Phys. Lett. **338**, 195 (2001).

[4] T. Takayanagi and Y. Kurosaki, J. Chem. Phys. **109**, 8929 (1998).

[5] H. J. Werner et al., Chem. Phys. Lett. **328**, 500 (2000).

[6] H. J. Werner, W. Bian, and U. Manthe, Chem. Phys. Lett. **313**, 647 (1999).

[7] D. Skouteris et al., Science **286**, 1713 (1999).

[8] N. Balakrishnan, J. Chem. Phys. **121**, 5563 (2004).

[9] C. Murray and A. J. Orr-Ewing, Int. Rev. Phys. Chem. **23**, 435 (2004).

[10] D. Towsend et al., Science **306**, 1158 (2005).

[11] X. Zhang, J. Rheinecker, and J. M. Bowman, J. Chem. Phys. **122**, 114313 (2005).

[12] I. W. M. Smith, Chem. Phys. Lett. **49**, 112 (1977).

[13] J. J. Margitan and R. T. Watson, J. Phys. Chem. **86**, 3819 (1982).

[14] W. J. Marinelli and H. S. Johnston, J. Chem. Phys. **77**, 1225 (1982).

[15] M. Mozurkewich and S. W. Benson, J. Phys. Chem. **88**, 6429 (1984).

[16] M. Mozurkewich, J. J. Lamb, and S. W. Benson, J. Phys. Chem. **88**, 6435 (1984).

[17] L. Oudejans and R. E. Miller, Annu. Rev. Phys. Chem. **52**, 607 (2001).

[18] J. M. Hutson, Annu. Rev. Phys. Chem. **41**, 123 (1990).

[19] R. A. Loomis and M. I. Lester, Annu. Rev. Phys. Chem. **48**, 643 (1997).

[20] M. D. Wheeler, M. Tsiouris, M. I. Lester, and G. Lendvay, J. Chem. Phys. **112**, 6590 (2000).

[21] M. I. Lester, B. V. Pond, D. T. Anderson, L. B. Harding, and A. F. Wagner, J. Chem. Phys. **113**, 9889 (2000).

[22] M. D. Marshall, B. V. Pond, and M. I. Lester, J. Chem. Phys. **118**, 1196 (2003).

[23] J. B. Davey, M. E. Greenslade, M. D. Marshall, M. I. Lester, and M. D. Wheeler, J. Chem. Phys. **121**, 3009 (2004).

[24] R. W. Randall, C. C. Chuang, and M. I. Lester, Chem. Phys. Lett. **200**, 113 (1992).

[25] D. T. Moore, L. Oudejans, and R. E. Miller, J. Chem. Phys. **110**, 197 (1999).

[26] L. Oudejans, D. T. Moore, and R. E. Miller, J. Chem. Phys. **110**, 209 (1999).

[27] J. Warnatz, *Combustion Chemistry*, Springler-Verlag, New York, 1984.

[28] M. J. Frost, P. Sharkey, and I. W. M. Smith, J. Phys. Chem. **97**, 12254 (1993).

[29] J. P. Senosiain, C. B. Musgrave, and D. M. Golden, Int. J. Chem. Kin. **35**, 464 (2003).

[30] R. P. Wayne, *Chemistry of Atmospheres: An introduction to the Chemistry of the Atmospheres of Earth, the Planets, and their satellites*, Oxford University Press, Oxford, 1991.

[31] A. Engdahl and B. Nelander, J. Chem. Phys. **118**, 7797 (2003).

[32] R. D. Hunt and L. Andrews, J. Chem. Phys. **88**, 3599 (1988).

[33] A. M. Smith, J. Agreiter, M. Hartle, C. Engel, and V. E. Bondybey, Chem. Phys. **189**, 315 (1994).

[34] J. P. Toennies and A. F. Vilesov, Annu. Rev. Phys. Chem. **49**, 1 (1998).

[35] M. Hartmann, R. E. Miller, J. P. Toennies, and A. F. Vilesov, Phys. Rev. Lett. **75**, 1566 (1995).

[36] K. Nauta and R. E. Miller, Science **283**, 1895 (1999).

[37] K. Nauta and R. E. Miller, Science **287**, 293 (2000).

[38] J. P. Toennies and A. F. Vilesov, Annu. Rev. Phys. Chem. **49**, 1 (1998).

[39] G. E. Douberly and R. E. Miller, J. Phys. Chem. B **107**, 4500 (2003).

[40] G. E. Douberly, J. M. Merritt, and R. E. Miller, Phys. Chem. Chem. Phys. **7**, 463 (2005).

[41] K. K. Lehmann and G. Scoles, Science **279**, 2065 (1998).

[42] L. D. Landau, J. Phys. USSR **5**, 71 (1941).

[43] L. Tisza, Nature **171**, 913 (1938).

[44] E. Andronikashvilli, J. Phys. **3**, 201 (1946).

[45] E. B. Gordon, V. V. Khmelenko, A. A. Pelmenev, E. A. Popov, and O. F. Pugachev, Chem. Phys. Lett. **155**, 301 (1989).

[46] R. E. Boltnev et al., Chem. Phys. **189**, 367 (1994).

[47] E. B. Gordon, A. A. Pelmenev, O. F. Pugachev, and V. V. Khmelenko, Chem. Phys. **61**, 35 (1981).

[48] E. B. Gordon, L. P. Mezhov-Deglin, O. F. Pugachev, and V. V. Khmelenko, Chem. Phys. Lett. **54**, 282 (1978).

[49] E. B. Gordon et al., Chem. Phys. **170**, 411 (1993).

[50] R. E. Boltnev et al., Low Temp. Phys. **23**, 567 (1997).

[51] E. W. Becker, Z. Phys. D **3**, 101 (1986).

[52] A. Scheidemann, B. Schilling, J. P. Toennies, and J. A. Northby, Physica. Rev. B **165**, 135 (1990).

[53] S. Goyal, D. L. Schutt, and G. Scoles, Phys. Rev. Lett. **69**, 933 (1992).

[54] T. E. Gough, M. Mengel, P. A. Rowntree, and G. Scoles, J. Chem. Phys. **83**, 4958 (1985).

[55] R. N. Barnett and K. B. Whaley, J. Chem. Phys. **99**, 9730 (1993).

[56] D. M. Brink and S. Stringari, Z. Phys. D **15**, 257 (1990).

[57] S. Grebenev et al., J. Chem. Phys. **112**, 4485 (2000).

[58] S. Grebenev, J. P. Toennies, and A. F. Vilesov, Science **279**, 2083 (1998).

[59] Y. Kwon and K. B. Whaley, Phys. Rev. Lett. **83**, 4108 (1999).

[60] Y. Kwon and K. B. Whaley, J. Chem. Phys. **119**, 1986 (2003).

[61] E. W. Draeger and D. M. Ceperley, Phys. Rev. Lett. **90**, 065301 (2003).

[62] C. Callegari et al., Phys. Rev. Lett. **83**, 5058 (1999).

[63] K. K. Lehmann and C. Callegari, J. Chem. Phys. **117**, 1595 (2002).

[64] N. Portner, J. P. Toennies, and A. F. Vilesov, J. Chem. Phys. **117**, 6054 (2002).

[65] M. Hartmann, F. Mielke, J. P. Toennies, A. F. Vilesov, and G. Benedek, Phys. Rev. Lett. **76**, 4560 (1996).

[66] A. J. Leggett, Rev. Mod. Phys. **71**, S318 (1999).

[67] S. Grebenev, B. Sartakov, J. P. Toennies, and A. F. Vilesov, Phys. Rev. Lett. **89**, 225301 (2003).

[68] S. Grebenev, B. G. Sartakov, J. P. Toennies, and A. F. Vilesov, J. Chem. Phys. **118**, 8656 (2003).

[69] K. Nauta and R. E. Miller, J. Chem. Phys. **115**, 10254 (2001).

[70] Y. Kwon and K. B. Whaley, Phys. Rev. Lett. **89**, 273401 (2003).

[71] Y. Kwon, P. Huang, M. V. Patel, D. Blume, and K. B. Whaley, J. Chem. Phys. **113**, 6469 (2000).

[72] F. Paesani and K. B. Whaley, J. Chem. Phys. **121**, 5293 (2004).

[73] K. Nauta and R. E. Miller, J. Chem. Phys. **115**, 10138 (2001).

[74] C. Callegari, K. K. Lehmann, R. Schmied, and G. Scoles, J. Chem. Phys. **115**, 10090 (2001).

[75] M. Y. Choi et al., Int. Rev. Phys. Chem. (2006).

[76] K. Nauta and R. E. Miller, J. Chem. Phys. **113**, 9466 (2000).

[77] K. Nauta and R. E. Miller, J. Chem. Phys. **115**, 8384 (2001).

[78] K. Nauta and R. E. Miller, Chem. Phys. Lett. **350**, 225 (2001).

[79] C. Callegari et al., J. Chem. Phys. **113**, 4636 (2000).

[80] K. E. Schmidt, S. Moroni, A. Sarsa, S. Fantoni, and S. Baroni, Phys. Rev. Lett. **90**, 143401 (2003).

[81] F. Paesani and K. B. Whaley, J. Chem. Phys. **121**, 4180 (2004).

[82] K. K. Lehmann, J. Chem. Phys. **114**, 4643 (2001).

[83] R. E. Zillich, Y. Kwon, and K. B. Whaley, Phys. Rev. Lett. **93**, 250401 (2004).

[84] C. M. Lindsay and R. E. Miller, J. Chem. Phys. **122**, 104306 (2005).

[85] P. A. Block, K. W. Jucks, L. G. Pedersen, and R. E. Miller, Chem. Phys. **139**, 15 (1989).

[86] R. J. Bemish, P. A. Block, L. G. Pedersen, W. T. Yang, and R. E. Miller, J. Chem. Phys. **99**, 8585 (1993).

[87] A. Guirao, M. Pi, and M. Barranco, Z. Phys. D **21**, 185 (1991).

[88] E. L. Knuth, B. Schilling, and J. P. Toennies, *On Scaling Parameters for Predicting Cluster Sizes in Free Jets*, volume 19, pages 270–276, Oxford Univ. Press, Oxford, 1995.

[89] E. L. Knuth and U. Henne, J. Chem. Phys. **110**, 2664 (1999).

[90] H. Buchenau, E. L. Knuth, J. A. Northby, J. P. Toennies, and C. Winkler, J. Chem. Phys. **92**, 6875 (1990).

[91] M. Lewerenz, B. Schilling, and J. P. Toennies, Chem. Phys. Lett. **206**, 381 (1993).

[92] J. Harms, J. P. Toennies, and F. Dalfovo, Phys. Rev. B **58**, 3341 (1998).

[93] P. Sindzingre, M. L. Klein, and D. M. Ceperley, Phys. Rev. Lett. **63**, 1601 (1989).

[94] K. K. Lehmann, Mol. Phys. **97**, 645 (1999).

[95] M. Lewerenz, B. Schilling, and J. P. Toennies, J. Chem. Phys. **106**, 5787 (1997).

[96] F. Stienkemeier, J. Higgins, W. E. Ernst, and G. Scoles, Phys. Rev. Lett. **74**, 3592 (1995).

[97] O. Bunermann, M. Mudrich, M. Weidemuller, and F. Stienkemeier, J. Chem. Phys. **121**, 8880 (2004).

[98] F. Stienkemeier, J. Higgins, W. E. Ernst, and G. Scoles, Z. Phys. B **98**, 413 (1995).

[99] F. Stienkemeier et al., Z. Phys. D **38**, 253 (1996).

[100] F. Stienkemeier, F. Meier, and H. O. Lutz, J. Chem. Phys. **107**, 10816 (1997).

[101] F. Ancilotto, P. B. Lerner, and M. W. Cole, J.Low Temp. Phys. **101**, 1123 (1995).

[102] M. Lewerenz, B. Schilling, and J. P. Toennies, J. Chem. Phys. **102**, 8191 (1995).

[103] E. Hirota, V. I. Goldanskii, R. Gomer, F. P. Schafer, and J. P. Toennies, *High-Resolution Spectroscopy of Transient Molecules*, Springer-Verlag, Berlin, 1985.

[104] C. L. Morter et al., Chem. Phys. Lett. **195**, 316 (1992).

[105] L. Yuan, J. DeSain, and R. F. Curl, J. Mol. Spectrosc. **187**, 102 (1998).

[106] D. W. Kohn, H. Clauberg, and P. Chen, Rev. Sci. Instrum. **63**, 4003 (1992).

[107] M. R. Cameron and S. H. Kable, Rev. Sci. Instrum. **67**, 283 (1996).

[108] K. D. Setzer, E. H. Fink, A. B. Alekseyev, H. P. Liebermann, and R. J. Buenker, J. Mol. Spectrosc. **206**, 181 (2001).

[109] M. Kareev, M. Sablier, and T. Fujii, J. Phys. Chem. A **104**, 7218 (2000).

[110] R. S. Ram, P. F. Bernath, and K. H. Hinkle, J. Chem. Phys. **110**, 5557 (1999).

[111] V. Aquilanti et al., J. Phys. Chem. A **101**, 6523 (1997).

[112] H. Bai and B. S. Ault, Chem. Phys. Lett. **188**, 126 (1992).

[113] P. Biggs, A. A. Boyd, C. E. Canosamas, D. M. Joseph, and R. P. Wayne, Measurement Science and Technology **2**, 675 (1991).

[114] J. U. Grabow, N. Heineking, and W. Stahl, Z. Naturforsch. A **46**, 914 (1991).

[115] F. J. Lovas, R. D. Suenram, T. Ogata, and S. Yamamoto, Astrophys. J. **399**, 325 (1992).

[116] D. T. Anderson, S. Davis, T. S. Zwier, and D. J. Nesbitt, Chem. Phys. Lett. **258**, 207 (1996).

[117] S. Davis, M. Farnik, D. Uy, and D. J. Nesbitt, Chem. Phys. Lett. **344**, 23 (2001).

[118] L. Li, J. T. Graham, and W. Weltner, J. Phys. Chem. A **105**, 11018 (2001).

[119] H. Wang, Z. Lu, and F. A. Kong, Chinese Chem. Lett. **12**, 971 (2001).

[120] M. L. Tsao, Z. D. Zhu, and M. S. Platz, J. Phys. Chem. A **105**, 8413 (2001).

[121] K. Kobayashi and T. J. Sears, Can. J. Phys. **79**, 347 (2001).

[122] C. A. Taatjes and J. F. Hershberger, Annu. Rev. Phys. Chem. **52**, 41 (2001).

[123] I. U. Goldschleger, A. V. Akimov, E. Y. Misochko, and C. A. Wight, J. Mol. Spectrosc. **205**, 269 (2001).

[124] G. Bucher, M. Halupka, C. Kolano, O. Schade, and W. Sander, Eur. J. Org. Chem. **2001**, 545 (2001).

[125] B. C. Chang et al., J. Mol. Spectrosc. **202**, 131 (2000).

[126] H. J. Deyerl, I. Fischer, and P. Chen, J. Chem. Phys. **110**, 1450 (1999).

[127] S. Davis, D. T. Anderson, G. Duxbury, and D. J. Nesbitt, J. Chem. Phys. **107**, 5661 (1997).

[128] X. Zhang et al., Rev. Sci. Instrum. **74**, 3077 (2003).

[129] J. M. Rost, J. C. Griffin, B. Friedrich, and D. R. Herschbach, Phys. Rev. Lett. **68**, 1299 (1992).

[130] P. A. Block, E. J. Bohac, and R. E. Miller, Phys. Rev. Lett. **68**, 1303 (1992).

[131] F. Dong and R. E. Miller, Science **298**, 1227 (2002).

[132] T. E. Gough, R. E. Miller, and G. Scoles, Faraday Disc. **71**, 77 (1981).

[133] W. L. Ebenstein and J. S. Muenter, J. Chem. Phys. **80**, 3989 (1984).

[134] P. L. Stiles, K. Nauta, and R. E. Miller, Phys. Rev. Lett. **90**, 135301 (2003).

[135] P. Botschwina, R. Oswald, J. Flugge, and M. Horn, Z. Phys. Chem. **188**, 29 (1995).

[136] N. M. Marinov et al., Combust. Flame **114**, 192 (1998).

[137] P. R. Westmoreland, A. M. Dean, J. B. Howard, and J. P. Longwell, J. Phys. Chem. **93**, 8171 (1989).

[138] U. Alkemade and K. H. Homann, Z. Phys. Chem. **161**, 19 (1989).

[139] S. E. Stein, J. A. Walker, M. M. Suryan, and A. Fahr, Symp. (Int.) Combust. **23**, 85 (1990).

[140] P. Botschwina, M. Horn, R. Oswald, and S. Schmatz, J. Electron. Spectrosc. **108**, 109 (2000).

[141] H. Honjou, M. Yoshimine, and J. Pacansky, J. Phys. Chem. **91**, 4455 (1987).

[142] A. Hinchcliffe, J. Mol. Struct. **37**, 295 (1977).

[143] C. H. Wu and R. D. Kern, J. Phys. Chem. **91**, 6291 (1987).

[144] N. M. Marinov, M. J. Castaldi, C. F. Melius, and W. Tsang, Combust. Sci. Technol. **128**, 295 (1997).

[145] I. Glassman, Symp. (Int.) Combust. **22**, 295 (1988).

[146] J. A. Miller, Symp. (Int.) Combust. **26**, 461 (1996).

[147] J. M. Goodings, D. K. Bohme, and C. W. Ng, Combust. Flame **36**, 27 (1979).

[148] D. B. Olson and H. F. Calcote, Symp. (Int.) Combust. **18**, 453 (1981).

[149] R. W. Fessender and R. H. Schuler, J. Chem. Phys. **38**, 2147 (1963).

[150] P. H. Kasai, J. Am. Chem. Soc. **94**, 5950 (1972).

[151] D. A. Ramsey and P. Thistlethwaite, Can. J. Phys. **44**, 1381 (1966).

[152] M. E. Jacox and D. E. Milligan, Chem. Phys. **4**, 45 (1974).

[153] M. Wyss, E. Riaplov, and J. P. Maier, J. Chem. Phys. **114**, 10355 (2001).

[154] J. W. Huang and W. R. Graham, J. Chem. Phys. **93**, 1583 (1990).

[155] G. Maier et al., J. Chem. Phys. **91**, 4763 (1989).

[156] J. M. Oakes and G. B. Ellison, J. Am. Chem. Soc. **105**, 2969 (1983).

[157] D. W. Minsek and P. Chen, J. Phys. Chem. **94**, 8399 (1990).

[158] B. Nagels, P. Bakker, L. J. F. Hermans, and P. L. Chapovsky, Phys. Rev. A **57**, 4322 (1998).

[159] H. J. Deyerl, I. Fischer, and P. Chen, J. Chem. Phys. **111**, 3441 (1999).

[160] K. Tanaka, T. Harada, K. Sakaguchi, K. Harada, and T. Tanaka, J. Chem. Phys. **103**, 6450 (1995).

[161] K. Tanaka, Y. Sumiyoshi, Y. Ohshima, Y. Endo, and K. Kawaguchi, J. Chem. Phys. **107**, 2728 (1997).

[162] P. Botschwina, M. Horn, J. Fluegge, and S. Seeger, J. Chem. Soc. Faraday Trans. **89**, 2219 (1993).

[163] R. Frochtenicht, J. P. Toennies, and A. F. Vilesov, Chem. Phys. Lett. **229**, 1 (1994).

[164] S. Goyal, D. L. Schutt, and G. Scoles, J. Phys. Chem. **97**, 2236 (1993).

[165] F. Stienkemeier, W. E. Ernst, J. Higgins, and G. Scoles, J. Chem. Phys. **102**, 615 (1995).

[166] K. Nauta and R. E. Miller, J. Chem. Phys. **113**, 10158 (2000).

[167] S. R. Yates and J. Gan, J. Agric. Food Chem. **46**, 755 (1998).

[168] Y. R. Lee and S. M. Lin, J. Chem. Phys. **108**, 134 (1998).

[169] J. C. Evans and R. A. Nyquist, Spectrochim. Acta **19**, 1153 (1963).

[170] T. Shimanouchi, J. Phys. Chem. Ref. Data **6**, 993 (1977).

[171] A. K. Wilson, D. E. Woon, K. A. Peterson, and T. H. Dunning, J. Chem. Phys. **110**, 7667 (1999).

[172] H. J. Werner et al., *MOLPRO, a package of ab initio programs*, Number 2002.1, Birmingham, UK, 2002.

[173] J. Kupper, J. M. Merritt, and R. E. Miller, J. Chem. Phys. **117**, 647 (2002).

[174] K. Nauta and R. E. Miller, *The Spectroscopy of Molecules and Unique Clusters in Superfluid Liquid Helium Droplets*, pages 775–792, Springer Verlag, 2001.

[175] P. L. Chapovsky and L. J. F. Hermans, Annu. Rev. Phys. Chem. **50**, 315 (2000).

[176] J. W. Cooley, Math. Comput. **15**, 363 (1961).

[177] M. Horn, M. Oswald, R. Oswald, and P. Botschwina, Phys. Chem. Chem. Phys. **99**, 323 (1995).

[178] P. Botschwina, *Personal Communication*, 2002.

[179] M. L. Dubernet and J. Hutson, J. Phys. Chem. A **98**, 5844 (1994).

[180] C. S. Maierle, G. C. Schatz, M. S. Gordon, P. Mccabe, and J. N. Connor, J. Chem. Soc. Faraday Trans. **93**, 709 (1997).

[181] P. Jungwirth, P. Zdanska, and B. Schmidt, J. Phys. Chem. A **102**, 7241 (1998).

[182] M. Bittererova and S. Biskupic, Chem. Phys. Lett. **299**, 145 (1999).

[183] M. Meuwly and J. M. Hutson, J. Chem. Phys. **112**, 592 (2000).

[184] M. Meuwly and J. M. Hutson, Phys. Chem. Chem. Phys. **2**, 441 (2000).

[185] J. Klos, G. Chalasinski, H. Werner, and M. M. Szczesniak, J. Chem. Phys. **115**, 3085 (2003).

[186] W. B. Zeimen, J. Klos, G. C. Groenenboom, and A. Avoird, J. Phys. Chem. **107**, 5110 (2003).

[187] D. M. Neumark, Annu. Rev. Phys. Chem. **43**, 153 (1992).

[188] K. Liu, A. Kolessov, J. W. Partin, I. Bezel, and C. Wittig, Chem. Phys. Lett. **299**, 374 (1999).

[189] K. Imura et al., J. Mol. Struct. **552**, 137 (2000).

[190] L. Andrews and R. D. Hunt, J. Chem. Phys. **89**, 3502 (1988).

[191] R. D. Hunt and L. Andrews, J. Phys. Chem. **92**, 3769 (1988).

[192] B. S. Ault, J. Chem. Phys. **68**, 4012 (1978).

[193] P. Zdanska, D. Nachtigallova, P. Nachtigall, and P. Jungwirth, J. Chem. Phys. **115**, 5974 (2001).

[194] M. J. Frisch et al., *Gaussian 03, Revision C.02, Gaussian, Inc., Wallingford, CT*, 2004.

[195] S. F. Boys and F. Bernardi, Mol. Phys. **19(4)**, 553 (1970).

[196] K. A. Peterson, D. Figgen, E. Goll, H. Stoll, and M. Dolg, J. Chem. Phys. **119**, 11113 (2003).

[197] M. Hartmann, R. E. Miller, J. P. Toennies, and A. F. Vilesov, Science **272**, 1631 (1996).

[198] B. K. Nauta and R. E. Miller, J. Chem. Phys. **117**, 4846 (2002).

[199] K. Nauta, D. T. Moore, and R. E. Miller, Faraday Disc. **113**, 261 (1999).

[200] C. H. Townes and A. L. Schawlow, *Microwave Spectroscopy*, Dover Publications, Inc., New York, 1975.

[201] M. L. Dubernet and J. M. Hutson, J. Chem. Phys. **101**, 1939 (1994).

[202] R. A. Frosh and H. M. Foley, Phys. Rev. **88**, 1337 (1952).

[203] Y. Endo, H. Kohguchi, and Y. Ohshima, Faraday Disc. **97**, 341 (1994).

[204] R. T. Carter, I. M. Povey, H. Bitto, and J. R. Huber, J. Chem. Phys. **104**, 5365 (1996).

[205] V. Jaccarino, J. G. King, R. A. Satten, and H. H. Stroke, Phys. Rev. **94**, 1798 (1954).

[206] H. H. Brown and J. G. King, Phys. Rev. **142**, 53 (1966).

[207] J. Brown and A. Carrington, *Rotational Spectroscopy of Diatomic Molecules*, Cambridge molecular science, 2003.

[208] Z. S. Huang, K. W. Jucks, and R. E. Miller, J. Chem. Phys. **85**, 6905 (1986).

[209] K. Nauta and R. E. Miller, J. Chem. Phys. **115**, 4508 (2001).

[210] N. N. Greenwood and A. Earnshaw, *Chemistry of the Elements*, Pergamon Press, Oxford, 1984.

[211] L. D. Davis, B. T. Feld, C. W. Zabel, and J. R. Zacharias, Phys. Rev. **76**, 1076 (1949).

[212] N. Halberstadt and K. C. Janda, Chem. Phys. Lett. **282**, 409 (1998).

[213] B. E. Callicoatt, K. Forde, L. F. Jung, T. Ruchti, and K. C. Janda, J. Chem. Phys. **109**, 10195 (1998).

[214] A. Scheidemann, B. Schilling, and J. P. Toennies, J. Phys. Chem. **97**, 2128 (1993).

[215] B. E. Callicoatt et al., J. Chem. Phys. **108**, 9371 (1998).

[216] T. Ruchti, K. Forde, B. E. Callicoatt, H. Ludwigs, and K. C. Janda, J. Chem. Phys. **109**, 10679 (1998).

[217] E. P. Hunter and S. G. Lias, J. Phys. Chem. Ref. Data **27**, 413 (1998).

[218] L. W. Buxton, E. J. Campbell, M. R. Keenan, T. J. Balle, and W. H. Flygare, Chem. Phys. **54**, 173 (1981).

[219] G. T. Fraser and A. S. Pine, J. Chem. Phys. **85**, 2502 (1986).

[220] M. Meuwly and J. M. Hutson, J. Chem. Phys. **119**, 8873 (2003).

[221] R. N. Sileo and T. A. Cool, J. Chem. Phys. **65**, 117 (1974).

[222] A. V. Fishchuk, P. E. S. Wormer, and A. Avoird, J. Phys. Chem. A (2006).

[223] A. V. Fishchuk, G. C. Groenenboom, and A. Avoird, J. Phys. Chem. A (2006).

[224] M. Jeziorska, P. Jankowski, and B. Jeziorski, J. Chem. Phys. **113**, 2957 (2000).

[225] F. J. M. Harren, S. Li, S. E. Bisson, and M. M. J. W. V. Herpen, Appl. Phys. B **75**, 329 (2002).

[226] C. Kreher, R. Theinl, and K. H. Gericke, J. Chem. Phys. **104**, 4481 (1996).

[227] B. K. Decker, G. He, I. Tokue, and R. G. Macdonald, J. Phys. Chem. A **105**, 5759 (2001).

[228] R. B. Metz, J. M. Pfeiffer, J. D. Thoemke, and F. F. Crim, Chem. Phys. Lett. **221**, 347 (1994).

[229] D. Troya, M. Gonzalez, G. S. Wu, and G. C. Schatz, J. Phys. Chem. A **105**, 2285 (2001).

[230] L. B. Harding, J. Phys. Chem. **100**, 10123 (1996).

[231] J. de Juan, S. Callister, H. Reisler, G. A. Segal, and C. Wittig, J. Chem. Phys. **89**, 1977 (1988).

[232] I. R. Sims and I. W. M. Smith, J. Chem. Soc. Faraday Trans. 2 **85**, 915 (1989).

[233] M. J. Frost, I. W. M. Smith, and R. D. Spencer-Smith, J. Chem. Soc. Faraday Trans. 2 **89**, 2355 (1993).

[234] J. M. Pfeiffer, R. B. Metz, J. D. Thoemke, E. W. III, and F. F. Crim, J. Chem. Phys. **104**, 4490 (1995).

[235] C. Kreher, J. L. Rinnenthal, and K. H. Gericke, J. Chem. Phys. **108**, 3154 (1998).

[236] R. D. Hunt and L. Andrews, Inorg. Chem. **26**, 3051 (1987).

[237] I. U. Goldschleger, A. V. Akimov, E. Y. Misochko, and C. A. Wight, Mendeleev Comm. , 43 (2001).

[238] A. C. Legon and J. C. Thorn, J. Chem. Soc. Faraday Trans. **89**, 4157 (1993).

[239] K. Hinds and A. C. Legon, Chem. Phys. Lett. **240**, 467 (1995).

[240] A. C. Legon and K. Hinds, Mol. Phys. **88**, 673 (1996).

[241] L. A. Curtiss, K. Raghavachari, G. W. Trucks, and J. A. Pople, J. Chem. Phys. **94**, 7221 (1991).

[242] M. W. Chase Jr, J. Phys. Chem. Ref. Data **4**, 1 (1998).

[243] F. M. Tao and Y. K. Pan, J. Chem. Phys. **97**, 4989 (1992).

[244] H. Lefebvre-Brion and R. W. Field, *Perturbations in the Spectra of Diatomic Molecules*, Academic Press, Orlando, Fla., 1986.

[245] J. E. Rode et al., J. Phys. Chem. A **109**, 11484 (2005).

[246] A. Nicklass, K. A. Peterson, A. Berning, H. J. Werner, and P. J. Knowles, J. Chem. Phys. **112**, 5624 (2000).

[247] R. J. LeRoy, *Level 7.7: A Computer Program for Solving the Radial Schrodinger Equation for Bound and Quasibound Levels*, 2005.

[248] W. W. Harper, S. A. Nizkorodov, and D. J. Nesbitt, J. Chem. Phys. **113**, 3670 (2000).

[249] T. J. Wallington et al., Int. J. Chem. Kin. **25**, 651 (1993).

[250] J. C. Polanyi and M. A. Nazar, Chem. Phys. **55**, 299 (1981).

[251] M. A. Wickramaaratchi, D. W. Setser, H. Hildebrandt, B. Korbitzer, and H. Heydtmann, Chem. Phys. **94**, 109 (1985).

[252] J. Zhou, J. J. Lin, W. Shiu, and K. Liu, J. Chem. Phys. **119**, 4997 (2003).

[253] W. Shiu, J. J. Lin, and K. Liu, Phys. Rev. Lett. **92**, 1 (4).

[254] J. Zhou, J. J. Lin, and K. Liu, J. Chem. Phys. **121**, 813 (2004).

[255] A. Gauss, J. Chem. Phys. **65**, 4365 (1976).

[256] J. C. Corchado and J. Espinosagarcia, J. Chem. Phys. **105**, 3160 (1996).

[257] T. Joseph, S. Rozeanne, and D. G. Truhlar, J. Chem. Phys. **87**, 7036 (1987).

[258] J. J. P. Stewart, J. Comput. Chem. **10**, 221 (1989).

[259] H. Kornweitz, A. Persky, and R. D. Levine, Chem. Phys. Lett. **289**, 125 (1998).

[260] M. J. T. Jordan and R. G. Gilbert, J. Chem. Phys. **102**, 5669 (1995).

[261] A. Persky, J. Phys. Chem. **100**, 689 (1996).

[262] D. Troya, J. Millan, I. Banos, and M. Gonzalez, J. Chem. Phys. **120**, 5181 (2004).

[263] M. E. Jacox, Chem. Phys. **42**, 133 (1979).

[264] G. L. Johnson and L. Andrews, J. Am. Chem. Soc. **102**, 5736 (1980).

[265] E. Y. Misochko, V. A. Benderskii, A. U. Goldschleger, A. V. Akimov, and A. F. Shestakov, J. Am. Chem. Soc. **117**, 11997 (1995).

[266] E. Y. Misochko et al., J. Chem. Phys. **106**, 3146 (1996).

[267] L. P. Davis, L. W. Burggraf, M. S. Gordon, and K. K. Baldridge, J. Am. Chem. Soc. **107**, 4415 (1984).

[268] Y. Okuno, S. Yokoyama, and S. Mashiko, J. Chem. Phys. **113**, 3136 (2000).

[269] J. C. Corchado and J. Espinosa-Garcia, J. Chem. Phys. **105**, 3152 (1996).

[270] C. Steel and A. F. Trotman-Dickenson, J. Chem. Soc. , 975 (1959).

[271] W. Forst and O. K. Rice, Can. J. Chem. **41**, 562 (1963).

[272] R. Renaud and L. C. Leitch, Can. J. Chem. **32**, 545 (1954).

[273] T. G. DiGiuseppe, J. W. Hudgens, and M. C. Lin, J. Phys. Chem. **86**, 36 (1982).

[274] X. D. Peng, R. Viswanathan, G. H. Smudde Jr, and P. C. Stair, Rev. Sci. Instrum. **63**, 3930 (1992).

[275] S. W. North, D. A. Blank, P. M. Chu, and Y. T. Lee, J. Chem. Phys. **102**, 792 (1994).

[276] T. Amano, P. F. Bernath, C. Yamada, Y. Endo, and E. Hirota, J. Chem. Phys. **77**, 5284 (1982).

[277] K. Nauta and R. E. Miller, J. Chem. Phys. **111**, 3426 (1999).

[278] R. B. L. Blanc, J. B. White, and P. F. Bernath, J. Mol. Spectrosc. **164**, 574 (1994).

[279] D. R. Lide, editor, *CRC Handbook of Chemistry and Physics*, volume 71, CRC Press, Boca Raton, 1990.

[280] P. F. Bernath, *Spectra of Atoms and Molecules*, Oxford University Press, New York, 1995.

[281] I. N. Levine, *Molecular Spectroscopy*, John Wiley and Sons, New York, 1975.

[282] C. Yamada, E. Hirota, and K. Kawaguchi, J. Chem. Phys. **75**, 5256 (1981).

[283] J. P. Toennies and A. F. Vilesov, Angew. Chem. Int. Ed. **43**, 2622 (2004).

[284] J. P. Toennies, A. F. Vilesov, and K. B. Whaley, Phys. Today. **54**, 31 (2001).

[285] E. J. Bohac and R. E. Miller, J. Chem. Phys. **98**, 2604 (1993).

[286] D. T. Moore and R. E. Miller, J. Chem. Phys. **118**, 9629 (2003).

[287] C. Murray, J. K. Pearce, S. Rudic, B. Retail, and A. J. Orr-Ewing, J. Phys. Chem. A **109**, 11093 (2005).

[288] Z. S. Huang and R. E. Miller, J. Chem. Phys. **86**, 6059 (1987).

[289] Z. S. Huang and R. E. Miller, J. Chem. Phys. **90**, 1478 (1989).

[290] J. M. Merritt, J. Kupper, and R. E. Miller, Phys. Chem. Chem. Phys. **7**, 67 (2005).

[291] S. Lebonnois, D. Toublanc, F. Hourdin, and P. Rannou, Icarus **152**, 384 (2001).

[292] X. Mercier, L. Pillier, J. F. Pauwels, and P. Desgroux, Comptes Rendus de l Academie des Sciences Serie Iv Physique Astrophysique **2**, 965 (2001).

[293] P. Casavecchia et al., Faraday Disc. **119**, 27 (2001).

[294] H. Lihavainen, Y. Viisanen, and M. Kulmala, J. Chem. Phys. **114**, 10031 (2001).

[295] G. A. Bethardy, F. J. Northrup, and R. G. Macdonald, J. Chem. Phys. **105**, 4533 (1996).

[296] D. L. Yang, T. Yu, M. C. Lin, and C. F. Melius, Chem. Phys. **177**, 271 (1993).

[297] L. R. Copeland, F. Mohammad, M. Zahedi, D. H. Volman, and W. M. Jackson, J. Chem. Phys. **96**, 5817 (1992).

[298] R. J. Balla, K. H. Casleton, J. S. Adams, and L. Pasternack, J. Phys. Chem. **95**, 8694 (1991).

[299] D. L. Yang, T. Yu, N. S. Wang, and M. C. Lin, Chem. Phys. **160**, 317 (1992).

[300] Q. Sun, D. L. Yang, J. M. Bowman, and M. C. Lin, J. Chem. Phys. **93**, 4730 (1990).

[301] D. L. Yang, T. Yu, M. C. Lin, and C. F. Melius, J. Chem. Phys. **97**, 222 (1992).

[302] W. P. Hess, J. L. Durant, and F. P. Tully, J. Phys. Chem. **93**, 6402 (1989).

[303] G. E. Bullock and R. Cooper, Trans. Faraday. Soc. **67**, 3258 (1971).

[304] V. S. Rao and A. K. Chandra, Chem. Phys. **192**, 247 (1995).

[305] R. J. Balla and L. Pasternack, J. Phys. Chem. **91**, 73 (1986).

[306] X. Li, N. Sayah, and W. M. Jackson, J. Chem. Phys. **81**, 833 (1984).

[307] I. R. Sims, J. L. Queffelec, D. Travers, J. Kartauser, and I. W. M. Smith, Chem. Phys. Lett. **211**, 461 (1993).

[308] D. L. Yang, M. C. Lin, K. Liu, and A. Wagner, *The Chemical Dynamics and Kinetics of Small Radicals*, World Scientific, 1996.

[309] G. Winnewisser, A. G. Maki, and D. R. Johnson, J. Mol. Spectrosc. **39**, 149 (1971).

[310] L. Herbert, I. W. M. Smith, and R. D. Spencer-Smith, Int. J. Chem. Kin. **24**, 791 (1992).

[311] N. Sayah, X. Li, J. F. Caballero, and W. M. Jackson, J. Photochem. Photobiol. A , 177 (1988).

[312] S. Petrie, J. Phys. Chem. A **106**, 11181 (2002).

[313] B. Wang, H. Hou, and Y. Gu, J. Phys. Chem. A **105**, 156 (2001).

[314] M. Solimannejad and M. E. Alikhani, Chem. Phys. Lett. **406**, 351 (2005).

[315] J. M. Merritt, S. Rudic, and R. E. Miller, J. Chem. Phys. **124**, 084301 (2006).

[316] K. Nauta and R. E. Miller, Chem. Phys. Lett. **346**, 129 (2001).

[317] C. J. Parkinson, P. M. Mayer, and L. Radom, J. Chem. Soc. Perkin Trans. 2 **11**, 2305 (1999).

[318] K. Sugawara, F. Ito, T. Nakanaga, H. Takeo, and C. Matsumura, J. Chem. Phys. **92**, 5328 (1990).

[319] P. D. Mallinson and A. Fayt, Mol. Phys. **32**, 473 (1976).

[320] I. Reinhard, C. Callegari, A. Conjusteau, K. K. Lehmann, and G. Scoles, Phys. Rev. Lett. **82**, 5036 (1999).

[321] S. Grebenev, M. Havenith, F. Madeja, J. P. Toennies, and A. F. Vilesov, J. Chem. Phys. **113**, 9060 (2000).

[322] M. Kunze, P. R. L. Markwick, N. Portner, J. Reuss, and M. Havenith, J. Chem. Phys. **116**, 7473 (2002).

[323] D. Kaur et al., Appl. Optics **29**, 119 (1990).

[324] O. Akin-Ojo, R. Bukowski, and K. Szalewicz, J. Chem. Phys. **119**, 8379 (2003).

[325] A. Slenczka, B. Dick, M. Hartmann, and J. P. Toennies, J. Chem. Phys. **115**, 10199 (2001).

[326] J. Tang, Y. Xu, A. R. W. McKellar, and W. Jager, Science **297**, 2030 (2002).

[327] X. Yunjie, W. Jager, J. Tang, and A. R. W. McKellar, Phys. Rev. Lett. **91**, 163401 (2003).

[328] B. Dick and A. Slenczka, J. Chem. Phys. **115**, 10206 (2001).

[329] K. Nauta and R. E. Miller, Phys. Rev. Lett. **82**, 4480 (1999).

[330] C. Callegari, A. Conjusteau, I. Reinhard, K. K. Lehmann, and G. Scoles, J. Chem. Phys. **113**, 10535 (2000).

[331] F. Winther et al., J. Mol. Spectrosc. **175**, 354 (1996).

[332] J. M. Merritt, G. E. Douberly, and R. E. Miller, J. Chem. Phys. **121**, 1309 (2004).

[333] C. M. Lindsay, W. K. Lewis, and R. E. Miller, J. Chem. Phys. **121**, 6095 (2004).

[334] T. E. Gough, R. E. Miller, and G. Scoles, Appl. Phys. Lett. **30**, 338 (1977).

[335] R. E. Miller, Science **240**, 447 (1988).

[336] Z. S. Huang, K. W. Jucks, and R. E. Miller, J. Chem. Phys. **85**, 3338 (1986).

[337] N. Halberstadt, P. Brechignac, J. A. Beswick, and M. Shapiro, J. Chem. Phys. **84**, 170 (1986).

[338] D. C. Dayton and R. E. Miller, Chem. Phys. Lett. **143**, 181 (1988).

[339] G. E. Douberly and R. E. Miller, J. Chem. Phys. **122**, 024306 (2005).

[340] A. Braun and M. Drabbels, Phys. Rev. Lett. **93**, 253401 (2004).

[341] L. Oudejans and R. E. Miller, Chem. Phys. **239**, 345 (1998).

[342] G. E. Ewing, J. Chem. Phys. **71**, 3143 (1979).

[343] Y. Tanaka, M. Kawasaki, and Y. Matsumi, Bull. Chem. Soc. Jap. **71**, 2539 (1998).

[344] D. J. Nesbitt and R. W. Field, J. Phys. Chem. **100**, 12735 (1996).

[345] J. Keske and B. H. Pate, Annu. Rev. Phys. Chem. **51**, 323 (2000).

[346] D. V. Lanzisera and L. Andrews, J. Phys. Chem. A **101**, 9660 (1997).

[347] D. V. Lanzisera and L. Andrews, J. Phys. Chem. A **101**, 7134 (1997).

[348] C. J. Cramer, *Essentials of computational chemistry : theories and models*, J. Wiley, New York, 2002.

[349] A. Zajaczkowski and J. Botor, Bulletin of Electrochemistry **7**, 378 (1991).

[350] R. Schmied et al., J. Chem. Phys. **121**, 2701 (2004).

[351] P. W. Atkins and R. S. Friedman, *Molecular Quantum Mechanics*, volume 3, Oxford University Press, New York, 1997.

[352] J. S. Coursey, D. J. Schwab, and R. A. Dragoset, *'Atomic Weights and Isotopic Composition'*, NIST, Physics Laboratory, Office of Electronic Commerce in Scientific and Engineering Data, 2004.

[353] K. Nauta, D. T. Moore, P. L. Stiles, and R. E. Miller, Science **292**, 481 (2001).

[354] J. V. V. Kasper, C. R. Pollock, R. F. Curl Jr, and F. K. Tittel, Chem. Phys. Lett. **77**, 211 (1981).

[355] S. Svanberg, G. Ecker, P. Lambropoulos, I. Sobelman, and H. Walther, *Atomic and Molecular Spectroscopy*, volume second, Springer-Verlag, Berlin Heidelburg, 1992.

[356] M. C. Heaven, Int. Rev. Phys. Chem. **24**, 375 (2005).

[357] M. A. Morrison and E. R. I. Abraham, In preparation (2006).

[358] K. von Haeften, A. Metzelthin, S. Rudolph, V. Staemmler, and M. Havenith, Phys. Rev. Lett. **95**, 215301 (2005).

[359] T. E. Gough, R. E. Miller, and G. Scoles, J. Mol. Spectrosc. **72**, 124 (1978).

[360] G. C. Dousmanis, T. M. Sanders Jr, and C. H. Townes, Phys. Rev. **100**, 1735 (1955).

[361] F. Vigliotti, M. Chergui, M. Dickgiesser, and N. Schwentner, Faraday Disc. **108**, 139 (1997).

[362] R. de Vivie and S. D. Peyerimhoff, J. Chem. Phys. **90**, 3660 (1988).

[363] S. E. Harris, Proc. IEEE **57**, 2096 (1969).

[364] M. M. Fejer, G. A. Magel, D. H. Jundt, and R. L. Byer, IEEE J. Quantum Elect. **28**, 2631 (1992).

[365] J. A. Armstrong, N. Bloembergen, J. Bucuing, and P. S. Pershan, Phys. Rev. **127**, 1918 (1962).

[366] P. E. Powers, T. J. Kulp, and S. E. Bisson, Optics Lett. **23**, 159 (1998).

[367] D. H. Jundt, Optics Lett. **22**, 1553 (1997).

[368] K. Schneider, P. Kramper, S. Schiller, and J. Mlynek, Optics Lett. **22**, 1293 (1997).

[369] M. M. J. W. van Herpen, S. E. Bisson, and F. J. M. Harren, Optics Lett. **28**, 2497 (2003).